

## Real-time reflectance-difference spectroscopy of GaAs molecular beam epitaxy homoepitaxial growth

A. Lastras-Martínez,<sup>1,a</sup> J. Ortega-Gallegos,<sup>1</sup> L. E. Guevara-Macías,<sup>1</sup>  
 O. Nuñez-Olvera,<sup>1</sup> R. E. Balderas-Navarro,<sup>1</sup> L. F. Lastras-Martínez,<sup>1</sup>  
 L. A. Lastras-Montañó,<sup>2</sup> and M. A. Lastras-Montañó<sup>3</sup>

<sup>1</sup>*Instituto de Investigación en Comunicación Óptica, Universidad Autónoma de San Luis Potosí, Alvaro Obregón 64, San Luis Potosí, SLP 78000, Mexico*

<sup>2</sup>*IBM T. J. Watson Research Center, Yorktown Heights, New York 10598, USA*

<sup>3</sup>*Department of Electrical and Computer Engineering, University of California, Santa Barbara, Santa Barbara, California 93106, USA*

(Received 23 December 2013; accepted 4 March 2014; published online 14 March 2014)

We report on real time-resolved Reflectance-difference (RD) spectroscopy of GaAs(001) grown by molecular beam epitaxy, with a time-resolution of 500 ms per spectrum within the 2.3–4.0 eV photon energy range. Through the analysis of transient RD spectra we demonstrated that RD line shapes are comprised of two components with different physical origins and determined their evolution during growth. Such components were ascribed to the subsurface strain induced by surface reconstruction and to surface stoichiometry. Results reported in this paper render RD spectroscopy as a powerful tool for the study of fundamental processes during the epitaxial growth of zincblende semiconductors. © 2014 Author(s). All article content, except where otherwise noted, is licensed under a Creative Commons Attribution 3.0 Unported License. [<http://dx.doi.org/10.1063/1.4868519>]

It is known that dimerized (001) surfaces of zincblende semiconductors are optically anisotropic.<sup>1</sup> Optical anisotropies have been associated to either the anisotropic response of surface dimers<sup>2–4</sup> or to the dimer-induced cubic-symmetry breakdown of the underlying atomic layers.<sup>5–8</sup> The anisotropic nature of (001) zincblende surfaces prompted the development of polarized-light techniques as optical, non-invasive probes for semiconductor surface characterization. One of such probes, Reflectance-difference spectroscopy (RDS),<sup>9</sup> is currently employed, along with Reflection high energy electron diffraction (RHEED), for the identification of GaAs (001) surface reconstructions.<sup>1,10</sup>

In addition to their application to static surfaces, reflectance-difference (RD) probes have been employed to study the dynamics of the epitaxial growth of zincblende semiconductors. Aspnes *et al.*,<sup>11</sup> first carried out single-wavelength dynamic RD measurements during GaAs Molecular beam epitaxy (MBE) growth and showed that abrupt changes in RD signal occur upon interrupting or allowing As flux while keeping the Ga flux on, thus following changes in surface stoichiometry. The combination of spectroscopic ellipsometry and RD turned out to be very successful in the investigation of complex surface dynamics under different growth conditions present in both MBE and Metal organic chemical vapor deposition (MOCVD) reactors, allowing for control during device fabrication.<sup>12</sup>

While single-wavelength RD measurements have shown the surface sensitivity of RD techniques to transients in surface stoichiometry occurring during epitaxy, the full potential of RD as a probe for monitoring epitaxial growth processes could be only realized through RD spectroscopic measurements. For zincblende semiconductors such an application demands of sub-second spectra acquisition times and the measurement of RD amplitudes in the  $10^{-4}$  to  $10^{-3}$  range. In the past these

<sup>a</sup>Electronic addresses: [alm@cactus.iico.uaslp.mx](mailto:alm@cactus.iico.uaslp.mx) and [alastras@gmail.com](mailto:alastras@gmail.com)



# Effect of surface states on the electrical properties of MBE grown modulation doped AlGaAs/GaAs

Alejandro Cisneros-de-la-Rosa, Irving Eduardo Cortes-Mestizo, Esteban Cruz-Hernández, and Víctor Hugo Méndez-García<sup>a)</sup>

Laboratorio Nacional, CIACyT-UASLP, Av. Sierra Leona #550, Col. Lomas 2a. Sección C.P. 78210, San Luis Potosí, S.L.P., Mexico

Luis Zamora-Peredo

Centro de Investigación en Micro y Nanotecnología, Universidad Veracruzana, Calzada Adolfo Ruiz Cortines #455, Frac. Costa Verde, C.P. 94292 Boca del Rio, Veracruz, Mexico

José Vulfrano González-Fernández, Raúl Balderas-Navarro, and Andrei Yu. Gorbachev

Instituto de Investigación en Comunicación Óptica, Universidad Autónoma de San Luis Potosí, Av. Karakorum 1470 Lomas 4a, C.P. 78210, San Luis Potosí, S.L.P., Mexico

Máximo López-López

Physics Department, Centro de Investigación y de Estudios Avanzados del Instituto Politécnico Nacional, Av. IPN 2508, Col. San Pedro Zacatenco, D.F. C.P. 07360, Mexico

(Received 13 November 2013; accepted 16 January 2014; published 10 February 2014)

The influence of near surface structure termination and surface treatments on the surface electric fields and mobility of modulation doped AlGaAs/GaAs heterostructures (MDH) were investigated. The built-in and surface electric fields were evaluated by photoreflectance spectroscopy, and these values were utilized to simulate the conduction band bending of the MDH. When the capping layer of the MDH was changed, both the built in internal electric field and the surface electric field are decreased, while the electron mobility of the samples is increased. After passivated the surface samples with Si, the surface electric fields were also reduced. Finally, a  $(\text{NH}_4)_2\text{S}_x$ -based treatment of the surface was applied, the surface electric field is annulled, and the conduction band modeling showed an important redistribution of carriers in the films. The electron mobility of the passivated samples does not show any change, neither the internal electric fields, corroborating the close relationship that exist between these two parameters. © 2014 American Vacuum Society. [<http://dx.doi.org/10.1116/1.4863677>]

## I. INTRODUCTION

Low-dimensional semiconductor systems research has acquired a great deal of interest in the route for optimizing electronic and optoelectronic devices. These systems are usually obtained when the nanometer size is reached, and at these dimensions, there exists a strong modification of the electronic and optical properties due to the quantum confinement imposed on the carriers.<sup>1</sup> Another important role in the fabrication and development of semiconductor devices is the semiconductor–vacuum interface in which surface states are created, having a detrimental effect on the optical and electrical properties of the devices.<sup>2</sup>

The surface states are created due to interruption of the periodic pattern imposed by the crystalline material atomic lattice arrangement. Top most dangling bonds produce changes at the surface potential that, for instance, bends the energy bands.

This project studies the changes induced by the surface states when modifying the cap layer structure of modulation doped AlGaAs/GaAs heterostructures (MDH). These structures are widely used in devices like high electron mobility transistor and also are employed in metrology science as the basic structure of the electrical resistance pattern<sup>3</sup> making

meritorious any characterization studies that may lead us to understand and improve their electrical properties.

On the other hand, photoreflectance spectroscopy (PR) is a fast-reading nondestructive characterization technique that has been used to characterize the MDH.<sup>4</sup> The typical short period damped oscillatory behavior of the PR spectra termed as Franz–Keldysh oscillations (FKO) is associated to internal AlGaAs/GaAs interface electric fields, while large period oscillations in the region between 1.45 and 1.75 eV are due to surface states.<sup>5</sup> Therefore, PR and Hall measurements, combined by energy band simulations, might provide a suitable scenario for the study of MDH, as it is intended in this article.

## II. EXPERIMENT

The MDH were grown by molecular beam epitaxy (MBE) on semi-insulating GaAs (100) substrates. The basic heterostructure is shown in Fig. 1. After the GaAs native oxides desorption process, a 1  $\mu\text{m}$ -thick GaAs buffer layer was deposited, followed by 7 nm undoped  $\text{Al}_{0.3}\text{Ga}_{0.7}\text{As}$  spacer layer (spacer 1). Next, the 80 nm-thick Si doped  $\text{Al}_{0.3}\text{Ga}_{0.7}\text{As}$  barrier was deposited with a carrier concentration of  $1.4 \times 10^{18} \text{ cm}^{-3}$ . Another spacer layer (spacer 2) of 7 nm-thick undoped AlGaAs was subsequently deposited. Finally, the structure was capped with undoped GaAs of thickness denoted by  $C_{\text{th}}$ . The surface states and/or near surface band

<sup>a)</sup>Electronic mail: victor.mendez@uaslp.mx

## Structural and Optical Properties of $\text{Ge}_{1-x}\text{Sn}_x$ Alloys Grown on GaAs (001) by R. F. Magnetron Sputtering

H. Pérez Ladrón de Guevara<sup>a</sup>, A. G. Rodríguez<sup>b</sup>, H. Navarro-Contreras<sup>b</sup>, and M. A. Vidal<sup>b</sup>

<sup>a</sup> Centro Universitario de los Lagos, Universidad de Guadalajara, Av. Enrique Díaz de León 1144, col. Paseos de la Montaña, Lagos de Moreno, Jalisco 47460, México

<sup>b</sup> Coordinación para la Innovación y la Aplicación de la Ciencia y la Tecnología (CIACYT), Universidad Autónoma de San Luis Potosí (UASLP), Álvaro Obregón 64, San Luis Potosí, S L P 78000, México

$\text{Ge}_{1-x}\text{Sn}_x$  alloys were grown on GaAs (001) substrates in a conventional R. F. magnetron sputtering system with two independent plasmas not simultaneous focus to substrate. We determined the in-plane and in-growth lattice parameters for different Sn concentrations by high resolution X-ray diffraction (HRXRD). We observed that  $\text{Ge}_{1-x}\text{Sn}_x$  layers with low Sn concentrations have pseudomorphic characteristics. But this layers relax at Sn concentrations higher than the ones growth on Ge (001) substrates. Raman spectroscopy confirms the Sn concentrations of the  $\text{Ge}_{1-x}\text{Sn}_x$  layers.

We also determined the band gap transitions and we found that the indirect-direct band gap crossover occurs as is predicted in  $\text{Ge}_{1-x}\text{Sn}_x$  alloys growth on Ge (001).

In modern semiconductor physics  $\text{Ge}_{1-x}\text{Sn}_x$  alloys represents the realization of a direct energy-gap material based fully on group IV elements. Single crystal  $\text{Ge}_{1-x}\text{Sn}_x$  alloys have interesting optical and electrical properties. It is experimentally reported that their fundamental band gap transforms from indirect to direct for  $x$  larger than 0.10 (1-6) even it is theoretically predicted than this transition occurs at lower Sn concentrations (7,8). These alloys are expected for developing optoelectronic infrared materials systems. In addition,  $\text{Ge}_{1-x}\text{Sn}_x$  would be expected to exhibit high carrier mobility because of a lower effective mass than that of Ge and the lack of polar optical scattering (1,9) inherent to III-V materials. However there are several challenges associated with the synthesis of these alloys due to the limited bulk solubility exhibited by Sn in Ge ( $x < 0.005$ ), a large lattice mismatch between Sn and Ge of 14.7% and lower surface free energy of Sn versus Ge leading to the surface segregation of Sn. To overcome Sn surface segregation it is necessary to grow at low temperatures, typically around 200 °C where it is possible to obtain single crystal  $\text{Ge}_{1-x}\text{Sn}_x$  epitaxial thin films (2,3,10). Additionally, the maximum equilibrium solid solution of  $\alpha$ -Sn in Ge and Ge in  $\alpha$ -Sn is less than 1 and 0.6%, respectively (11). However the growth of these alloys in nonequilibrium conditions allowed us to obtain single phase  $\text{Ge}_{1-x}\text{Sn}_x$  alloys with Sn concentrations between  $x = 0.01$  to 0.14 on Ge (001) substrates by using a R. F. Magnetron Sputtering (12).

$\text{Ge}_{1-x}\text{Sn}_x$  layers has been used as buffer layers in order to integrate group IV an III-V elements such as Si (13-16) and GaAs (17). At the moment no one is trying to use III-V

## High-quality InN films on MgO (100) substrates: The key role of 30° in-plane rotation

V. D. Compeán García,<sup>1</sup> I. E. Orozco Hinostrroza,<sup>2</sup> A. Escobosa Echavarría,<sup>3</sup>  
 E. López Luna,<sup>1</sup> A. G. Rodríguez,<sup>1</sup> and M. A. Vidal<sup>1</sup>

<sup>1</sup>Coordinación para la Innovación y Aplicación de la Ciencia y Tecnología (CIACyT),  
 Universidad Autónoma de San Luis Potosí (UASLP), Álvaro Obregón 64, 78000 San Luis Potosí, Mexico

<sup>2</sup>Instituto Potosino de Investigación Científica y Tecnológica, Camino a la Presa San José 2055,  
 Col. Lomas 4a Sección, 78216 San Luis Potosí, Mexico

<sup>3</sup>Electric Engineering Department, Centro de Investigación y Estudios Avanzados del IPN,  
 Apartado Postal 14-740, 07000 México D.F., Mexico

(Received 21 February 2014; accepted 3 May 2014; published online 14 May 2014)

High crystalline layers of InN were grown on MgO(100) substrates by gas source molecular beam epitaxy. Good quality films were obtained by means of an in-plane rotation process induced by the annealing of an InN buffer layer to minimize the misfit between InN and MgO. *In situ* reflection high-energy electron diffraction showed linear streaky patterns along the [01 $\bar{1}$ 0] azimuth and a superimposed diffraction along the [11 $\bar{2}$ 0] azimuth, which correspond to a 30°  $\alpha$ -InN film rotation. This rotation reduces the mismatch at the MgO/InN interface from 19.5% to less than 3.5%, increasing the structural quality, which was analyzed by high-resolution X-ray diffraction and Raman spectroscopy. Only the (0002) *c* plane diffraction of  $\alpha$ -InN was observed and was centered at  $2\theta = 31.4^\circ$ . Raman spectroscopy showed two modes corresponding to the hexagonal phase: E1(LO) at  $591\text{ cm}^{-1}$  and E2(high) at  $488\text{ cm}^{-1}$ . Hall effect measurements showed a carrier density of  $9 \times 10^{18}\text{ cm}^{-3}$  and an electron Hall mobility of  $340\text{ cm}^2/(\text{V s})$  for a film thickness of 140 nm. © 2014 AIP Publishing LLC. [<http://dx.doi.org/10.1063/1.4876760>]

Over the last few years, the hexagonal and cubic phases of the semiconductor InN have attracted much interest from both fundamental and practical points of view. The interest in this semiconductor and the complete III-nitride alloy system increased after the correct determination of the fundamental band-gap energy of InN from the original value of 1.9 (Ref. 1) to 0.67 eV,<sup>2–4</sup> which meant that InN has the lowest band gap of any known III-nitride binary compound or alloy. This extended the expected emission range of III-nitride alloys from deep-UV (AlN) down to the near-IR region (InN). InN also exhibits exceptional transport properties, such as a very small electron effective mass at the  $\Gamma$  point ( $0.07 m_0$ ), which may lead to high electron mobilities, high saturation velocities, a pronounced band-filling effect in samples with electron concentrations in the order of  $10^{18}$ – $10^{19}\text{ cm}^{-3}$ ,<sup>3</sup> a surface accumulation layer with ultra-high electron density, and very high saturation and peak drift velocities.<sup>5–7</sup> These unique properties make InN a potential material for a wide range of devices, such as tandem solar cells, infrared emitters, and high-speed and high-frequency electronic devices. As a consequence, a great deal of effort has been dedicated to improving the crystal quality of InN layers using different substrates to grow high-quality InN and its InGaIn alloys, and numerous studies of the optical and electrical properties of InN can be found in the literature.<sup>1–8</sup>

One of the problems of III-nitride systems is that no native substrates exist; for example, InN has a lattice mismatch of 25% with sapphire, 8% with Si(111), 37.4% with GaAs, and 11% with GaN. High-quality single-crystal InN is very difficult to obtain because of this. Magnesium oxide (MgO) has been used to grow cubic InN with a buffer layer

of cubic gallium nitride ( $\beta$ -GaN),<sup>9–11</sup> because of the large lattice mismatch between InN(100) and MgO(100) of  $\sim 18\%$ . If a buffer layer of GaN is not used then poor-quality polycrystalline  $\alpha$ -InN is obtained.<sup>9,12</sup>

In this study, we report the growth of high-quality  $\alpha$ -InN and discuss the effect of annealing on the low-temperature (LT)-InN buffer layer. In addition, we characterize the structural quality of the  $\alpha$ -InN by *in situ* and real-time reflection high-energy electron diffraction (RHEED), X-ray diffraction (XRD), and Raman spectroscopy.

InN films were grown by gas source molecular beam epitaxy (GS-MBE) on (100)-oriented MgO substrates using an InN buffer layer grown at a low substrate temperature (LT) of  $T_s = 300^\circ\text{C}$ , as described in the next section.

The *in situ* real-time surface characterization was performed by RHEED with an acceleration voltage of 12 kV. Atomic Force Microscopy (AFM) in tapping mode was used to study surface morphology. The structural properties were studied using a high-resolution X-ray diffraction (HRXRD) system with a PANalytical MRD X-ray diffractometer, using the  $K\alpha_1$  line emission ( $1.54059\text{ \AA}$ ) from a Cu target as the X-ray source and a 2 bounce hybrid monochromator made of a (220) germanium crystal. The voltage and applied current were fixed at 40 mV and 20 mA, respectively. Room temperature Raman spectra were measured with a 514.5 nm excitation laser line and the electrical properties were evaluated by Hall measurements in the van der Pauw configuration system at 300 K.

Before growing LT-InN, the substrate was cleaned in a trichloroethylene and acetone ultrasonic bath for 10 min. The MgO substrate was introduced into a vacuum chamber and was then transferred to the growth chamber and thermally

RESEARCH ARTICLE

Open Access

# Tetramer formation in *Arabidopsis* MADS domain proteins: analysis of a protein-protein interaction network

Carlos Espinosa-Soto<sup>1,2</sup>, Richard GH Immink<sup>3</sup>, Gerco C Angenent<sup>3,4</sup>, Elena R Alvarez-Buylla<sup>5\*</sup> and Stefan de Folter<sup>1\*</sup>

## Abstract

**Background:** MADS domain proteins are transcription factors that coordinate several important developmental processes in plants. These proteins interact with other MADS domain proteins to form dimers, and it has been proposed that they are able to associate as tetrameric complexes that regulate transcription of target genes. Whether the formation of functional tetramers is a widespread property of plant MADS domain proteins, or it is specific to few of these transcriptional regulators remains unclear.

**Results:** We analyzed the structure of the network of physical interactions among MADS domain proteins in *Arabidopsis thaliana*. We determined the abundance of subgraphs that represent the connection pattern expected for a MADS domain protein heterotetramer. These subgraphs were significantly more abundant in the MADS domain protein interaction network than in randomized analogous networks. Importantly, these subgraphs are not significantly frequent in a protein interaction network of TCP plant transcription factors, when compared to expectation by chance. In addition, we found that MADS domain proteins in tetramer-like subgraphs are more likely to be expressed jointly than proteins in other subgraphs. This effect is mainly due to proteins in the monophyletic MIKC clade, as there is no association between tetramer-like subgraphs and co-expression for proteins outside this clade.

**Conclusions:** Our results support that the tendency to form functional tetramers is widespread in the MADS domain protein-protein interaction network. Our observations also suggest that this trend is prevalent, or perhaps exclusive, for proteins in the MIKC clade. Because it is possible to retrodict several experimental results from our analyses, our work can be an important aid to make new predictions and facilitates experimental research on plant MADS domain proteins.

**Keywords:** MADS domain proteins, Protein-protein interaction network, Transcription factors, Tetramers, Subgraph abundance, *Arabidopsis thaliana*

\*Correspondence: eabuylla@gmail.com; sdfolter@langebio.cinvestav.mx

<sup>5</sup>Departamento de Ecología Funcional, Instituto de Ecología, Universidad Nacional Autónoma de México, Ap. Postal 70-275, 3er Circ. Ext. Jto. Jard. Bot., CU, C.P. 04510 Mexico, D.F., Mexico

<sup>1</sup>Laboratorio Nacional de Genómica para la Biodiversidad (Langebio), Centro de Investigación y de Estudios Avanzados del Instituto Politécnico Nacional (CINVESTAV-IPN), Km 9.6 Libramiento Norte Carretera León, C.P. 36821 Irapuato, Mexico

Full list of author information is available at the end of the article

## Effects of Spin-Dependent Interactions on Polarization of Bright Polariton Solitons

M. Sich, F. Fras, J. K. Chana, M. S. Skolnick, and D. N. Krizhanovskii

*Department of Physics and Astronomy, University of Sheffield, Sheffield, S3 7RH, United Kingdom*

A. V. Gorbach, R. Hartley, and D. V. Skryabin

*Department of Physics, University of Bath, Bath, BA2 7AY, United Kingdom*

S. S. Gavrilov

*Institute of Solid State Physics RAS, Chernogolovka, 142432, Russia*

E. A. Cerda-Méndez, K. Biermann, R. Hey, and P. V. Santos

*Paul-Drude-Institut für Festkörperelektronik, 10117 Berlin, Germany*

(Received 21 June 2013; published 28 January 2014)

We report on the spin properties of bright polariton solitons supported by an external pump to compensate losses. We observe robust circularly polarized solitons when a circularly polarized pump is applied, a result attributed to phase synchronization between nondegenerate TE and TM polarized polariton modes at high momenta. For the case of a linearly polarized pump, either  $\sigma^+$  or  $\sigma^-$  circularly polarized bright solitons can be switched on in a controlled way by a  $\sigma^+$  or  $\sigma^-$  writing beam, respectively. This feature arises directly from the widely differing interaction strengths between co- and cross-circularly polarized polaritons. In the case of orthogonally linearly polarized pump and writing beams, the soliton emission on average is found to be unpolarized, suggesting strong spatial evolution of the soliton polarization. The observed results are in agreement with theory, which predicts stable circularly polarized solitons and unstable linearly polarized solitons.

DOI: [10.1103/PhysRevLett.112.046403](https://doi.org/10.1103/PhysRevLett.112.046403)

PACS numbers: 71.36.+c, 42.65.Pc, 42.65.Tg, 78.55.Cr

*Introduction.*—Solitons are broadly investigated across many areas of physics, including nonlinear optics [1] and cold atom physics [2,3]. Optical and matter wave solitons form when photon or particle interactions are able to compensate for the dispersive spreading of wave packets. The spin or polarization degree of freedom gives rise to the richness of nonlinear effects. Temporal vector solitons consisting of two polarization components have been investigated in birefringent fiber cavity lasers [4] and nonlinear lattices [5]. The realization of the spinor atom BEC stimulated the theoretical investigation of a variety of phenomena such as spin textures and vortices [6,7], magnetic solitons [8,9], and bright-dark soliton complexes [10], which arise from spin-dependent atomic scattering.

Strong exciton-photon coupling in semiconductor microcavities enables the formation of half-light half-matter bosonic quasiparticles (2D polaritons) [11,12]. Polaritons have been used to demonstrate condensation [13], superfluidity [14], and dark [15] and bright [16–19] solitons. Nonlinear spin-dependent interactions of co- and cross-circularly polarized photons may have different strengths [20]. Conversely, interactions of co- and cross-circularly polarized polaritons not only differ in strength but also have opposite signs such that polaritons with parallel spins repel, while those with opposite spins attract [11]. The interplay of the two polariton spin components naturally leads to a variety

of possible nonlinear states, expanding the possibilities to control the dynamics and response to external stimuli. Spin multistability [21] of exciton-polariton states has recently been reported [22,23], expanding on previous research into nonlinear polarization effects in optical resonators [21,24]. Polariton spin switching [25–27], and more recently, conservative (i.e., without gain) dark polariton half-solitons (vector solitons) were also observed [28].

The bright polariton solitons observed recently [18] can be switched on and off on a picosecond time scale and have well-defined size (2–4  $\mu\text{m}$ ) and amplitude. Importantly, polariton-polariton interactions are 2–3 orders of magnitude larger than the nonpolaritonic ones achieved in the weak coupling regime. In this Letter, we investigate the spin properties of polariton solitons, which may create opportunities in ultrafast all-optical digital signal processing [29,30], where spin-based architectures have considerable potential [31,32]. Furthermore, we report the symmetry breaking in the vector polariton soliton system arising from spin-dependent interparticle interactions.

The polariton solitons propagate in a dissipative environment where losses are fully compensated by gain from an external continuous wave (cw) pump permitting the scalability of possible polariton circuits [32,33]. We find that when the background cw pump and the local pulsed writing beam (WB) which triggers the soliton [see Fig. 1(a)]

## High-quality InN films on MgO (100) substrates: The key role of 30° in-plane rotation

V. D. Compeán García,<sup>1</sup> I. E. Orozco Hinostrroza,<sup>2</sup> A. Escobosa Echavarría,<sup>3</sup>  
 E. López Luna,<sup>1</sup> A. G. Rodríguez,<sup>1</sup> and M. A. Vidal<sup>1</sup>

<sup>1</sup>Coordinación para la Innovación y Aplicación de la Ciencia y Tecnología (CIACyT),  
 Universidad Autónoma de San Luis Potosí (UASLP), Álvaro Obregón 64, 78000 San Luis Potosí, Mexico

<sup>2</sup>Instituto Potosino de Investigación Científica y Tecnológica, Camino a la Presa San José 2055,  
 Col. Lomas 4a Sección, 78216 San Luis Potosí, Mexico

<sup>3</sup>Electric Engineering Department, Centro de Investigación y Estudios Avanzados del IPN,  
 Apartado Postal 14-740, 07000 México D.F., Mexico

(Received 21 February 2014; accepted 3 May 2014; published online 14 May 2014)

High crystalline layers of InN were grown on MgO(100) substrates by gas source molecular beam epitaxy. Good quality films were obtained by means of an in-plane rotation process induced by the annealing of an InN buffer layer to minimize the misfit between InN and MgO. *In situ* reflection high-energy electron diffraction showed linear streaky patterns along the [01 $\bar{1}$ 0] azimuth and a superimposed diffraction along the [11 $\bar{2}$ 0] azimuth, which correspond to a 30°  $\alpha$ -InN film rotation. This rotation reduces the mismatch at the MgO/InN interface from 19.5% to less than 3.5%, increasing the structural quality, which was analyzed by high-resolution X-ray diffraction and Raman spectroscopy. Only the (0002) *c* plane diffraction of  $\alpha$ -InN was observed and was centered at  $2\theta = 31.4^\circ$ . Raman spectroscopy showed two modes corresponding to the hexagonal phase: E1(LO) at  $591\text{ cm}^{-1}$  and E2(high) at  $488\text{ cm}^{-1}$ . Hall effect measurements showed a carrier density of  $9 \times 10^{18}\text{ cm}^{-3}$  and an electron Hall mobility of  $340\text{ cm}^2/(\text{V s})$  for a film thickness of 140 nm. © 2014 AIP Publishing LLC. [<http://dx.doi.org/10.1063/1.4876760>]

Over the last few years, the hexagonal and cubic phases of the semiconductor InN have attracted much interest from both fundamental and practical points of view. The interest in this semiconductor and the complete III-nitride alloy system increased after the correct determination of the fundamental band-gap energy of InN from the original value of 1.9 (Ref. 1) to 0.67 eV,<sup>2-4</sup> which meant that InN has the lowest band gap of any known III-nitride binary compound or alloy. This extended the expected emission range of III-nitride alloys from deep-UV (AlN) down to the near-IR region (InN). InN also exhibits exceptional transport properties, such as a very small electron effective mass at the  $\Gamma$  point ( $0.07 m_0$ ), which may lead to high electron mobilities, high saturation velocities, a pronounced band-filling effect in samples with electron concentrations in the order of  $10^{18}$ – $10^{19}\text{ cm}^{-3}$ ,<sup>3</sup> a surface accumulation layer with ultra-high electron density, and very high saturation and peak drift velocities.<sup>5-7</sup> These unique properties make InN a potential material for a wide range of devices, such as tandem solar cells, infrared emitters, and high-speed and high-frequency electronic devices. As a consequence, a great deal of effort has been dedicated to improving the crystal quality of InN layers using different substrates to grow high-quality InN and its InGaIn alloys, and numerous studies of the optical and electrical properties of InN can be found in the literature.<sup>1-8</sup>

One of the problems of III-nitride systems is that no native substrates exist; for example, InN has a lattice mismatch of 25% with sapphire, 8% with Si(111), 37.4% with GaAs, and 11% with GaN. High-quality single-crystal InN is very difficult to obtain because of this. Magnesium oxide (MgO) has been used to grow cubic InN with a buffer layer

of cubic gallium nitride ( $\beta$ -GaN),<sup>9-11</sup> because of the large lattice mismatch between InN(100) and MgO(100) of  $\sim 18\%$ . If a buffer layer of GaN is not used then poor-quality polycrystalline  $\alpha$ -InN is obtained.<sup>9,12</sup>

In this study, we report the growth of high-quality  $\alpha$ -InN and discuss the effect of annealing on the low-temperature (LT)-InN buffer layer. In addition, we characterize the structural quality of the  $\alpha$ -InN by *in situ* and real-time reflection high-energy electron diffraction (RHEED), X-ray diffraction (XRD), and Raman spectroscopy.

InN films were grown by gas source molecular beam epitaxy (GS-MBE) on (100)-oriented MgO substrates using an InN buffer layer grown at a low substrate temperature (LT) of  $T_s = 300^\circ\text{C}$ , as described in the next section.

The *in situ* real-time surface characterization was performed by RHEED with an acceleration voltage of 12 kV. Atomic Force Microscopy (AFM) in tapping mode was used to study surface morphology. The structural properties were studied using a high-resolution X-ray diffraction (HRXRD) system with a PANalytical MRD X-ray diffractometer, using the  $K\alpha_1$  line emission ( $1.54059\text{ \AA}$ ) from a Cu target as the X-ray source and a 2 bounce hybrid monochromator made of a (220) germanium crystal. The voltage and applied current were fixed at 40 mV and 20 mA, respectively. Room temperature Raman spectra were measured with a 514.5 nm excitation laser line and the electrical properties were evaluated by Hall measurements in the van der Pauw configuration system at 300 K.

Before growing LT-InN, the substrate was cleaned in a trichloroethylene and acetone ultrasonic bath for 10 min. The MgO substrate was introduced into a vacuum chamber and was then transferred to the growth chamber and thermally

---

## Graph entropy as tool for understanding complex urban networks. The case of Ensenada city, Mexico

---

Antonio Aguilera\*

El Colegio de San Luis, A.C.,  
Parque de Macul 155, Fracc. Colinas del Parque,  
C.P. 78299, San Luis Potosí, San Luis Potosí, Mexico  
Fax: +52-444-8110101  
E-mail: [aaguilera@colsan.edu.mx](mailto:aaguilera@colsan.edu.mx)  
\*Corresponding author

Edgardo Ugalde

Instituto de Física,  
Universidad Autónoma de San Luis Potosí,  
Av. Manuel Nava 6 Zona Universitaria,  
C.P. 78290, San Luis Potosí, San Luis Potosí, Mexico  
E-mail: [ugalde@ifisica.uaslp.mx](mailto:ugalde@ifisica.uaslp.mx)

**Abstract:** Spatial structure of cities is the substratum over which human urban life develops. Understanding the relevance of the streets that form such substratum is fundamental to understand the movements of people in the city. Our purpose in this study is to propose and explore methods to find relevant streets sets that conforms the basis of complex urban networks. We used two methods based on previous work by Volchenkov and Blanchard (2008) and Shetty and Adibi (2005), and a method developed by us. To illustrate the use of these tools, we performed an analysis of the main streets network of the coastal city of Ensenada, Mexico.

**Keywords:** graph entropy; urban structure; complex urban networks.

**Reference** to this paper should be made as follows: Aguilera, A. and Ugalde, E. (2014) 'Graph entropy as tool for understanding complex urban networks. The case of Ensenada city, Mexico', *Int. J. Society Systems Science*, Vol. 6, No. 1, pp.87–99.

**Biographical notes:** Antonio Aguilera is a Professor in El Colegio de San Luis, a Mexican Public Research Center in Social Sciences. He is a National Researcher Level I. His research involves the development of computer models of spatial socio-economic phenomena and spatial analysis methods. He is a member of the National Research System of Mexico and the European Social Simulation Association.

Edgardo Ugalde is a Professor in the Physics Institute of the Universidad Autónoma de San Luis Potosí, Mexico. He is a National Researcher Level II. His research interests are dynamic systems, discrete mathematics and modelling and data analysis. He is a member of the National Research System of Mexico, and the Mexican Academy of Sciences. In 2011, he received the prize 'Jorge Lomnitz Adler' from the Institute of Physics of the Universidad Nacional Autónoma de México (UNAM).



# Entropía de grafos y su uso para medir la inteligibilidad de la ciudad<sup>1</sup>

## *Graph entropy as a means of measuring the intelligibility of a city*

Antonio Aguilera Ontiveros\* y Edgardo Ugalde Saldaña\*\*

### INTRODUCCIÓN

Los seres humanos nos movemos dentro de nuestros ambientes urbanos basados principalmente en la construcción de mapas cognitivos (Haq y Giroto, 2003). Se han identificado tres clases de relaciones espaciales que forman el contenido de la cognición espacial, éstas relaciones son de tipo topológico, proyectivo y métrico o euclidiano (Haq y Giroto, 2003). Además, se ha encontrado que el entendimiento de las relaciones topológicas precede el entendimiento de las relaciones proyectivas y euclidianas (Haq y Giroto, 2003). Shemyakin (1962), citado por Haq y Giroto, (2003), menciona que existen dos tipos de representaciones topológicas: los mapas de ruta y los mapas de reconocimiento. Los primeros son construidos a través del trazo mental de la ruta de movimiento a través de un área, mientras que los segundos son representaciones de la configuración general de la mutua disposición de los objetos locales. De lo anterior se deriva una distinción entre las variables topológicas locales y las ideas topológicamente derivadas acerca de la configuración general del entorno.

---

<sup>1</sup> Este trabajo fue parcialmente apoyado por el Consejo Nacional de Ciencia y Tecnología de México a través del proyecto 101366. Nuestro agradecimiento.

\* El Colegio de San Luis, A. C. (aaguilera@colsan.edu.mx).

\*\* Instituto de Física, Universidad Autónoma de San Luis Potosí (ugalde@ifisica.uaslp.mx).



SUBMIT YOUR

SIGN UP

Home > Journal of Vacuum Science & Technology B, Nanotechnology and Microelectronics: Materials, Processing, Measurement, and Phenomena > Volume



32, Issue 2 > 10.1116/1.4863677

Published Online: February 2014 Accepted: January 2014

# Effect of surface states on the electrical properties of MBE grown modulation doped AlGaAs/GaAs

Alejandro Cisneros-de-la-Rosa, Irving Eduardo Cortes-Mestizo, Esteban Cruz-Hernández, and Víctor Hugo Méndez-García<sup>a)</sup> more...

View

Journal of Vacuum Science & Technology B, Nanotechnology and Microelectronics: Materials, Processing, Measurement, and Phenomena **32**, 02  
doi: <http://dx.doi.org/10.1116/1.4863677>



PDF

ABSTRACT

FULL TEXT

FIGURES

CITED BY

TOOLS

SHARE

III-V semiconductors · Surface states · Electric fields · Electron mobility · Passivation

## ABSTRACT

## Research Article

# Characterization and Biocompatibility of Chitosan Gels with Silver and Gold Nanoparticles

**C. Sámano-Valencia,<sup>1,2</sup> G. A. Martínez-Castañón,<sup>1,2</sup> F. Martínez-Gutiérrez,<sup>3</sup>  
F. Ruiz,<sup>1,4</sup> J. F. Toro-Vázquez,<sup>3</sup> J. A. Morales-Rueda,<sup>3</sup> L. F. Espinosa-Cristóbal,<sup>5</sup>  
N. V. Zavala Alonso,<sup>2</sup> and N. Niño Martínez<sup>4</sup>**

<sup>1</sup> Doctoral Program in Materials Science and Engineering, Autonomous University of San Luis Potosí, Salvador Nava Avenue s/n, University Campus, 78290 San Luis Potosí, SLP, Mexico

<sup>2</sup> Master and Doctoral Program in Advanced Dentistry, Faculty of Dentistry, Autonomous University of San Luis Potosí, Salvador Nava Avenue No. 2, University Campus, 78290 San Luis Potosí, SLP, Mexico

<sup>3</sup> Faculty of Chemistry, Autonomous University of San Luis Potosí, Salvador Nava Avenue No. 6, University Campus, 78290 San Luis Potosí, SLP, Mexico

<sup>4</sup> Faculty of Science, Autonomous University of San Luis Potosí, Salvador Nava Avenue s/n, University Campus, 78290 San Luis Potosí, SLP, Mexico

<sup>5</sup> Faculty of Dentistry, Juarez University of Durango State, Predio Canoas s/n, Los Ángeles, 34000 Durango, DGO, Mexico

Correspondence should be addressed to G. A. Martínez-Castañón; [mtzcastanon@fciencias.uaslp.mx](mailto:mtzcastanon@fciencias.uaslp.mx)

Received 12 May 2014; Accepted 19 August 2014; Published 15 September 2014

Academic Editor: Ruibing Wang

Copyright © 2014 C. Sámano-Valencia et al. This is an open access article distributed under the Creative Commons Attribution License, which permits unrestricted use, distribution, and reproduction in any medium, provided the original work is properly cited.

The presence of bacterial resistance to antibiotics is a very important issue and the search of new alternatives is necessary. In this work, a combination of chitosan gel with silver or gold nanoparticles was prepared and characterized using thermal, rheology, bactericide, and biocompatibility analyses. ESEM images were also taken to visualize the incorporation of the nanoparticles into the gel matrix. Thermal analysis showed a better thermal stability in the chitosan-gold nanoparticles gels compared to the chitosan-silver nanoparticles gels. Rheology analyses showed that the viscosity of the gels decreased when velocity increased and there were differences in viscosity when silver and gold nanoparticles concentrations change. ESEM images showed the presence of agglomerates of silver and gold nanoparticles into the gel matrix with a good distribution; in some cases the formation of microstructures was found. Bactericide results show that these materials present an antibacterial activity against *S. aureus*, *S. mutans*, and *E. coli*. The biocompatibility test showed neither negative reaction nor wound healing delay after the application of the gels in an *in vivo* test. The gels with silver and gold nanoparticles could be used to treat wound infections in oral or skin applications.

## 1. Introduction

The development of bacterial resistance to antibiotics has become an important health problem; it is common in isolates from healthy persons and from patients with community acquired infections in developing countries. Resistance is increasing, particularly to first line, inexpensive, and broad-spectrum antibiotics but also to the new drugs; therefore the search of new alternatives is necessary [1, 2]. In the specific case of dental caries there are reports of bacterial resistance to

the substances used to prevent this disease [3]. Dental caries is one of the most common oral diseases all over the world and *Streptococcus mutans* is its main etiological agent [4]. The role of *Streptococcus mutans* in the development of dental caries is well established but the no life threatening nature of dental caries has minimized its importance in human health; however the economic cost for the treatment of this oral disease is high [5, 6]; that is why the prevention approach and the search of new ways for the treatment of dental caries are very important.

**Effects of silver nanoparticles on the bonding three adhesive systems**



I. Torres-Gallegos<sup>1</sup>, G.A. Martinez-Castañon<sup>1,\*</sup>, N.V. Zavala-Alonso<sup>1</sup>, J.P. Loyola-Rodriguez<sup>1</sup>, N. Patiño-Marin<sup>1</sup>, J.F. Reyes-Macias<sup>1</sup>, N. Niño-Martínez<sup>2</sup>, Facundo Ruiz<sup>2</sup>

<sup>1</sup> Autonomous University of San Luis Potosí, San Luis Potosí, Mexico  
<sup>2</sup> Faculty of Science, Autonomous University of San Luis Potosí, San Luis Potosí, Mexico

**Purpose:** Endemic dental fluorosis has increased in many countries; several researchers have found that dental fluorosis adversely affects the bonding of composites to enamel, thereby compromising clinical success. The need for a simpler and more effective procedure has motivated manufacturers to develop new adhesive systems. The aim of this study was to evaluate the effect of adding silver nanoparticles into three commercial adhesive systems (Excite™, Adper Prompt L-Pop™ and AdheSE™) bonded to moderate fluorotic enamel using a micro-tensile bond strength test (μTBS). Contact angle was also measured in order to verify the adhesive system wettability.

**Methods and materials:** 10 nm, spherical silver nanoparticles were prepared by a chemical method in an aqueous media, then mixed with the commercial adhesive systems at 1:1 ratio, applied to the fluorotic enamel surface and then micro-tensile bond strength and contact angle measurements were conducted.

**Results:** According to Table 1, the commercial adhesive systems achieved the lowest micro-tensile bond strength with the highest adhesive failure mode related with the highest contact angle. The bond strength achieved in all the experimental adhesive systems was statistically higher and showed the highest cohesive failures related to the lowest contact angle.

**Table 1 – Mean microtensile bond strength, failure mode and contact angle of the different adhesive systems.**

	EX™	EX+™	APL-P™	APL-P+™	ASE™	ASE+™
μTBS (MPa)	11 ± 2.1©	19 ± 5.4*	14 ± 2*	20 ± 4*	16 ± 3*	19 ± 3.5*
Contact angle	46 ± 0.6	0	30 ± 0.5	0	28 ± 0.4	0
Failure mode	C A M 35 40 25	C A M 45 25 30	C A M 30 60 10	C A M 40 10 50	C A M 40 35 25	C A M 55 15 30

n = 120. Results are expressed in MPa. EX™, Excite; EX+™, Excite with silver nanoparticles; APL-P™, Adper Prompt L-Pop; APL-P+™, Adper Prompt L-Pop with nanoparticles; ASE™, AdheSE; ASE+™, AdheSE with silver nanoparticles. ©: control group, EX™ group. One-way ANOVA test showed statistically significant differences (p < 0.05) in all the groups when comparing with the control group. There was a statistically significant differences in the failure mode (Chi-square test).

**Conclusion:** Adding silver nanoparticles to the adhesive systems, in order to decrease their contact angle, improve their wettability and their tensile bond strength.

**Keywords:** Fluorotic enamel; Microtensile test; Silver nanoparticles

<http://dx.doi.org/10.1016/j.dental.2014.08.310>

**Influence of fluoride mouthwash containing nanohydroxyapatite on dentin interface microhardness**



G. Pereira<sup>1,\*</sup>, M. Prado<sup>1</sup>, D.C.R.S. Oliveira<sup>2</sup>, L.R. Menezes<sup>1</sup>, L.T. Prieto<sup>2</sup>, L.A.M.S. Paulillo<sup>2</sup>

<sup>1</sup> Restorative Dentistry Department, Dental School, Federal University of Rio De Janeiro, RJ, Brazil  
<sup>2</sup> Restorative Dentistry Department, Piracicaba Dental School, State University of Campinas, SP, Brazil

**Purpose:** The aim of this study was to evaluate the influence of a fluoride mouthwash containing nanohydroxyapatite on dentin bonding interface microhardness of direct resin composite restorations.

**Methods and materials:** Forty human premolars were sectioned and restored with a three-step adhesive system (Scotchbond Multi-Purpose, 3M/ESPE) or a self-etch adhesive system (Clearfill SE Bond, Kuraray) with a conventional resin-based composite Filtek Z350XT (3M/ESPE). After the initial microhardness measurements, the restored samples were fixed in acrylic plates for a study in situ. Ten volunteers participated using the plates for one week with the placebo mouthwash, one week as a wash-out, and one week using the testing fluoride mouthwash containing nanohydroxyapatite. The final microhardness measurements were evaluated and data were analyzed by ANOVA and Tukey's test submitted for multiple comparisons (α = 0.05).

**Results:** There were statistical significant differences between the mouthwash treatments with both adhesive systems tested (p < 0.001). The nanohydroxyapatite used in this in situ mouthwash study was an influencing factor on the dentin interface microhardness of resin composite restorations. Mean values taken from Tukey's test are shown in Table 1.

**Table 1**

Experimental group	Microhardness	
	Initial	Final
Clearfill SE (+ testing mouthwash)	42.59 (0.5) Ba	44.33 (0.6) Aa
Clearfill SE (+ placebo mouthwash)	41.29 (0.5) Aa	40.4 (1.0) Ab
ScotchBond MP (+ testing mouthwash)	42.15 (0.4) Bb	45.42 (0.6) Aa
ScotchBond MP (+ placebo mouthwash)	39.66 (0.6) Aab	40.35 (0.5) Ab

Means followed by different capital letters in the same line and small letters in the same column were significantly different (p < 0.05).

**Conclusion:** The fluoride mouthwash containing nanohydroxyapatite was able to increase the dentin microhardness of direct resin composite restorations regardless the adhesive



# Evaluation of the antibacterial activity of an indoor waterborne architectural coating containing Ag/TiO<sub>2</sub> under different relative humidity environments



C. Dominguez-Wong<sup>\*</sup>, G.M. Loredó-Becerra, C.C. Quintero-González, M.E. Noriega-Treviño, M.E. Compeán-Jasso, N. Niño-Martínez, I. DeAlba-Montero, Facundo Ruiz

Facultad de Ciencias, Universidad Autónoma de San Luis Potosí, Alvaro Obregón #64, Col. Centro, San Luis Potosí, S.L.P., C.P. 78000, Mexico

## ARTICLE INFO

### Article history:

Received 15 March 2014

Accepted 11 July 2014

Available online 17 July 2014

### Keywords:

Antibacterial surface

JIS Z2801

Silver

Nanoparticles

Titanium dioxide

Humidity

## ABSTRACT

Silver nanoparticles synthesized on titanium dioxide (Ag/TiO<sub>2</sub>), an effective antibacterial additive, were added to a commercial paint and its antimicrobial activity was evaluated. Microbiological tests against *Escherichia coli* and Methicillin-resistant *Staphylococcus aureus* were performed under high relative humidity (RH > 90%) and low (RH ≈ 14%). A remarkable difference in cell recovery under high and low humidity was found.

© 2014 Elsevier B.V. All rights reserved.

## 1. Introduction

Nosocomial infections play an important role in mortality and morbidity associated with infections [1,2,3,4], along with the transmission related to food preparation [5]. There is an increasing interest in the production of commercial hygienic surfaces, which would help to decrease the transmission of infections, avoiding human losses and having an important economic impact.

In the titanium dioxide decorated with silver nanoparticles [6] (Ag/TiO<sub>2</sub>) where Ti Pure<sup>®</sup> R-902 from Dupont<sup>™</sup>, titanium dioxide particles have already been functionalized in order to have a better dispersion into the paint formulation, is expected that TiO<sub>2</sub> function as a vehicle maintaining the silver nanoparticles (which are deposited on top of it) homogeneously dispersed, with a synergistic effect between silver [7] and together with titanium dioxide [8,9].

The Woodrow Wilson International Center for Scholars has created the Nanotechnology Consumer Products Inventory [10], which contains around 400 products with silver and this number keep on growing due to the extensive use of silver as an antibacterial. In spite of the latter, the activity of silver in dry conditions (RH ≈ 22%) and temperature of 21 °C has been reported to fail [11], therefore the necessity to evaluate the antibacterial activity in two levels of relative

humidity and temperature. Regarding to the evaluation of antibacterial activity in paints, specific methods designed for testing antibacterial activity on paint films are scarce and adaptations are very common. Two of the most reported methods are the Zone of inhibition/Kirby–Bauer test [12–15], along with the Japanese standard JIS Z2801 or ISO 22196 [16,17], and for the evaluation with a dry inoculum reports have been found in the research of Askew [18,19,11]. The goal of this work was to observe the results of the evaluation of a paint with a silver based antibacterial additive under high and low relative humidity, to find out if the performance of the titanium dioxide decorated with silver nanoparticles was similar to that reported with the evaluation of a silver based coating [11] which failed to perform under realistic conditions.

## 2. Materials and methods

Ag/TiO<sub>2</sub> was synthesized according to Niño et al. [6] (for a molar ratio of TiO<sub>2</sub>:Ag of 25:1) via aqueous reduction. It was physically characterized with Transmission Electron Microscopy using a JEOL JEM-1230 (at 100 kV). Minimum Inhibitory Concentration against *Escherichia coli* ATCC 8739 was obtained by Broth Microdilution [20] in order to characterize the Ag/TiO<sub>2</sub>.

For the paint preparation, a commercial vinyl-acrylic paint was used: Comex<sup>®</sup> Vinimex, the blank (Paint-blank) was prepared adding 15% of water as indicated in the label; for the hygienic paint (Paint+Ag/TiO<sub>2</sub>), 15% v/v was added of Ag/TiO<sub>2</sub> still in the

<sup>\*</sup> Corresponding author. Tel.: +52 4448262466/+52 4442074331.

E-mail address: [cdominguezwong@hotmail.com](mailto:cdominguezwong@hotmail.com) (C. Dominguez-Wong).

## Case report

**Livedoid vasculopathy (LV) associated with sticky platelets syndrome type 3 (SPS type 3) and enhanced activity of plasminogen activator inhibitor (PAI-1) anomalies**Claudio Castillo-Martínez<sup>1</sup>, MD, Benjamín Moncada<sup>1</sup>, MD, Rodrigo Valdés-Rodríguez<sup>1</sup>, MD, and Francisco J. González<sup>2</sup>, PhD

<sup>1</sup>Dermatology Department, Hospital Central "Ignacio Morones Prieto", Universidad Autónoma de San Luis Potosí, San Luis Potosí, SLP, México, and <sup>2</sup>Coordinación para la Innovación y la Aplicación de la Ciencia y la Tecnología, San Luis Potosí, México,

**Correspondence**

Benjamín Moncada, MD  
Departamento de Dermatología  
Hospital Central "Ignacio Morones Prieto"  
Avenida Venustiano Carranza 2395  
Zona Universitaria  
CP 78290 San Luis Potosí, SLP  
México  
Email: moncadab@uaslp.mx

Conflict of Interest: None.

Funding: None.

Financial Disclosure: None reported.

doi: 10.1111/j.1365-4632.2012.05786.x

**Case report**

We report the case of a 12-year-old girl Mexican mestizo, who had for the past six months a red linear pattern with several painful ulcerations in both extremities and subsequent white porcelain-like atrophy of the skin (Fig. 1a). A clinical diagnosis of atrophy blanche was made, and on histology grounds thrombosis of dermal arterioles, with only scattered mononuclear cells near the affected arterioles. The absence of polymorphonuclear cells, as well as the lack of leukocytoclasia in the blood vessels, was noteworthy (Fig. 2). Routine laboratory work was unremarkable, and a thrombophilia profile was performed (Table 1). Two anomalies were found, leading to permanent anti-aggregation therapy with acetylsalicylic acid (81 mg) daily, obtaining a full recovery after four months (Fig. 1b). There was no family history of thrombotic events.

**Discussion**

Livedoid vasculopathy (LV), also called atrophy blanche, is one of many dermatological diseases that reveal internal pathology, which affects primarily the lower extremities following a linear pattern, characterized by skin ulceration and subsequent scarring. Frequently this condition falls on the scope of cutaneous small blood vessels.<sup>1</sup> There is confusion, which leads clinicians into the idea of treating this disease with immunosuppressive therapy, for the misnomer of vasculitis, without the knowledge that the affected patients are often found to have an inherited or acquired defect that makes them hypercoagulable.<sup>2</sup> The histopathology hallmark is hyalinization and thrombosis of small vessels, due to an abnormal coagulation state rather than leukocytoclastic vasculitis. It has been found that affected patients with LV may have multiple defects that render them prone to

# Polarimetric pixel using Seebeck nanoantennas

Alexander Cuadrado,<sup>1</sup> Edgar Briones,<sup>2</sup>  
Francisco J. González,<sup>2</sup> and Javier Alda<sup>1,\*</sup>

<sup>1</sup>*Applied Optics Complutense Group, University Complutense of Madrid,  
C/ Arcos de Jalón, 118, 28037 Madrid, Spain*

<sup>2</sup>*Universidad Autónoma de San Luis Potosí, Coordinación para la Innovación y Aplicación de  
la Ciencia y la Tecnología, Sierra Leona, 550, Lomas 2a Sección, CIACYT Building, 78210,  
San Luis Potosí, SLP, Mexico*

[\\*javier.alda@ucm.es](mailto:javier.alda@ucm.es)

**Abstract:** Optical nanoantennas made of two metals are proposed to produce a Seebeck voltage proportional to the Stokes parameters of a light beam. The analysis is made using simulations in the electromagnetic and thermal domains. Each Stokes parameter is independently obtained from a dedicated nanoantenna configuration.  $S_1$  and  $S_2$  rely on the combination of two orthogonal dipoles.  $S_3$  is given by arranging two Archimedian spirals with opposite orientations. The analysis also includes an evaluation of the error associated with the Seebeck voltage, and the crosstalk between Stokes parameters. The results could lead to the conception of polarization sensors having a receiving area smaller than  $10\lambda^2$ . We illustrate these findings with a design of a polarimetric pixel.

© 2014 Optical Society of America

**OCIS codes:** (040.6808) Thermal (uncooled) IR detectors, arrays and imaging; (110.5405) Polarimetric imaging; (250.5403) Plasmonics; (230.5440) Polarization-selective devices.

---

## References and links

1. P. Bharadwaj, B. Deutsch, and L. Novotny, "Optical antennas," *Adv. Opt. Photon.* **1**, 438–483 (2009).
2. L. Novotny and N. van Hulst, "Antennas for light," *Nat. Photonics* **5**, 83–90 (2011).
3. J. Alda, C. Fumeaux, I. Codreanu, J. Schaefer, and G. Boreman, "A deconvolution method for two-dimensional spatial-response mapping of lithographic infrared antennas," *Appl. Opt.* **38**, 3993–4000 (1998).
4. L. Tang, S. E. Kocabas, S. Latif, A. K. Okay, D.-S. Ly-Gagnon, K. C. Sraswat, and D. A. B. Miller, "Nanometer-scale germanium photodetector enhanced by a near-field dipole antenna," *Nat. Photonics* **2**, 226–229 (2008).
5. C. Fumeaux, W. Herrmann, F. K. Kneubühl, and H. Rothuizen, "Nanometer thin-film Bi-NiO-Bi diodes for detection and mixing of 30 THz radiation," *Infrared Phys. Technol.* **39**, 123–183 (1998).
6. F. Gonzalez and G. Boreman, "Comparison of dipole, bowtie, spiral and log-periodic IR antennas," *Infrared Phys. Technol.* **46**(5), 418–428 (2005).
7. A. Cuadrado, J. Alda, and F. J. Gonzalez, "Distributed bolometric effect in optical antennas and resonant structures," *J. Nanophotonics* **6**, 063512 (2012).
8. A. Cuadrado, J. Alda, and F. J. Gonzalez, "Multiphysics simulation of optical nanoantennas working as distributed bolometers in the infrared," *J. Nanophotonics* **7**, 073093 (2013).
9. A. Cuadrado, M. Silva-López, F. J. González, and J. Alda "Robustness of antenna-coupled distributed bolometers," *Opt. Lett.* **38**(19), 3784–3787 (2013).
10. C. Fu, "Antenna-coupled Thermopiles," M.S. Dissertation, University of Central Florida, (1998).
11. G. P. Szakmany, P. Krenz, L. C. Scheneider, A. O. Orlov, G. H. Bernstein, and W. Porod, "Nanowire thermocouple characterization platform," *IEEE Trans. Nanotechnol.* **12**(3), 309–313 (2013).
12. D. M. Rowe, *Thermoelectrics Handbook: Macro to Nano* (Taylor and Francis, 2006).
13. F. J. Gonzalez, C. Fumeaux, J. Alda, and G. D. Boreman, "Thermal-impedance model of electrostatic discharge effects on microbolometers," *Microwave Opt. Technol. Lett.* **26**, 291–293 (2000).

## Resistance-based Biosensor of Multi-Walled Carbon Nanotubes

E. S. Kolosovas-Machuca<sup>1</sup>, G. Vera-Reveles<sup>1,2</sup>, M. C. Rodríguez-Aranda<sup>3</sup>, L. C. Ortiz-Dosal<sup>1</sup>, Emmanuel Segura-Cardenas<sup>4</sup>, Francisco J. Gonzalez<sup>1</sup>

<sup>1</sup>Universidad Autónoma de San Luis Potosí, Coordinación para la Innovación y la Aplicación de la Ciencia y la Tecnología, San Luis Potosí, México <sup>2</sup>Departamento de Ciencias Básicas, Instituto Tecnológico de San Luis Potosí, S/N Col. UPA, Soledad de Graciano Sánchez, SLP, México <sup>3</sup>Centro de Investigación y de Estudios Avanzados del I.P.N. Unidad Querétaro, Fracc. Real de Juriquilla, Querétaro, Qro., C.P., México <sup>4</sup>Instituto de Investigación en Comunicación Óptica. Universidad Autónoma de San Luis Potosí, San Luis Potosí, México

### Abstract

Multi-Walled Carbon Nanotubes (MWNTs) are a good choice for resistive biosensors due to their great resistance changes when immunoreactions take place, they are also low-cost, are more biocompatible than single-walled carbon nanotubes and resistive measurement equipment is usually not expensive and readily available. In this work a novel resistive biosensor based on the immobilization of an antigen through a silanization process over the surface of Multi-Walled Carbon Nanotubes (MWNTs) is reported. Results show that the biosensor increases its conductivity when adding the antigen and decreases when adding the antibody making them good candidates for disease diagnosis.

**KEYWORDS:** Biosensor, multi-walled carbon nanotubes, resistive sensor

### INTRODUCTION

The early detection of pathogens plays a crucial role in the prevention of disease spread. The most sensitive and specific assay diagnosis for infectious disease are the laboratory-



## Seebeck nanoantennas for solar energy harvesting

E. Briones,<sup>1,a)</sup> J. Briones,<sup>2</sup> A. Cuadrado,<sup>3</sup> J. C. Martinez-Anton,<sup>3</sup> S. McMurtry,<sup>4</sup> M. Hehn,<sup>4</sup> F. Montaigne,<sup>4</sup> J. Alda,<sup>3</sup> and F. J. Gonzalez<sup>1</sup>

<sup>1</sup>CIACyT, Universidad Autonoma de San Luis Potosi, San Luis Potosi 78210 SLP, Mexico

<sup>2</sup>Department of Mathematics and Physics, ITESO, Jesuit University of Guadalajara, Tlaquepaque, 45604 Jalisco, Mexico

<sup>3</sup>Faculty of Optics and Optometry, Universidad Complutense de Madrid, 28037 Madrid, Spain

<sup>4</sup>Institut Jean Lamour, CNRS, Université de Lorraine, F-54506 Vandoeuvre Les Nancy, France

(Received 2 July 2014; accepted 26 August 2014; published online 5 September 2014)

We propose a mid-infrared device based on thermocouple optical antennas for light sensing and energy harvesting applications. We numerically demonstrate that antennas are able to generate low-power dc signals by benefiting of the thermoelectric properties of the metals that constitute them. We theoretically evaluate the optical-to-electrical conversion efficiency for harvesting applications and finally discuss strategies to increase its performance. Thermocouple optical antennas therefore open the route toward the design of photovoltaic devices. © 2014 AIP Publishing LLC. [<http://dx.doi.org/10.1063/1.4895028>]

Over the last decade, the idea of using resonant nanoantennas for solar energy harvesting has gained considerable attention,<sup>1,2</sup> as they introduce a means to capture the optical energy of free-propagating waves and to localize it into small volumes, providing thus an enabling technology for energy gathering in the far-infrared region.<sup>3,4</sup> These nanostructures take advantage of the wave nature of the electromagnetic radiation in order to transfer the optical energy to localized resonant currents,<sup>5,6</sup> which are subsequently exploited to recover or sense the confined energy,<sup>7-9</sup> opening thereby a route for the engineering of solar devices.

A successful incorporation of nanoantennas into photovoltaic technology relies on the implementation of an efficient retrieving mechanism, currently non-existent. In this context, nanoantennas coupled to high-speed rectifiers (known as “rectennas”), based on tunnel barriers, have been extensively explored during the last years as optical harvesting devices.<sup>10-14</sup> In spite of the high theoretical efficiency they can reach,<sup>15-17</sup> rectennas exhibit low efficiencies due to the poor performance of the current rectifiers at optical frequencies.<sup>18</sup> As we wait for an efficient rectifier to be developed, other harvesting mechanisms must be explored.<sup>19</sup>

In this letter, we explore a device which combines the use of nanoantennas (to confine the optical energy) with the thermoelectric properties of their metallic interfaces<sup>20-22</sup> (in order to recover such energy). The proposed devices consist of metallic thermocouples shaped as nano-antennas (Seebeck nanoantennas) sized to resonate to mid-infrared wavelengths. We show by means of simulations that these devices work by exploiting the temperature gradient caused by the resonant currents in the structures, which in turn generate a dc voltage  $V_{OC}$  by Seebeck effect at their “open ends;”<sup>23,24</sup> hence defining a mechanism to harvest the optical energy.

We investigate the conversion efficiency of Seebeck nanoantennas from both theoretical and numerical simulations approaches, evaluating their potential as power

micro-generators that retrieve the infrared energy. We analyze two types of structures, a square and an Archimedean spiral antennas (shown in Fig. 1), widely used for broadband applications at microwave and GHz frequencies, here scaled-down to infrared wavelengths.<sup>25-27</sup> The analysis is performed by using the commercial software COMSOL Multiphysics (ver3.5a) based on the finite-element method. This commercial package includes a platform where both the electromagnetic and thermal domains are fully integrated, as required for the present analysis.

We choose the so-called self-similarly spiral nanoantennas as convenient systems for solar applications since their electrical impedance behavior is ideally frequency-independent that leads to a broadband optical absorption.<sup>28</sup> These types of structures respond to any linearly polarized mid-infrared wave but exhibit a better performance for the right-handed circularly polarized light (RHCP),<sup>26</sup> confining the electric field  $E$  at its center. However, left-handed circularly polarized light (LHCP) spirals should be also included into a single device in order to fully benefit of the unpolarized sunlight.

Thin-film thermocouples are then conformed from spiral nanoantennas by building up their arms with dissimilar metals. The chosen power generators have one Ti-Ni interface placed at the center of the structures, what indeed optimizes the harvesting of thermal energy (as Joule heating is stronger there). On the other hand, materials with a considerable



FIG. 1. Schematic representation of the proposed Seebeck nanoantennas: (a) a square spiral and (b) an Archimedean spiral. These geometries consist of two symmetrical arms made of dissimilar metals, what creates a thermocouple. For each arm, the cross section is 200 nm width  $\times$  100 nm thick. Substrates consist of 1.2  $\mu\text{m}$  thick  $\text{SiO}_2$  layers.

<sup>a)</sup>Author to whom correspondence should be addressed. Electronic mail: edgar.briones@uaslp.mx

# Seebeck nanoantennas for the detection and characterization of infrared radiation

Edgar Briones,<sup>1</sup> Alexander Cuadrado,<sup>2</sup> Joel Briones,<sup>3</sup> Ramón Díaz de León,<sup>4</sup> Juan Carlos Martínez-Antón,<sup>2</sup> Stefan McMurtry,<sup>5</sup> Michel Hehn,<sup>5</sup> François Montaigne,<sup>5</sup> Javier Alda,<sup>2</sup> and Francisco Javier González<sup>1,\*</sup>

<sup>1</sup>*Coordinación para la Innovación y la Aplicación de la Ciencia y la Tecnología, Universidad Autónoma de San Luis Potosí, Sierra Leona 550, Lomas 2a Sección, SLP, México*

<sup>2</sup>*Applied Optics Complutense Group, University Complutense of Madrid, Faculty of Optics and Optometry, C/ Arcos de Jalón, 118. 28037, Madrid, Spain*

<sup>3</sup>*Departamento de Física, Universidad de Santiago de Chile (USACH), 9170124 Santiago, Chile*

<sup>4</sup>*Instituto Tecnológico de San Luis Potosí, Av. Tecnológico, S/N Col UPA, Soledad de Graciano Sánchez, México*

<sup>5</sup>*Institut Jean Lamour, CNRS, Université de Lorraine, Bd des Aiguillettes, BP70239, F-54506 Vandoeuvre Les Nancy, France*

\*[javier.gonzalez@uaslp.mx](mailto:javier.gonzalez@uaslp.mx)

**Abstract:** Arrays of metallic thermocouples in the shape of spiral nanoantennas are proposed as infrared detectors, which use the thermoelectric properties of the metallic interfaces to generate electrical DC signals. The responsivity of these types of antennas is evaluated from both theoretical and numerical perspectives pointing out its potential as infrared sensors. Moreover, the same structures can be used to characterize the state of polarization of the optical near fields with a spatial resolution comparable to the wavelength.

©2014 Optical Society of America

**OCIS codes:** (040.3060) Infrared; (040.5570) Quantum detector.

---

## References and links

1. P. Mühlischlegel, H. J. Eisler, O. J. F. Martin, B. Hecht, and D. W. Pohl, "Resonant Optical Antennas," *Science* **308**(5728), 1607–1609 (2005).
2. L. Novotny and N. van Hulst, "Antennas for light," *Nat. Photonics* **5**(2), 83–90 (2011).
3. W. L. Barnes, A. Dereux, and T. W. Ebbesen, "Surface plasmon subwavelength optics," *Nature* **424**(6950), 824–830 (2003).
4. F. Neubrech, T. Kolb, R. Lovrincic, G. Fehsold, A. Pucci, J. Aizpurua, T. W. Cornelius, M. E. Toimil-Molares, R. Neumann, and S. Karim, "Resonances of individual metal nanowires in the infrared," *Appl. Phys. Lett.* **89**(25), 253104 (2006).
5. R. L. Olmon, P. M. Krenz, A. C. Jones, G. D. Boreman, and M. B. Raschke, "Near-field imaging of optical antenna modes in the mid-infrared," *Opt. Express* **16**(25), 20295–20305 (2008).
6. S. Vedantam, H. Lee, J. Tang, J. Conway, M. Staffaroni, and E. Yablonovitch, "A plasmonic dimple lens for nanoscale focusing of light," *Nano Lett.* **9**(10), 3447–3452 (2009).
7. P. Biagioni, J. S. Huang, and B. Hecht, "Nanoantennas for visible and infrared radiation," *Rep. Prog. Phys.* **75**(2), 024402 (2012).
8. G. A. E. Vandenbosch and Z. Ma, "Upper bounds for the solar energy harvesting efficiency of nano-antennas," *Nano Energy* **1**(3), 494–502 (2012).
9. Z. Ma and G. A. E. Vandenbosch, "Optimal solar energy harvesting efficiency of nano-rectenna systems," *Sol. Energy* **88**, 163–174 (2013).
10. D. Dregely, R. Taubert, J. Dorfmueller, R. Vogelgesang, K. Kern, and H. Giessen, "3D optical Yagi-Uda nanoantenna array," *Nat Commun* **2**, 267 (2011).
11. F. J. González, B. Ilic, J. Alda, and G. D. Boreman, "Antenna-Coupled Infrared Detectors for Imaging Applications," *IEEE J. Sel. Top. Quantum Electron.* **11**(1), 117–120 (2005).
12. C. Fumeaux, M. A. Gritz, I. Codreanu, W. L. Schaich, F. González, and G. D. Boreman, "Measurement of the resonant lengths of infrared dipole antennas," *Infrared Phys. Technol.* **41**(5), 271–281 (2000).
13. F. González and G. Boreman, "Comparison of dipole, bowtie, spiral and log-periodic IR antennas," *Infrared Phys. Technol.* **46**(5), 418–428 (2005).
14. P. Krenz, J. Alda, and G. Boreman, "Orthogonal infrared dipole antenna," *Infrared Phys. Technol.* **51**(4), 340–343 (2008).
15. C. Fumeaux, W. Herrmann, F. Kneubühl, and H. Rothuizen, "Nanometer thin-film Ni-NiO-Ni diodes for detection and mixing of 30 THz radiation," *Infrared Phys. Technol.* **39**(3), 123–183 (1998).



Contents lists available at ScienceDirect

Toxicology Letters

journal homepage: [www.elsevier.com/locate/toxlet](http://www.elsevier.com/locate/toxlet)



# Silver nanoparticles induce anti-proliferative effects on airway smooth muscle cells. Role of nitric oxide and muscarinic receptor signaling pathway

Manuel A. Ramírez-Lee<sup>a,1</sup>, Héctor Rosas-Hernández<sup>a,d,1</sup>, Samuel Salazar-García<sup>a</sup>, José Manuel Gutiérrez-Hernández<sup>c</sup>, Ricardo Espinosa-Tanguma<sup>b</sup>, Francisco J. González<sup>c</sup>, Syed F. Ali<sup>d</sup>, Carmen González<sup>a,d,\*</sup>

<sup>a</sup> Universidad Autónoma de San Luis Potosí, Facultad de Ciencias Químicas, San Luis Potosí, Mexico

<sup>b</sup> Universidad Autónoma de San Luis Potosí, Facultad de Medicina, San Luis Potosí, Mexico

<sup>c</sup> Universidad Autónoma de San Luis Potosí, Coordinación para la Innovación y la Aplicación de la Ciencia y la Tecnología, San Luis Potosí, Mexico

<sup>d</sup> Neurochemistry Laboratory, Division of Neurotoxicology, National Center for Toxicological Research, FDA, Jefferson, AR, USA

## HIGHLIGHTS

- AgNPs induce anti-proliferative and apoptotic effects on airway smooth muscle cells.
- AgNPs activate muscarinic receptor pathway.
- Nitric oxide production is necessary for AgNPs muscarinic receptor activation.
- AgNPs could be a ligand for muscarinic receptor.

## ARTICLE INFO

### Article history:

Received 2 July 2013

Received in revised form 23 October 2013

Accepted 24 October 2013

Available online xxx

### Keywords:

Nitric oxide

Muscarinic receptor

Silver nanoparticles

Airway

Proliferation

Apoptosis

## ABSTRACT

Silver nanoparticles (AgNPs) are used to manufacture materials with new properties and functions. However, little is known about their toxic or beneficial effects on human health, especially in the respiratory system, where its smooth muscle (ASM) regulates the airway contractility by different mediators, such as acetylcholine (ACh) and nitric oxide (NO). The aim of this study was to evaluate the effects of AgNPs on ASM cells. Exposure to AgNPs induced ACh-independent expression of the inducible nitric oxide synthase (iNOS) at 100  $\mu\text{g}/\text{mL}$ , associated with excessive production of NO. AgNPs induced the muscarinic receptor activation, since its blockage with atropine and blockage of its downstream signaling pathway inhibited the NO production. AgNPs at 10 and 100  $\mu\text{g}/\text{mL}$  induced ACh-independent prolonged cytotoxicity and decreased cellular proliferation mediated by the muscarinic receptor-iNOS pathway. However, the concentration of 100  $\mu\text{g}/\text{mL}$  of AgNPs induced muscarinic receptor-independent apoptosis, suggesting the activation of multiple pathways. These data indicate that AgNPs induce prolonged cytotoxic and anti-proliferative effects on ASM cells, suggesting an activation of the muscarinic receptor-iNOS pathway. Further investigation is required to understand the full mechanisms of action of AgNPs on ASM under specific biological conditions.

© 2013 Published by Elsevier Ireland Ltd.

## 1. Introduction

Nanoparticles (NPs) are a particular kind of nanomaterials (Fiorino, 2010), which are structures that have one or more external dimensions in the nanoscale (1–100 nm). NPs have been widely

used in the late years due to unique properties attributable to their size (British Standards Institution, 2007). Among all the synthesized NPs the most studied are silver (AgNPs) (Project on Emerging Nanotechnologies, 2010), employed in medical (Chen and Schluesener, 2008; Chaloupka et al., 2010) and industrial (Bystrzejewska-Piotrowska et al., 2009) applications, mainly due to their antimicrobial properties (Morones et al., 2005). It has been estimated that approximately 14% of AgNPs consumer products could potentially release silver particles into the air during their use entering into the human body throughout inhalation to the respiratory system (Benn et al., 2010; Quadros and Marr, 2010).

\* Corresponding author at: Universidad Autónoma de San Luis Potosí, Facultad de Ciencias Químicas, Av. Manuel Nava Núm. 6., Col. Universitaria, 78210 San Luis Potosí, Mexico. Tel.: +52 444 8262440x566.

E-mail addresses: [cgonzalez.uaslp@gmail.com](mailto:cgonzalez.uaslp@gmail.com), [gonzalez.castillocarmen@fcq.uaslp.mx](mailto:gonzalez.castillocarmen@fcq.uaslp.mx) (C. González).

<sup>1</sup> These authors contributed equally in the realization of this work.

# Steerable optical antennas by selective heating

Alexander Cuadrado,<sup>1</sup> Francisco Javier González,<sup>2</sup> and Javier Alda<sup>1,\*</sup>

<sup>1</sup>Applied Optics Complutense Group, University Complutense of Madrid, C/Arcos de Jalón, 118, 28037 Madrid, Spain

<sup>2</sup>Universidad Autónoma de San Luis Potosí, Coordinación para la Innovación y Aplicación de la Ciencia y la Tecnología, Sierra Leona, 550, Lomas 2a Seccion, CIACYT Building, 78210, San Luis Potosí, SLP, Mexico

\*Corresponding author: j.alda@opt.ucm.es

Received January 3, 2014; revised February 6, 2014; accepted February 21, 2014;  
posted February 26, 2014 (Doc. ID 204031); published March 24, 2014

Directional steerability can be obtained for an array of optical antennas through selective heating of the individual elements. Heating changes electrical conductivity of the heated element, which affects the phase of the generated currents. The variation in temperature can be obtained by modifying the biasing point of the individual elements of the array, which would allow fast reconfiguration. The numerical evaluation of the performance of an array of a reduced number of antennas (2 and 3) shows the feasibility of this approach. © 2014 Optical Society of America

OCIS codes: (040.3060) Infrared; (250.5403) Plasmonics; (050.6624) Subwavelength structures; (050.5745) Resonance domain; (050.1755) Computational electromagnetic methods; (110.5100) Phased-array imaging systems.

<http://dx.doi.org/10.1364/OL.39.001957>

Optical antennas and resonant structures have found their place in the field of nanophotonics because of their relevant properties of electric field enhancement and excitation of plasmon resonances [1,2]. When optical antennas are used as detectors, their small footprint and selective properties in terms of polarization and wavelength selectivity can be fully exploited [3]. Most of their appealing characteristics are intrinsic to the antenna's nature. Moreover, some advances developed in the radio frequency and microwave spectra have been translated into the optical regime using optical antennas. This Letter deals with a concept that has been solved long ago at lower frequencies: the phased array antenna and its reconfigurable steerability [4]. This feature is possible because of the capability to control the phase differences among the elements of an array of antennas. Reconfigurable and steerable optical antennas are difficult to realize because the transmission of the phase information is not very efficient. Besides, they show poor flexibility in the spatial configuration once they are already fabricated. However, when resonant elements are close enough, their mutual interaction modifies the angular pattern, as happens with Yagi-Uda arrangements [5], or by moving the feed point in fluorescence measurements enhanced by plasmonic nanoantennas [6]. An interesting approach of coherent emission has been demonstrated recently; it uses the variation of the optical path along a dielectric waveguide using selective heating and dielectric nanoantennas that behave as substrate-to-air couplers [7]. In this Letter, we address the steering problem by modifying the electromagnetic characteristics of the device using temperature as the driving parameter.

The classical approach to design an effective antenna is to apply an impedance-matching condition that compensates the imaginary part of the impedance of the load. However, there are situations where this condition is not fulfilled. In those cases, an additional phase shift appears associated with the noncompensated imaginary part of the impedance. Actually, for fabricated optical antennas, although the geometry is already fixed, it is possible to detune the antenna and create an additional imaginary part of the complex impedance just by changing the temperature. In those cases, the built-in currents are shifted

with respect to the matching condition (see dashed line in the plot of Fig. 1). Some previous works have analyzed the variation of antenna performance with temperature [8–11]. This dependence is specially relevant for optical antennas. The values of both the real and imaginary parts of the electric permittivity of metals change with temperature. This affects the material behavior as a nonperfect conductor. Then, a change in temperature modifies the resistivity of the metal for low and high frequencies. It alters the skin depth, producing a variation of the complex impedance and therefore a modification of the optical characteristics of the resonant element. Optically, this has been experimentally demonstrated in reflectarrays [12]. Also, in the DC or low-frequency regime, it is being routinely used by bolometric detectors and it is exploited by optical antennas working as distributed bolometers [11]. If we are interested in a greater effect at high frequencies, the temperature variation needs to be larger. A significant variation in temperature can be caused, for example, by a change of the biasing current or voltage. The effect of modifying the bias voltage of fabricated nanoantennas has been analyzed previously, and shows a relevant increase in temperature of several hundreds of Kelvin when raising bias voltage by a very few volts [10]. As a consequence, if the elements of

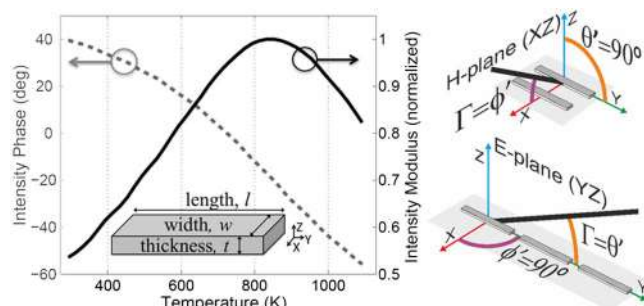


Fig. 1. Plot on the left represents the modulus (solid line) and phase (dashed line) of the generated intensity at the feed point of the dipole as a function of temperature. The inset shows the dimensional parameters of a dipole. On the right, we show the coordinate system used for the parallel two-dipole arrangement and the collinear three-dipole arrangement.

distortion of the downconverted baseband data. Therefore, the downconverted data were distorted after transmitting several kilometers of SMF in the DM system.

#### 4. CONCLUSION

The MW generation and upconversion performance levels were experimentally compared using a cascade SD-MZM OCS quadrupling frequency technique based on two modulation types. The 622 Mbps (1.25 Gbps)/15 GHz upconversion signals demonstrated the highest receiver sensitivity and the lowest power penalty by EM, which were  $-18.64$  dBm ( $-18.22$  dBm) and  $0.45$  dB ( $0.47$  dB) over a 20 km SMF error-free transmission. Additionally, the root-mean-square (RMS) jitter and signal-to-noise ratio were 23.3 ps (26.7 ps) and 22.75 dB (20.04 dB), respectively. The proposed technique demonstrated exceptional potential regarding its application to wireless access networks operating at the microwave band and can be extended to the millimeter-wave band.

#### ACKNOWLEDGMENT

The authors would like to thank the National Science Council of the Republic of China for their financial support under grant NSC 102-2622-E-027-015-CC3.

#### REFERENCES

1. J. Yu, G.K. Chang, Z. Jia, A. Chowdhury, M.F. Huang, H.C. Chien, Y.T. Hsueh, W. Jian, C. Liu, and Z. Dong, Cost-effective optical millimeter technologies and field demonstrations for very high throughput wireless-over-fiber access systems, *J Lightwave Technol* 28 (2010), 2376–2397.
2. A. Chowdhury, K. Chuang, H.C. Chien, D. Yeh, J. Yu, and G.K. Chang, Field demonstration of bi-directional millimeter wave RoF systems inter-operable with 60 GHz multi-gigabit CMOS transceivers for in-building hd video and data delivery, In: *Optical Fiber Communication Conference and Exposition and the National Fiber Optic Engineers Conference*, 2011, pp. 1–3.
3. C. Lim, A. Nirmalathas, M. Bakaul, P. Gamage, K.L. Lee, Y. Yang, D. Novak, and R. Waterhouse, Fiber-wireless networks and subsystem technologies, *J Lightwave Technol* 28 (2010), 390–405.
4. G. Keiser, *Overview of optical fiber communications*, McGraw-Hill, New York, 2010, pp. 1–14.
5. J. Yao, *Microwave photonics*, *J Lightwave Technol* 27 (2009), 314–335.
6. J. Liu, H.C. Chien, S.H. Fan, B. Chen, J. Yu, S. He, and G.K. Chang, Efficient optical millimeter-wave generation using a frequency-tripling Fabry-Perot laser with sideband injection and synchronization, *IEEE Photon Technol Lett* 23 (2011), 1325–1327.
7. Y.F. Wu, C.H. Yeh, C.W. Chow, F.Y. Shih, and S. Chi, Employing external injection-locked Fabry-Perot laser scheme for mm-wave generation, *Laser Phys* 21 (2011), 718–721.
8. C.H. Yeh, C.W. Chow, Y.F. Liu, and C.L. Pan, Using dual-mode self-locked semiconductor laser for optical millimeter-wave application, *Laser Phys* 21 (2011), 496–499.
9. S. Pan and J. Yao, Frequency-switchable microwave generation based on a dual-wavelength single-longitudinal-mode fiber laser incorporating a high-finesse ring filter, *Opt Express* 17 (2009), 12167–12173.
10. M.I. Memon, G. Mezosi, B. Li, D. Lu, Z. Wang, M. Sorel, and S. Yu, Generation and modulation of tunable mm-wave optical signals using semiconductor ring laser, *IEEE Photon Technol Lett* 21 (2009), 733–735.
11. Y.T. Hsueh, Z. Jia, H.C. Chien, J. Yu, and G.K. Chang, A novel bidirectional 60-GHz radio-over-fiber scheme with multiband signal generation using a single intensity modulator, *IEEE Photon Technol Lett* 21 (2009), 1338–1340.
12. A. Chowdhury, H.C. Chien, Y.T. Hsueh, and G.K. Chang, Advanced system technologies and field demonstration for in-building optical-

- wireless network with integrated broadband services, *J Lightwave Technol* 27 (2010), 1920–1927.
13. L. Chen, X. Lei, S. Wen, and J. Yu, A novel radio over fiber system with dwdm mm-wave generation and wavelength reuse for upstream data connection, *Opt Express* 15 (2007), 5893–5897.
14. P.T. Shih, J. Chen, C.T. Lin, W.J. Jiang, H.S. Huang, P.C. Peng, and S. Chi, Optical millimeter-wave signal generation via frequency 12-tupling, *J Lightwave Technol* 28 (2010), 71–78.
15. T. Wang, H. Chen, M. Chen, J. Zhang, and S. Xie, High-spectral-purity millimeter-wave signal optical generation, *J Lightwave Technol* 27 (2009), 2044–2051.
16. C.T. Lin, J. Chen, S.P. Dai, P.C. Peng, and S. Chi, Impact of nonlinear transfer function and imperfect splitting ratio of MZM on optical upconversion employing double sideband with carrier suppression modulation, *J Lightwave Technol* 26 (2008), 2449–2459.

© 2014 Wiley Periodicals, Inc.

## INFRARED IMAGING IN THE ANALYSIS OF PLANAR ANTENNAS

H. Díaz de León Torres,<sup>1</sup> S. Kolosovas-Machuca,<sup>1</sup> Jorge Simón,<sup>2</sup> Gustavo Vera-Reveles,<sup>1,3,4</sup> Edgar Briones,<sup>1</sup> and Francisco J. González<sup>1</sup>

<sup>1</sup>Coordinación para la Innovación y la Aplicación de la Ciencia y la Tecnología, Universidad Autónoma de San Luis Potosí, SLP, México; Corresponding author: javier.gonzalez@uaslp.mx

<sup>2</sup>Academia de Tecnologías de la Información y Telemática, Universidad Politécnica de San Luis Potosí, SLP, México

<sup>3</sup>Departamento de Físico-Matemáticas, Facultad de Ingeniería, Universidad Autónoma de San Luis Potosí, SLP, México

<sup>4</sup>Departamento de Ciencias Básicas, Instituto Tecnológico de San Luis Potosí, SLP, México

Received 28 October 2013

**ABSTRACT:** In this study, a noninvasive method based on infrared thermography is presented to obtain the resonant frequency of a dipole antenna in the microwave region. The study was performed by visualizing the temperature increase due to the Joule heating of the antenna fed by a voltage source. Results show a significant increase in dissipated heat at 830 MHz where the resonance is expected. This method can be used to measure planar antennas noninvasively and in-situ without having to take them to a specialized antenna-measurement facility. © 2014 Wiley Periodicals, Inc. *Microwave Opt Technol Lett* 56:1610–1612, 2014; View this article online at [wileyonlinelibrary.com](http://wileyonlinelibrary.com). DOI 10.1002/mop.28396

**Key words:** microwave planar antennas; infrared imaging; thermography; joule heating; half-wave dipole

### 1. INTRODUCTION

Planar antennas have been used for transmitting or receiving electromagnetic radiation for diverse purposes. They became popular in the 1970's due to their inexpensive cost of fabrication, low-profile, and attractive radiation characteristics [1], they are extensively used for space-borne applications [2, 3], today they are used for government and commercial applications such as satellites, missiles, cars, and handheld or mobile devices [4].

Testing of planar antennas by standard techniques requires the use of expensive equipment and special facilities [5, 6]. In this work, a method based on infrared imaging systems is used to test planar antennas. This method takes advantage of the thermal heating of the antennas' surface caused by Joule heating due to the induced current on the antennas. Surface distribution of current can thus be obtained from the thermal distribution by using the Joule heating equation, with the calculated surface



## Book drawings of complete bipartite graphs

Etienne de Klerk<sup>a</sup>, Dmitrii V. Pasechnik<sup>b</sup>, Gelasio Salazar<sup>c,\*</sup>

<sup>a</sup> Department of Econometrics and Operations Research, Tilburg University, The Netherlands

<sup>b</sup> Department of Computer Science, University of Oxford, Wolfson Building, Parks Road, Oxford, OX1 3QD, UK

<sup>c</sup> Instituto de Física, Universidad Autónoma de San Luis Potosí, San Luis Potosí, SLP, 78000, Mexico

### ARTICLE INFO

#### Article history:

Received 16 October 2012

Received in revised form 21 October 2013

Accepted 10 November 2013

Available online 28 November 2013

#### Keywords:

2-page crossing number

Book crossing number

Complete bipartite graphs

Zarankiewicz conjecture

### ABSTRACT

We recall that a *book* with  $k$  pages consists of a straight line (the *spine*) and  $k$  half-planes (the *pages*), such that the boundary of each page is the spine. If a graph is drawn on a book with  $k$  pages in such a way that the vertices lie on the spine, and each edge is contained in a page, the result is a  $k$ -page *book drawing* (or simply a  $k$ -page *drawing*). The *page number* of a graph  $G$  is the minimum  $k$  such that  $G$  admits a  $k$ -page embedding (that is, a  $k$ -page drawing with no edge crossings). The  $k$ -page *crossing number*  $\nu_k(G)$  of  $G$  is the minimum number of crossings in a  $k$ -page drawing of  $G$ . We investigate the page numbers and  $k$ -page crossing numbers of complete bipartite graphs. We find the exact page numbers of several complete bipartite graphs, and use these page numbers to find the exact  $k$ -page crossing number of  $K_{k+1,n}$  for  $k \in \{3, 4, 5, 6\}$ . We also prove the general asymptotic estimate  $\lim_{k \rightarrow \infty} \lim_{n \rightarrow \infty} \nu_k(K_{k+1,n}) / (2n^2/k^2) = 1$ . Finally, we give general upper bounds for  $\nu_k(K_{m,n})$ , and relate these bounds to the  $k$ -planar crossing numbers of  $K_{m,n}$  and  $K_n$ .

© 2013 Elsevier B.V. All rights reserved.

### 1. Introduction

In [6], Chung, Leighton, and Rosenberg proposed the model of embedding graphs in books. We recall that a *book* consists of a line (the *spine*) and  $k \geq 1$  half-planes (the *pages*), such that the boundary of each page is the spine. In a *book embedding*, each edge is drawn on a single page, and no edge crossings are allowed. The *page number* (or *book thickness*)  $p(G)$  of a graph  $G$  is the minimum  $k$  such that  $G$  can be embedded in a  $k$ -page book [3, 12, 6, 14]. Not surprisingly, determining the page number of an arbitrary graph is NP-complete [6].

In a *book drawing* (or  $k$ -page *drawing*, if the book has  $k$  pages), each edge is drawn on a single page, but edge crossings are allowed. The  $k$ -page *crossing number*  $\nu_k(G)$  of a graph  $G$  is the minimum number of crossings in a  $k$ -page drawing of  $G$ .

Instead of using a straight line as the spine and half-planes as pages, it is sometimes convenient to visualize a  $k$ -page drawing using the equivalent *circular model*. In this model, we view a  $k$ -page drawing of a graph  $G = (V, E)$  as a set of  $k$  circular drawings of graphs  $G^{(i)} = (V, E^{(i)})$  ( $i = 1, \dots, k$ ), where the edge sets  $E^{(i)}$  form a  $k$ -partition of  $E$ , and such that the vertices of  $G$  are arranged identically in the  $k$  circular drawings. In other words, we assign each edge in  $E$  to exactly one of the  $k$  circular drawings. In Fig. 1 we illustrate a 3-page drawing of  $K_{4,5}$  with 1 crossing.

Very little is known about the page numbers or  $k$ -page crossing numbers of interesting families of graphs. Even computing the page number of a planar graph is a nontrivial task; Yannakakis proved [24] that four pages always suffice, and sometimes are required, to embed a planar graph. It is a standard exercise to show that the page number  $p(K_n)$  of the complete graph  $K_n$  is  $\lceil n/2 \rceil$ . Much less is known about the  $k$ -page crossing numbers of complete graphs. A thorough treatment of  $k$ -page crossing numbers (including estimates for  $\nu_k(K_n)$ ), with general lower and upper bounds, was offered by Shahrokhi et al. [22].

\* Corresponding author. Tel.: +52 444 8262362; fax: +52 4448133874.

E-mail addresses: [g.salazar@ifisica.uaslp.mx](mailto:g.salazar@ifisica.uaslp.mx), [gelasio.salazar@gmail.com](mailto:gelasio.salazar@gmail.com) (G. Salazar).

# Photoluminescence shift in frustules of two pennate diatoms and nanostructural changes to their pores

Nubia V. Arteaga-Larios,<sup>a</sup> Yuri Nahmad,<sup>b</sup> Hugo R. Navarro-Contreras,<sup>c</sup> Armando Encinas<sup>b</sup> and J. Viridiana García-Meza<sup>a\*</sup>

**ABSTRACT:** The diatom silicified cell wall (frustule) contains pore arrays at the micro- to nanometer scale that display efficient luminescence within the visible spectrum. Morphometric analysis of the size and arrangement of pores was conducted to observe whether any correlation exists with the photoluminescence (PL) of two diatom species of different ages. UV-excited PL displays four clearly defined peaks within the blue-region spectrum, on top of the broad PL characteristic of synthetic porous silicon dioxide, recorded for reference and where discrete lines are absent. A set of shifted emission lines was observed when diatom cultures reached adulthood. These discrete line shifts correlate with structural changes observed in adult frustules: reduction in pore diameter; appearance of pores within pores, 10 nm in size; an increase in the gap distance between stria; and the deposition of several girdle bands with a concomitant increase in the diatom waist length, as well as the appearance of pores on such bands. Destruction of the pores results in the disappearance of all discrete emission lines. The PL shifts are correlated with a substantial increment of Si–OH groups adsorbed on the frustule surface, as revealed by Fourier transform infrared spectroscopy. Copyright © 2014 John Wiley & Sons, Ltd.

**Keywords:** photoluminescence; diatoms; nanostructured pores; morphometric analysis; OH radicals

## Introduction

In 1990, Canham (1) discovered that porous silicon displayed efficient luminescence within the visible spectrum, at ambient temperature. Since then, extensive studies on nanostructured porous silicon and porous silica (PSO), have been conducted (1,2). PSO is a versatile material because its photoluminescence (PL), high specific area and pore density confer optical properties that can be manipulated at the nanometer scale. A myriad of applications of PSO are possible because of its diverse electric and optical properties: in photovoltaic conversion and the manufacture of photonic devices, as well as in chemical sensors, biosensors, adsorbent material, membranes and catalysis hosts. Moreover, PSO is a biocompatible material (3), so it can also be used as a drug carrier through the body, and as a building material in the synthesis of bone implants (4).

The diatom cell wall is a naturally occurring structure made of amorphous silica (SiO<sub>2</sub>) known as a 'siliceous frustule'; it has features on the micro- and nano-scale and has been shown to display PL properties (5). Diatoms are unicellular microalgae (photoautotrophic eukaryote) that assimilate dissolved silicic acid from the media to synthesize a frustule of amorphous SiO<sub>2</sub> (5). In terms of its morphology, each frustule has two assembled 'valves', resulting in a jewel-box-like structure; the joint between the valves is called the 'girdle band' or 'cingulum' and is also of a siliceous nature. In addition, the frustules possess an exquisite ornamental (striated) and functional arrangement of pores, ranging from nano- to micrometers in diameter. In other words, the diatom frustule is a nanostructured porous silica material, with efficient PL properties, and thus possesses the potential to be used as a building block for optical devices (6,7).

The use of diatoms rather than synthetic material has the advantage of avoiding the lengthy nano-technological methods commonly used to synthesize nanometric-sized PSO (4). Thus, alternative methodologies to produce PSO are desirable; one of which may be to take advantage of diatom frustules (7). Further, many biological systems naturally function as optical and photonic devices, with several interesting properties; they also generate intricate nanostructures more complex or ordered than anything that might be produced using artificial techniques (8).

Here, we present a study on two species of diatoms *Amphora* and *Gomphocymbella* (9) with silicified frustules of different ages (young and adult). Electron transmission microscopy was used to visualize frustule morphology and any changes with age. The UV-excited PL emitted was studied and was compared between both species of diatoms, of different ages, and with the PL of synthetic porous SiO<sub>2</sub>. Finally, the frustules were further studied by means of Fourier transform infrared (FTIR) spectroscopy to establish any possible correlation between the surface chemistry and the PL emission characteristics.

\* Correspondence to: J. Viridiana García-Meza, Geomicrobiology Laboratory, Institute of Metallurgy-DICIM, UASLP, Sierra Leona 550, 78210 SLP, México. E-mail: jvgm@uaslp.mx

<sup>a</sup> Geomicrobiology Laboratory, Institute of Metallurgy-DICIM, UASLP, Sierra Leona 550, 78210 SLP, México

<sup>b</sup> Institute of Physics, UASLP, Dr. Manuel Nava 8, 78217 SLP, México

<sup>c</sup> CIACyT, Center for the Innovation and Application of Science and Technology, UASLP, Sierra Leona 550, 78210 SLP, México

# An experimental electronic model for a neuronal cell

I Campos-Cantón<sup>1</sup>, A Rangel-López<sup>2</sup>, G Martel-Gallegos<sup>1</sup>,  
S Zarazúa<sup>3</sup> and A Vertiz-Hernández<sup>2</sup>

<sup>1</sup> Facultad de Ciencias, Universidad Autónoma de San Luis Potosí (UASLP),  
Alvaro Obregón 64, 78000 San Luis Potosí, SLP, Mexico

<sup>2</sup> Coordinación Académica Región Altiplano, Universidad Autónoma de San Luis  
Potosí (UASLP), Alvaro Obregón 64, 78000 San Luis Potosí, SLP, Mexico

<sup>3</sup> Facultad de Ciencias Químicas, Universidad Autónoma de San Luis Potosí  
(UASLP), Alvaro Obregón 64, 78000 San Luis Potosí, SLP, Mexico

E-mail: [icampos@ciencias.uaslp.mx](mailto:icampos@ciencias.uaslp.mx)

Received 10 December 2013, revised 14 January 2014

Accepted for publication 3 February 2014

Published 5 March 2014

## Abstract

Over the last two decades, the study of information transmission in living beings has acquired great relevance, because it regulates and conducts the functioning of all of the organs in the body. In information transmission pathways, the neuron plays an important role in that it receives, transmits, and processes electrical signals from different parts of the human body; these signals are transmitted as electrical impulses called action potentials, and they transmit information from one neuron to another. In this work, and with the aim of developing experiments for teaching biological processes, we implemented an electronic circuit of the neuron cell device and its mathematical model based on piecewise linear functions.

Keywords: neurons, synapses, analogue circuits, H–H model, linear systems

(Some figures may appear in colour only in the online journal)

## 1. Introduction

The nervous system is composed of excitable cells: the neurons. Neurons can generate electric signals to transmit information. The exchange of  $\text{Na}^+$  and  $\text{K}^+$  ions across the neuronal membrane generates these electrical signals. Ordinarily, neurons generate a negative electric potential, called the resting membrane potential (typically  $-70$  mV) (figure 1), as result of a net efflux of  $\text{K}^+$  across neuronal membranes, which are predominantly  $\text{K}^+$ -permeable, and the intracellular accumulation of anions and proteins. This resting membrane potential can be modified in response to stimuli from receptor potentials or synapses. If the membrane potential



# Chua's circuit and its characterization as a filter

I Campos-Cantón<sup>1</sup>, O A Segura-Cisneros<sup>2</sup>,  
R E Balderas-Navarro<sup>2</sup> and E Campos-Cantón<sup>3</sup>

<sup>1</sup>Facultad de Ciencias, Universidad Autonoma de San Luis Potosi (UASLP), Mexico

<sup>2</sup>Instituto de Investigación en Comunicación Óptica, Universidad Autónoma de San Luis Potosí (UASLP), Alvaro Obregón 64, 78000 San Luis Potosí, SLP, Mexico

<sup>3</sup>División de Matemáticas Aplicadas, Instituto Potosino de Investigación Científica y Tecnológica (IPICYT), Camino a la Presa San José 2055, 78216 San Luis Potosí, SLP, Mexico

E-mail: [icampos@ciencias.uaslp.mx](mailto:icampos@ciencias.uaslp.mx)

Received 4 June 2014, revised 4 August 2014

Accepted for publication 27 August 2014

Published 22 September 2014

## Abstract

This article deals with Chua's circuit characterization from the point of view of a filter based on the concept of piecewise linear functions. Furthermore, experiments are developed for teaching electronic systems that can be used for novel filtering concepts. The frequency range in which they are tested is from 20 Hz to 20 kHz, due to the audio spectrum comprised in this frequency range. The node associated with the capacitor and Chua's diode is used as input, and the node for another capacitor and the coil is used as output, thereby establishing one input-output relationship for each system case given by the piecewise linear functions. The experimental result shows that Chua's circuit behaves as a bandpass filter-amplifier, with a maximum frequency around 3 kHz and bandwidth between 1.5 kHz and 5.5 kHz. The results presented in this paper can motivate engineering students to pursue applications of novel electrical circuits based on topics that are of potential interest in their future research studies.

Keywords: filters, Chua's circuit, piecewise linear functions, analog electronics

## 1. Introduction

Filters are key elements in a wide variety of electronic applications. Among them we can mention the wireless transceivers [1] and information retrieval in direct transmission [2], for which a band pass filter is used to extract the embedded desired signal in a sum of different



ARTÍCULO ORIGINAL

## Clorhidrato de pioglitazona: una perspectiva analítico-instrumental por espectroscopia Raman y HPLC

Jesús Fernando Vértiz-Beltrán,\*\* Raquel Ávila-Rodríguez,\* Rocío Terrones-Gurrola,\* Luis Abelardo Camacho,\*\*\*\* Azahel Rangel-López,\* Isaac Campos-Cantón,\*\*\* Ángel Antonio Vértiz-Hernández\*

\* Coordinación Académica Región Altiplano,\*\* Facultad de Ciencias Químicas, \*\*\* Facultad de Ciencias, Universidad Autónoma de San Luis Potosí.

\*\*\*\* Facultad de Medicina, Universidad Juárez del Estado de Durango.

*Pioglitazone hydrochloride a instrumental analytical perspective by Raman spectroscopy and HPLC*

### ABSTRACT

**Introduction.** The thiazolidinediones (pioglitazone) increases the action of insulin and produces the glycemic control in the patients with type 2 diabetes mellitus. Also, the pharmacological effect may be affected by the purity and pioglitazone plasma concentration. Therefore, the instrumental techniques offer a tool for characterization, identification and/or quantification of the pioglitazone; Raman spectroscopy offers several advantages due to its easy application methodology and structural analysis and the HPLC technique is the gold standard vs. other qualitative and quantitative techniques. **Objective.** The aim of this work is to develop and validate analytical techniques for the characterization of pioglitazone hydrochloride by Raman spectroscopy and quantitative analysis in human plasma by HPLC. **Material and methods.** The pioglitazone hydrochloride was analyzed by Raman spectroscopy with a 678 mW power and 3 integration time seconds. The analytical method for quantification by HPLC was validated with the guidelines of the NOM-177SSA1-1998. **Results.** The Raman technique allowed us to elucidate the functional groups of the pioglitazone hydrochloride and the HPLC technique was linear, accurate, precise, specific and sensitive in the range of 30 to 2,000 ng/mL under the chromatographic conditions specified. **Conclusions.** The structure analysis by Raman spectroscopy allowed us a complete characterization of the functional groups of pioglitazone hydrochloride effectively and non-destructively. Likewise, the analytical technique for the pioglitazone hydrochloride quantification by HPLC was

### RESUMEN

**Introducción.** La pioglitazona incrementa la acción de la insulina, por ello disminuye la insulinoresistencia en la diabetes mellitus tipo 2. Asimismo, la pureza y la concentración plasmática de la pioglitazona modifican el efecto farmacológico; las técnicas instrumentales ofrecen caracterización, identificación y/o cuantificación de estas moléculas farmacológicas. La espectroscopia Raman es de fácil metodología y aplicación en el análisis estructural y el HPLC representa el estándar de oro entre muchas técnicas cualitativas y cuantitativas. **Objetivo.** Desarrollar y validar las técnicas por espectroscopia Raman y HPLC para la caracterización del clorhidrato de pioglitazona. **Material y métodos.** Se analizó el clorhidrato de pioglitazona por espectroscopia Raman bajo una potencia de 678 mW y un tiempo de integración de 3 s; asimismo, la técnica por HPLC se validó bajo los lineamientos de la NOM-177SSA1-1998. **Resultados.** La espectroscopia Raman permitió dilucidar los grupos funcionales de la molécula de clorhidrato de pioglitazona sin extracción de la muestra; sin embargo, no demostró ser lineal, exacta y precisa en un rango de 30 a 2,000 ng/mL. El análisis HPLC fue lineal, exacto, preciso, sensible, selectivo y robusto en un rango de 30 a 2,000 ng/mL. **Conclusiones.** La espectroscopia Raman permitió una completa caracterización de los grupos funcionales de manera eficaz y no destructiva, no así un análisis cuantitativo; asimismo, la técnica analítica por HPLC demostró ser lineal, exacta, precisa, sensible, selectiva y robusta en un rango de 30 a 2,000 ng/mL permitiéndonos hacer un confiable análisis cuantitativo de clorhidrato de pioglitazona.



Praise Worthy Prize

International Review of  
Electrical Engineering  
(IREE)

HOME PRAISE WORTHY PRIZE ABOUT LOGIN REGISTER SEARCH CURRENT  
ARCHIVES ANNOUNCEMENTS OTHER JOURNALS DOWNLOAD ISSUES SUBMIT YOUR PAPER  
SPECIAL ISSUE

Home > Vol 9, No 3 (2014) > **Martínez Montejano**

## **Generalization of a model-based controller for the n-level cascaded H-bridge multilevel converter used as a shunt active filter**

*Roberto Carlos Martínez Montejano<sup>(1\*)</sup>, R. Castillo Meraz<sup>(2)</sup>, I. Campos-Cantón<sup>(3)</sup>, M. F. Martínez-Montejano<sup>(4)</sup>*

<sup>(1)</sup> Universidad Autónoma de San Luis Potosí, Mexico

<sup>(2)</sup> Universidad Autónoma de San Luis Potosí, Mexico

<sup>(3)</sup> Universidad Autónoma de San Luis Potosí, Mexico

<sup>(4)</sup> Research and Development Department of Alstom Power, Mexico

<sup>(\*)</sup> Corresponding author

### **DOI's assignment:**

*the author of the article can submit [here](#) a request for assignment of a DOI number to this resource!*

**Cost of the service: euros 10,00 (for a DOI)**

### **Abstract**

The general function of the multilevel inverter is to synthesize a desired AC voltage from several levels of DC voltages. For this reason, multilevel converters are ideal for connecting either in series or in parallel an AC grid with renewable energy sources such as photovoltaics, fuel cells or with energy storage devices such as capacitors or batteries. For more levels of voltages, the total



Praise Worthy Prize

International Review of  
Electrical Engineering  
(IREE)

HOME	PRAISE WORTHY PRIZE	ABOUT	LOGIN	REGISTER	SEARCH	CURRENT
ARCHIVES	ANNOUNCEMENTS	OTHER JOURNALS	DOWNLOAD ISSUES	SUBMIT YOUR PAPER		
SPECIAL ISSUE						

Home > Vol 9, No 1 (2014) > **Montejano**

---

## Phase Locked Loop based on adaptive observer

Roberto Carlos Martínez Montejano<sup>(1\*)</sup>, Raúl Castillo Meraz<sup>(2)</sup>, Ricardo Eliu Lozoya Ponce<sup>(3)</sup>, Isaac Campos Cantón<sup>(4)</sup>, Misael Francisco Martínez Montejano<sup>(5)</sup>, Rogelio Osvaldo Lozoya Ponce<sup>(6)</sup>

- (1) Universidad Autónoma de San Luis Potosí,
- (2) Universidad Autónoma de San Luis Potosí,
- (3) Universidad Autónoma de San Luis Potosí,
- (4) Universidad Autónoma de San Luis Potosí,
- (5) Research and Development Department of Alstom Power,
- (6) Universidad Autónoma de San Luis Potosí,
- (\*) Corresponding author

### DOI's assignment:

the author of the article can submit [here](#) a request for assignment of a DOI number to this resource!

Cost of the service: euros 10,00 (for a DOI)

### Abstract

*A phase Locked Loop is a control system that generates an alternating signal with a bounded phase respect to an input signal, a feedback loop makes a comparison between these two signals and modifies its output signal frequency. This paper presents a PLL scheme which is aimed to estimate the angular frequency of the input voltage as well as a low pass filter function for cleaning this distorted signal. A prototype based on operational amplifiers has been built and simulations and experimental results are*

# Relation Between Heart Beat Fluctuations and Cyclic Alternating Pattern During Sleep in Insomnia Patients.

R. de León-Lomelí, J.S. Murguía, I. Chouvarda, *IEEE Member*, MO Mendez, *IEEE Member*, E. González-Galván, A. Alba, *EMBS Member*, G. Milioli, A. Grassi, MG. Terzano, L. Parrino.

**Abstract**— Insomnia is a condition that affects the nervous and muscular system. Thirty percent of the population between 18 and 60 years suffers from insomnia. The effects of this disorder involve problems such as poor school or job performance and traffic accidents. In addition, patients with insomnia present changes in the cardiac function during sleep. Furthermore, the structure of electroencephalographic A-phases, which builds up the Cyclic Alternating Pattern during sleep, is related to the insomnia events. Therefore, the relationship between these brain activations (A-phases) and the autonomic nervous system would be of interest, revealing the interplay of central and autonomic activity during insomnia. With this goal, a study of the relationship between A-phases and heart rate fluctuations is presented. Polysomnography recording of five healthy subjects, five sleep misperception patients and five patients with psychophysiological insomnia were used in the study. Detrended Fluctuation Analysis (DFA) was used in order to evaluate the heart rate dynamics and this was correlated with the number of A-phases. The results suggest that pathological patients present changes in the dynamics of the heart rate. This is reflected in the modification of A-phases dynamics, which seems to modify of heart rate dynamics.

## I. INTRODUCTION

Insomnia is a condition where the subject experiences an inability to sleep, which prevent the human body from resting, and therefore affects the nervous and muscular system. The effects of this disorder often involve problems such as poor school or job performance, traffic accidents and also are related with cardiac fails [1]. In this paper we consider two types of primary insomnia: psychophysiological insomnia and paradoxical insomnia which are compared with subjects without sleep disorders [2].

Research supported by SEP-CONACyT grant CB-2010 154623 and CB-2012 180604.

R. de León- Lomelí, is with the Universidad Autónoma de San Luis Potosí México were she is currently working toward the PhD degree. e-mail: roxy\_dl@hotmail.com.

I. Chouvarda is at the Lab of Medical Informatics, Aristotle University of Thessaloniki, Greece.

M. Mendez, A. S.Murguía, A. Alba, and E. González are with the Universidad Autónoma de San Luis Potosí, Diagonal Sur S/N, Zona Universitaria, San Luis Potosí, S.L.P., México

L. Parrino, A. Grassi, and M. Terzano are at Sleep Disorders Centre, Department of Neurology, University of Parma, Parma, Italy.

Previous studies showed that insomnia has a relationship with CAP (Cyclic Alternating Pattern) [3]. CAP is a periodic activity reflected in the EEG during non-REM sleep, and is characterized by sequences of transient electrocortical events, called A-phases, deviating from the baseline of the EEG activity, and occurs repeatedly in 2 to 60 seconds interval. Increased CAP (generally, also the number of A-phases increase) itself may indicate unstable sleep and / or sleep disturbance, and can also be used to identify patterns associated with some sleep disorders. A-phases are identified as A1, A2 and A3, and are closely related to the stages of sleep wakefulness and NREM [2].

A-phases are classified in three groups based on the observed frequency information:

- i. A1-phase. It is characterized by bursts and k-complexes of Delta waves (0.5 Hz - 4 Hz).
- ii. A2-phase. It has rapid EEG waves that cover between 20% and 50% of the A-phase duration.
- iii. A3-phase. It is characterized by Alpha (8 Hz - 12 Hz) and Beta waves (12 Hz - 30 Hz), which cover more than 50% of the A-phase duration [3].

Moreover, the dynamics of the heart rate could be characterized by the Heart Rate Variability (HRV), computed as the time between the detection of consecutive R peaks, obtained from an electrocardiogram signal [4]. Previous analysis focused on the HRV signals in apnea patients and other pathologies, finding a correlation grade between them, using DFA as analysis method.

However the correlation between A-phases and heart dynamics in sleep stages has not been analyzed before. And even there is little information about the interaction of the time series in HRV and EEG sleep periods [4] [5] [6].

The main goal of this study is to investigate potential correlation between the A-phases and the HRV signals and to understand the effect of insomnia in them. DFA analysis of HRV is applied and its changes with sleep macro and micro structure are discussed.

## II. METHODS AND MATERIALS

### A. Mathematical analysis

In 1994 C. K. Peng et al. [7] proposed a method, referred to as Detrended Fluctuation Analysis (DFA) that enables the

## Image encryption with an improved cryptosystem based on a matrix approach

M. T. Ramírez-Torres

*Instituto de Investigación en Comunicación Óptica, UASLP  
Álvaro Obregón No. 64 Centro, C.P. 78000 San Luis Potosí, S.L.P., México  
tulio.torres@alumnos.uaslp.edu.mx*

J. S. Murguía\*

*Facultad de Ciencias, Universidad Autónoma de San Luis Potosí UASLP  
Álvaro Obregón No. 64 Centro, C.P. 78000 San Luis Potosí, S.L.P., México  
ondeleto@uaslp.mx*

M. Mejía Carlos

*Instituto en Investigación en Comunicación Óptica, UASLP  
Álvaro Obregón No. 64 Centro, C.P. 78000 San Luis Potosí, S.L.P., México  
marcela.mejia@uaslp.mx*

Received 26 February 2014

Accepted 8 March 2014

Published 21 April 2014

This paper carries out the image encryption with a revised and modified cryptosystem based on a rule-90 cellular automaton. For this purpose, we used an appropriate and convenient matrix approach to implement the main components of the encryption system, two indexed families of permutations and a pseudo-random bit generator. Furthermore, we modify the encryption scheme for improving its security. This makes our encryption proposal resist some common attacks, e.g. chosen plain-text attack, and the encryption and decryption processes are performed in a flexible way. Also, some security aspects of the cryptosystem are evaluated with a series of statistical tests exhibiting good results. It is believed that this proposal fits naturally in the present digital technology and is capable of achieving high levels of performance.

*Keywords:* Encryption system; matrix approach; image processing.

PACS Nos.: 05.40.-a, 05.45.-a, 05.45.Tp.

### 1. Introduction

Since ancient times, the search of algorithms or procedures to protect different kind of information has been a complex issue. Nowadays, with the great advances in technology, there has been an increasing interest to have better and more efficient

\*Corresponding author.

## Measurement of the shear strain of the $\text{Gd}_2\text{O}_3/\text{GaAs}(001)$ interface by photoreflectance difference spectroscopy

N. A. Ulloa-Castillo,<sup>1,a)</sup> L. F. Lastras-Martínez,<sup>1,b)</sup> R. E. Balderas-Navarro,<sup>1,2,c)</sup>  
 R. Herrera-Jasso,<sup>1</sup> and A. Lastras-Martínez<sup>1</sup>

<sup>1</sup>Instituto de Investigación en Comunicación Óptica, Universidad Autónoma de San Luis Potosí,  
 Alvaro Obregón 64, San Luis Potosí 78000, Mexico

<sup>2</sup>Paul-Drude-Institut für Festkörperelektronik, Hausvogteiplatz 5-7, 10117 Berlin, Germany

(Received 2 August 2014; accepted 27 October 2014; published online 6 November 2014)

In this work, we report on photoreflectance (PR) and photoreflectance-difference (PR-D) measurements of GaAs(001) upon deposition of  $\text{Gd}_2\text{O}_3$  thin films. The study is focused on two different substrates: a semi-insulating (SI) with Cr impurities and a Si-doped  $n$ -type. PR-D results show that  $\text{Gd}_2\text{O}_3$  induces a tensile strain on the GaAs surface and a direct piezo-electric dipole is created. Such strain changes the crystal symmetry from cubic to orthorhombic and renders the quadratic electro-optic (QEO) component anisotropic. For the SI substrate, both linear electro-optic (LEO) and QEO components contribute to the PR-D spectrum, whereas the  $n$ -type PR-D spectrum is dominated by the LEO component. In both cases, a tensile strain induces a rigid redshift of  $\sim 20$  meV to low energies of the  $E_1$  and  $E_1 + \Delta_1$  optical transitions. © 2014 AIP Publishing LLC.  
[\[http://dx.doi.org/10.1063/1.4901168\]](http://dx.doi.org/10.1063/1.4901168)

The high- $\kappa$  dielectric/III-V interface is extremely important for metal-oxide-semiconductor (MOS) technology and can exhibit either a high or low interface state density depending on both the intrinsic properties of III-V surfaces and the nature of their oxidation chemistry.<sup>1,2</sup> In particular,  $\text{Gd}_2\text{O}_3$  has been investigated due to its high dielectric constant,<sup>3,4</sup> large band gap<sup>5</sup> and excellent thermodynamical stability in semiconductors.<sup>6,7</sup> As a matter of fact, a low interfacial density of states was demonstrated in  $\text{Gd}_2\text{O}_3/\text{GaAs}$  MOS devices.<sup>8,9</sup> However, as GaAs has piezo-electric character, a polarization charge will be induced by the stress at the insulator-semiconductor interface when the dielectric layer is deposited, thus modifying the electric properties at the interface by this induced charge. In this regard, probing of interface states evolution for process control during interface formation is of particular importance, preferably *in situ*. Optical spectroscopies are non-invasive and can be operated in any environment.

Two linear optical spectroscopies employed to probe surface piezo-electric phenomena in semiconductors are reflectance-difference (RD) and photoreflectance-difference (PR-D) spectroscopies.<sup>10-13</sup> On the (001) surface of zinc-blende semiconductors, RD measures the difference in reflectivity between  $[110]$  and  $[1\bar{1}0]$  light polarizations,<sup>10,14</sup> whereas PR-D accounts for the difference between a PR spectrum for polarized probe light (along either  $[110]$  or  $[1\bar{1}0]$ ) and the corresponding spectrum for unpolarized probe light.<sup>15</sup> Furthermore, PR spectra comprise both linear electro-optic (LEO) and quadratic electro-optic (QEO) components. PR-D spectra involve only the LEO component as the QEO contribution is nominally isotropic. However, when the crystal symmetry is modified, as in the case of an

external stress applied along  $[110]$ , the QEO component becomes anisotropic as well.<sup>16</sup> For instance, the strain caused by dimers at the GaAs(001)- $c(4 \times 4)$  surface reconstruction induces a direct piezo-electric dipole (DPD) that opposes the electric field ( $F$ ) of the space-charge layer within the first tens monolayers into the crystal.<sup>10</sup> Another example is the hydrocarbon ring molecule adsorption onto the As surface dimers of GaAs(001)- $c(4 \times 4)$ , which reduces the surface band bending causing an increment of  $F$ .<sup>17</sup> Therefore, a modification of the surface states influences significantly the surface electro-optical properties.<sup>18</sup>

In this work, we report on *in situ* PR and PR-D measurements of two GaAs(001) surfaces: a semi-insulating (SI) with Cr impurities and a Si-doped  $n$ -type. PR and PR-D measurements were done around  $E_1$  and  $E_1 + \Delta_1$  optical transitions in order to investigate changes of the surface states caused by modifications in the surface electric field upon deposition of  $\text{Gd}_2\text{O}_3$  on GaAs. The results for the SI substrate show that  $\text{Gd}_2\text{O}_3$  modifies the GaAs(001) by building up a tensile shear strain which renders the QEO component anisotropic, whereas, for the  $n$ -type substrate, the LEO component dominates the lineshapes even after  $\text{Gd}_2\text{O}_3$  deposition. We note that, because we are interested on the PR-D evolution upon surface modifications, the critical points at  $E_1$  (2.92 eV) and  $E_1 + \Delta_1$  (3.13 eV) optical transitions were used, as the penetration depth of the probe light is only 170 Å for GaAs. This contrasts the case at  $E_0$  (1.42 eV), where probe light can penetrate down to the back-face in thin GaAs substrates, thus washing out any optical anisotropy coming from the front surface.

PR and PR-D measurements were carried out in ultra-high vacuum (UHV) on the S1 and S2 substrates which are described in Table I. Both samples were chemical etched in  $\text{H}_2\text{O}:\text{H}_2\text{SO}_4:\text{H}_2\text{O}_2$  (1:5:1) and immediately introduced into the UHV chamber. The samples were then heated up gradually to obtain a clear  $(1 \times 1)$  reconstruction as monitored by

<sup>a)</sup>Electronic mail: nulloa@cactus.iico.uaslp.mx

<sup>b)</sup>Electronic mail: lfm@cactus.iico.uaslp.mx

<sup>c)</sup>Electronic mail: rbn@cactus.iico.uaslp.mx and balderas@pdi-berlin.de

## Real-time reflectance-difference spectroscopy of GaAs molecular beam epitaxy homoepitaxial growth

A. Lastras-Martínez,<sup>1,a</sup> J. Ortega-Gallegos,<sup>1</sup> L. E. Guevara-Macías,<sup>1</sup>  
 O. Nuñez-Olvera,<sup>1</sup> R. E. Balderas-Navarro,<sup>1</sup> L. F. Lastras-Martínez,<sup>1</sup>  
 L. A. Lastras-Montañó,<sup>2</sup> and M. A. Lastras-Montañó<sup>3</sup>

<sup>1</sup>*Instituto de Investigación en Comunicación Óptica, Universidad Autónoma de San Luis Potosí, Alvaro Obregón 64, San Luis Potosí, SLP 78000, Mexico*

<sup>2</sup>*IBM T. J. Watson Research Center, Yorktown Heights, New York 10598, USA*

<sup>3</sup>*Department of Electrical and Computer Engineering, University of California, Santa Barbara, Santa Barbara, California 93106, USA*

(Received 23 December 2013; accepted 4 March 2014; published online 14 March 2014)

We report on real time-resolved Reflectance-difference (RD) spectroscopy of GaAs(001) grown by molecular beam epitaxy, with a time-resolution of 500 ms per spectrum within the 2.3–4.0 eV photon energy range. Through the analysis of transient RD spectra we demonstrated that RD line shapes are comprised of two components with different physical origins and determined their evolution during growth. Such components were ascribed to the subsurface strain induced by surface reconstruction and to surface stoichiometry. Results reported in this paper render RD spectroscopy as a powerful tool for the study of fundamental processes during the epitaxial growth of zincblende semiconductors. © 2014 Author(s). All article content, except where otherwise noted, is licensed under a Creative Commons Attribution 3.0 Unported License. [<http://dx.doi.org/10.1063/1.4868519>]

It is known that dimerized (001) surfaces of zincblende semiconductors are optically anisotropic.<sup>1</sup> Optical anisotropies have been associated to either the anisotropic response of surface dimers<sup>2–4</sup> or to the dimer-induced cubic-symmetry breakdown of the underlying atomic layers.<sup>5–8</sup> The anisotropic nature of (001) zincblende surfaces prompted the development of polarized-light techniques as optical, non-invasive probes for semiconductor surface characterization. One of such probes, Reflectance-difference spectroscopy (RDS),<sup>9</sup> is currently employed, along with Reflection high energy electron diffraction (RHEED), for the identification of GaAs (001) surface reconstructions.<sup>1,10</sup>

In addition to their application to static surfaces, reflectance-difference (RD) probes have been employed to study the dynamics of the epitaxial growth of zincblende semiconductors. Aspnes *et al.*,<sup>11</sup> first carried out single-wavelength dynamic RD measurements during GaAs Molecular beam epitaxy (MBE) growth and showed that abrupt changes in RD signal occur upon interrupting or allowing As flux while keeping the Ga flux on, thus following changes in surface stoichiometry. The combination of spectroscopic ellipsometry and RD turned out to be very successful in the investigation of complex surface dynamics under different growth conditions present in both MBE and Metal organic chemical vapor deposition (MOCVD) reactors, allowing for control during device fabrication.<sup>12</sup>

While single-wavelength RD measurements have shown the surface sensitivity of RD techniques to transients in surface stoichiometry occurring during epitaxy, the full potential of RD as a probe for monitoring epitaxial growth processes could be only realized through RD spectroscopic measurements. For zincblende semiconductors such an application demands of sub-second spectra acquisition times and the measurement of RD amplitudes in the  $10^{-4}$  to  $10^{-3}$  range. In the past these

<sup>a</sup>Electronic addresses: [alm@cactus.iico.uaslp.mx](mailto:alm@cactus.iico.uaslp.mx) and [alastras@gmail.com](mailto:alastras@gmail.com)

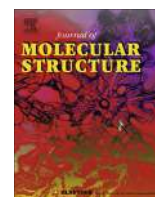






Contents lists available at ScienceDirect

## Journal of Molecular Structure

journal homepage: [www.elsevier.com/locate/molstruc](http://www.elsevier.com/locate/molstruc)

## Important role of molecular packing and intermolecular interactions in two polymorphs of (Z)-2-phenyl-3-(4-(pyridin-2-yl)phenyl)acrylonitrile. Preparation, structures, and optical properties



M. Judith Percino<sup>a,\*</sup>, Margarita Cerón<sup>a</sup>, Paulina Ceballos<sup>a</sup>, Guillermo Soriano-Moro<sup>a</sup>, M. Eugenia Castro<sup>a</sup>, Víctor M. Chapela<sup>a</sup>, José Bonilla-Cruz<sup>b</sup>, Marisol Reyes-Reyes<sup>c</sup>, Román López-Sandoval<sup>d</sup>, Maxime A. Siegler<sup>e</sup>

<sup>a</sup>Lab. de Polímeros, Centro de Química, Instituto de Ciencias, Universidad Autónoma de Puebla, Complejo de Ciencias, ICUAP, Edif. 103H, 22 Sur y San Claudio, C.P. 72570 Puebla, Puebla, Mexico

<sup>b</sup>Centro de Investigación en Materiales Avanzados S.C. (CIMAV-Unidad Monterrey), Av. Alianza Norte 22, Autopista Monterrey-Aeropuerto km 10, PIIT, Apodaca, Nuevo León C.P. 666600, Mexico

<sup>c</sup>Universidad Autónoma de San Luis Potosí, Instituto de Investigación en Comunicación Óptica, Av. Karakorum 1470, C.P. 78210 San Luis Potosí, S.L.P., Mexico

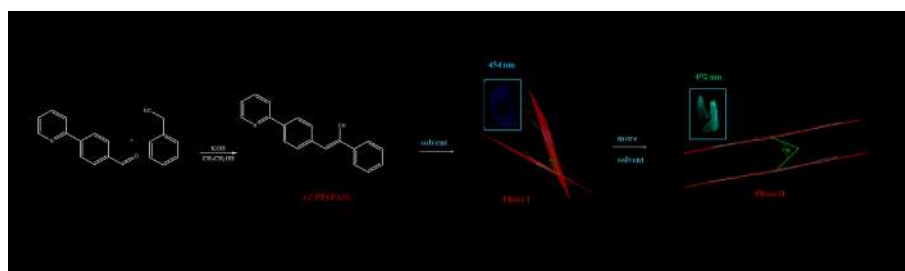
<sup>d</sup>Instituto Potosino de Investigación Científica y Tecnológica, Camino a la Presa de San José N° 2055, C.P. 78216 San Luis Potosí, S.L.P., Mexico

<sup>e</sup>Department of Chemistry, Johns Hopkins University, New Chemistry Building, 3400 N. Charles St., Baltimore, MD 21218, USA

## HIGHLIGHTS

- Solvent effect on molecular conformation.
- Solid state fluorescence.
- Solid-state fluorescence dependence of polymorphism.

## GRAPHICAL ABSTRACT



## ARTICLE INFO

## Article history:

Received 27 November 2013

Received in revised form 15 April 2014

Accepted 29 April 2014

Available online 20 May 2014

## Keywords:

Polymorphism-emission

Single-crystal X-ray diffraction

Packing-emission

Solvent effect

Bilayer membrane

Phenylacetonitrile

## ABSTRACT

The novel compound **Z**-2-phenyl-3-(4-(pyridin-2-yl)phenyl)acrylonitrile (**PPyPAN**) was synthesized from the condensation reaction between phenylacetonitrile and 4-(pyridin-2-yl)benzaldehyde. This compound crystallizes in two forms: polymorph **I** (triclinic,  $P = 1$ ,  $Z' = 2$ ) and polymorph **II** (orthorhombic,  $Pbc2_1$ ,  $Z' = 2$ ). The molecular structures and optical properties of the two polymorphs have been characterized via <sup>1</sup>H NMR, EI, FTIR, UV–Vis spectroscopy, DSC, single-crystal and XRPD. The molecular structure, packing properties, and intermolecular interactions were examined for both polymorphs of **PPyPAN** in order to interpret the emission properties. A subtle change in the molecular conformation (e.g., a rotation around single C–C bonds) found for both polymorph plays an important role in their solid-state properties. The structure and optical properties of the new structures were well characterized and showed unique features for both polymorphic phases. For phase **I**, we observed an excitation spectrum with an  $\lambda_{ex}$  at 325–346 nm, which is the maximum excitation or absorption wavelength for the lowest  $S_0 \rightarrow S_1$  transition, which is characteristic to the  $\pi-\pi^*$  transition, and an emission spectrum with an  $\lambda_{em}^{max}$  at 454 nm. For phase **II**, the excitation spectrum showed an  $\lambda_{ex}^{max}$  at 325 nm, whereas the  $\lambda_{em}^{max}$  showed a red-shift to 492 nm.

© 2014 Elsevier B.V. All rights reserved.

\* Corresponding author. Tel.: +52 222 2295500x7285; fax: +52 222 2295551.

E-mail address: [judith.percino@correo.buap.mx](mailto:judith.percino@correo.buap.mx) (M.J. Percino).

# Interfacial insertion of a poly(3,4-ethylenedioxythiophene): poly(styrenesulfonate) layer between the poly(3-hexyl thiophene) semiconductor and cross-linked poly(vinyl alcohol) insulator layer in organic field-effect transistors

Isidro Cruz-Cruz<sup>1</sup>, Ana C B Tavares<sup>1</sup>, Marisol Reyes-Reyes<sup>2</sup>, Román López-Sandoval<sup>3</sup> and Ivo A Hümmelgen<sup>1,4</sup>

<sup>1</sup> Departamento de Física, Universidade Federal do Paraná, Caixa Postal 19044, 81531-990- Curitiba, PR, Brazil

<sup>2</sup> Instituto de Investigación en Comunicación Óptica, Universidad Autónoma de San Luis Potosí, Álvaro Obregón 64, San Luis Potosí 78000, México

<sup>3</sup> Advanced Materials Department, IPICYT, Camino a la presa San José 2055, Col. Lomas 4a sección, San Luis Potosí 78216, México

E-mail: [iah@fisica.ufpr.br](mailto:iah@fisica.ufpr.br)

Received 1 November 2013, revised 2 December 2013

Accepted for publication 5 December 2013

Published 22 January 2014

## Abstract

The role of a thin layer of conductive poly(3,4-ethylenedioxythiophene) doped with polystyrene sulfonate (PEDOT : PSS), inserted between the gate dielectric and the active layer in poly(3-hexylthiophene)-based transistors was investigated. The devices were fabricated in the bottom-gate top-contact geometry by using cross-linked poly(vinyl alcohol) as the dielectric, whereas the PEDOT : PSS layer was prepared by using an aged aqueous dispersion with addition of different amounts of dimethyl sulfoxide (DMSO) as a secondary dopant. Under these conditions, both a significant reduction in the number of electrically active traps at the interface with the semiconductor and an improvement in the field-effect mobility were obtained, whereas the low power consumption was preserved. The threshold voltage was also displaced by approximately  $-1$  V.

Keywords: interface, organic field-effect transistor, poly(3,4-ethylenedioxythiophene): poly(styrenesulfonate), aged PEDOT : PSS dispersion, secondary doping, P3HT-based transistors

(Some figures may appear in colour only in the online journal)

## 1. Introduction

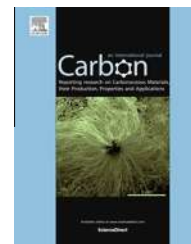
Organic field-effect transistors (OFETs) belong to the most important components in organic electronics. It is very

important to obtain high-performance transistor devices able to operate under room environment conditions (preferably), characterized by low power consumption, high field-effect charge carrier mobility and long-term stability. Some alternatives to acquire these conditions have been proposed, such as hybrid blends of inorganic nanostructured materials

<sup>4</sup> Author to whom any correspondence should be addressed.

Available at [www.sciencedirect.com](http://www.sciencedirect.com)

ScienceDirect

journal homepage: [www.elsevier.com/locate/carbon](http://www.elsevier.com/locate/carbon)

# Oxygen to carbon atoms ratio effect on the size, morphology and purity of functionalized carbon nanoshells by using alcohol mixtures as carbon source

Emmanuel Segura-Cardenas <sup>a</sup>, Román López-Sandoval <sup>b</sup>, Daniel Hernández-Arriaga <sup>a</sup>, Judith Percino <sup>c</sup>, Victor M. Chapela <sup>c</sup>, Marisol Reyes-Reyes <sup>a,\*</sup>

<sup>a</sup> Instituto de Investigación en Comunicación Óptica, Universidad Autónoma de San Luis Potosí, Álvaro Obregón 64, San Luis Potosí 78000, Mexico

<sup>b</sup> Advanced Materials Department, IPICYT, Camino a la Presa San José 2055, Col. Lomas 4a Sección, San Luis Potosí 78216, Mexico

<sup>c</sup> Lab. de Polímeros, Centro de Química, Instituto de Ciencias, Universidad Autónoma de Puebla, Complejo de Ciencias, ICUAP, Edif. 103H, 22 Sur y San Claudio, C.P. 72570 Puebla, Puebla, Mexico

## ARTICLE INFO

### Article history:

Received 7 November 2013

Accepted 22 April 2014

Available online 29 April 2014

## ABSTRACT

The effect of the ratio of oxygen to carbon atoms (O/C) on the morphology of carbon nanostructures has been studied by varying the methanol and ethanol ratio in the reaction mixtures. Notable morphological differences in the synthesized carbon nanostructures are observed as a function of the O/C ratio. At a high O/C ratio, i.e., using methanol (O/C = 1), the synthesized carbon nanoshells (CNS) are faceted. Moreover, other faceted nanostructures, such as triangular and hexagonal, are observed in this strong oxidative environment. Decreasing the O/C ratio in the mixture by adding ethanol induces changes in the CNS morphology; they are less faceted and favor only the growth of single-walled carbon nanotubes mixed with the CNSs. The importance of the O/C ratio is corroborated by replacing ethanol (O/C = 0.5) with polyethylene glycol (O/C = 0.5) in the methanol:ethanol reaction mixture. Finally, at very low O/C ratios, i.e., methanol:octanol mixtures, CNS are obtained and no faceted nanostructures or SWCNT are found. Thus, adjusting the O/C ratio is a method for obtaining high purity samples of CNS. Moreover, the use of the alcohols during the synthetic process is a simple and green method of functionalizing CNS.

© 2014 Elsevier Ltd. All rights reserved.

## 1. Introduction

Since the discovery of fullerenes [1], different types of carbon nanostructures have been synthesized due to the excellent ability of carbon to exist in various allotropic forms, such as carbon nanotubes (CNT) [2], carbon nanohorns [3], and carbon nano-onions [4–18]. An important form of the carbon

allotrope structure is the carbon nano-onion, which is a concentric, multishell cluster with a diameter ranging from a few nanometers to tens of nanometers [5,16]. Carbon nano-onions can encapsulate other non-carbon materials; when these carbon nano-onions are encapsulating nanoparticles, they are called carbon nanocapsules or carbon nanoshells (CNS). Several physical and chemical methods have been

\* Corresponding author.

E-mail address: [reyesm@iico.uaslp.mx](mailto:reyesm@iico.uaslp.mx) (M. Reyes-Reyes).

<http://dx.doi.org/10.1016/j.carbon.2014.04.080>

0008-6223/© 2014 Elsevier Ltd. All rights reserved.



Cite this: *CrystEngComm*, 2014, 16, 8591

## The effect of the supramolecular network of (Z)-3-(4-(diphenylamino)phenyl)-2-(pyridin-2-yl)-acrylonitrile on the fluorescence behavior of a single crystal: experimental and theoretical studies†

M. Judith Percino,\*<sup>a</sup> Margarita Cerón,<sup>a</sup> Guillermo Soriano-Moro,<sup>a</sup> M. Eugenia Castro,<sup>a</sup> Víctor M. Chapela,<sup>a</sup> José Bonilla,<sup>b</sup> Marisol Reyes-Reyes<sup>c</sup> and Román López-Sandoval<sup>d</sup>

The molecular structure and molecular interactions of an  $\alpha,\beta$ -unsaturated nitrile, such as the interaction between adjacent molecules of (Z)-3-(4-(diphenylamino)phenyl)-2-(pyridin-2-yl)-acrylonitrile (Z-DPPyACN) throughout the 4-diphenylamino moiety with the phenyl and pyridyl rings, play an important role in the self-assembly behaviors and optical properties of its powder and single-crystal forms. The crystal packing exhibits multiple C-H $\cdots\pi$  and CH $\cdots$ HC edge-to-face interactions that contribute to the supramolecular network between adjacent molecules. The resulting molecular structure resembles a pinwheel which exhibits a strong emission intensity at three different wavelengths. The crystal belongs to the monoclinic space group  $P2_1/n$ , with dimensions  $a = 12.9551(2)$ ,  $b = 11.29300(15)$ ,  $c = 14.6992(3)$  Å,  $\beta = 115.648(2)^\circ$  and  $Z = 4$ . The single-crystal compound shows three emission maxima at 533, 569, and 607 nm, whereas the powder and the molecules in an aggregated state show maximum emission intensities that are dependent on the nature of the solvent. The Z-DPPyACN dye's optical properties show a Stokes shift caused by the reorganization of the molecule in the excited state, as effected by the solvent polarity. This indicates a large change in the dipole moment of dye molecules upon excitation due to an intramolecular charge transfer interaction. From a theoretical point of view, the molecular geometry, electronic structure, and excitation energies are reported using density functional theory and compared with the experimentally determined one photon absorption and emission spectra.

Received 14th February 2014,  
Accepted 1st July 2014

DOI: 10.1039/c4ce00327f

www.rsc.org/crystengcomm

## Introduction

Aromatic amines are among the most important reagents used as nanodevice materials,<sup>1–20</sup> and they serve to covalently attach various compounds to light-emitting layers.<sup>14,21,22</sup> Furthermore, they have been tested as blue emitters in organic LEDs<sup>23</sup> and as components of electroluminescent bipolar devices.<sup>24</sup>

The use of *N*-phenyl substituents in aromatic amines has resulted in superior performance in materials chemistry.<sup>25–33</sup> For

example, the introduction of *N*-phenyl substituents into *trans*-aminostilbene led to considerable bathochromic shifts and higher fluorescence quantum yields compared to *N*-alkyl substituents, which suggests a substantial interaction of the *N*-phenyl with the aminostilbene groups (conjugated structure).<sup>34</sup> Yang *et al.*<sup>34</sup> reported that the excited-state process of *N*-phenyl substituents in *trans*-aminostilbene is a consequence of the more planar geometry and the strong orbital interactions between the *N*-phenyl and the aminostilbene groups. In the particular case of *p*-diphenylaminostilbene, the compound displayed a second absorption band at shorter wavelengths as well as a single intense long-wavelength band, and the former was assigned to *trans*-stilbene. This second band near 300 nm was assigned as a consequence of an electronic transition mainly localized in the triphenylamine moiety. Among the aromatic amines, triphenylamine (NPh<sub>3</sub>) and its derivatives are very important in photoscience. These compounds have been used extensively as the hole transport material in organic electroluminescent devices.<sup>35–51</sup>

Triphenylamines, with their characteristic propeller starburst molecular structure, have been widely used in

<sup>a</sup> Lab. de Polímeros, Centro de Química, Instituto de Ciencias, Universidad Autónoma de Puebla, Complejo de Ciencias, ICUAP, Edif. 103H, 22 Sur y San Claudio, C.P. 72570 Puebla, Puebla, Mexico. E-mail: judith.percino@correo.buap.mx;

Fax: +52 222 2295551; Tel: +52 222 2295500 x 7285

<sup>b</sup> Centro de Investigación en Materiales Avanzados S.C. (CIMA-UNIDAD Monterrey), PIIT, Av. Alianza Norte 22, Autopista Monterrey-Aeropuerto Km 10, Apodaca-Nuevo León, C.P. 666600, Mexico


<sup>c</sup> Universidad Autónoma de San Luis Potosí, Instituto de Investigación en Comunicación Óptica, Av. Karakorum 1470, C.P. 78210, San Luis Potosí, S.L.P., Mexico

<sup>d</sup> Instituto Potosino de Investigación Científica y Tecnológica, Camino a la Presa de San José No. 2055, C.P. 78216, San Luis Potosí, S.L.P., Mexico

† CCDC 985348. For crystallographic data in CIF or other electronic format see DOI: 10.1039/c4ce00327f

# Acousto-optic Modulators Based on Flexural Acoustic Waves and its Application to Mode-locked Fiber Lasers

Miguel A. Bello Jiménez, Christian Cuadrado-Laborde, Antonio Díez, Jose L. Cruz, and Miguel V. Andrés

Author Information ▾  Find other works by these authors ▾

Latin America Optics and Photonics Conference · OSA Technical Digest (online) (Optical Society of America, 2014), paper LTh2C.3 · <https://doi.org/10.1364/L>

## Not Accessible

Your account may give you access

[Back to Abstract](#)

## Access

To view this article you will need to login or make a payment.

If you have arrived on this page from an external web site and wish to view the article abstract first, click on the link below.

## Citation

M. A. Bello Jiménez, C. Cuadrado-Laborde, A. Díez, J. L. Cruz, and M. V. Andrés, "Acousto-optic Modulators Based on Flexural Acoustic Waves and its Application to Mode-locked Fiber Lasers," in *Latin America Optics and Photonics Conference*, OSA Technical Digest (online) (Optical

# Experimental Investigation of Fused Biconical Fiber Couplers for Measuring Refractive Index Changes in Aqueous Solutions

Marco V. Hernández-Arriaga, Miguel A. Bello-Jiménez, A. Rodríguez-Cobos,  
and Miguel V. Andrés, *Member, IEEE*

**Abstract**—A detailed experimental study of a simple and compact fiber optic sensor based on a fused biconical fiber coupler is presented, in which the sensitivity is improved by operating the coupler beyond the first coupling cycle. The sensor is demonstrated to perform high sensitivity measurements of refractive index changes by means of variation of sugar concentration in water. The device is operated to achieve a linear transmission response, allowing a linear relation between the sugar concentration and the output signal. The initial sensitivity was measured as 0.03 units of normalized transmission per unit of sugar concentration (g/100 mL), with a noise detection limit of a sugar concentration of 0.06 wt% of sugar concentration. Improvements in sensitivity were studied by operating the coupler beyond their first coupling cycles; achieving an improved sensitivity of 0.15 units of normalized transmission per unit of sugar concentration, and a minimum detection limit of 0.012 wt% of sugar concentration. From this result, the minimum detectable refractive index change is estimated as  $2 \times 10^{-5}$  refractive index unit.

**Index Terms**—Fiber optic sensor, fused biconical fiber coupler, refractive index sensor.

## I. INTRODUCTION

FIBER-OPTIC couplers have attracted considerable attention in recent years for their ability to detect small changes in the refractive index (RI) of liquid solutions. A fiber coupler is a four-port device with a transmission spectrum that is strongly affected by the refractive index of the surrounding medium due to the evanescent field that is generated along the coupling region [1]. This effect has proven to be useful for sensing applications [2]. Recent approaches of fiber-coupler based RI sensors include fused biconical fiber couplers [3]–[7], optical microfibers [8]–[12], photonic crystal fibers [13], [14], and specially designed

two-core optical fibers [15], [16], all of them offering the advantages of high sensitivity, *in situ* measurements, compact size, and immunity to external electromagnetic interference. Most of these sensors are codified in wavelength and the achieved sensitivities are in the range of 1,125 to 30,100 nanometer (nm) per refractive index unit (RIU), with a minimum detection limit of  $4 \times 10^{-4}$  to  $4 \times 10^{-7}$  RIU, respectively.

From the point of view of implementation, the necessity of expensive equipment, such as optical spectrum analyzers, for measuring the shift in wavelength heavily affects the use of fiber-coupler based RI sensors. Thus, it is worthwhile to consider an alternative scheme based on the dependence of the power coupling on the surrounding medium. The two complementary outputs of a fiber coupler enable a straightforward normalization, i.e. the ratio between the difference and the addition, which automatically compensates for power fluctuations. In earlier works the dependence of the power coupling of traditional fused biconical tapered couplers on the external RI has been presented and it has been proposed that it is possible to use such a structure to develop a fiber based refractometer [1], [17]. Tazawa et al. [2] have implemented this power measurement approach to demonstrate a biosensor with estimated  $4 \times 10^{-6}$  RIU detection limit. Recently, it has been demonstrated that modal interferometers based on integrated waveguides provide one of the best resolutions ever reported ( $2.5 \times 10^{-7}$  RIU) [18]. A fused biconical couplers is, in fact, a modal interferometer in which the phase difference between the symmetric and antisymmetric supermodes determine the power distribution at the output fibers. Small changes of the external RI do not modify substantially the coupling coefficient, but they generate a significant phase difference between supermodes. In terms of fiber-coupler based RI sensors, this last point deserves particular attention for the detection of slight changes in the refractive index of aqueous solutions. Although several schemes have reported this effect [1], [2], [17], they did not study the conditions for an optimal performance of the reported device. Here our purpose is the experimental analysis of a fused biconical fiber coupler, operated beyond the first coupling cycle, with a power transmission that depends on the surrounding medium.

The objective is not only to gain insights into the dynamics of this kind of device, but also looking forwards an improvement of its performance. Based on this motivation, the

Manuscript received July 10, 2015; revised August 26, 2015; accepted August 27, 2015. Date of publication September 16, 2015; date of current version December 10, 2015. This work was supported in part by Promep under Grant DSA/103.5/14/10476 and in part by the Consejo Nacional de Ciencia y Tecnología under Grant 206425 and Grant 222476. The associate editor coordinating the review of this paper and approving it for publication was Dr. Anna G. Mignani.

M. V. Hernández-Arriaga, M. A. Bello-Jiménez, and A. Rodríguez-Cobos are with the Instituto de Investigación en Comunicación Óptica, Universidad Autónoma de San Luis Potosí, San Luis Potosí 78210, Mexico (e-mail: dmxsol@hotmail.com; m.bello@cactus.iico.uaslp.mx; roca@cactus.iico.uaslp.mx).

M. V. Andrés is with the Departamento de Física Aplicada y Electromagnetismo, Institute of Materials Science, Universidad de Valencia, Valencia 46100, Spain (e-mail: miguel.andres@uv.es).

Digital Object Identifier 10.1109/JSEN.2015.2475320

# Long-cavity all-fiber ring laser actively mode locked with an in-fiber bandpass acousto-optic modulator

C. Cuadrado-Laborde,<sup>1,2,3,\*</sup> M. Bello-Jiménez,<sup>1,4</sup> A. Díez,<sup>1</sup> J. L. Cruz,<sup>1</sup> and M. V. Andrés<sup>1</sup>

<sup>1</sup>Departamento de Física Aplicada, ICMUV, Universidad de Valencia, Dr. Moliner 50, Burjassot E-46100, Spain

<sup>2</sup>CIOp (CONICET La Plata-CIC), P.O. Box 3, Gonnet 1897, Buenos Aires, Argentina

<sup>3</sup>Facultad de Ciencias Exactas e Ingeniería, Universidad Católica de La Plata, Buenos Aires, Argentina

<sup>4</sup>Instituto de Investigación en Comunicación Óptica (IICO), Universidad Autónoma de San Luis Potosí, Av. Karakorum 1470, Lomas 4a Secc., 78210 San Luis Potosí, S.L.P., Mexico

\*Corresponding author: Christian.Cuadrado@uv.es

Received October 17, 2013; revised November 16, 2013; accepted November 18, 2013;  
posted November 22, 2013 (Doc. ID 199674); published December 19, 2013

We demonstrate low-frequency active mode locking of an erbium-doped all-fiber ring laser. As the mode locker, we used a new in-fiber bandpass acousto-optic modulator showing 74% modulation depth, 3.7 dB power insertion losses, 4.5 nm of optical bandwidth, and 20 dB of nonresonant light suppression. The laser generates 330 ps mode-locked pulses over a 10 ns pedestal, at a 1.538 MHz frequency, with 130 mW of pump power. © 2013 Optical Society of America

OCIS codes: (140.4050) Mode-locked lasers; (140.3510) Lasers, fiber; (140.3500) Lasers, erbium; (230.1040) Acousto-optical devices.

<http://dx.doi.org/10.1364/OL.39.000068>

Many applications encompassing micromachining, biomedicine, optical measurement instruments, and high-resolution ranging (lidar) systems, among others, demand few megahertz frequency, subnanosecond pulse width fiber laser systems. Low-repetition-rate femtosecond or picosecond lasers could serve as a seed source for a chirped pulse amplification system to generate high-energy pulses. These requirements preclude the use of standard *Q*-switched lasers. In mode-locked lasers, output light pulses have subnanoseconds pulse widths but repetition rates generally above the tens-of-megahertz regime. One solution employed in this case is to use pulse pickers. However, the reduction of the repetition rate with this method introduces energy losses and backreflection, impairs the signal-to-noise ratio, and increases complexity. For this reason, very recently, low-frequency mode-locked lasers have been proposed as an alternative to overcome these difficulties [1–4]. For mode-locked lasers, lower repetition rates require longer laser cavities; however, for fiber cavities this is not a major issue, since the fiber may be easily spooled. It is also worth mentioning that all these proposals were based on passive mode-locking techniques. However, when subnanosecond pulses at about 1 MHz repetition rate are required, it is worthwhile to investigate the possibility of using active mode locking. There are applications in which an active mode-locking scheme is preferred, e.g., for applications needing synchronization to a master clock or when several laser sources or instruments must be operated synchronously, and, in addition, active mode locking prevents start and multiple peak problems that passive approaches may present. One element that is key in the development of an actively mode-locked strictly all-fiber laser is the modulator [5]. The use of in-fiber modulators is an attractive solution, because there will be potentially low losses and it prevents etalon formation, which can

frustrate the mode locking, and provides a robust all-fiber cavity [6,7].

In an optical fiber, the fundamental mode guided by the core and the modes supported by the cladding can be coupled by a periodic perturbation [8]. The optical coupling takes place at the optical wavelength that verifies the phase-matching condition between the optical modes and the periodicity of the perturbation. The acousto-optic modulator (AOM) proposed in this work could be seen as an acoustically induced long-period grating (AI-LPG) with a core mode blocker (CMB) in the middle. Figure 1(a) depicts the operation principle by coupling the LP<sub>01</sub> core mode to a cladding mode. Thus, the core mode LP<sub>01</sub> is first coupled to a cladding mode by the first part of the AI-LPG and bypasses the CMB via cladding propagation, later being coupled back to the core mode LP<sub>01</sub> by the second part of the AI-LPG. The device works as a bandpass filter, and thus light whose wavelength does not verify the phase-matching condition

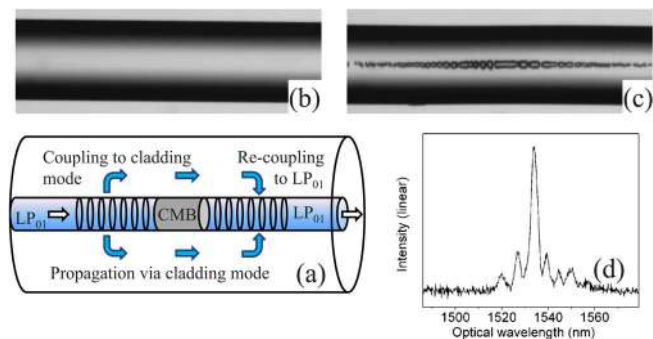


Fig. 1. (a) Schematic of the AOM operation principle. Optical fiber (b) before and (c) after the electrical arch discharges. (d) Spectrum in transmission of the AOM when the piezoelectric is excited with a sinusoidal signal at 769 kHz and 40 V.

## Modulador acusto-óptico en amplitud de fibra óptica basado en ondas acústicas de flexión

M. Bello-Jiménez

*Instituto de Investigación en Comunicación Óptica, Universidad Autónoma de San Luis Potosí,  
Av. Karakorum 1470 Lomas 4a Secc., 78210 San Luis Potosí, S.L.P, México,  
e-mail: m.bello@cactus.iico.uaslp.mx*

C. Cuadrado-Laborde

*Optical Metrology Lab., Instituto de Física Rosario (CONICET-UNR),  
Ocampo y Esmeralda, S2000EZP Rosario, Argentina,  
e-mail: christian.cuadrado@uv.es*

A. Díez, J. L. Cruz, y M. V. Andrés

*Departamento de Física Aplicada y Electromagnetismo, ICMUV, Universidad de Valencia,  
c/ Dr. Moliner 50, Burjassot, 46100 Valencia, España,  
e-mail: antonio.diez@uv.es; jose.l.cruz@uv.es; miguel.andres@uv.es*

Received 18 December 2013; accepted 8 April 2014

Se reporta un estudio experimental de la operación de un modulador acusto-óptico (MAO) de fibra óptica basado en la interacción acusto-óptica producida por ondas acústicas de flexión estacionarias. Concentramos nuestra atención en los efectos de reducir el diámetro en la fibra óptica como mecanismo para optimizar la respuesta espectral del MAO. Como caso particular reportamos un modulador de 70  $\mu\text{m}$  de diámetro con una alta profundidad de modulación (60 %), bajas pérdidas por inserción (1.3 dB) y un ancho ancho de banda a 3 dB de 40 nm que opera en el rango de los megahertz. Los resultados obtenidos demuestran que el incluir fibras estrechadas se puede considerar como un grado extra de libertad en el diseño del modulador para controlar el ancho de banda.

*Descriptores:* Fibras ópticas; moduladores ópticos; dispositivos acusto-ópticos.

An experimental study of an in-fiber acousto-optic modulator (AOM) based on the acousto-optic interaction produced by standing flexural acoustic waves is reported. We focus our attention in the effects of a gradual reduction in the optical fiber as the mechanisms to improve the spectral response of the AOM. As a particular case we report a 70- $\mu\text{m}$  fiber AOM. Our approach permits the implementation of high modulation depth (60 %), low optical loss (1.3 dB) and a 3 dB broad modulation bandwidth of 40 nm, operating in the MHz frequency range. The experimental results demonstrate that including tapered optical fibers can be regarded as an extra degree of freedom to control the optical bandwidth of the modulator.

*Keywords:* Fiber optics; optical modulators; acousto-optical devices.

PACS: 42.81.-i; 07.60.Vg; 42.79.Hp; 42.79.Jq.

### 1. Introducción

En años recientes los dispositivos acusto-ópticos (AO) de fibra óptica basados en onda acústicas de flexión han recibido un gran interés debido a sus aplicaciones como desplazadores de frecuencia [1], filtros AO sintonizables [2] y moduladores de luz [3], los cuales tienen un gran potencial de aplicación en el marco del desarrollo de dispositivos AO todo-fibra. Su principio de operación se basa en el acoplamiento intermodal inducido por una onda acústica de flexión; cuando la onda acústica se propaga a lo largo de la fibra esta produce una perturbación periódica en el índice de refracción la cual puede conllevar a un acoplamiento intermodal resonante entre el modo fundamental del núcleo y alguno de los modos del revestimiento en la fibra óptica [1-3]. El resultado de esta interacción AO es similar al obtenido por una rejilla asimétrica convencional de periodo largo (LPG, long period fiber grating), de tal forma que podemos analizar esta interacción acusto-óptica como la versión dinámica de una

LPG asimétrica, cuya transmisión se puede controlar dinámicamente mediante la amplitud y frecuencia de la onda acústica. A la salida del dispositivo solo la luz que permanece guiada por el núcleo es transmitida, y la transmisión exhibe uno o varios picos de atenuación a las longitudes de onda donde ocurre el acoplamiento intermodal resonante.

En el marco del desarrollo de moduladores AO de fibra óptica que exploten las ventajas de la interacción acusto-óptica se han propuesto varias alternativas [4-13]. Entre estas, hemos propuesto una técnica de modulación basada en el acoplamiento intermodal inducido por ondas acústicas de flexión estacionarias en una fibra estándar [12,13]. Este nuevo tipo de modulador proporciona una modulación estable que puede emplearse para realizar el amarre de modos activo en un láser pulsado todo-fibra. Sin embargo, el esquema de modulación limita su funcionamiento a anchos de banda reducidos (1.5 nm), lo que es una limitante para sistemas que requieren un mayor ancho de banda. En este trabajo nuestro propósito es reportar una versión mejorada del modulador AO e im-





## High-quality InN films on MgO (100) substrates: The key role of 30° in-plane rotation

V. D. Compeán García,<sup>1</sup> I. E. Orozco Hinostrroza,<sup>2</sup> A. Escobosa Echavarría,<sup>3</sup>  
E. López Luna,<sup>1</sup> A. G. Rodríguez,<sup>1</sup> and M. A. Vidal<sup>1</sup>

<sup>1</sup>Coordinación para la Innovación y Aplicación de la Ciencia y Tecnología (CIACyT),  
Universidad Autónoma de San Luis Potosí (UASLP), Álvaro Obregón 64, 78000 San Luis Potosí, Mexico

<sup>2</sup>Instituto Potosino de Investigación Científica y Tecnológica, Camino a la Presa San José 2055,  
Col. Lomas 4a Sección, 78216 San Luis Potosí, Mexico

<sup>3</sup>Electric Engineering Department, Centro de Investigación y Estudios Avanzados del IPN,  
Apartado Postal 14-740, 07000 México D.F., Mexico

(Received 21 February 2014; accepted 3 May 2014; published online 14 May 2014)

High crystalline layers of InN were grown on MgO(100) substrates by gas source molecular beam epitaxy. Good quality films were obtained by means of an in-plane rotation process induced by the annealing of an InN buffer layer to minimize the misfit between InN and MgO. *In situ* reflection high-energy electron diffraction showed linear streaky patterns along the [01 $\bar{1}$ 0] azimuth and a superimposed diffraction along the [11 $\bar{2}$ 0] azimuth, which correspond to a 30°  $\alpha$ -InN film rotation. This rotation reduces the mismatch at the MgO/InN interface from 19.5% to less than 3.5%, increasing the structural quality, which was analyzed by high-resolution X-ray diffraction and Raman spectroscopy. Only the (0002) *c* plane diffraction of  $\alpha$ -InN was observed and was centered at  $2\theta = 31.4^\circ$ . Raman spectroscopy showed two modes corresponding to the hexagonal phase: E1(LO) at  $591\text{ cm}^{-1}$  and E2(high) at  $488\text{ cm}^{-1}$ . Hall effect measurements showed a carrier density of  $9 \times 10^{18}\text{ cm}^{-3}$  and an electron Hall mobility of  $340\text{ cm}^2/(\text{V s})$  for a film thickness of 140 nm. © 2014 AIP Publishing LLC. [<http://dx.doi.org/10.1063/1.4876760>]

Over the last few years, the hexagonal and cubic phases of the semiconductor InN have attracted much interest from both fundamental and practical points of view. The interest in this semiconductor and the complete III-nitride alloy system increased after the correct determination of the fundamental band-gap energy of InN from the original value of 1.9 (Ref. 1) to 0.67 eV,<sup>2-4</sup> which meant that InN has the lowest band gap of any known III-nitride binary compound or alloy. This extended the expected emission range of III-nitride alloys from deep-UV (AlN) down to the near-IR region (InN). InN also exhibits exceptional transport properties, such as a very small electron effective mass at the  $\Gamma$  point ( $0.07 m_0$ ), which may lead to high electron mobilities, high saturation velocities, a pronounced band-filling effect in samples with electron concentrations in the order of  $10^{18}$ – $10^{19}\text{ cm}^{-3}$ ,<sup>3</sup> a surface accumulation layer with ultra-high electron density, and very high saturation and peak drift velocities.<sup>5-7</sup> These unique properties make InN a potential material for a wide range of devices, such as tandem solar cells, infrared emitters, and high-speed and high-frequency electronic devices. As a consequence, a great deal of effort has been dedicated to improving the crystal quality of InN layers using different substrates to grow high-quality InN and its InGaIn alloys, and numerous studies of the optical and electrical properties of InN can be found in the literature.<sup>1-8</sup>

One of the problems of III-nitride systems is that no native substrates exist; for example, InN has a lattice mismatch of 25% with sapphire, 8% with Si(111), 37.4% with GaAs, and 11% with GaN. High-quality single-crystal InN is very difficult to obtain because of this. Magnesium oxide (MgO) has been used to grow cubic InN with a buffer layer

of cubic gallium nitride ( $\beta$ -GaN),<sup>9-11</sup> because of the large lattice mismatch between InN(100) and MgO(100) of  $\sim 18\%$ . If a buffer layer of GaN is not used then poor-quality polycrystalline  $\alpha$ -InN is obtained.<sup>9,12</sup>

In this study, we report the growth of high-quality  $\alpha$ -InN and discuss the effect of annealing on the low-temperature (LT)-InN buffer layer. In addition, we characterize the structural quality of the  $\alpha$ -InN by *in situ* and real-time reflection high-energy electron diffraction (RHEED), X-ray diffraction (XRD), and Raman spectroscopy.

InN films were grown by gas source molecular beam epitaxy (GS-MBE) on (100)-oriented MgO substrates using an InN buffer layer grown at a low substrate temperature (LT) of  $T_s = 300^\circ\text{C}$ , as described in the next section.

The *in situ* real-time surface characterization was performed by RHEED with an acceleration voltage of 12 kV. Atomic Force Microscopy (AFM) in tapping mode was used to study surface morphology. The structural properties were studied using a high-resolution X-ray diffraction (HRXRD) system with a PANalytical MRD X-ray diffractometer, using the  $K\alpha_1$  line emission ( $1.54059\text{ \AA}$ ) from a Cu target as the X-ray source and a 2 bounce hybrid monochromator made of a (220) germanium crystal. The voltage and applied current were fixed at 40 mV and 20 mA, respectively. Room temperature Raman spectra were measured with a 514.5 nm excitation laser line and the electrical properties were evaluated by Hall measurements in the van der Pauw configuration system at 300 K.

Before growing LT-InN, the substrate was cleaned in a trichloroethylene and acetone ultrasonic bath for 10 min. The MgO substrate was introduced into a vacuum chamber and was then transferred to the growth chamber and thermally

# Chua's circuit and its characterization as a filter

I Campos-Cantón<sup>1</sup>, O A Segura-Cisneros<sup>2</sup>,  
R E Balderas-Navarro<sup>2</sup> and E Campos-Cantón<sup>3</sup>

<sup>1</sup>Facultad de Ciencias, Universidad Autonoma de San Luis Potosi (UASLP), Mexico

<sup>2</sup>Instituto de Investigación en Comunicación Óptica, Universidad Autónoma de San Luis Potosí (UASLP), Alvaro Obregón 64, 78000 San Luis Potosí, SLP, Mexico

<sup>3</sup>División de Matemáticas Aplicadas, Instituto Potosino de Investigación Científica y Tecnológica (IPICYT), Camino a la Presa San José 2055, 78216 San Luis Potosí, SLP, Mexico

E-mail: [icampos@ciencias.uaslp.mx](mailto:icampos@ciencias.uaslp.mx)

Received 4 June 2014, revised 4 August 2014

Accepted for publication 27 August 2014

Published 22 September 2014

## Abstract

This article deals with Chua's circuit characterization from the point of view of a filter based on the concept of piecewise linear functions. Furthermore, experiments are developed for teaching electronic systems that can be used for novel filtering concepts. The frequency range in which they are tested is from 20 Hz to 20 kHz, due to the audio spectrum comprised in this frequency range. The node associated with the capacitor and Chua's diode is used as input, and the node for another capacitor and the coil is used as output, thereby establishing one input-output relationship for each system case given by the piecewise linear functions. The experimental result shows that Chua's circuit behaves as a bandpass filter-amplifier, with a maximum frequency around 3 kHz and bandwidth between 1.5 kHz and 5.5 kHz. The results presented in this paper can motivate engineering students to pursue applications of novel electrical circuits based on topics that are of potential interest in their future research studies.

Keywords: filters, Chua's circuit, piecewise linear functions, analog electronics

## 1. Introduction

Filters are key elements in a wide variety of electronic applications. Among them we can mention the wireless transceivers [1] and information retrieval in direct transmission [2], for which a band pass filter is used to extract the embedded desired signal in a sum of different

# Effect of surface states on the electrical properties of MBE grown modulation doped AlGaAs/GaAs

Alejandro Cisneros-de-la-Rosa, Irving Eduardo Cortes-Mestizo, Esteban Cruz-Hernández, and Víctor Hugo Méndez-García<sup>a)</sup>

Laboratorio Nacional, CIACyT-UASLP, Av. Sierra Leona #550, Col. Lomas 2a. Sección C.P. 78210, San Luis Potosí, S.L.P., Mexico

Luis Zamora-Peredo

Centro de Investigación en Micro y Nanotecnología, Universidad Veracruzana, Calzada Adolfo Ruiz Cortines #455, Frac. Costa Verde, C.P. 94292 Boca del Rio, Veracruz, Mexico

José Vulfrano González-Fernández, Raúl Balderas-Navarro, and Andrei Yu. Gorbachev

Instituto de Investigación en Comunicación Óptica, Universidad Autónoma de San Luis Potosí, Av. Karakorum 1470 Lomas 4a, C.P. 78210, San Luis Potosí, S.L.P., Mexico

Máximo López-López

Physics Department, Centro de Investigación y de Estudios Avanzados del Instituto Politécnico Nacional, Av. IPN 2508, Col. San Pedro Zacatenco, D.F. C.P. 07360, Mexico

(Received 13 November 2013; accepted 16 January 2014; published 10 February 2014)

The influence of near surface structure termination and surface treatments on the surface electric fields and mobility of modulation doped AlGaAs/GaAs heterostructures (MDH) were investigated. The built-in and surface electric fields were evaluated by photoreflectance spectroscopy, and these values were utilized to simulate the conduction band bending of the MDH. When the capping layer of the MDH was changed, both the built in internal electric field and the surface electric field are decreased, while the electron mobility of the samples is increased. After passivated the surface samples with Si, the surface electric fields were also reduced. Finally, a  $(\text{NH}_4)_2\text{S}_x$ -based treatment of the surface was applied, the surface electric field is annulled, and the conduction band modeling showed an important redistribution of carriers in the films. The electron mobility of the passivated samples does not show any change, neither the internal electric fields, corroborating the close relationship that exist between these two parameters. © 2014 American Vacuum Society. [<http://dx.doi.org/10.1116/1.4863677>]

## I. INTRODUCTION

Low-dimensional semiconductor systems research has acquired a great deal of interest in the route for optimizing electronic and optoelectronic devices. These systems are usually obtained when the nanometer size is reached, and at these dimensions, there exists a strong modification of the electronic and optical properties due to the quantum confinement imposed on the carriers.<sup>1</sup> Another important role in the fabrication and development of semiconductor devices is the semiconductor–vacuum interface in which surface states are created, having a detrimental effect on the optical and electrical properties of the devices.<sup>2</sup>

The surface states are created due to interruption of the periodic pattern imposed by the crystalline material atomic lattice arrangement. Top most dangling bonds produce changes at the surface potential that, for instance, bends the energy bands.

This project studies the changes induced by the surface states when modifying the cap layer structure of modulation doped AlGaAs/GaAs heterostructures (MDH). These structures are widely used in devices like high electron mobility transistor and also are employed in metrology science as the basic structure of the electrical resistance pattern<sup>3</sup> making

meritorious any characterization studies that may lead us to understand and improve their electrical properties.

On the other hand, photoreflectance spectroscopy (PR) is a fast-reading nondestructive characterization technique that has been used to characterize the MDH.<sup>4</sup> The typical short period damped oscillatory behavior of the PR spectra termed as Franz–Keldysh oscillations (FKO) is associated to internal AlGaAs/GaAs interface electric fields, while large period oscillations in the region between 1.45 and 1.75 eV are due to surface states.<sup>5</sup> Therefore, PR and Hall measurements, combined by energy band simulations, might provide a suitable scenario for the study of MDH, as it is intended in this article.

## II. EXPERIMENT

The MDH were grown by molecular beam epitaxy (MBE) on semi-insulating GaAs (100) substrates. The basic heterostructure is shown in Fig. 1. After the GaAs native oxides desorption process, a 1  $\mu\text{m}$ -thick GaAs buffer layer was deposited, followed by 7 nm undoped  $\text{Al}_{0.3}\text{Ga}_{0.7}\text{As}$  spacer layer (spacer 1). Next, the 80 nm-thick Si doped  $\text{Al}_{0.3}\text{Ga}_{0.7}\text{As}$  barrier was deposited with a carrier concentration of  $1.4 \times 10^{18} \text{ cm}^{-3}$ . Another spacer layer (spacer 2) of 7 nm-thick undoped AlGaAs was subsequently deposited. Finally, the structure was capped with undoped GaAs of thickness denoted by  $C_{\text{th}}$ . The surface states and/or near surface band

<sup>a)</sup>Electronic mail: victor.mendez@uaslp.mx

## Measurement of the shear strain of the $\text{Gd}_2\text{O}_3/\text{GaAs}(001)$ interface by photoreflectance difference spectroscopy

N. A. Ulloa-Castillo,<sup>1,a)</sup> L. F. Lastras-Martínez,<sup>1,b)</sup> R. E. Balderas-Navarro,<sup>1,2,c)</sup>  
 R. Herrera-Jasso,<sup>1</sup> and A. Lastras-Martínez<sup>1</sup>

<sup>1</sup>Instituto de Investigación en Comunicación Óptica, Universidad Autónoma de San Luis Potosí,  
 Alvaro Obregón 64, San Luis Potosí 78000, Mexico

<sup>2</sup>Paul-Drude-Institut für Festkörperelektronik, Hausvogteiplatz 5-7, 10117 Berlin, Germany

(Received 2 August 2014; accepted 27 October 2014; published online 6 November 2014)

In this work, we report on photoreflectance (PR) and photoreflectance-difference (PR-D) measurements of GaAs(001) upon deposition of  $\text{Gd}_2\text{O}_3$  thin films. The study is focused on two different substrates: a semi-insulating (SI) with Cr impurities and a Si-doped  $n$ -type. PR-D results show that  $\text{Gd}_2\text{O}_3$  induces a tensile strain on the GaAs surface and a direct piezo-electric dipole is created. Such strain changes the crystal symmetry from cubic to orthorhombic and renders the quadratic electro-optic (QEO) component anisotropic. For the SI substrate, both linear electro-optic (LEO) and QEO components contribute to the PR-D spectrum, whereas the  $n$ -type PR-D spectrum is dominated by the LEO component. In both cases, a tensile strain induces a rigid redshift of  $\sim 20$  meV to low energies of the  $E_1$  and  $E_1 + \Delta_1$  optical transitions. © 2014 AIP Publishing LLC.  
<http://dx.doi.org/10.1063/1.4901168>

The high- $\kappa$  dielectric/III-V interface is extremely important for metal-oxide-semiconductor (MOS) technology and can exhibit either a high or low interface state density depending on both the intrinsic properties of III-V surfaces and the nature of their oxidation chemistry.<sup>1,2</sup> In particular,  $\text{Gd}_2\text{O}_3$  has been investigated due to its high dielectric constant,<sup>3,4</sup> large band gap<sup>5</sup> and excellent thermodynamical stability in semiconductors.<sup>6,7</sup> As a matter of fact, a low interfacial density of states was demonstrated in  $\text{Gd}_2\text{O}_3/\text{GaAs}$  MOS devices.<sup>8,9</sup> However, as GaAs has piezo-electric character, a polarization charge will be induced by the stress at the insulator-semiconductor interface when the dielectric layer is deposited, thus modifying the electric properties at the interface by this induced charge. In this regard, probing of interface states evolution for process control during interface formation is of particular importance, preferably *in situ*. Optical spectroscopies are non-invasive and can be operated in any environment.

Two linear optical spectroscopies employed to probe surface piezo-electric phenomena in semiconductors are reflectance-difference (RD) and photoreflectance-difference (PR-D) spectroscopies.<sup>10-13</sup> On the (001) surface of zinc-blende semiconductors, RD measures the difference in reflectivity between [110] and  $[1\bar{1}0]$  light polarizations,<sup>10,14</sup> whereas PR-D accounts for the difference between a PR spectrum for polarized probe light (along either [110] or  $[1\bar{1}0]$ ) and the corresponding spectrum for unpolarized probe light.<sup>15</sup> Furthermore, PR spectra comprise both linear electro-optic (LEO) and quadratic electro-optic (QEO) components. PR-D spectra involve only the LEO component as the QEO contribution is nominally isotropic. However, when the crystal symmetry is modified, as in the case of an

external stress applied along [110], the QEO component becomes anisotropic as well.<sup>16</sup> For instance, the strain caused by dimers at the GaAs(001)- $c(4 \times 4)$  surface reconstruction induces a direct piezo-electric dipole (DPD) that opposes the electric field ( $F$ ) of the space-charge layer within the first tens monolayers into the crystal.<sup>10</sup> Another example is the hydrocarbon ring molecule adsorption onto the As surface dimers of GaAs(001)- $c(4 \times 4)$ , which reduces the surface band bending causing an increment of  $F$ .<sup>17</sup> Therefore, a modification of the surface states influences significantly the surface electro-optical properties.<sup>18</sup>

In this work, we report on *in situ* PR and PR-D measurements of two GaAs(001) surfaces: a semi-insulating (SI) with Cr impurities and a Si-doped  $n$ -type. PR and PR-D measurements were done around  $E_1$  and  $E_1 + \Delta_1$  optical transitions in order to investigate changes of the surface states caused by modifications in the surface electric field upon deposition of  $\text{Gd}_2\text{O}_3$  on GaAs. The results for the SI substrate show that  $\text{Gd}_2\text{O}_3$  modifies the GaAs(001) by building up a tensile shear strain which renders the QEO component anisotropic, whereas, for the  $n$ -type substrate, the LEO component dominates the lineshapes even after  $\text{Gd}_2\text{O}_3$  deposition. We note that, because we are interested on the PR-D evolution upon surface modifications, the critical points at  $E_1$  (2.92 eV) and  $E_1 + \Delta_1$  (3.13 eV) optical transitions were used, as the penetration depth of the probe light is only 170 Å for GaAs. This contrasts the case at  $E_0$  (1.42 eV), where probe light can penetrate down to the back-face in thin GaAs substrates, thus washing out any optical anisotropy coming from the front surface.

PR and PR-D measurements were carried out in ultra-high vacuum (UHV) on the S1 and S2 substrates which are described in Table I. Both samples were chemical etched in  $\text{H}_2\text{O}:\text{H}_2\text{SO}_4:\text{H}_2\text{O}_2$  (1:5:1) and immediately introduced into the UHV chamber. The samples were then heated up gradually to obtain a clear  $(1 \times 1)$  reconstruction as monitored by

<sup>a)</sup>Electronic mail: nulloa@cactus.iico.uaslp.mx

<sup>b)</sup>Electronic mail: lfm@cactus.iico.uaslp.mx

<sup>c)</sup>Electronic mail: rbn@cactus.iico.uaslp.mx and balderas@pdi-berlin.de

## Real-time reflectance-difference spectroscopy of GaAs molecular beam epitaxy homoepitaxial growth

A. Lastras-Martínez,<sup>1,a</sup> J. Ortega-Gallegos,<sup>1</sup> L. E. Guevara-Macías,<sup>1</sup>  
 O. Nuñez-Olvera,<sup>1</sup> R. E. Balderas-Navarro,<sup>1</sup> L. F. Lastras-Martínez,<sup>1</sup>  
 L. A. Lastras-Montañó,<sup>2</sup> and M. A. Lastras-Montañó<sup>3</sup>

<sup>1</sup>*Instituto de Investigación en Comunicación Óptica, Universidad Autónoma de San Luis Potosí, Alvaro Obregón 64, San Luis Potosí, SLP 78000, Mexico*

<sup>2</sup>*IBM T. J. Watson Research Center, Yorktown Heights, New York 10598, USA*

<sup>3</sup>*Department of Electrical and Computer Engineering, University of California, Santa Barbara, Santa Barbara, California 93106, USA*

(Received 23 December 2013; accepted 4 March 2014; published online 14 March 2014)

We report on real time-resolved Reflectance-difference (RD) spectroscopy of GaAs(001) grown by molecular beam epitaxy, with a time-resolution of 500 ms per spectrum within the 2.3–4.0 eV photon energy range. Through the analysis of transient RD spectra we demonstrated that RD line shapes are comprised of two components with different physical origins and determined their evolution during growth. Such components were ascribed to the subsurface strain induced by surface reconstruction and to surface stoichiometry. Results reported in this paper render RD spectroscopy as a powerful tool for the study of fundamental processes during the epitaxial growth of zincblende semiconductors. © 2014 Author(s). All article content, except where otherwise noted, is licensed under a Creative Commons Attribution 3.0 Unported License. [<http://dx.doi.org/10.1063/1.4868519>]

It is known that dimerized (001) surfaces of zincblende semiconductors are optically anisotropic.<sup>1</sup> Optical anisotropies have been associated to either the anisotropic response of surface dimers<sup>2–4</sup> or to the dimer-induced cubic-symmetry breakdown of the underlying atomic layers.<sup>5–8</sup> The anisotropic nature of (001) zincblende surfaces prompted the development of polarized-light techniques as optical, non-invasive probes for semiconductor surface characterization. One of such probes, Reflectance-difference spectroscopy (RDS),<sup>9</sup> is currently employed, along with Reflection high energy electron diffraction (RHEED), for the identification of GaAs (001) surface reconstructions.<sup>1,10</sup>

In addition to their application to static surfaces, reflectance-difference (RD) probes have been employed to study the dynamics of the epitaxial growth of zincblende semiconductors. Aspnes *et al.*,<sup>11</sup> first carried out single-wavelength dynamic RD measurements during GaAs Molecular beam epitaxy (MBE) growth and showed that abrupt changes in RD signal occur upon interrupting or allowing As flux while keeping the Ga flux on, thus following changes in surface stoichiometry. The combination of spectroscopic ellipsometry and RD turned out to be very successful in the investigation of complex surface dynamics under different growth conditions present in both MBE and Metal organic chemical vapor deposition (MOCVD) reactors, allowing for control during device fabrication.<sup>12</sup>

While single-wavelength RD measurements have shown the surface sensitivity of RD techniques to transients in surface stoichiometry occurring during epitaxy, the full potential of RD as a probe for monitoring epitaxial growth processes could be only realized through RD spectroscopic measurements. For zincblende semiconductors such an application demands of sub-second spectra acquisition times and the measurement of RD amplitudes in the  $10^{-4}$  to  $10^{-3}$  range. In the past these

<sup>a</sup>Electronic addresses: [alm@cactus.iico.uaslp.mx](mailto:alm@cactus.iico.uaslp.mx) and [alastras@gmail.com](mailto:alastras@gmail.com)



# Structure, electronic properties, and aggregation behavior of hydroxylated carbon nanotubes

A. B. López-Oyama,<sup>1</sup> R. A. Silva-Molina,<sup>1</sup> J. Ruíz-García,<sup>1</sup> R. Gámez-Corrales,<sup>2</sup> and R. A. Guirado-López<sup>1,a)</sup>

<sup>1</sup>*Instituto de Física “Manuel Sandoval Vallarta,” Universidad Autónoma de San Luis Potosí, Álvaro Obregón 64, 78000 San Luis Potosí, San Luis Potosí, Mexico*

<sup>2</sup>*Departamento de Física, Universidad de Sonora, Apartado Postal 5-088, 83190, Hermosillo, Sonora, Mexico*

(Received 22 June 2014; accepted 16 October 2014; published online 3 November 2014)

We present a combined experimental and theoretical study to analyze the structure, electronic properties, and aggregation behavior of hydroxylated multiwalled carbon nanotubes (OH-MWCNT). Our MWCNTs have average diameters of  $\sim 2$  nm, lengths of approximately 100–300 nm, and a hydroxyl surface coverage  $\theta \sim 0.1$ . When deposited on the air/water interface the OH-MWCNTs are partially soluble and the floating units interact and link with each other forming extended foam-like carbon networks. Surface pressure-area isotherms of the nanotube films are performed using the Langmuir balance method at different equilibration times. The films are transferred into a mica substrate and atomic force microscopy images show that the foam like structure is preserved and reveals fine details of their microstructure. Density functional theory calculations performed on model hydroxylated carbon nanotubes show that low energy atomic configurations are found when the OH groups form molecular islands on the nanotube's surface. This patchy behavior for the OH species is expected to produce nanotubes having reduced wettabilities, in line with experimental observations. OH doping yields nanotubes having small HOMO-LUMO energy gaps and generates a nanotube  $\rightarrow$  OH direction for the charge transfer leading to the existence of more hole carriers in the structures. Our synthesized OH-MWCNTs might have promising applications. © 2014 AIP Publishing LLC. [<http://dx.doi.org/10.1063/1.4900546>]

## I. INTRODUCTION

Single- and multi-walled carbon nanotubes (CNTs) have attracted increasing attention in the last years due to their potential applications in electronics, opto-electronics, and biosensors.<sup>1,2</sup> They possess exceptional properties such as great mechanical strength, low density, high elasticity, as well as a remarkable ability to adapt and switch between various buckled morphologies, such as rings, kinks, rackets, and foam-like configurations, which clearly makes them capable of accommodating and sustaining large local strains.<sup>3</sup> In particular, the properties of foam-like nanostructures<sup>4-7</sup> made of CNTs have been extensively analyzed in the past few years. These low-density carbon materials can be obtained by means of different synthetic procedures and their experimental characterization has revealed interesting microstructural features and novel chemical, electronic, and transport properties. As representative examples we would like to mention first the work of Cao *et al.*<sup>8</sup> where vertically aligned CNTs exhibit super-compressible foam like behavior. These authors found that, under compression, the nanotubes form zigzag buckles that can fully unfold to their original length upon load release. Hermant and co-workers<sup>9</sup> synthesized single-walled carbon nanotube (SWCNT) composite foams by allowing the self-assembly of SWCNTs on a water-oil

interface. They observed that varying the concentration of nanotubes at the interface leads to a marked change in the foam morphology, strongly altering the distribution of pores sizes as well as the porosity percentage and skeletal density of the samples. Nabeta *et al.*<sup>10</sup> have obtained nanotube foams by simply mixing SWCNTs in an aqueous solution of gelatin. In a second step, the gelatin is thermally removed and the resulting solid is a macroscopically highly porous sponge that is mechanically strong and electrically conducting. We would also like to mention the work of Worsley and co-workers<sup>11</sup> in which the fabrication of ultra-low-density carbon nanotube foams that simultaneously exhibit high electrical conductivities and robust mechanical properties is achieved. The previous report is important to emphasize since the authors use carbon nanoparticles as a binder to crosslink randomly oriented bundles of SWCNTs, leading to the formation of nanostructured materials which exhibit elastic behavior up to strains as large as  $\sim 80\%$ . Finally, we also underline the paper by Alvizo-Paez and co-workers<sup>5</sup> in which the synthesis of foam-like two-dimensional networks made of nitrogen doped multi-walled carbon nanotubes (MWCNT) on the air-water interface has been achieved. It is found that nitrogen doping reduces van der Waals interactions among tubes and provides them with a polar character that makes stable  $CN_x$  dispersions in water. The thickness of the as-synthesized films corresponds to one monolayer and the authors reported that more packed structures could be obtained by increasing the surface pressure.

<sup>a)</sup> Author to whom correspondence should be addressed. Electronic mail: [guirado@ifisica.uaslp.mx](mailto:guirado@ifisica.uaslp.mx)

See discussions, stats, and author profiles for this publication at: <https://www.researchgate.net/publication/267810202>

# Structure, electronic properties, and aggregation behavior of hydroxylated carbon nanotubes

Article in *The Journal of Chemical Physics* · November 2014

Impact Factor: 2.95 · DOI: 10.1063/1.4900546

---

READS

110

5 authors, including:



[Anna López-Oyama](#)

Instituto Politécnico Nacional

6 PUBLICATIONS 17 CITATIONS

[SEE PROFILE](#)



[Ramon Antonio Silva-Molina](#)

Universidad Autónoma de San Luis Potosí

11 PUBLICATIONS 5 CITATIONS

[SEE PROFILE](#)



[Jaime Ruiz-Garcia](#)

Universidad Autónoma de San Luis Potosí

67 PUBLICATIONS 1,029 CITATIONS

[SEE PROFILE](#)



[R. A. Guirado-Lopez](#)

Universidad Autónoma de San Luis Potosí

57 PUBLICATIONS 709 CITATIONS

[SEE PROFILE](#)

## Structure, electronic properties, and aggregation behavior of hydroxylated carbon nanotubes

A. B. López-Oyama, R. A. Silva-Molina, J. Ruíz-García, R. Gámez-Corrales, and R. A. Guirado-López

Citation: *The Journal of Chemical Physics* **141**, 174703 (2014); doi: 10.1063/1.4900546

View online: <http://dx.doi.org/10.1063/1.4900546>

View Table of Contents: <http://scitation.aip.org/content/aip/journal/jcp/141/17?ver=pdfcov>

Published by the [AIP Publishing](#)

---

### Articles you may be interested in

Structure, stability, and electronic property of carbon-doped gold clusters  $Au_nC^-$  ( $n = 1-10$ ): A density functional theory study

*J. Chem. Phys.* **139**, 244312 (2013); 10.1063/1.4852179

Atomic vacancy defects in the electronic properties of semi-metallic carbon nanotubes

*J. Appl. Phys.* **109**, 083716 (2011); 10.1063/1.3573782

Ab initio study of semiconducting carbon nanotubes adsorbed on the Si(100) surface: Diameter- and registration-dependent atomic configurations and electronic properties

*J. Appl. Phys.* **100**, 124304 (2006); 10.1063/1.2400404

Ab initio study of the effect of water adsorption on the carbon nanotube field-effect transistor

*Appl. Phys. Lett.* **89**, 243110 (2006); 10.1063/1.2397543

Amphoteric doping of carbon nanotubes by encapsulation of organic molecules: Electronic properties and quantum conductance

*J. Chem. Phys.* **123**, 024705 (2005); 10.1063/1.1931547

---



**2014 Special Topics**

PEROVSKITES | 2D MATERIALS | MESOPOROUS MATERIALS | BIOMATERIALS/ BIOELECTRONICS | METAL-ORGANIC FRAMEWORK MATERIALS

**AIP** | APL Materials

**Submit Today!**



# Structure, electronic properties, and aggregation behavior of hydroxylated carbon nanotubes

A. B. López-Oyama,<sup>1</sup> R. A. Silva-Molina,<sup>1</sup> J. Ruíz-García,<sup>1</sup> R. Gámez-Corrales,<sup>2</sup> and R. A. Guirado-López<sup>1,a)</sup>

<sup>1</sup>*Instituto de Física “Manuel Sandoval Vallarta,” Universidad Autónoma de San Luis Potosí, Álvaro Obregón 64, 78000 San Luis Potosí, San Luis Potosí, Mexico*

<sup>2</sup>*Departamento de Física, Universidad de Sonora, Apartado Postal 5-088, 83190, Hermosillo, Sonora, Mexico*

(Received 22 June 2014; accepted 16 October 2014; published online 3 November 2014)

We present a combined experimental and theoretical study to analyze the structure, electronic properties, and aggregation behavior of hydroxylated multiwalled carbon nanotubes (OH-MWCNT). Our MWCNTs have average diameters of  $\sim 2$  nm, lengths of approximately 100–300 nm, and a hydroxyl surface coverage  $\theta \sim 0.1$ . When deposited on the air/water interface the OH-MWCNTs are partially soluble and the floating units interact and link with each other forming extended foam-like carbon networks. Surface pressure-area isotherms of the nanotube films are performed using the Langmuir balance method at different equilibration times. The films are transferred into a mica substrate and atomic force microscopy images show that the foam like structure is preserved and reveals fine details of their microstructure. Density functional theory calculations performed on model hydroxylated carbon nanotubes show that low energy atomic configurations are found when the OH groups form molecular islands on the nanotube's surface. This patchy behavior for the OH species is expected to produce nanotubes having reduced wettabilities, in line with experimental observations. OH doping yields nanotubes having small HOMO-LUMO energy gaps and generates a nanotube  $\rightarrow$  OH direction for the charge transfer leading to the existence of more hole carriers in the structures. Our synthesized OH-MWCNTs might have promising applications. © 2014 AIP Publishing LLC. [<http://dx.doi.org/10.1063/1.4900546>]

## I. INTRODUCTION

Single- and multi-walled carbon nanotubes (CNTs) have attracted increasing attention in the last years due to their potential applications in electronics, opto-electronics, and biosensors.<sup>1,2</sup> They possess exceptional properties such as great mechanical strength, low density, high elasticity, as well as a remarkable ability to adapt and switch between various buckled morphologies, such as rings, kinks, rackets, and foam-like configurations, which clearly makes them capable of accommodating and sustaining large local strains.<sup>3</sup> In particular, the properties of foam-like nanostructures<sup>4-7</sup> made of CNTs have been extensively analyzed in the past few years. These low-density carbon materials can be obtained by means of different synthetic procedures and their experimental characterization has revealed interesting microstructural features and novel chemical, electronic, and transport properties. As representative examples we would like to mention first the work of Cao *et al.*<sup>8</sup> where vertically aligned CNTs exhibit super-compressible foam like behavior. These authors found that, under compression, the nanotubes form zigzag buckles that can fully unfold to their original length upon load release. Hermant and co-workers<sup>9</sup> synthesized single-walled carbon nanotube (SWCNT) composite foams by allowing the self-assembly of SWCNTs on a water-oil

interface. They observed that varying the concentration of nanotubes at the interface leads to a marked change in the foam morphology, strongly altering the distribution of pores sizes as well as the porosity percentage and skeletal density of the samples. Nabeta *et al.*<sup>10</sup> have obtained nanotube foams by simply mixing SWCNTs in an aqueous solution of gelatin. In a second step, the gelatin is thermally removed and the resulting solid is a macroscopically highly porous sponge that is mechanically strong and electrically conducting. We would also like to mention the work of Worsley and co-workers<sup>11</sup> in which the fabrication of ultra-low-density carbon nanotube foams that simultaneously exhibit high electrical conductivities and robust mechanical properties is achieved. The previous report is important to emphasize since the authors use carbon nanoparticles as a binder to crosslink randomly oriented bundles of SWCNTs, leading to the formation of nanostructured materials which exhibit elastic behavior up to strains as large as  $\sim 80\%$ . Finally, we also underline the paper by Alvizo-Paez and co-workers<sup>5</sup> in which the synthesis of foam-like two-dimensional networks made of nitrogen doped multi-walled carbon nanotubes (MWCNT) on the air-water interface has been achieved. It is found that nitrogen doping reduces van der Waals interactions among tubes and provides them with a polar character that makes stable  $CN_x$  dispersions in water. The thickness of the as-synthesized films corresponds to one monolayer and the authors reported that more packed structures could be obtained by increasing the surface pressure.

<sup>a)</sup> Author to whom correspondence should be addressed. Electronic mail: [guirado@ifisica.uaslp.mx](mailto:guirado@ifisica.uaslp.mx)

We would like to emphasize that the Langmuir balance method used in Ref. 5 has played a fundamental role to synthesize stable foam-like dispersions of CNTs in a large variety of solvents. It is also useful for transferring and spreading carbon nanotubes on solid surfaces and isolating thus both single and multi-walled CNTs from bundles. In addition, the inter-tube distance and the final superstructures can be finely controlled before transfer by the compression process in the Langmuir balance, being also relatively easy to carry out multiple (or alternating) layer deposition as well as *in situ* alignments of the films by patterning and chemical modification of the solid substrates. It is important to precise that the basic requirement for the preparation of such materials is the use of carbon nanotubes that strongly adsorb in the gas-liquid (or liquid-liquid) interface. To achieve the previous surfactant-like behavior, the partial wetting of the CNTs needs to be achieved by altering their solubility in one of the phases. As is well known, as grown carbon nanotubes are hydrophobic and coagulate easily in any solvent even if they are forced to disperse initially by ultra-sonication. However, a standard procedure to overcome this problem is to perform the functionalization of the surface by using molecular species that allow them to acquire a polar character and become water soluble.<sup>12,13</sup> This can be done by employing acid treatments at low temperatures, involving, for example, the use of H<sub>2</sub>SO<sub>4</sub>/HNO<sub>3</sub> mixtures. The previous procedure induces surface changes by the insertion of OH groups, an insertion process that is accompanied by bundle exfoliation and etching of the carbon material.<sup>2</sup>

The addition of hydroxyl groups to carbon nanostructures has been realized in spheroidal fullerenes,<sup>14–19</sup> carbon fibers,<sup>20</sup> and CNTs.<sup>13,21–24</sup> In particular, SWCNTs functionalized with hydroxyl group terminated moieties have been synthesized by Zhang and co-workers. All prepared nanotube derivatives were found to form stable suspensions in polar solvents such as water, ethanol, and dimethylformamide, providing thus compatibility with biomaterials and improving their potential applications in life sciences. We would also like to refer to the work of Zaman *et al.*<sup>25</sup> where the microstructure, density, and hardness of alumina ceramics containing homogeneous dispersions of hydroxylated SWCNTs are analyzed. The inclusion of OH-SWCNTs in the Al<sub>2</sub>O<sub>3</sub> matrix resulted in refined alumina grains as well as in an electrical conductivity 7.5 times higher when compared with the untreated samples. Finally, we mention the work of Bradley and collaborators<sup>26</sup> in which MWCNTs have been surface functionalized using the Fenton hydroxylation reaction. The authors perform an extensive characterization of the as-synthesized OH-MWCNTs samples using x-ray photoelectron and Raman spectroscopies, high-resolution transmission electron microscopy, nitrogen adsorption data, and water adsorption isotherms. MWCNTs with surface oxygen levels of ~22% are obtained together with some low-level disruption of the very outermost layers as a result of hydroxylation. Furthermore, water vapor adsorption by the hydroxylated nanotube surface leads to the formation of isotherms that are characteristic of a relatively high number of hydrogen bonding interactions. At this point it is important to precise that, despite the previous extensive experimen-

tal characterization, it is clear that a more precise knowledge of the atomic structure of the OH over-layer needs to be achieved for developing a more complete understanding of many fundamental processes that have been observed in these systems in solid and aqueous environments. The latter are especially relevant to analyze mostly within the framework of biological and medical applications since the precise details of the solvent/nanotube-surface interaction determines their wettability, adsorption properties, and aggregation behavior.

We would like to comment that even if it is always possible to estimate and identify the number and type of molecules adsorbed on MWCNTs, it is very difficult to elucidate the precise geometrical structure of the adsorbed phases that exist on the surface of such small objects, and that play of course a fundamental role on the properties observed on a macroscopic scale. The synthetic routes that are currently used for the functionalization of CNTs are generally not thermodynamically controlled and can allow the preparation of meta-stable molecular structures that could lead to the appearance of novel phenomena. It is thus of fundamental importance to bring important details of the atomic structure that go beyond the current experimental evidence and, as a consequence, theoretical studies dedicated to analyze the energetics and electronic properties of carbon nanotubes functionalized with OH species must be performed in order to shed some more light into the understanding of the measured data.

In this work, we present thus a combined experimental and theoretical study dedicated to analyze the structure, electronic properties, and aggregation behavior of hydroxylated multiwalled carbon nanotubes (OH-MWCNT). We consider MWCNTs having average diameters of ~1.8 nm, nanotube lengths varying in the range of 100–300 nm, and a hydroxyl surface coverage  $\theta$  of ~0.1. We will show that, when deposited on the air/water interface, our OH-MWCNTs are partially soluble and form extended foam-like carbon networks. As is well known, water adsorption properties strongly depend on the amount and surface distribution of OH groups since they act as primary sites at which H<sub>2</sub>O attachment occurs by specific hydrogen bonding interactions. Consequently, to better understand the hydration behavior of OH-MWCNTs and to separate the intrinsic properties of hydroxylated carbon nanotubes from solvent contributions and tube-tube interactions, we perform pseudo-potential density functional theory (DFT) calculations addressing OH adsorption on model CNTs. Our data show that low energy atomic configurations are found when the OH groups form molecular islands on the nanotube's surface, being characterized by robust hydrogen-bonding networks. This patchy behavior for the OH species is expected to produce carbon nanotubes having reduced wettabilities, in line with our experimental observations. Furthermore, OH doping (i) yields carbon compounds having small HOMO-LUMO energy gaps, (ii) increases the number of energy levels in the electronic spectra, allowing for more interband excitations, and (iii) generates a nanotube  $\rightarrow$  OH direction for the charge transfer that leads to the existence of more hole carriers in the carbon structures, which are all facts that might strongly change the

transport properties of the samples. The nanotube films are transferred into a mica substrate and atomic force microscopy images show that the foam like structure is still preserved, also revealing fine details of their microstructure. Our here-reported nanotube patterns have been of great interest for a long time and are expected to be of fundamental importance for the development of novel materials and many engineering applications.

## II. MATERIALS AND METHODS

### A. Reagents

The chemicals used in our experiments included  $\text{HNO}_3$  (Fermont, Monterrey, México) and  $\text{H}_2\text{SO}_4$  98% (Fagalab, Sinaloa, México) acids, as well as MWCNTs (Sigma-Aldrich, St. Louis, MO, USA) which were used without further purification. The functionalization process was performed using Milli-Q water (18.3  $\text{m}\Omega$  cm of resistivity).

### B. Functionalization

The oxidation of MWCNTs was carried out using 4 ml of a 1:3 volume/volume ratio of  $\text{HNO}_3/\text{H}_2\text{SO}_4$  acid mixture at 80 °C for 3 h, after which the sample was filtered and washed with ultrapure water. In a second step, the MWCNTs were transferred to the furnace at 40 °C for 15 h under vacuum. Finally, in order to prove the surface functionalization FTIR and XPS experiments were performed.

### C. Isotherms and Langmuir-Blodgett studies

A Langmuir trough (601-BAM, Nima Technology Ltd., England) equipped with two symmetrically arranged barriers, whose surface pressure precision is 0.1 mN/m, was employed to obtain measurements of surface pressure ( $\Pi$ )-area ( $A$ ) isotherms. The surface pressure,  $\pi = \gamma_0 - \gamma$ , that is, the surface tension difference of the clean and nanotube-covered water surface was measured using the Wilhelmy plate method. The Langmuir balance was placed on an optical table inside a dust-free room and the barrier speed was set to 20  $\text{cm}^2/\text{min}$ . Finally, we deposited 50  $\mu\text{l}$  of OH-MWCNTs solution on a clean water surface in a drop wise fashion with a micropipette (Rainin Instrument LLC, CA). Several independent experiments were performed and the system was allowed to stand in the trough for 0.5, 5.5, 6.5, 7.5 h before compression. Another set of compression/expansion cycling experiments were done in which the first compression/expansion was performed 12 h after sample deposition. The cycles were repeated three times. Further cycles were done on the films at 21 and 40 h after deposition of the sample. All isotherms were measured at  $298.15 \pm 0.1$  K. After equilibrium was reached, the surface pressure-area isotherm was recorded. For transferring the films, a solid substrate was placed at the middle of the trough and the mobile arm of the dipper was set to a transfer speed of 1 mm/min for an upward stroke. The transfer was performed at a surface pressure of 10 mN/m onto freshly cleaved mica.

### D. Brewster angle microscopy

A Brewster angle microscope (BAM, Mod. I-ELLI 2000, Nanofilm Technology GmbH) with a 10 $\times$  objective was used to obtain OH-MWCNTs images *in situ*, at different compression areas or surface pressures. Images were recorded and analyzed using appropriate software from Nanofilm Technology GmbH.

### E. Atomic force microscopy

OH-MWCNTs Langmuir-Blodgett films formed on freshly cleaved mica were observed on an AFM (Digital, Mod. Nanoscope IIIa, USA) in contact mode using silicon nitride cantilevers (model NSC15, from MicroMash, USA) at room temperature.

### F. Computational details

The structural and electronic properties of model hydroxylated carbon nanotubes will be obtained within the DFT approach using the ultra soft pseudo-potential approximation for the electron-ion interaction and a plane wave basis set for the wave functions as implemented in the Quantum-Espresso code.<sup>27</sup> We consider a finite length armchair (5,5) open-ended tube containing 100 atoms where the dangling bonds at the ends are tied off with hydrogen atoms yielding a  $\text{C}_{100}\text{H}_{20}$  structure. Guided by the experimental data we assume in all cases an hydroxyl surface coverage of  $\sim 10\%$  and consider several initial configurations of the OH groups, namely: (i) uniformly distributed on the surface, (ii) clustered on one side of the nanotube, as well as (iii) adsorbed phases with different degrees of molecular aggregation. In all our calculations, the cutoff energy for the plane wave expansion is taken to be 476 eV. A cubic supercell with a side dimension as large as 35 Å was employed in the calculations and the  $\Gamma$  point for the Brillouin zone integration. In all cases, we use the Perdew-Burke-Ernzerhof (PBE) pseudopotential<sup>28</sup> and perform fully unconstrained structural optimizations for all our considered structures using the conjugate gradient method. We include in addition the London dispersion interaction as implemented in the Quantum-Espresso code.<sup>27</sup> The convergence in energy was set as 1 meV and the structural optimization was performed until a value of less than 1 meV/Å was achieved for the remaining forces for each atom. We also analyze the diffusion properties of our OH species chemisorbed on the nanotube's surface and, in that case, we determine the minimum energy paths as well as the transition states by applying the nudged elastic band (NEB) methodology.<sup>29</sup> The NEB calculation scheme is a chain-of-states method where a set of images between the initial and final states must be created to achieve a smooth curve. In our case, the relatively small size of our hydroxylated carbon nanotubes will ensure that the calculations for the reaction pathways will remain computationally tractable. We use from seven to nine images to determine the energy profiles, which have been found to be enough to reveal the different stages of the OH migration in our carbon nanostructures. The relevant energy barriers between well-defined initial and final atomic configurations are obtained by

calculating the energy difference of the initial position and the saddle point of each one of the energy profiles.

### III. RESULTS AND DISCUSSION

#### A. Hydroxylated carbon nanotubes

Both sonication and acid treatment processes required to modify the chemical nature of the carbon nanotube's side wall are drastic conditions that naturally lead to the opening of the tube caps, the formation of holes, as well as to an oxidative etching along the walls, which are all facts that increases the nanotube's solubility. The final CNT units are fragments with lengths that vary in the range of 100 and 300 nm and have average diameters of  $\sim 2.0$  nm, as inferred from the Raman spectra of the samples. In addition, the EDS analysis by TEM reveals the following composition: carbon 68.79%, oxygen 13.78%, and the support components as traces, which confirm the presence of OH groups attached to nanotube surface.

#### B. FTIR

Fig. 1 shows the IR-spectrum of our synthesized OH-MWCNTs. The spectra displays a broad and intense O-H band centered at  $3443.8\text{ cm}^{-1}$  which together with the peaks located at  $1063.7\text{ cm}^{-1}$ , attributed to C-O stretching, as well as the one located at  $1390.98\text{ cm}^{-1}$  assigned to C-OH contributions, provide further evidence for the presence of hydroxyl groups on the nanotube surface. We believe that the additional band placed at  $1223.5\text{ cm}^{-1}$  also corresponds to vibrations of the C-O(H) bond but located in a different chemical environment. As is well known, the integrity of the hexagonal structure of CNTs is corroborated in the IR spectra by the appearance of a peak at  $1532\text{--}1560\text{ cm}^{-1}$ , elucidating the existence of carbon double bonding (C=C). We consider that the notable quenching of this C=C contribution in Fig. 1 could also be correlated with the emergence of the additional peak at  $1634.1\text{ cm}^{-1}$ , being typically assigned to carbonyl (C=O) stretching vibrations, although some C=C absorption and O-H bending vibrations are also located in that

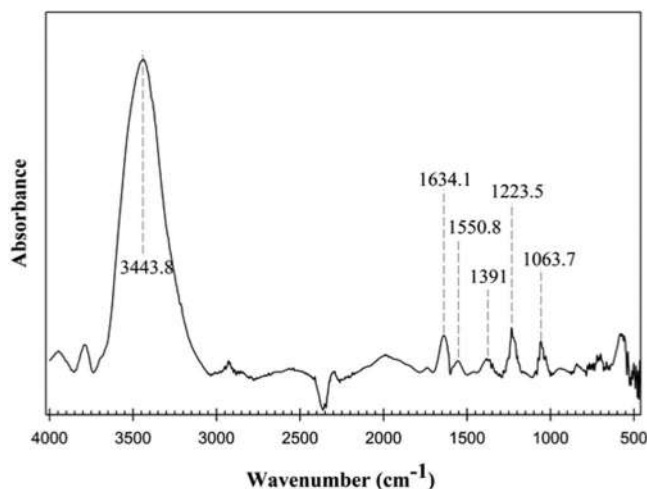


FIG. 1. FTIR spectra of OH-MWCNTs.

frequency range. In any case, the previous result could imply the possibility of having some degree of carbonyl groups on the nanotube's surface.<sup>7,30</sup> Even if IR spectroscopy does not provide a quantitative measure of functional group concentrations, it has been very helpful in revealing the identity of the principal functional groups present on the surface of our MWCNTs.

#### C. XPS

We show now in Fig. 2 the data corresponding to XPS measurements performed on our OH-MWCNTs samples. XPS can also provide us with valuable information concerning the CNT surface composition by determining the binding energy of photoelectrons ejected when our hydroxylated carbon nanotubes are irradiated with X rays. In addition to compositional analysis, XPS can give us information related with the chemical environment of surface species based on the peak-fitting of XP spectral envelopes. In Fig. 2, we present, as a representative example, the spectral deconvolution of the C(1s) XPS region of our OH-MWCNTs. The C(1s) signal can be decomposed into five peaks located at binding energies of 284.5 eV, 285.7 eV, 286.45 eV, 288.2 eV, and 290.5 eV. The C(1s) peak at 284.5 eV binding energy [labelled as (i)] is associated with unmodified carbon (C-C). The next three peaks, denoted as (ii), (iii), and (iv) correspond to three different oxygen-containing environments, namely: 285.7 eV (C-OH), 286.45 eV (C=O), and 288.2 eV (COOH), respectively. Finally, the peak at 290.5 eV (v) is originated by the  $\pi\text{-}\pi^*$  shake-up features. As is well known, the concentration of each adsorbed species evaluated from the relative intensity of the peak components in the C(1s) and O(1s) spectra (not shown), can be misleading since preferred adsorption sites for the various ad-species and different molecular orientations may originate photoelectron yields appreciably different from the real ad-species concentrations. However, from our XPS data we can estimate an approximate OH surface coverage of 13%.

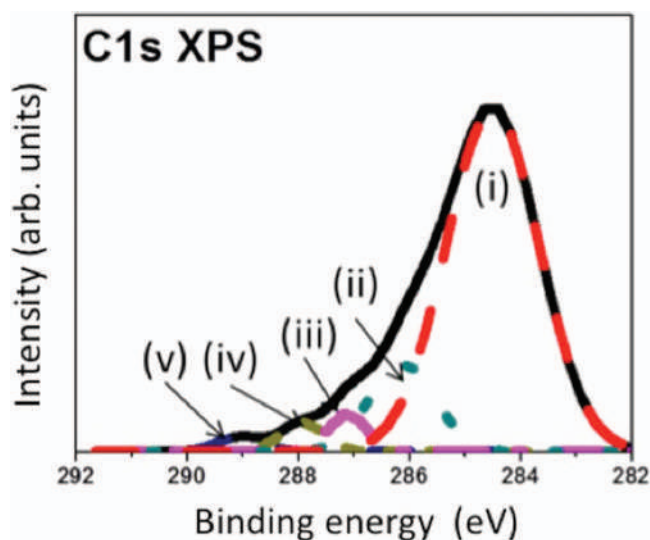


FIG. 2. XPS spectrum of the C(1s) line of OH-MWCNTs. The main peak located at 284.5 eV is deconvoluted into five peaks located at 284.5 eV (i), 285.7 eV (ii), 286.45 eV (iii), 288.2 eV (iv), and 290.5 eV (v).

#### D. Isotherms and BAM

OH-MWCNTs isotherms were obtained using ultra-pure water as a sub phase. Langmuir isotherms were measured in two different ways. In the first case, we performed independent experiments with different equilibration times of 0.5, 5.5, 6.5, and 7.5 h. In the second kind of experiments, we allow the sample for longer equilibration times of 12, 24, and 40 h. In Fig. 3, we show our data for the first set of experiments. The isotherm obtained at 0.5 h [Fig. 3(a)-i] shows a very low surface pressure which indicates that the OH-MWCNTs surface density remains quite low, a fact that is clearly reflected by the presence of small dot structures that move quickly in the corresponding BAM image shown in Fig. 3(b)-i. Significant surface pressure readings were typically obtained at 5.5 h together with a shift of the isotherm to higher areas, which implies that more OH-MWCNTs are diffusing from the bulk to the air/water interface and are being trapped by it. This behavior was also observed by Alvizo-Paez *et al.*<sup>5</sup> using nitrogen-doped carbon nanotubes. However, our diffusion

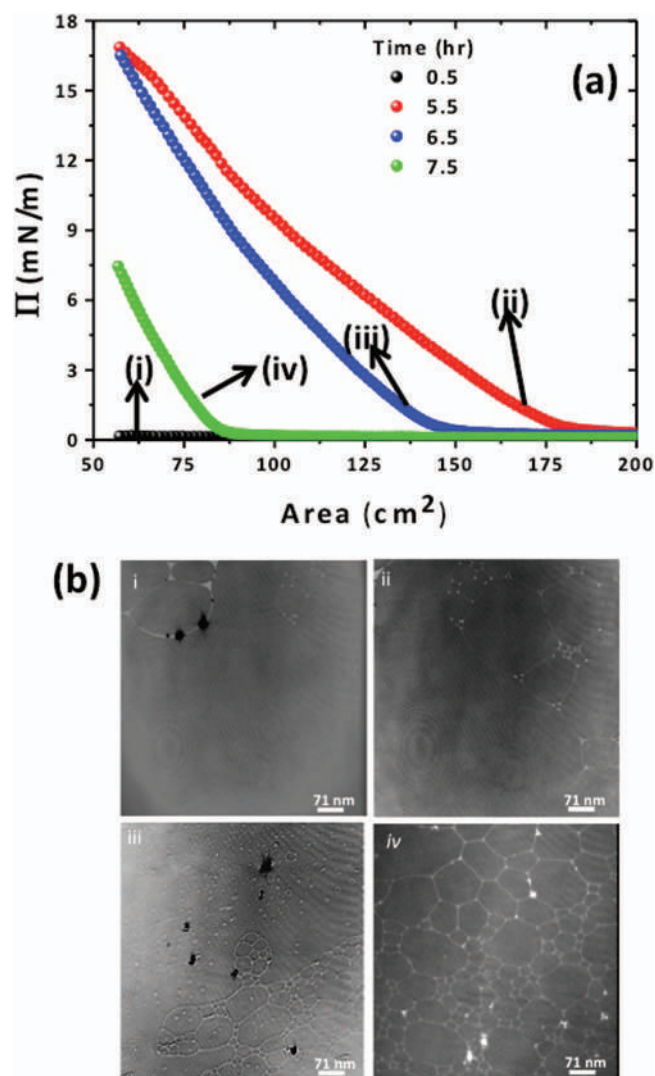


FIG. 3. (a) Langmuir isotherms for different evaporation solvent times from 0.5 (solid line), 5.5 (dotted line), 6.5 (dashed-dotted line), and 7.5 h (dashed line). (b) BAM images were taken as the isotherms recorded and are consistent with the compaction of the OH-MWCNTs at the air/water interface. The bar size is of 71 nm.

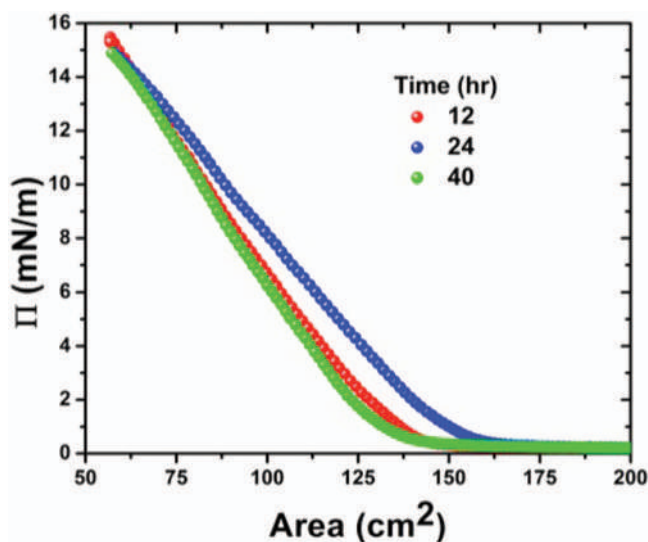


FIG. 4. Langmuir isotherms at repeated compression/expanded cycles for 50  $\mu\text{l}$  of hydroxylated carbon nanotubes measured at 12, 24, and 40 h after sample deposition.

times were shorter than those measured in Ref. 5, which possibly means that our samples are less hydrophilic and that the OH-MWCNTs are trapped more readily at the interface.

At longer equilibration times (6.5 and 7.5 h) and despite having more hydroxylated nanotubes at the air/water interface, we now note in Fig. 3(a) an isotherm shift to lower areas, as indicated by the position of isotherms *iii* and *iv*. This result can be explained if, when moving from isotherms *ii* to *iii*, we assume that OH-MWCNTs form more ordered phases. Actually, the corresponding BAM images presented in Fig. 3(b) reveal that this is indeed the case; when comparing images *i*–*iv* we clearly note, as time evolves, the gradual formation of more compact and structured nanotube arrays. We observe from Figs. 3(b)-*iii* and 3(b)-*iv* that the dominant mesostructure is a two-dimensional foam-like array made of nanotube rings of different sizes and symmetries. The formation of this type of foam-like mesostructures at the air/water interface has been already reported for several related systems, namely: in lipid Langmuir monolayers as well as charged colloidal particles,<sup>28,29</sup> which might indicate that the formation of foam-like configurations are mainly governed by the properties of the air/water interface itself and that slightly depend on the particular molecular system. The compression-expansion experiments at longer equilibration times (second set of experiments) shown in Fig. 4 reveal a similar isotherm behavior. From 12 to 24 h we note a shift on the  $\Pi$ - $A$  curve to higher areas but, from 24 to 40 h, the isotherm shifted back to lower values of  $A$ , almost to the same position as the isotherm obtained at 12 h. As in Fig. 3(a), this initial shift to higher areas could be due to an increase in the surface density of OH-MWCNTs. However, for longer equilibration times, we believe that there is a reorganization of the hydroxylated nanotubes at the interface, maintaining the surface density but forming more compact and rigid monolayers (as evidenced by the low compressibility of the samples).

Finally, Fig. 5 shows two typical BAM images of the foam-like structures stabilized at the air/water interface

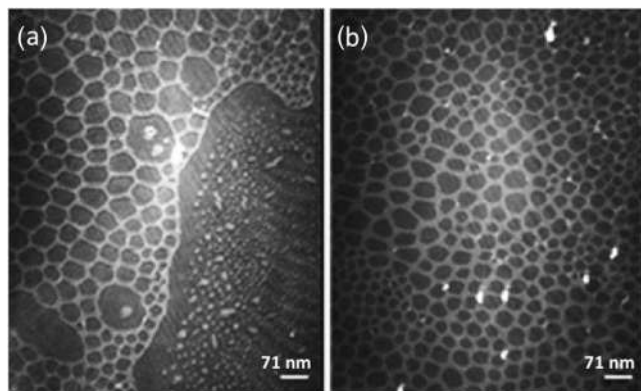


FIG. 5. BAM images of hydroxylated carbon nanotubes at different equilibration times. Formation of complex nanotube networks at the air/water interface for (a) 6 and (b) 12 h after sample deposition. The bar size is of 71 nm.

after allowing the sample to diffuse for 6 [Fig. 5(a)] and 12 [Fig. 5(b)] h. We observe again from both images the coexistence of a condensed phase and a gaseous phase. However, at 6 h [Fig. 5(a)] we appreciate, as an additional feature, the formation of a high density of white dots belonging to the condensed phase. Notice that these white dots are well separated from the foam-like structure which indicates, on the one hand, that there exist a strong repulsive interaction between these two types of nanotube conformations and, on the other hand, illustrates the richness of the nanotube-solvent and intertube interactions.

However, the presence of the 2D foam-like structure indicates that there is coexistence of phases, a condensed phase (the foam structure) and a low-density gas-like phase (the dark areas consisting mostly of bare water). When the gas phase is present, the surface pressure is normally very low, a few tens of a mN/m. However, note that the images shown in Fig. 5 were obtained at surface pressures of about 10 mN/m, which is inconsistent with the presence of the large amount of the gas phase that is observed in the BAM images. This could only mean that the foam-like structure is not highly compressed; that is, the cells walls of the foam structure present a resistance against compression. This could result from the inability of the carbon nanotubes to slide side by side smoothly as the film is compressed. This inability must come from the “friction” produced by the molecular islands of OH groups attached to the nanotubes predicted by our DFT calculations (see below). However, as time evolves the system relaxes, as it occurs in Figure 4, and in the next compression the surface pressure take-off area per molecule of the isotherm might move to lower areas. However, note that both Figures 3(b) and 5 show foam-like structures but the thickness of the cell walls are thicker and the foam cells are smaller in Figure 5, an observation that is consistent with the idea that, at longer times, more carbon nanotubes diffuse from the bulk to the air/water interface.

### E. Atomic force microscopy

This technique was employed to obtain a more precise geometrical characterization of the foam-like OH-MWCNTs mesostructures presented in Secs. III D. Fig. 6(a) shows a

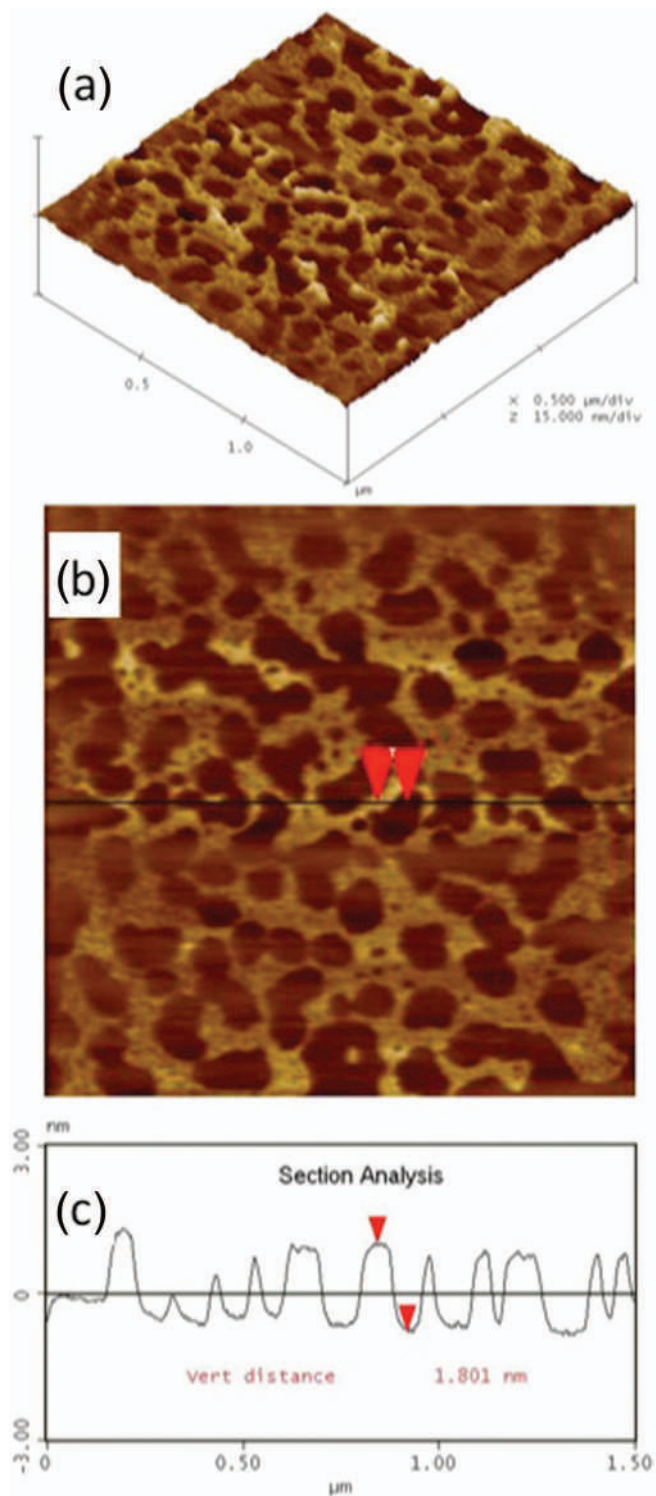


FIG. 6. Representative (a) 3D and (b) 2D images of a nanotube network transferred to a solid mica substrate. (c) Height profile where it is shown that the diameter of an isolated OH-MWCNT is of the order of 1.8 Å, very close to the value inferred from the Raman spectra of the samples.

representative three-dimensional view of a transferred OH-MWCNT film by using the Langmuir-Blodgett technique. The deposition on the mica substrate was realized for a surface pressure of 10 mN/m. In this particular case, we would like to remark that we were surprised to find the nanotube network shown in Figs. 6(a) and 6(b). Actually, at the previous

surface pressure conditions, the BAM images show the existence of a continuous film, being thus the foam-like nanotube array below the lateral resolution of the Brewster angle microscopy. Still, Figs. 6(a) and 6(b) are representative images of all our Langmuir-Blodgett transfer experiments and it is important to remark that the foam-like structures are robust enough to be transferred onto a solid substrate. In Fig. 6(c), we show a height profile for a well-defined region of the nanotube network [marked with arrows in Fig. 6(b)], revealing a maximum height of approximately 1.8 nm. The previous value is of the order of the nanotube diameter found by the Raman spectra of the samples, which is of the order of 2 nm.

## F. DFT studies

The hydroxylation of the external surface of MWCNTs performed in Sec. III A was of fundamental importance to obtain partially soluble OH-MWCNTs units at the air/water interface. The floating units were found to interact and link with each other forming extended foam-like carbon networks. The previous films were later on transferred onto a solid mica substrate, leading to the formation of robust nanotube arrays which are ready to be integrated in to various practical devices. Consequently, in order to understand the origin of the unexpected partial solubility of our OH-covered MWCNTs, we analyze the local structure and electronic properties of hydroxyl species adsorbed on model carbon nanotubes by performing extensive pseudo-potential DFT calculations.

In Fig. 7, we show first our optimized atomic configurations for a single and two OH molecules attached to a finite length (5,5) carbon nanotube. From Fig. 7(a), we obtain that one hydroxyl group is strongly bonded to the carbon surface with an adsorption energy of 2.17 eV and a C–OH bond length of 1.48 Å. In addition, we found a C–O–H angle of  $107^\circ$  and a nanotube  $\rightarrow$  OH charge transfer of  $0.17e$  (obtained within the Lowdin scheme), being originated by the large electronegativity of oxygen atoms. The strong interaction between the OH group and the nanotube surface is also reflected in the electronic structure of the system. Upon single OH adsorption, the energy difference between the highest occupied and lowest unoccupied molecular orbitals is  $\sim 0.6$  eV, which represents a notable reduction of the energy gap when compared with the value obtained in the bare  $C_{100}H_{20}$  structure (0.85 eV). Finally, we have analyzed, using the NEB methodology, the diffusion properties of the OH molecule on the nanotube surface. We calculate an energy barrier as the hydroxyl group moves from the on-top adsorption shown in Fig. 7(a), to an adjacent one, to be of the order of 1 eV. The previous energy value could imply that, in real systems, we will have strongly bound molecular species and the absence of uncontrolled diffusion caused by the available thermal energy.

In Figs. 7(b) and 7(c), we show our results for the adsorption of two OH groups. We consider two contrasting arrays, namely: hydroxyls attached as a pair of neighboring molecules on the same C–C bond [Fig. 7(b)] and as isolated species on the carbon network [Fig. 5(c)]. The former configuration is more stable than the latter by 0.8 eV. We found

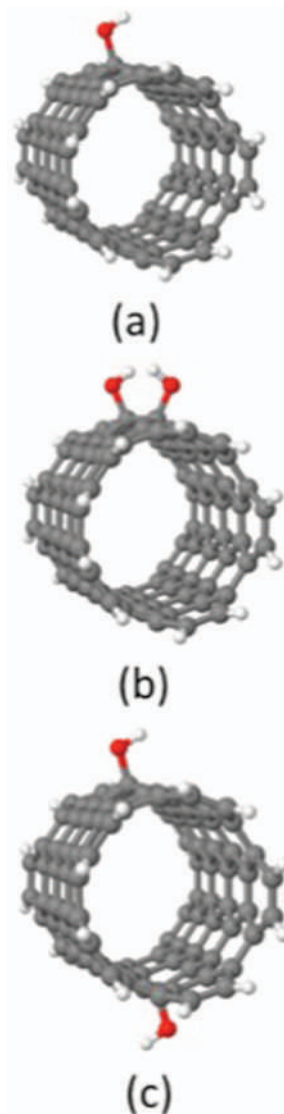


FIG. 7. Calculated low-energy atomic configurations for (a) the  $C_{100}H_{20}+OH$  structure as well as for (b) and (c) two isomers of the  $C_{100}H_{20}+(OH)_2$  nanotube compound.

C–OH bond lengths of  $\sim 1.45$  Å as well as C–O–H angles of  $\sim 107^\circ$ , being of the order of the ones obtained in the isolated case [Fig. 7(a)]. The two OH groups in Fig. 7(b) are attached to the carbon nanotube with an adsorption energy of 2.5 eV and receive a total charge of  $0.31e$ , a value that is notably increased when compared to the one obtained in Fig. 7(a). Interestingly, our here-obtained relative stability is in line with the experimental data reported by Meier and Kieguel<sup>31</sup> addressing the adsorption of two OH molecules on  $C_{60}$  (so-called fullerene diol), where the OH groups located in close proximity define the lowest energy atomic array. The high stability of the atomic configuration shown in Fig. 7(b) is also correlated with the values obtained for the diffusion energy barriers of the adsorbed hydroxyl species. In Fig. 8, we plot the diffusion path followed by one of the adsorbed OHs (marked with an arrow) belonging to the more stable structure shown in Fig. 7(b) (defined as Im1). In this case, the direct energy barrier  $E^{\ddagger}$  opposing a single molecular displacement is of the

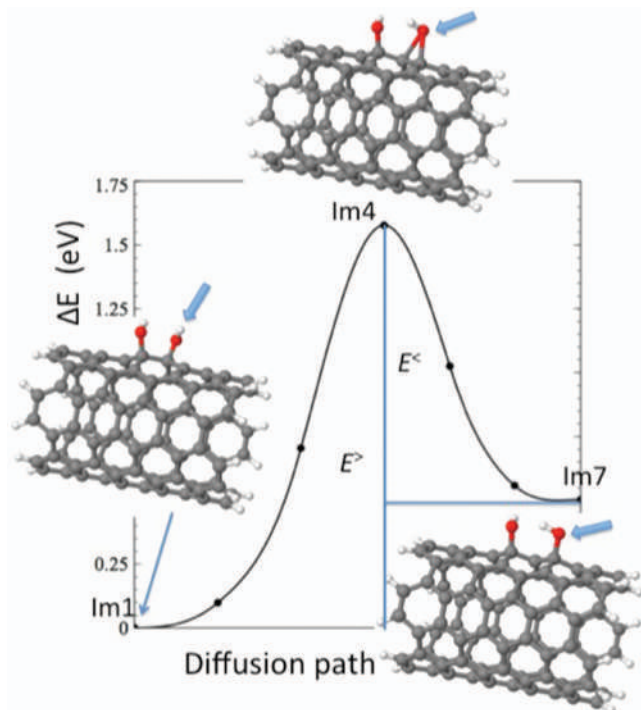


FIG. 8. Migration path connecting the stable atomic configuration for the  $C_{100}H_{20}+(OH)_2$  structure shown in Figure 5(b) (defined as Im1) with the one specified in the inset of the figure as Im7. The OH molecule involved in the diffusion process is marked with an arrow.

order of 1.6 eV. This value is considerably increased when compared to the one found for similar displacements of isolated OH species (1 eV), implying the formation of highly stable OH pairs. Furthermore, from Fig. 8 we also appreciate that the reverse energy barrier  $E^<$  is smaller and of the order of 1 eV. It is thus easier to form OH dimers on the nanotube surface rather than splitting the already formed hydroxyl pairs.

Guided by our compositional analysis we assume now a hydroxyl surface coverage of 10% and, in Fig. 9, we present our optimized atomic configurations for the  $C_{100}H_{20}+(OH)_{10}$  system. As is well known, the stability of molecular overlayers is the result of a complex balance between molecule-surface and molecule-molecule interactions, a balance which dictates the tendency towards the formation of ordered or disordered phases. Overlayers with different molecular structure are expected to have different physicochemical properties such as optical response or catalytic activity and, as a consequence, they can be spectroscopically distinguishable. Clearly, for our here-considered value of  $\theta = 0.1$  the number of possible adsorbed configurations considerably increases. However, it is not the purpose of our work to perform an extensive exploration of all resulting adsorbed arrays, but instead to try to reveal general tendencies concerning the OH–OH intermolecular interactions and stability of these compounds. As a general strategy, we will compare the properties of the more contrasting arrays, namely, a homogeneous distribution and an aggregated configuration of adsorbed OHs, also including adsorbed phases with different degrees of molecular clustering on the nanotube surface. We organize our optimized arrays from the most stable shown in Fig. 9(a) to the less stable structure presented in Fig. 9(d).

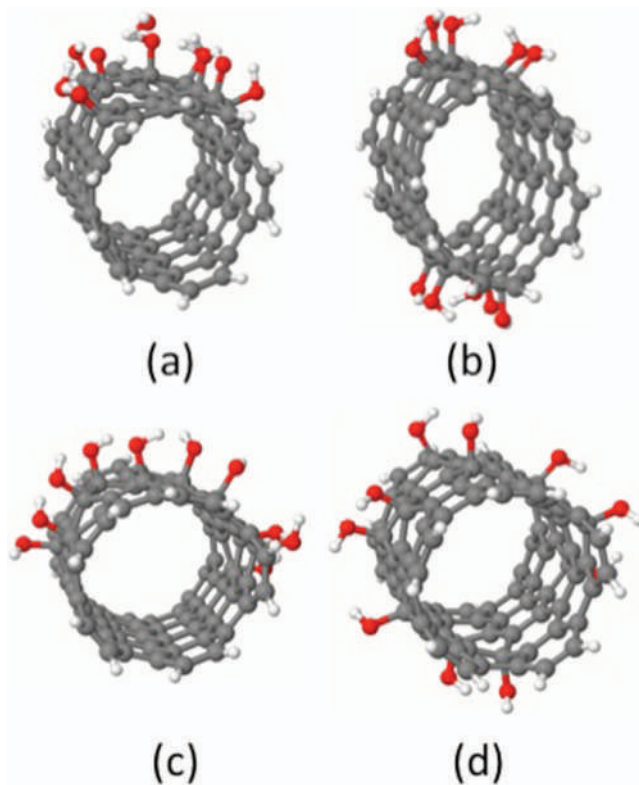


FIG. 9. (a)–(d) Calculated low-energy atomic configurations for various isomers of the  $C_{100}H_{20}+(OH)_{10}$  hydroxylated nanotube.

From the figure we note that low energy atomic configurations are found when the OH groups aggregate on the nanotube surface forming molecular islands of different sizes [Figs. 9(a)–9(c)] being characterized by robust hydrogen-bonded networks. In contrast, the (highly water soluble) uniform distribution of OH groups [Fig. 9(d)] is the less stable atomic configuration, differing by 3.4 eV when compared to the structure shown in Fig. 9(a). In Fig. 9(d), the relatively large distance between the chemisorbed hydroxyl molecules naturally excludes the formation of a hydrogen-bonding network on the carbon surface, increasing as a consequence the total energy of the system. Actually, when moving from Figs. 9(a)  $\rightarrow$  9(b)  $\rightarrow$  9(c)  $\rightarrow$  9(d), we obtain energy differences of 1.35  $\rightarrow$  0.96  $\rightarrow$  1.14 eV between neighboring isomers, clearly defining the preferred adsorbed arrays.

The patchy behavior characterizing the low energy adsorbed phases shown in Fig. 9 is expected to produce hydroxylated carbon nanotubes having reduced wettabilities, in line with our experimental observations, which could also be tested by performing contact angle experiments on the hydroxylated carbon nanotubes films. As in the previous cases, we found for the highly stable structure shown in Fig. 9(a) a total nanotube  $\rightarrow$  (OH)<sub>10</sub> charge transfer of  $2e$  while, for the random distribution of OH groups [Fig. 9(d)], we calculate a transferred charge of  $1.6e$ . The previous data could imply that OH overlayers with a higher degree of molecular clustering will be more negatively charged. In addition, our here-obtained nanotube  $\rightarrow$  (OH)<sub>n</sub> direction for the charge transfer leads to the existence of more hole carriers in the carbon structures, a fact that is expected to strongly change the transport



properties of the samples. Finally, we would like to comment that the contrasting adsorbed phases shown in Fig. 9 define the  $C_{100}H_{20}+(OH)_{10}$  complexes as very appropriate systems to analyze the role played by the London dispersion forces on the structure and energetics of our low hydroxylated nanotubes. We include the London correction as implemented in the Quantum-Espresso code and reoptimize all the atomic arrays shown in Fig. 9 (not shown). On the one hand, we obtain that the lowest energy atomic configuration is the same, with variations in the atomic positions as large as 0.1 Å and, on the other hand, we found that the adsorption energies increases by values as large as 0.2 eV but still, the energy ordering shown in Fig. 9 is maintained.

Following our previous results, it is clear that OH doping can be an effective mechanism for modifying the electronic properties of carbon nanotubes. In order to explore this further, we plot in Fig. 10 the average density of states (ADOS) of some representative hydroxylated carbon nanotubes. In Fig. 10(a), we show first the energy level distribution of the bare  $C_{100}H_{20}$  model structure and, in Figs. 10(b) and 10(c), we present the eigenvalue spectra for the optimized atomic configurations shown in Figs. 9(a) and 9(d), respectively. When comparing the three calculations we observe notable differences in the electronic spectra all along the energy range, but particularly in the location and degeneracy of the eigenvalues around the Fermi level,  $\epsilon_f$ . Notice that in the hydroxylated nanotubes a peak in the ADOS arises at  $\epsilon_f$ , being originated by the inclusion of the oxygen atoms in the carbon structure. The previous variations are expected to affect the optical spectra of the nanotubes since the different separation (and amount) of the energy levels might lead to a different distribution of electronic excitations. Additional calculations and experimental measurements are currently under way to explore the optical response of our hydroxylated carbon compounds. On the one hand, we believe that the absorption spectra could be used to distinguish tubes with specific OH attachments and, on the other hand, their optical response could define them as efficient donor (acceptor) components in the design of solar cell devices.

In order to further test the stability of our low energy atomic arrays shown in Fig. 9, we study again the migration properties of the chemisorbed OH groups. In Figs. 11(a) and 11(b), we plot, as representative examples, our calculated diffusion paths (using nine images) followed by two different hydroxyl groups (marked with arrows) belonging to the more stable structure shown in Fig. 9(a). The moving OHs are located in different positions in the molecular island and their energetics associated with the different displacements will help us to analyze the ability of hydroxyl species to cluster on the nanotube's surface. As already observed in Fig. 8 we notice from both calculations shown in Fig. 9 that moving hydroxyl groups away from the molecular island requires very high direct energy barriers,  $E^>$ , being of the order of 2.1 [Fig. 11(a)] and 1.6 [Fig. 11(b)] eV, implying the formation of robust OH aggregates on the nanotube surface. In contrast, the reverse energy barriers,  $E^<$ , are considerably smaller having values of 0.23 and 0.7 eV in Figs. 11(a) and 11(b), respectively. The previous reverse energy barriers clearly define, on the one hand, the clustering of the OH groups as effective

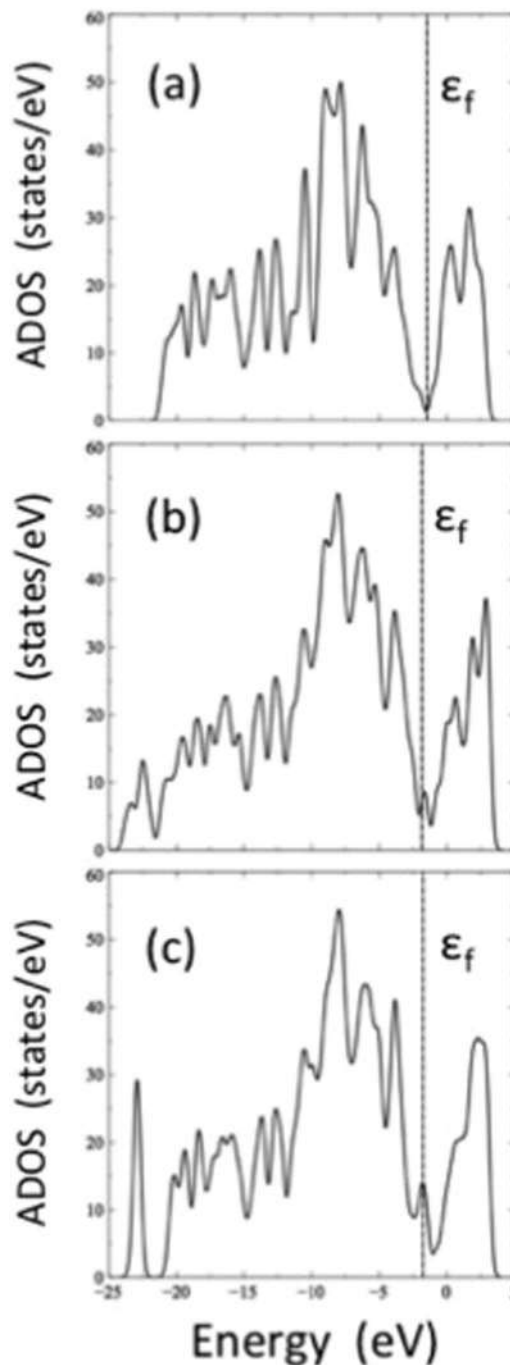


FIG. 10. Calculated average density of states (ADOS) for (a) the bare  $C_{100}H_{20}$  nanotube, as well as for the  $C_{100}H_{20}+(OH)_{10}$  hydroxylated nanotubes shown in (b) Figs. 7(a), 7(c), and 7(d). The Fermi energy is marked as a vertical line.

trapping centers for additional hydroxyl species located in close proximity and, on the other hand, the different values for  $E^<$  as a function of the local atomic environment might lead to a complex anisotropic island growth mode. Finally, we would like to emphasize that the properties of aggregated forms of hydroxylated carbon nanotubes, as the ones shown in Figs. 3 and 5, are also important to explore and define the following step in our study. Obviously, the implementation of DFT methods to determine the interaction mechanism between different hydroxylated carbon nanotubes would be

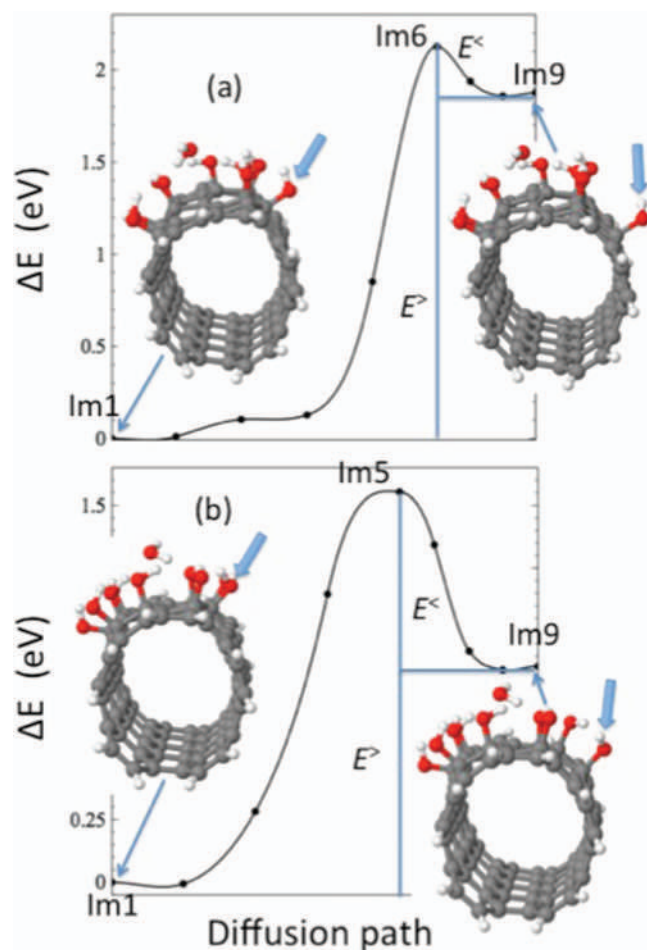


FIG. 11. In (a) and (b), we plot the migration paths connecting the stable atomic configurations for the  $C_{100}H_{20}+(OH)_{10}$  structure defined in the inset as Im1, with the one specified at the end of the paths labeled as Im9. In both cases, the OH molecule involved in the diffusion process is marked with an arrow.

computationally prohibited. In this sense, the use of continuum theoretical models<sup>32</sup> to analyze the energetics and mechanical stability in these kinds of systems becomes highly relevant. Calculations along this line of research are currently under way.

#### IV. CONCLUSIONS

In this work, we have presented a combined experimental and theoretical study dedicated to analyze the structure, electronic properties, and aggregation behavior of hydroxylated multiwalled carbon nanotubes (OH-MWCNT). In order to prove the carbon nanotubes functionalization, both FTIR and XPS measurements were performed in our samples, clearly revealing the identity of the molecular species present on the surface of our carbon nanostructures. Our synthesized OH-MWCNTs were found to be partially soluble at the air/water and the floating units interact and link with each other forming extended foam-like carbon networks. Surface pressure-area isotherms of the nanotube films are performed using the Langmuir balance method and reveal an interesting isotherm behavior, as well as the formation of complex nanotube patterns when varying the conditions of the compression/expansion

experiments. The OH-MWCNTs films are transferred into a mica substrate and atomic force microscopy images show that the foam like structure is still preserved and also reveals fine details of their microstructure. Our density functional theory calculations show that low energy atomic configurations are obtained when the OH groups form molecular islands on the nanotube's surface, which are expected to produce hydroxylated nanotubes having reduced wettabilities in line with our experimental observations. We have demonstrated that OH doping of CNTs can be an effective mechanism for modifying their electronic properties. Adsorption of OH species yields carbon nanotubes having small HOMO-LUMO energy gaps and generates a nanotube  $\rightarrow$  OH direction for the charge transfer leading to the existence of more hole carriers in the carbon structures. The previous results are expected to strongly alter the transport properties of our samples and define our synthesized OH-MWCNTs films as very promising carbon nanostructures for the development of novel materials and many engineering applications.

#### ACKNOWLEDGMENTS

The authors would like to acknowledge the financial support from CONACyT through Grant Nos. 169345, 164594, 131862, and 297004. Computer resources from the Acarus Supercomputer Center of the Universidad de Sonora, Sonora, México as well as from the Centro Nacional de Supercomputo (CNS) of the Instituto Potosino de Investigación Científica y Tecnológica (IPICYT), SLP, México are acknowledged. We also thank Emmanuel Vazquez-Martinez for his assistance in preparing the AFM images.

- <sup>1</sup>P. M. Ajayan and O. Z. Zhou, "Carbon nanotubes applications," *Top. Appl. Phys.* **80**, 391–425 (2001).
- <sup>2</sup>V. Datsyuk *et al.*, "Chemical oxidation of multiwalled carbon nanotubes," *Carbon* **46**, 833–840 (2008).
- <sup>3</sup>J. Kathi and K. Y. Rhee, "Surface modification of multi-walled carbon nanotubes using 3-aminopropyltriethoxysilane," *J. Mater. Sci.* **43**, 33–37 (2008); A. E. Cohen and L. Mahadevan, "Kinks, rings, and rackets in filamentous structures," *Proc. Natl. Acad. Sci. U.S.A.* **100**, 12141–12146 (2003); C. R. Chang, L. H. Lu, J. H. Liu, and W. Chen, "Ring formation mechanism of single-walled carbon nanotubes: Energy conservation between curvature elasticity and inter-tube adhesion," *Chem. Phys.* **393**, 123–128 (2012).
- <sup>4</sup>S. Shokooi, A. Arefazar, and R. Khosrokhavar, "Silane coupling agents in polymer-based reinforced composites: A review," *J. Reinforced Plast. Compos.* **27**, 473–485 (2008).
- <sup>5</sup>E. R. Alvizo-Paez *et al.*, "Transparent foamlike 2D networks of nitrogen-doped multiwalled carbon nanotubes obtained by self-assembly," *J. Phys. Chem. C* **115**, 11447–11452 (2011); J. L. Hernández-López *et al.*, "Trapping, pattern formation and ordering of polyelectrolyte/single-wall carbon nanotube complexes at the air/water and air/solid interfaces," *J. Phys. Chem. B* **110**, 23179–23191 (2006).
- <sup>6</sup>J.-H. Lee *et al.*, "Wear properties of 3-aminopropyltriethoxysilane-functionalized carbon nanotubes reinforced ultra high molecular weight polyethylene nanocomposites," *Polym. Eng. Sci.* **50**, 1433–1439 (2010).
- <sup>7</sup>M. Lavorgna *et al.*, "Silanization and silica enrichment of multiwalled carbon nanotubes: Synergistic effects on the thermal-mechanical properties of epoxy nanocomposites," *Eur. Polym. J.* **49**, 428–438 (2013).
- <sup>8</sup>A. Cao *et al.*, "Super-compressible foamlike carbon nanotube films," *Science* **310**, 1307–1310 (2005).
- <sup>9</sup>M. C. Hermant *et al.*, "The incorporation of single-walled carbon nanotubes into polymerized high internal phase emulsions to create conductive foams with a low percolation threshold," *Compos. Sci. Technol.* **69**, 656–662 (2009).

- <sup>10</sup>M. Nabeta and M. Sano, "Nanotube foam prepared by gelatin gel as a template," *Langmuir* **21**, 1706–1708 (2005).
- <sup>11</sup>M. A. Worsley *et al.*, "Carbon scaffolds for stiff and highly conductive monolithic oxide-carbon nanotube composites," *Chem. Mater.* **23**, 3054–3061 (2011).
- <sup>12</sup>X.-J. Huang *et al.*, "Wet chemical needlelike assemblies of single-walled carbon nanotubes on a silicon surface," *Langmuir* **23**, 991–994 (2007).
- <sup>13</sup>Y. Chen and J. Zhang, "Diameter controlled growth of single-walled carbon nanotubes from SiO<sub>2</sub> nanoparticles," *Carbon* **49**, 3316–3324 (2011).
- <sup>14</sup>C. Kirchner *et al.*, "Cytotoxicity of colloidal CdSe and CdSe/ZnS nanoparticles," *Nano Lett.* **5**, 331–338 (2005).
- <sup>15</sup>G. Wang *et al.*, "Electrostatic-gated transport in chemically modified glass nanopore electrodes," *J. Am. Chem. Soc.* **128**, 7679–7686 (2006).
- <sup>16</sup>L. Vast *et al.*, "Chemical functionalization by a fluorinated trichlorosilane of multi-walled carbon nanotubes," *Nanotechnology* **15**, 781 (2004).
- <sup>17</sup>F. Irani, A. Jannesari, and S. Bastani, "Effect of fluorination of multiwalled carbon nanotubes (MWCNTs) on the surface properties of fouling-release silicone/MWCNTs coatings," *Prog. Org. Coat.* **76**, 375–383 (2013).
- <sup>18</sup>B. Ghiadi *et al.*, "Rapid, one-pot synthesis of highly-soluble carbon nanotubes functionalized by L-arginine," *Russ. J. Phys. Chem. A* **87**, 649–653 (2013).
- <sup>19</sup>D. Rosenthal *et al.*, "Combined XPS and TPD study of oxygen-functionalized carbon nanofibers grown on sintered metal fibers," *Carbon* **48**, 1835–1843 (2010).
- <sup>20</sup>C. Velasco-Santos *et al.*, "Improvement of thermal and mechanical properties of carbon nanotube composites through chemical functionalization," *Chem. Mater.* **15**, 4470–4475 (2003).
- <sup>21</sup>M. Gnyba *et al.*, "Raman investigation of minor component reaction during polymer synthesis process," *Proc. SPIE* **5258**, 182–185 (2003).
- <sup>22</sup>I. Simkiene *et al.*, "Hybrid system of iron porphyrin on aminosilanized c-Si," *Photon. Nanostruct. – Fundam. Appl.* **5**, 129–135 (2007).
- <sup>23</sup>S. Pruneanu *et al.*, "Self-assembly of DNA-templated polypyrrole nanowires: Spontaneous formation of conductive nanopores," *Adv. Funct. Mater.* **18**, 2444–2454 (2008).
- <sup>24</sup>S. Gan, P. Yang, and W. Yang, "Photoactivation of Alkyl C–H and silanization: A simple and general route to prepare high-density primary amines on inert polymer surfaces for protein immobilization," *Biomacromolecules* **10**, 1238–1243 (2009).
- <sup>25</sup>A. C. Zaman *et al.*, "OH and COOH functionalized single walled carbon nanotubes-reinforced alumina ceramic nanocomposites," *Ceram. Int.* **38**, 1287–1293 (2012).
- <sup>26</sup>R. H. Bradley *et al.*, "Surface studies of hydroxylated multi-wall carbon nanotubes," *Appl. Surf. Sci.* **258**, 4835–4843 (2012).
- <sup>27</sup>P. Giannozzi *et al.*, "QUANTUM ESPRESSO: a modular and open-source software project for quantum simulations of materials," *J. Phys.: Condens. Matter* **21**, 395502 (2009).
- <sup>28</sup>J. P. Perdew, K. Burke, and M. Ernzerhof, "Generalized gradient approximation made simple," *Phys. Rev. Lett.* **77**, 3865–3868 (1996).
- <sup>29</sup>G. Henkelman, B. P. Uberuaga, and H. Jonsson, "A climbing image nudged elastic band method for finding saddle points and minimum energy paths," *J. Chem. Phys.* **113**, 1–4 (2000).
- <sup>30</sup>X.-L. Ling *et al.*, "Preparation and characterization of hydroxylated multi-walled carbon nanotubes," *Colloids Surf. A* **421**, 9–15 (2013).
- <sup>31</sup>M. S. Meier and J. Kiegiel, "Preparation and characterization of the fullerene diols 1,2-C<sub>60</sub>(OH)<sub>2</sub>, 1,2-C<sub>70</sub>(OH)<sub>2</sub> and 5,6-C<sub>70</sub>(OH)<sub>2</sub>," *Org. Lett.* **3**, 1717–1719 (2001).
- <sup>32</sup>J. Zhao *et al.*, "A theoretical analysis of cohesive energy between carbon nanotubes, graphene, and substrates," *Carbon* **57**, 108–119 (2013); "Binding energy and mechanical stability of single- and multi-walled carbon nanotube serpentines," *J. Chem. Phys.* **140**, 204704 (2014).



# Chunking dynamics: heteroclinics in mind

Mikhail I. Rabinovich<sup>1</sup>, Pablo Varona<sup>2\*</sup>, Irma Tristan<sup>1</sup> and Valentin S. Afraimovich<sup>3</sup>

<sup>1</sup> BioCircuits Institute, University of California, San Diego, La Jolla, CA, USA

<sup>2</sup> Grupo de Neurocomputación Biológica, Departamento de Ingeniería Informática, Escuela Politécnica Superior, Universidad Autónoma de Madrid, Madrid, Spain

<sup>3</sup> Instituto de Investigación en Comunicación Óptica, Universidad Autónoma de San Luis Potosí, San Luis Potosí, México

## Edited by:

Tobias Alecio Mattei, Ohio State University, USA

## Reviewed by:

Maurizio Mattia, Istituto Superiore di Sanità, Italy

Hiroshi Okamoto, RIKEN Brain Science Institute, Japan

## \*Correspondence:

Pablo Varona, Grupo de Neurocomputación Biológica, Departamento de Ingeniería Informática, Escuela Politécnica Superior, Universidad Autónoma de Madrid, C/Francisco Tomás y Valiente, 11, 28049 Madrid, Spain  
e-mail: pablo.varona@uam.es

Recent results of imaging technologies and non-linear dynamics make possible to relate the structure and dynamics of functional brain networks to different mental tasks and to build theoretical models for the description and prediction of cognitive activity. Such models are non-linear dynamical descriptions of the interaction of the core components—brain modes—participating in a specific mental function. The dynamical images of different mental processes depend on their temporal features. The dynamics of many cognitive functions are transient. They are often observed as a chain of sequentially changing metastable states. A stable heteroclinic channel (SHC) consisting of a chain of saddles—metastable states—connected by unstable separatrices is a mathematical image for robust transients. In this paper we focus on hierarchical chunking dynamics that can represent several forms of transient cognitive activity. Chunking is a dynamical phenomenon that nature uses to perform information processing of long sequences by dividing them in shorter information items. Chunking, for example, makes more efficient the use of short-term memory by breaking up long strings of information (like in language where one can see the separation of a novel on chapters, paragraphs, sentences, and finally words). Chunking is important in many processes of perception, learning, and cognition in humans and animals. Based on anatomical information about the hierarchical organization of functional brain networks, we propose a cognitive network architecture that hierarchically chunks and super-chunks switching sequences of metastable states produced by winnerless competitive heteroclinic dynamics.

**Keywords:** cognitive dynamics, stable heteroclinic channel, transient dynamics, low dimensionality of brain activity, hierarchical sequences, chunking and superchunking, cognition modeling principles

## INTRODUCTION

Chunking is a dynamical phenomenon that the brain uses for processing long informational sequences. The concept of chunk was introduced by Miller (1956). His key notion is that short-term storage is not rigid but amenable to strategies such as chunking that can expand its capacity. Miller's work drew plenty of attention to the concept of short-term memory and its functional characteristics. Chunking involves two processes: concatenation of units in a block and segmentation of the blocks. In general, chunking is related to the hierarchical organization of perceptual, cognitive, or behavioral sequential activity. In particular, in motor control (see Rosenbaum et al., 1983) sequences can consist of sub-sequences and these can in turn consist of sub-sub-sequences, etc. The natural hierarchical organization of long sequences is a result of the activity of specific brain functional networks. Such networks include many different brain areas and some of them are also organized in a hierarchical manner. A well-known example is Broca's area that has been suggested to act as a "supramodal syntactic processor," able to process any type of hierarchically organized sequences (Grossman, 1980; Tettamanti and Weniger, 2006), a hypothesis based on the findings that this region is not only involved in processing language syntax (Musso et al., 2003), but also in syntax like aspects of non-linguistic tasks, for example, the performance of specific movements and music (Fadiga

et al., 2009) as several fMRI studies (Bahlmann et al., 2008, 2009) seem to confirm. Clerget et al. hypothesize that motor behavior shares some similarities with language (Clerget et al., 2013), namely that a complex action can be viewed as a chain of subordinate movements, which need to be combined according to certain rules in order to reach a given goal (Dehaene and Changeux, 1997; Dominey et al., 2003; Botvinick, 2008).

What are the mechanisms that transform the extremely complex, noisy, and many-dimensional brain activity into a rather regular, low-dimensional, and even predictable cognitive behavior, e.g., what are the mechanisms underlying the dynamics of the mind, including chunking? This is one of the most challenging questions in today's neuro- and cognitive science. Recent continuous advances in non-invasive brain imaging allow assessing the structural connectivity of the brain and the corresponding evolution of the spatio-temporal activity in detail.

In our view, metastability is a key element of transient cognitive dynamics participating in chunking processes. The idea of the spatiotemporal organization of brain dynamic activity through transient, metastable states emerged more than 15 years ago (Kelso, 1995; Friston, 1997). According to this scenario, such dynamics can be represented as a sequential switching between different metastable states (for a description of the mathematical basis of this scenario see Rabinovich et al., 2008a,b). Metastable

transient dynamics represent a balance between the segregation of focused cognitive processing and the flexible integration of distributed brain areas. Such integration is necessary for the performance of a specific cognitive function (Bressler and Kelso, 2001; Meehan and Bressler, 2012). The existence of connections that are prevalent over long periods of time supports the well-regarded concept of a hierarchical organization of neural processing (Engel et al., 2001), which is the basis for the understanding of the origin of the chunking dynamics. Because the dimensionality of cognition depends on the number of activated (in contrast to the potentially observable) metastable states, it is important to remember that the brain chooses the necessary metastable states and suppresses those which are irrelevant to the goal of the cognitive process, resulting in a reduced dimensionality. The low-dimensionality of brain cognitive dynamics is based on two important issues: first, the manner of the cognitive task encoding—an external or internal stimulus determining a specific cognitive task excites a set of elements of the community networks which are responsible for the performance of such cognitive activities; and second, the existence of a specific hierarchical organization of the global brain networks that operate for the performance of a specific cognitive task by a moderate number of brain modes.

Based on experimental data suggesting that the processing of sequential cognitive activity on computational grounds is implemented in the brain by spatiotemporally pattern dynamics (see also Sahin et al., 2009), we build here a general dynamical model that produces hierarchical chunking of sequences, which suggests a plausible neural mechanism of chunking dynamics in the brain. This model is reasonably low-dimensional, which allows a detailed dynamical analysis.

## MATERIALS AND METHODS

A top-down approach to model transient cognitive dynamics taking into account the experimental observations described in the introduction is to use kinetic equations for the description of spatiotemporal mental modes that contain the discussed metastable states as equilibrium points. The set of brain patterns that sequentially change in the process of the cognitive task performance determine the spatial structure of the modes and the associated connection matrix among them. Using such type of models we can integrate our knowledge about the description of brain activity based on these new ideas related to heteroclinic sequences and their interactions, i.e., heteroclinic networks.

As a top-down departing point, we need a mathematical object that can describe robust transient dynamics and their associated information processing. Once we have this object, we can implement it through a set of canonic equations that can be used to study transient activity at different brain description levels, and in particular to address chunking dynamics. A mathematical image of robust transient sequential dynamics must have two principal features. First, it must be resistant to noise and reliable even in the context of small variations in initial conditions, so that the succession of states visited by the system (its trajectory, or transient) is stable. Second, the transients must be input-specific to contain information about what caused them. These are two fundamental contradictions regarding the use of transient dynamics

for the description of brain activity. Transient dynamics are inherently unstable: any transient depends on initial conditions and cannot be reproduced from arbitrary initial conditions. On the other hand, dynamical robustness in principle prevents sensitivity to informative perturbations. These contradictions can be solved through the concept of metastability, which was introduced to cognitive science at the end of the last century (Kelso, 1995; Friston, 1997, 2000; Fingelkurts and Fingelkurts, 2006; Oullier and Kelso, 2006; Gros, 2007; Ito et al., 2007).

A stable heteroclinic channel (SHC) is a mathematical object that meets the above discussed requirements, which can implement such stable transients. A SHC is defined by a sequence of successive metastable “saddle” states that are connected by separatrices. Under proper conditions, all the trajectories in the neighborhood of these saddle metastable states that form the chain remain in the channel, ensuring robustness and reproducibility over a wide range of control parameters (Rabinovich et al., 2008b). The stability of a channel means that trajectories in the channel do not leave it until the end of the channel is reached.

A simple model to implement SHCs is a generalized Lotka–Volterra equation with  $N$  interactive elements:

$$\frac{dA_i(t)}{dt} = A_i(t)F\left(\sigma_i(S_k) - \sum_{j=1}^N \rho_{ij}A_j(t)\right) + A_i(t)\eta_i(t)$$

$$i = 1, \dots, N \quad (1)$$

where  $A_i(t) \geq 0$  is the activity rate of element  $i$ ,  $\sigma_i$  is the gain function that controls the impact of the stimulus,  $S_k$  is an environmental stimulus,  $\rho_{ij}$  determines the interaction between the variables,  $\eta_i$  represents the noise level, and  $F$  is a function, in the simplest case a linear function. The state portrait of the system often contains a heteroclinic sequence linking saddle points. These saddles can be interpreted as successive and temporary winners in a never-ending competitive game, i.e., winnerless competition (WLC) dynamics (Rabinovich et al., 2001, 2006). In neural systems, because a representative model must produce sequences of connected neuronal population states (the saddle points), the neural connectivity  $\rho_{ij}$  must be asymmetric, as determined by the theoretical examination of this model (Huerta and Rabinovich, 2004). Although many connection statistics probably work for stable heteroclinic-type dynamics, it is likely that connectivity within biological networks is, to some extent at least, the result of optimization by evolution and synaptic plasticity. It is important to emphasize that Equation (1) is just an elementary building block for different levels of the chunking hierarchy that we will describe below.

Models like the generalized Lotka–Volterra equations allow establishing the conditions necessary for transient stability, and display stable, sequential, and cyclic activation of its components, the simplest variant of WLC. A network with several degrees of freedom and asymmetric connections can generate structurally stable sequences—transients, each shaped by one input. Asymmetric inhibitory connectivity helps to solve the apparent paradox that sensitivity and reliability can coexist in a network (Huerta and Rabinovich, 2004; Nowotny and Rabinovich, 2007; Rabinovich et al., 2008b; Rabinovich and Varona, 2011). The

neurons or modes participating in a SHC are assigned by the stimulus, by virtue of their direct and/or indirect input from the neurons activated by that stimulus. The joint action of the external input and a stimulus-dependent connectivity matrix defines the stimulus-specific heteroclinic channel. In addition, asymmetric inhibition coordinates the sequential activity and keeps a heteroclinic channel stable.

The WLC concept is directly related to the sequential dynamics of metastable states that are activated by inputs that do not destroy the origin of a competitive process. This paradigm can explain and predict many dynamical phenomena in neural networks with excitatory and inhibitory synaptic connections. Based on the requirement of the stability, this formalism has been used (i) to assess the dynamical origin of finite working memory (WM) capacity based upon WLC amongst available informational items (Bick and Rabinovich, 2009; Rabinovich et al., 2012); (ii) to build a dynamical model of information binding for transients that can describe the interaction of different sensory information flows that are generated concurrently (Rabinovich et al., 2010a); (iii) to model the sequential interaction between emotion and cognition (Rabinovich et al., 2010b); (iv) to represent attention dynamics (Rabinovich et al., 2013); and (v) to assess the dynamics of pathological states in mental disorders (Bystritsky et al., 2012; Rabinovich et al., 2013). Here we focus on a model of hierarchical chunking dynamics that can represent several forms of cognitive activity such as WM and speech construction.

As we discussed in the Introduction, chunking is grouping or categorizing related issues or information into smaller, most meaningful and compact units. Think about how hard it would be to read a long review paper without chapters, subchapters, paragraphs, and separated sentences. Chunking is a naturally occurring process that can be actively used to break down problems in order to think, understand, and make improvisation more efficiently. This is because it is easier to process chunked tasks or perceptual data. In particular, it is much easier to learn and recall such data. Mathematically, the “chunking principle” can be viewed as the transformation of a chain of metastable states along a transient process to the chain of groups of such states. It is a key dynamical idea that nature may use to make cognitive information processing more effective in the context of a complex environment.

Chunking processes in human perception, learning, and performance of a cognitive task can be both automatic and directly linked to the environmental stimuli, and controllable by a goal-oriented intrinsic signal (Gobet et al., 2001). It is important to note that chunking is a strategy that supports increasing speed and accuracy through the formation of hierarchical memory structures and complex task-dependent behavioral sequences. Two competitive processes form temporal chunking sequences—one separates long sequences into shorter groups of information items to be easily performed, and the second connects them to express a long sequence as a unified thought or behavioral action (Friederici et al., 2011; Chekaf and Matha, 2012).

Hierarchical chunking dynamics can be implemented in a model of cognitive networks whose information processing relies on SHCs. **Figure 1** illustrates a chunking heteroclinic cognitive network for two hierarchical informational groups—elementary

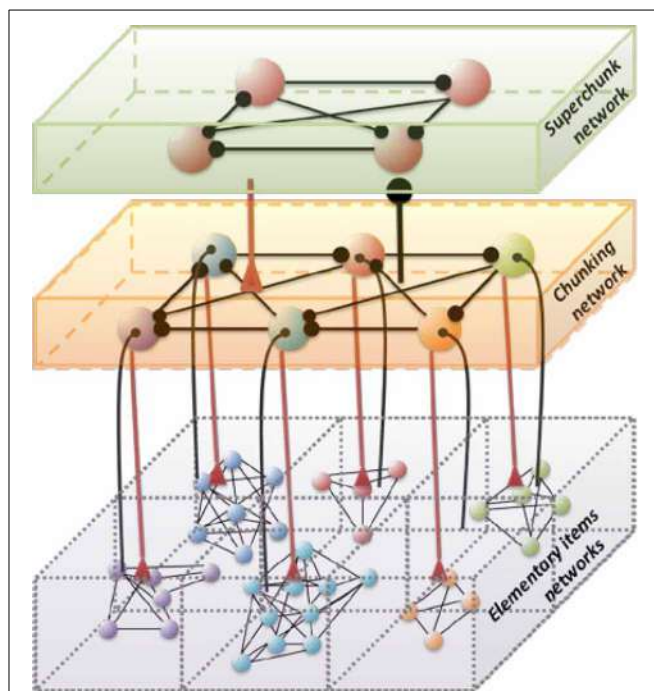


**FIGURE 1 | Architecture of the three level cognitive network responsible for the grouping of informational items.** Each level of hierarchy is described by its own Lotka–Volterra type Equations (see 2–6) with connection matrices  $\rho$ ,  $\xi$  and  $\zeta$ . Black circles represent inhibitory connections; triangles represent excitatory connections responsible for the choosing of the informational items or units (metastable states). Spheres represent the informational items or units (metastable states). Different colors indicate different chunks. All connections inside the elementary items are inhibitory.

items and chunking (integrated) informational items including many elementary units interacting through dynamical connections. It is reasonable to hypothesize that functionally there are two different cognitive networks from at least two different hierarchical levels that are responsible for the: (i) organization of the sequence of items inside chunks, and (ii) the formation of the chunk sequence. In particular, this hypothesis is supported by an experiment with chunking during visuomotor sequence learning (Sakai et al., 2003). It has been shown that each motor cluster is processed as a single memory unit—a chunk. A learned visuomotor sequence is a sequence of chunks that contains several elementary movements. The authors of this work have shown that a key role in the process of chunking formation is played by a brain network including the dominant parietal area, the basal ganglia, and the presupplementary motor area (see also Ribas-Fernandes et al., 2011 and Bor and Seth, 2012, where authors discuss the chunking structure of conscious processes).

Below we suggest a three level hierarchical model for the description of the chunking dynamics. Inhibition plays a key role in this model as is responsible for the execution of three functions: (i) competition between elementary informational items in order to produce stable sequences of metastable states, (ii) generation of the chunking sequence, and (iii) control of the performance of the sequential task. In recent years, the investigation of the hierarchical control between different levels of representation and

information processing has become one of the hot subjects in cognitive science. This issue is important for understanding how the mind controls behavior and itself. In particular, the relationship between chunking (a sequence-level process) and task-set inhibition (a task-level process) in the performance of task sequences was investigated in (Koch et al., 2006; Schneider, 2007; Li et al., 2010), for a description of “chunks of chunks”—“superchunks” see Rosenberg and Feigensohn (2013).

To understand the emergence of hierarchical chunking dynamics in a model we need to depart from Equation (1) in the following direction, c.f. **Figure 1**):

$$\dot{X}_i^{lk} = X_i^{lk} \left( \sigma_i^{lk}(S, C) \cdot Y^{lk} - \sum_j \rho_{ij}^{lk}(S, C) X_j^{lk} \right) \quad (2)$$

$$\tau \dot{Y}^{lk} = Y^{lk} \left( \left( V^l - \beta(C) \sum_i X_i^{lk} \right) - Z^{lk} \right) \quad (3)$$

$$\theta(C) \dot{Z}^{lk} = \sum_m \xi_i^{km}(S, C) Y^{lm} - Z^{lk} \quad (4)$$

$$T \dot{V}^l = V^l \left( \left( 1 - \delta(C) \sum_j Y^{lj} \right) - W^l \right) \quad (5)$$

$$\Theta(C) \dot{W}^l = \sum_q \zeta^{lq}(S, C) V^q - W^l \quad (6)$$

Here  $X_i^{lk}$  characterizes the  $i$ -th informational item associated with the  $k$ -th chunk and  $l$ -th superchunk,  $\sigma_i^{lk}(S, C)$  is the growth rate for each informational item determined by the stimulus  $S$  and the cognitive task  $C$ , and  $\rho_{ij}^{lk}(S, C)$  is the matrix of inhibitory connections among basic informational items. In this model  $Y^{lk}$  characterizes the  $k$ -th chunk associated to the  $l$ -th superchunk  $V^l$ , with corresponding characteristic times  $\tau$  and  $T$ , respectively, and  $\beta(C)$  represents the strength of the inhibition between the informational items and the chunk, and  $\delta(C)$  between the chunks and the superchunk. Also,  $Z^{lk}$  describes the synaptic dynamics for the  $k$ -th chunk associated to the  $l$ -th superchunk with  $\xi_i^{km}(S, C)$ , the matrix of inhibitory connections between chunks (black circles in **Figure 1**); and  $W^l$  describes the synaptic dynamics for the  $l$ -th superchunk with  $\zeta^{lq}(S, C)$ , the matrix of inhibitory connections between superchunks, the corresponding characteristic times are  $\theta(C)$  and  $\Theta(C)$ . In this model,  $\beta(C)$  and  $\delta(C)$  are adaptation parameters that determine the timing relationship between a basic informational chain and the chunking and superchunking modulation. The chunking variables also satisfy the generalized Lotka–Volterra—canonic equations which allows them to form a stable sequence. Because of this, in fact, chunking variables play the role of cognitive controllers. The parameters for Equations (3)–(5) in the simulations below were chosen with this scope. Since chunking dynamics has to take into account of the characteristic time of the chunk formation, the competition between different chunks has to be delayed—we used for this an inhibition described by a first order kinetic model. At the same time,

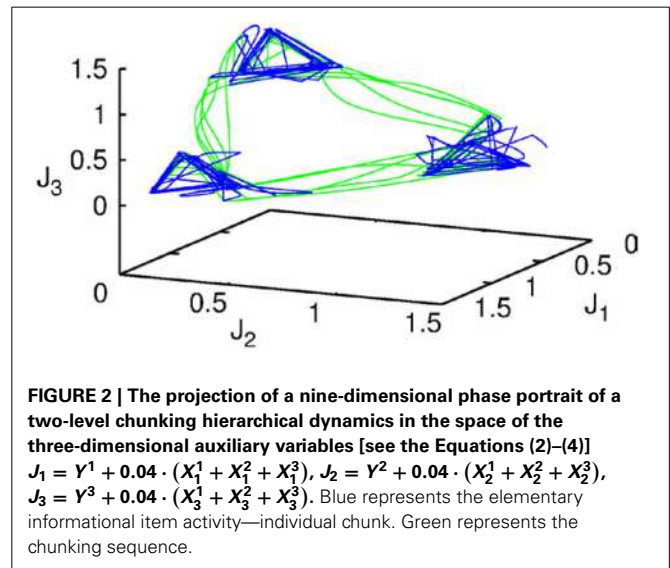
the competition among elementary informational items is implemented by fixed weight  $\rho_{ij}$  instantaneous synapses. The same logic has been applied for the description of the highest level of the hierarchy—the superchunks.

### RESULTS: HIERARCHICAL SEQUENCES—CHUNKING AND SUPER-CHUNKING

Let us first represent the phase portrait of a simple two-level chunking dynamics. We carried out numerical simulations of the model for the dynamics within chunks of informational items for the following parameters  $N^k = 3$ ,  $M = 3$  (number of “chunks” or “episodes”),  $\sigma^1 = [7.24, 5.85, 8.30]$ ,  $\sigma^2 = [9.93, 6.00, 5.18]$ ,  $\sigma^3 = [8.29, 7.86, 9.16]$ , and given these values,  $\rho_{ii}^k = 1.0$ ,  $\rho_{i_n-i_{i_n}}^k = \frac{\sigma_{i_n}^k}{\sigma_{i_n}^k} + 0.51$ , and  $\rho_{i_n+i_{i_n}}^k = \frac{\sigma_{i_n+1}^k}{\sigma_{i_n}^k} - 0.5$ ,  $i = 1, \dots, N^k$ ,  $k = 1, \dots, M$  as well as the parameters considered for the synaptic dynamics described by Equations (3) and (4):  $\tau = 0.7$ ,  $\theta = 2.0$ ,  $\xi^{kk} = 1.0$ ,  $\xi^{k_n k_{n+1}} = 1.4$  and  $\xi^{k_n k_{n-1}} = 0.5$ ,  $k = 1, \dots, M$  and  $\beta = 0.01$ . The results of these simulations are shown in **Figures 2, 3**.

**Figure 2** shows the phase portrait of the chunking dynamics when the superchunk formation is absent: the system is described by Equations (2)–(4),  $V = 1$ . This example illustrates a closed chunking sequence (green) that consists of several heteroclinic cycles that represent the elementary chunks (blue). In general, the number of elementary items in each chunk are different and the chunking sequence can be open.

**Figure 3** illustrates the timing between chunks along the sequence. The emergence of the chunking sequence shown in **Figure 2** is the result of a modulational instability in the two-level hierarchical network whose dynamics is described by Equations (2)–(4). This instability is oscillatory. The characteristic period of the oscillation is  $\Delta T$ . The analytical investigation of the dependence of  $\Delta T$  on the control parameters  $\tau$ ,  $\theta$ ,  $\beta$  and connection matrices  $\rho$ ,  $\xi$  is a non-realistic problem because of the non-linear feedback between the dynamical variables  $X$  and  $Y$ . However, it is reasonable to think that the key parameter in this problem is



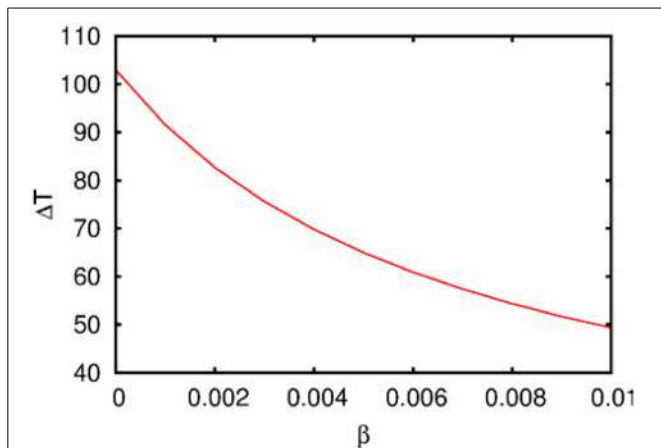


**FIGURE 3 | The dependence of the chunking interval timing [see Equation (1)] on the control parameter  $\beta$ .** One can see that the chunking interval strongly decreases together with the increasing of the adaptation parameter  $\beta$ . When  $\beta$  increases the effective excitation of variable  $Y$  decreases.

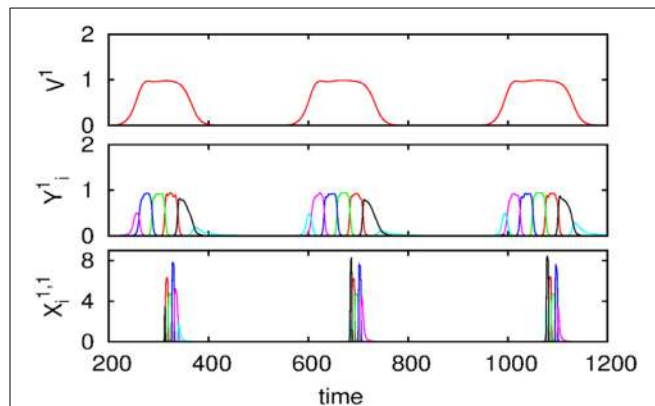


**FIGURE 4 | Time series of the sequences of the three-level hierarchy—108 items grouped in 18 chunks of 6 items; these chunks form 3 superchunks of 6 elements each displaying reproducible dynamics according to the model (2)–(6).** Different colors correspond to different items inside each group (switching the color means moving from the previous item to the next one).

$\beta$  which determines the level of excitability of variable  $Y$  and, according to the feedback, also controls the excitability of  $X$  (term  $\sigma_i^{lk}(S, C) \cdot X_i^{lk} \cdot Y^{lk}$ ) in the right hand side of Equation (2). In **Figure 3** we represent the numerical analysis of the dependence of  $\Delta T$  on the parameter  $\beta$ —increasing  $\beta$ , i.e., decreasing the excitability leads to the decreasing of the timing interval  $\Delta T$ .

We also carried out numerical simulations of a high-dimensional model that describes the dynamics of chunk and super-chunk formation with the following parameters:  $N^{lk} = 6$ ,  $M^l = 6$  (number of chunks),  $P = 3$  (number of superchunks),  $\sigma^{l1} = [6.94, 5.11, 8.94, 5.86, 8.33, 9.62]$ ,  $\sigma^{l2} = [5.48, 5.66, 5.39, 9.89, 9.99, 5.82]$ ,  $\sigma^{l3} = [7.65, 8.98, 9.21, 6.02, 5.71, 5.12]$ ,  $\sigma^{l4} = [7.61, 7.73, 5.62, 7.93, 5.80, 5.39]$ ,  $\sigma^{l5} = [5.11, 9.99, 5.52, 5.66, 5.50, 8.21]$ ,  $\sigma^{l6} = [5.84, 9.39, 7.08, 5.16, 8.37, 6.87]$ , and given these values,  $\rho_{ii}^{lk} = 1.0$ ,  $\rho_{i_n - i_n}^{lk} = \frac{\sigma_{i_n - 1}^{lk}}{\sigma_{i_n}^{lk}} + 0.5$

$$1, \rho_{i_n + i_n}^{lk} = \frac{\sigma_{i_n + 1}^{lk}}{\sigma_{i_n}^{lk}} - 0.5, i = 1, \dots, N^{lk}, k = 1, \dots, M^l, l = 1, \dots,$$

$$P, \text{ and } \rho_{i_n}^{lk} = \rho_{i_n - 1}^{lk} + \frac{\sigma_i^{lk} - \sigma_{i_n - 1}^{lk}}{\sigma_{i_n}^{lk}} + 2, i \neq \{i_{n-1}, i_n, i_{n+1}\}, \text{ as}$$

well as the parameters considered for the synaptic dynamics between chunks described by the equations  $\tau = 0.8$ ,  $\theta = 2.0$ ,  $\xi_l^{kk} = 1.0$ ,  $\xi_l^{k_n k_{n-1}} = 0.5$ ,  $\xi_l^{k_n k_{n+1}} = 1.4$ ,  $\xi_2^{k_n k_{n+1}} = 1.3$ ,  $\xi_3^{k_n k_{n+1}} = 1.5$ ,  $k = 1, \dots, M^l$ ,  $l = 1, \dots, P$ ,  $\xi_l^{k k_n} = \xi_l^{k_n - 1 k_n} + 2$ ,  $k \neq \{k_{n-1}, k_n, k_{n+1}\}$ , and  $\beta = 0.01$ . Finally, the parameters for the synaptic dynamics between superchunks were  $T = 5$ ,  $\Theta = 10$ ,  $\zeta^{ll} = 1.0$ ,  $\zeta^{l_n l_{n-1}} = 0.5$ ,  $\zeta^{l_n l_{n+1}} = 1.4$ ,  $l = 1, \dots, P$ , and  $\delta = 0.01$ . The result of these simulations are displayed in **Figure 4**, which shows three levels of information hierarchy: original informational chain (lower panel), chunked chain (middle panel), and superchunking chain (upper panel).

As illustrated in **Figure 2**, the sequence of chunks can be considered as a heteroclinic cycle of metastable states where each metastable state itself is a heteroclinic cycle of elementary informational items. Based on this self-similarity, we can expect that

the chunking chain as a result of a second heteroclinic instability generates the next level of modulation—the superchunk sequence. Our expectation is confirmed in **Figure 4** that shows the time series of the three level network (2)–(6) (c.f. **Figure 1**) dynamics. In this figure, one can see the generation of sequences of superchunks. All together, the sequences informational items, chunks and superchunks can be interpreted as “words,” “sentences,” and “paragraphs.”

For the sake of simplicity we have illustrated here the phenomenon of stability just for a closed-loop clustered chunking-superchunking sequence. In the general case of open sequence, it is possible to formulate the sufficient conditions for the existence and stability of the non-closed channel based on the estimation of the saddle values of the metastable states (elementary items)—the channel is stable in the case that all of them are larger than one in absolute value (Afraimovich et al., 2004; Bick and Rabinovich, 2010). The formulation of the necessary conditions is a more complex problem and is still under consideration. The imposed stability conditions determine the behavior of the trajectories inside the neighborhood of the heteroclinic network independently of the initial conditions as computer experiments have confirmed (Afraimovich et al., 2004; Bick and Rabinovich, 2010).

The above described numerical results can be justified by an analytical study of the system

$$\begin{cases} \dot{X}_i^k = X_i^k \left( \sigma_i^k \cdot Y^k - \sum_{j=1}^{N^k} \rho_{ij}^k X_j^k \right), \\ \tau \dot{Y}^k = Y^k \left( 1 - \beta \sum_{i=1}^{N^k} X_i^k - Z^k \right), \\ \theta \dot{Z}^k = \sum_{m=1}^M \xi^{km} Y^m - Z^k \end{cases} \quad (7)$$



$i = 1, \dots, N^k$ ,  $k = 1, \dots, M$ . For the sake of simplicity, let us assume that  $\tau = \theta \ll 1$ , so one can apply geometric singular perturbation theory (see, for instance, Jones, 1995; Hek, 2010 and references therein). In order to avoid confusion, it is important to say that the assumption  $\tau = \theta \ll 1$  implies that, in contrast to the dynamics of  $X$ , the chunking dynamics is a composition of fast and slow motions. The fast motions lead variables  $Y$ -th and  $Z$ -th to a neighborhood of the slow manifold in the phase space. The evolution of the chunk variables on this manifold in the vicinity of the metastable states is much slower than the  $X$  variables. This corresponds to the intuitively clear fact that the “enveloping” variables mimic the averaging

dynamics of  $X$ . Computer experiments confirm this explanation (see Figure 4).

The limit slow manifold has the equations  $Y^k \left(1 - \beta \sum_{i=1}^{N^k} X_i^k - Z^k\right) = 0$ ,  $\sum_{m=1}^M \xi^{km} Y^m - Z^k = 0$ , thus,  $\sum_{m=1}^M \xi^{km} Y^m = 1 - \beta \sum_{i=1}^{N^k} X_i^k$ . Denote by  $\xi$  the  $m \times m$ -matrix  $\xi^{km}$ . If  $\det \xi \neq 0$ , we find

$$Y^k = \frac{1}{\det \xi} \left( \sum_{m=1}^M \eta^{mk} - \beta \sum_{m=1}^M \eta^{mk} \sum_{i=1}^{N^m} X_i^m \right) \quad (8)$$

**Table 1 | Sequential dynamics in neural and cognitive systems.**

Phenomenon/image	Model	References	Comments
Voting paradox / Structurally stable heteroclinic cycle	Kinetic (rate) equation, Lotka–Volterra model	Krupa, 1997; Stone and Armbruster, 1999; Ashwin et al., 2003; Postlethwaite and Dawes, 2005	J. C. Borda and the Marquis de Condorcet (De Borda, 1781; Saari, 1995) analyzed the process of plurality elections at the French Royal Academy of Sciences. They predicted the absence of a winner in a 3 step voting process (Condorcet’s triangle)
Learning sequences	Hopfield type non-symmetric networks with time delay including spiking neuron models	Amari, 1972; Kleinfeld, 1986; Sompolinsky and Kanter, 1986; Minai and Levy, 1993; Deco and Rolls, 2005	Networks proposed to explain the generation of rhythmic motor patterns and the recognition and recall of sequences
Latching dynamics	Potts network is able to hop from one discrete attractor to another under random perturbation to make a sequence	Treves, 2005; Russo et al., 2008; Russo and Treves, 2011; Linkerhand and Gros, 2013	The dynamics can involve sequences of continuously latching transient states
Sequential memory with synaptic dynamics / Chaotic itinerancy sequences of Milnor attractors or attractor ruins	Spike-frequency-adaptation mechanism Noisy dynamical systems. Cantor coding	Tsuda, 2009	Proposed to be involved in episodic memory and itinerant process of cognition
Winnerless sequential switchings along metastable states/Stable heteroclinic channel	Generalized coupled Lotka–Volterra equations	Afraimovich et al., 2004; Rabinovich et al., 2008a,b	Information processing with transient dynamics at many different description levels from simple networks to cognitive processes
Winnerless competitive dynamics in spiking brain networks	Random inhibitory networks of spiking neurons in the striatum	Ponzi and Wickens, 2010	Neurons form assemblies that fire in sequential coherent episodes and display complex identity–temporal spiking patterns even when cortical excitation is constant or fluctuating noisily
Sequences of sequences / Hierarchical transient sequences	Recognition of sequence of sequences based on a continuous dynamical model	Kiebel et al., 2009	Speech can be considered as a sequence of sequences and can be implemented robustly by a dynamical model based on Bayesian inference. recognition dynamics disclose inference at multiple time scales

where  $\eta^{km}$  is the cofactor of the entry  $\xi^{mk}$  of the matrix  $\xi$ . Substituting this expression into the first equation of the system (7) we obtain the system

$$\dot{X}_i^k = X_i^k \left( \sigma_i^k \frac{1}{\det \xi} \sum_{m=1}^M \eta^{mk} - \sum_{j=1}^{N^k} \rho_{ij}^k X_j^k - \frac{\beta}{\det \xi} \sum_{m=1}^M \eta^{mk} \sum_{i=1}^{N^k} X_i^m \right) \quad (9)$$

$i = 1, \dots, N^k$ ,  $k = 1, \dots, M$ , which is similar to the binding model described in Rabinovich et al. (2010a). In particular, the “in-chunk” dynamics in (9) corresponds to the dynamics in the modality subspace in Rabinovich et al. (2010a). The main peculiarity of the system (9) is that the rates of coupling coefficients between different chunks have the common factor  $\beta$ , so if  $\beta = 0$  then the interaction between different chunks is absent. Similarly to the study in Rabinovich et al. (2010a), one can impose conditions under which there exists a heteroclinic cycle for each chunk and successive heteroclinic connections between saddle points in different cycles. The last claim has the form  $\beta > \beta_{cr}$  where  $\beta_{cr}$  depends on the parameters of the system (9). If  $\tau$  is small then because of the geometric singular perturbation theory, the imposed conditions shall guarantee the existence of a heteroclinic network in the original system (7) corresponding to the “in-chunk” and “inter-chunk” dynamics.

Observations on the temporal chunk signal have focused on the use of pauses in behavior to probe chunk structures in WM. On the basis of some of these studies, a hierarchical process model has been proposed, which consists of four hierarchical levels describing different kind of pauses. The lowest level consists of pauses between strokes within letters. On higher levels, there are pauses between letters, words, and phrases. Each level is associated with a larger amount of processing when retrieving these chunks from memory (Cheng and Rojas-Anaya, 2006). Writing may be an effective approach to the study of cognitive phenomena that involves the processing of chunks. In Cheng and Rojas-Anaya (2003), it was demonstrated that in the writing of simple number sequences the duration of pauses between written elements (digits) that are within a chunk are shorter than the pauses between elements across the boundary of chunks. This temporal signal is apparent in un-aggregated data for individual participants in single trials. Mathematically the time intervals between chunks and super-chunks are controlled by parameter  $\beta$  (see Equation 3).

## DISCUSSION

In this paper we have shown how the architecture of hierarchical mental model networks affected their associated functions. The discussed examples illustrate that networks with metastable states having several unstable separatrices exhibit very diverse cognitive functions (behavior). Complex heteroclinic networks allow completely new dynamical phenomena, and one of the primary challenges is the assessment of the existence and stability of hierarchical—chunking processes that can represent cognitive activity.

It is important to remind that the modeling of cycling and sequential dynamics in behavior and cognition has a long history (see several representative efforts in **Table 1**). Most of these

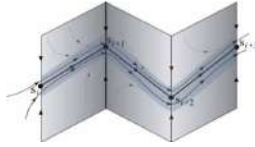
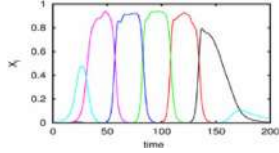
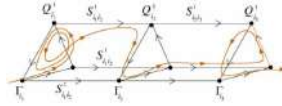
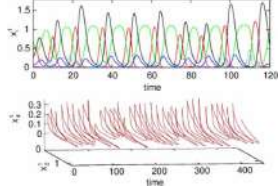
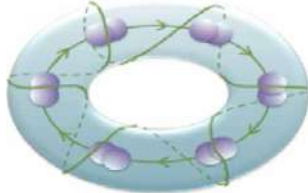
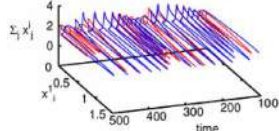
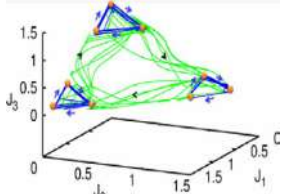
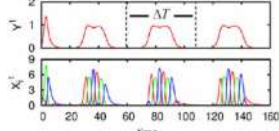
models are based on Hopfield type networks. The main problem there is to keep the stability of the recall sequences against noise.

The results of chunking dynamics reported in this paper can be viewed as relevant in the description of different cognitive tasks. For example, in WM, humans encode items and synthesize them. With that, we give meaning to ideas and find a relevant place for them in our cognitive world. In these actions the interaction between WM and chunking are reciprocal—first of all WM is the “engine” of chunking, and on the other hand, the chunking makes WM capacity higher.

The model of chunking dynamics discussed in this paper relies on heteroclinic dynamics. It is important to emphasize that the main features of the SHC do not depend on the specific model used. The conditions of existence and the dynamical features of SHCs can be implemented in a wide variety of models: from simple Lotka–Volterra descriptions to complex Hodgkin–Huxley models, and from small networks to large ensembles of many elements (Varona et al., 2002; Venaille et al., 2005; Nowotny and Rabinovich, 2007; Rabinovich et al., 2012). The intrinsic hierarchical nature of the SHC at different temporal and spatial scales allows implementing many types of cognitive dynamics. Within this framework, brain networks can be viewed as non-equilibrium systems and their associated computations as unique patterns of transient activity, controlled by incoming input. The results of these computations can be reproducible, robust against noise, and easily decoded. Using asymmetric inhibition appropriately, the space of possible states of large neural systems can be restricted to connected saddle points, forming SHCs. These channels can be thought of as underlying reliable transient brain dynamics. **Table 2** summarizes four types of heteroclinic networks that can describe different aspects of sequential dynamics in cognitive processes: (i) A canonic heteroclinic network that produces reproducible sequential switching from one metastable state to another inside one modality (like in a simple WM task); (ii) A network displaying inhibitory-based heteroclinic binding dynamics that is responsible for the stable perception of a subject based on three different modalities; (iii) Two different modalities dynamically coordinated by excitatory connections; (iv) A chunking heteroclinic network that controls the grouping of elements of sequential behavior.

Mathy and Feldman have recently suggested to use the Kolmogorov complexity and compressibility (Mathy and Feldman, 2012) for the definition of a “chunk”: a chunk is a unit in a maximally compressed code. The authors presented a series of experiments in which they manipulated the compressibility of stimulus sequences by introducing sequential patterns of variable length. To explore the influence of chunking on the capacity limits of WM, and departing from Bick and Rabinovich (2009), authors in Li et al. (2013) have suggested a model for chunking in sequential WM. This model also uses hierarchical bidirectional inhibition-connected neural networks with WLC. Assuming no interaction between a basic sequence and a chunked sequence, and the existence of an upper bound to the inhibitory weights the network, authors show that chunking increases the number of memorized items in WM from the “magical number” 7–16 items. The optimal number of chunks and the number of the memorized items in each chunk correspond to the “magical number 4.”

**Table 2 | Heteroclinics in mind.**

Phenomenon	Network formalism*	Phase portrait	Time series
Sequential heteroclinic switching	$\dot{X}_i = X_i \left( \sigma_i - \sum_{j=1}^N \rho_{ij} X_j \right)$		
Sequential heteroclinic binding and information flow	$\dot{X}_i^j = X_i^j \left( \sigma_i^j - \sum_{j=1}^N \rho_{ij}^j X_j^j - \sum_{m=1}^L \sum_{j=1}^N \xi_{ij}^{lm} X_j^m \right)$		
Heteroclinic cooperation	$\tau^m \dot{X}_i^m = X_i^m \cdot \left[ \sigma_i^m - \sum_{j=1}^{K^m} \rho_{ij}^m X_j^m + \sum_{k=1}^M \sum_{j=1}^{K^m} \xi_{ij}^{mk} X_j^k \right]$		
Hierarchical chunking memory and learning	$\begin{aligned} \dot{X}_i^k &= X_i^k \left( \sigma_i^k \cdot \gamma^k - \sum_j \rho_{ij}^k X_j^k \right) \\ \tau \dot{\gamma}^k &= \gamma^k \left( \left( 1 - \beta \sum_i X_i^k \right) - Z^k \right) \\ \theta \dot{Z}^k &= \sum_{m=1}^M \xi^{km} \gamma^m - Z^k \end{aligned}$		

\*See the definition of the variables and parameters in the text.

Recent experiments have confirmed the existence of three levels of cognitive hierarchy—see Rosenberg and Feigenson (2013). In this paper authors reported that infants can unify the representation of chunks into “super-chunks.”

The chunking models discussed above can be generalized on more complex cases. In particular, by adding attention control in the network hierarchy, it is possible to analyze the binding of sequences of chunks. The brain could use such binding to perform many cognitive functions like the coordination of visual perception with speech comprehension, or the coordination of music chunks and word chunks in singing processes. It is well-known that viewing a speaker’s articulatory movements substantially improves a listener’s ability to understand spoken words, especially under noisy environmental conditions like in a crowded cocktail party. Ross and coauthors claimed that this effect is most pronounced when the auditory input is weakest. As a result of attentional binding—multisensory integration—, substantial gain in multisensory speech enhancement is achieved at even the lowest signal-to noise ratios (Ross et al., 2007).

The dynamics of hierarchical heteroclinic networks is also able to explain and predict the coordination of behavioral elements with different time scales (for a study about the coordination of sensorimotor dynamics see Jantzen and Kelso, 2007). Functionally, such kind of synchronization can be the result of

learning—the changing of the strength of inhibitory connections between agents at the different levels of the hierarchy in order to coordinate the dynamics with different time scales (see Figure 3). Additionally, it is important to note that the winnerless competitive learning process itself can be chaotic (Komarov et al., 2010), which provides wider possibilities for adaptability.

**ACKNOWLEDGMENTS**

Mikhail I. Rabinovich acknowledges support from ONR grant N00014310205. Pablo Varona was supported by MINECO TIN2012-30883. Irma Tristan acknowledges support from the UC-MEXUS-CONACYT Fellowship. Valentin S. Afraimovich was partially supported by Ohio University Glidden Professorship program.

**REFERENCES**

Afraimovich, V. S., Zhigulin, V. P., and Rabinovich, M. I. (2004). On the origin of reproducible sequential activity in neural circuits. *Chaos* 14, 1123. doi: 10.1063/1.1819625  
 Amari, S.-I. (1972). Learning patterns and pattern sequences by self-organizing nets of threshold elements. *IEEE Trans. Comput.* C-21, 1197–1206. doi: 10.1109/T-C.1972.223477  
 Ashwin, P., Field, M., Rucklidge, A. M., and Sturman, R. (2003). Phase resetting effects for robust cycles between chaotic sets. *Chaos* 13, 973–981. doi: 10.1063/1.1586531

- Bahlmann, J., Schubotz, R. I., and Friederici, A. D. (2008). Hierarchical artificial grammar processing engages Broca's area. *Neuroimage* 42, 525–534. doi: 10.1016/j.neuroimage.2008.04.249
- Bahlmann, J., Schubotz, R. I., Mueller, J. L., Koester, D., and Friederici, A. D. (2009). Neural circuits of hierarchical visuo-spatial sequence processing. *Brain Res.* 1298, 161–170. doi: 10.1016/j.brainres.2009.08.017
- Bick, C., and Rabinovich, M. I. (2009). Dynamical origin of the effective storage capacity in the brain's working memory. *Phys. Rev. Lett.* 103:218101. doi: 10.1103/PhysRevLett.103.218101
- Bick, C., and Rabinovich, M. I. (2010). On the occurrence of stable heteroclinic channels in Lotka–Volterra models. *Dyn. Syst.* 25, 1–14. doi: 10.1080/14689360903322227
- Bor, D., and Seth, A. K. (2012). Consciousness and the prefrontal parietal network: insights from attention, working memory, and chunking. *Front. Psychol.* 3:1–14. doi: 10.3389/fpsyg.2012.00063
- Botvinick, M. M. (2008). Hierarchical models of behavior and prefrontal function. *Trends Cogn. Sci.* 12, 201–208. doi: 10.1016/j.tics.2008.02.009
- Bressler, S. L., and Kelso, J. A. S. (2001). Cortical coordination dynamics and cognition. *Trends Cogn. Sci.* 5, 26–36. doi: 10.1016/S1364-6613(00)01564-3
- Bystritsky, A., Nierenberg, A. A., Feusner, J. D., and Rabinovich, M. (2012). Computational non-linear dynamical psychiatry: a new methodological paradigm for diagnosis and course of illness. *J. Psychiatr. Res.* 46, 428–435. doi: 10.1016/j.jpsychires.2011.10.013
- Chekaif, M., and Matha, F. (2012). “Chunking memory span of categorizable objects,” in *53rd Annual Meeting of the Psychonomic Society* (Minneapolis, MN: Psychonomic Society Publication).
- Cheng, P. C. H., and Rojas-Anaya, H. (2003). “Writing out a temporal signal of chunks: patterns of pauses reflect the induced structure of written number sequences,” in *Proceedings of the 27th Annual Conference of the Cognitive Science Society* (Mahwah, NJ: Lawrence Erlbaum), 424–429.
- Cheng, P. C.-H., and Rojas-Anaya, H. (2006). “A temporal signal reveals chunk structure in the writing of word phrases,” in *Proceedings of the Twenty-Eighth Annual Conference of the Cognitive Science Society* (Mahwah, NJ: Lawrence Erlbaum).
- Clerget, E., Andres, M., and Olivier, E. (2013). Deficit in complex sequence processing after a virtual lesion of left BA45. *PLoS ONE* 8:e63722. doi: 10.1371/journal.pone.0063722
- De Borda, J. C. (1781). *Memoire sur les Elections au Scrutin*. Paris: Academie Royale des Sciences.
- Deco, G., and Rolls, E. T. (2005). Sequential memory: a putative neural and synaptic dynamical mechanism. *J. Cogn. Neurosci.* 17, 294–307. doi: 10.1162/0898929053124875
- Dehaene, S., and Changeux, J. P. (1997). A hierarchical neuronal network for planning behavior. *Proc. Natl. Acad. Sci. U.S.A.* 94, 13293–13298. doi: 10.1073/pnas.94.24.13293
- Dominey, P. F., Hoen, M., Blanc, J.-M., and Lelekov-Boissard, T. (2003). Neurological basis of language and sequential cognition: evidence from simulation, aphasia, and ERP studies. *Brain Lang.* 86, 207–225. doi: 10.1016/S0093-934X(02)00529-1
- Engel, A. K., Fries, P., and Singer, W. (2001). Dynamic predictions: oscillations and synchrony in top-down processing. *Nat. Rev. Neurosci.* 2, 704–716. doi: 10.1038/35094565
- Fadiga, L., Craighero, L., and D'Ausilio, A. (2009). Broca's area in language, action, and music. *Ann. N.Y. Acad. Sci.* 1169, 448–458. doi: 10.1111/j.1749-6632.2009.04582.x
- Fingelkurts, A. A., and Fingelkurts, A. A. (2006). Timing in cognition and EEG brain dynamics: discreteness versus continuity. *Cogn. Process.* 7, 135–162. doi: 10.1007/s10339-006-0035-0
- Friederici, A. D., Bahlmann, J., Friedrich, R., and Makuuchi, M. (2011). The neural basis of recursion and complex syntactic hierarchy. *Biolinguistics* 5, 87–104. Available online at: <http://www.biolinguistics.eu/index.php/biolinguistics/article/view/170>
- Friston, K. J. (1997). Transients, metastability, and neuronal dynamics. *Neuroimage* 5, 164–171. doi: 10.1006/nimg.1997.0259
- Friston, K. J. (2000). The labile brain. II. Transients, complexity and selection. *Philos. Trans. R. Soc. Lond. B Biol. Sci.* 355, 237–252. doi: 10.1098/rstb.2000.0561
- Gobet, F., Lane, P. C. R., Croker, S., Cheng, P. C.-H., Jones, G., Oliver, I., et al. (2001). Chunking mechanisms in human learning. *Trends Cogn. Sci.* 5, 236–243. doi: 10.1016/S1364-6613(00)01662-4
- Gros, C. (2007). Neural networks with transient state dynamics. *New J. Phys.* 9, 109. doi: 10.1088/1367-2630/9/4/109
- Grossman, M. (1980). A central processor for hierarchically-structured material: evidence from Broca's aphasia. *Neuropsychologia* 18, 299–308. doi: 10.1016/0028-3932(80)90125-6
- Hek, G. (2010). Geometric singular perturbation theory in biological practice. *J. Math. Biol.* 60, 347–386. doi: 10.1007/s00285-009-0266-7
- Huerta, R., and Rabinovich, M. (2004). Reproducible sequence generation in random neural ensembles. *Phys. Rev. Lett.* 93:238104. doi: 10.1103/PhysRevLett.93.238104
- Ito, J., Nikolaev, A. R., and van Leeuwen, C. (2007). Dynamics of spontaneous transitions between global brain states. *Hum. Brain Mapp.* 28, 904–913. doi: 10.1002/hbm.20316
- Jantzen, K. J., and Kelso, J. S. (2007). “Neural coordination dynamics of human sensorimotor behavior: a review,” in *Handbook of Brain Connectivity*, eds V. K. Jirsa and A. McIntosh (Berlin; Heidelberg: Springer), 421–461.
- Jones, C. K. R. T. (1995). Geometric singular perturbation theory. *Lect. Notes Math.* 1609, 44–118. doi: 10.1007/BFb0095239
- Kelso, J. A. S. (1995). *Dynamic Patterns: The Self-Organization of Brain and Behavior*. Cambridge, MA: The MIT Press.
- Kiebel, S. J., von Kriegstein, K., Daunizeau, J., and Friston, K. J. (2009). Recognizing sequences of sequences. *PLoS Comput. Biol.* 5:e1000464. doi: 10.1371/journal.pcbi.1000464
- Kleinfeld, D. (1986). Sequential state generation by model neural networks. *Proc. Natl. Acad. Sci. U.S.A.* 83, 9469–9473. doi: 10.1073/pnas.83.24.9469
- Koch, I., Philipp, A. M., and Gade, M. (2006). Chunking in task sequences modulates task inhibition. *Psychol. Sci.* 17, 346–350. doi: 10.1111/j.1467-9280.2006.01709.x
- Komarov, M. A., Osipov, G. V., and Burtsev, M. S. (2010). Adaptive functional systems: learning with chaos. *Chaos* 20, 045119. doi: 10.1063/1.3521250
- Krupa, M. (1997). Robust heteroclinic cycles. *J. Nonlinear Sci.* 7, 129–176. doi: 10.1007/BF02677976
- Li, G., Ning, N., Ramanathan, K., He, W., Pan, L., and Shi, L. (2013). Behind the magical numbers: hierarchical chunking and the human working memory capacity. *Int. J. Neural Syst.* 23:1350019. doi: 10.1142/S0129065713500196
- Li, K. Z. H., Blair, M., and Chow, V. S. M. (2010). Sequential performance in young and older adults: evidence of chunking and inhibition. *Neuropsychol. Dev. Cogn. Sect. B Aging Neuropsychol. Cogn.* 17, 270–295. doi: 10.1080/13825580903165428
- Linkerhand, M., and Gros, C. (2013). Generating functionals for autonomous latching dynamics in attractor relict networks. *Sci. Rep.* 3:2042. doi: 10.1038/srep02042
- Mathy, E., and Feldman, J. (2012). What's magic about magic numbers? Chunking and data compression in short-term memory. *Cognition* 122, 346–362. doi: 10.1016/j.cognition.2011.11.003
- Meehan, T. P., and Bressler, S. L. (2012). Neurocognitive networks: findings, models, and theory. *Neurosci. Biobehav. Rev.* 36, 2232–2247. doi: 10.1016/j.neubiorev.2012.08.002
- Miller, G. A. (1956). The magical number seven plus or minus two: some limits on our capacity for processing information. *Psychol. Rev.* 63, 81–97. doi: 10.1037/h0043158
- Minai, A. A., Levy, W. B. (1993). “Sequence learning in a single trial,” in *INNS World Congress on Neural Networks* (Hillsdale, NJ: Erlbaum), 505–508.
- Musso, M., Moro, A., Glauche, V., Rijntjes, M., Reichenbach, J., Büchel, C., et al. (2003). Broca's area and the language instinct. *Nat. Neurosci.* 6, 774–781. doi: 10.1038/nn1077
- Nowotny, T., and Rabinovich, M. I. (2007). Dynamical origin of independent spiking and bursting activity in neural microcircuits. *Phys. Rev. Lett.* 98:128106. doi: 10.1103/PhysRevLett.98.128106
- Oullier, O., and Kelso, J. A. S. (2006). Neuroeconomics and the metastable brain. *Trends Cogn. Sci.* 10, 353–354. doi: 10.1016/j.tics.2006.06.009
- Ponzi, A., and Wickens, J. (2010). Sequentially switching cell assemblies in random inhibitory networks of spiking neurons in the striatum. *J. Neurosci.* 30, 5894–5911. doi: 10.1523/JNEUROSCI.5540-09.2010
- Postlethwaite, C. M., and Dawes, J. H. P. (2005). Regular and irregular cycling near a heteroclinic network. *Nonlinearity* 18, 1477–1509. doi: 10.1088/0951-7715/18/4/004

- Rabinovich, M., Huerta, R., and Laurent, G. (2008a). Neuroscience. Transient dynamics for neural processing. *Science* 321, 48–50. doi: 10.1126/science.1155564
- Rabinovich, M., Tristan, I., and Varona, P. (2013). Neural dynamics of attentional cross-modality control. *PLoS ONE* 8:e64406. doi: 10.1371/journal.pone.0064406
- Rabinovich, M., Volkovskii, A., Lecanda, P., Huerta, R., Abarbanel, H. D., and Laurent, G. (2001). Dynamical encoding by networks of competing neuron groups: winnerless competition. *Phys. Rev. Lett.* 87:68102. doi: 10.1103/PhysRevLett.87.068102
- Rabinovich, M. I., Afraimovich, V. S., Bick, C., and Varona, P. (2012). Information flow dynamics in the brain. *Phys. Life Rev.* 9, 51–73. doi: 10.1016/j.plrev.2011.11.002
- Rabinovich, M. I., Afraimovich, V. S., and Varona, P. (2010a). Heteroclinic binding. *Dyn. Syst. An Int. J.* 25, 433–442. doi: 10.1080/14689367.2010.515396
- Rabinovich, M. I., Huerta, R., Varona, P., and Afraimovich, V. S. (2006). Generation and reshaping of sequences in neural systems. *Biol. Cybern.* 95, 519–536. doi: 10.1007/s00422-006-0121-5
- Rabinovich, M. I., Huerta, R., Varona, P., and Afraimovich, V. S. (2008b). Transient cognitive dynamics, metastability, and decision making. *PLoS Comput Biol* 4:e1000072. doi: 10.1371/journal.pcbi.1000072
- Rabinovich, M. I., Muezzinoglu, M. K., Strigo, I., and Bystritsky, A. (2010b). Dynamical principles of emotion-cognition interaction: mathematical images of mental disorders. *PLoS ONE* 5:e12547. doi: 10.1371/journal.pone.0012547
- Rabinovich, M. I., and Varona, P. (2011). Robust transient dynamics and brain functions. *Front. Comput. Neurosci.* 5:24. doi: 10.3389/fncom.2011.00024
- Ribas-Fernandes, J. J. E., Solway, A., Diuk, C., McGuire, J. T., Barto, A. G., Niv, Y., et al. (2011). A neural signature of hierarchical reinforcement learning. *Neuron* 71, 370–379. doi: 10.1016/j.neuron.2011.05.042
- Rosenbaum, D. A., Kenny, S. B., and Derr, M. A. (1983). Hierarchical control of rapid movement sequences. *J. Exp. Psychol. Hum. Percept. Perform.* 9, 86–102. doi: 10.1037/0096-1523.9.1.86
- Rosenberg, R. D., and Feigenson, L. (2013). Infants hierarchically organize memory representations. *Dev. Sci.* 16, 610–621. doi: 10.1111/desc.12055
- Ross, L. A., Saint-Amour, D., Leavitt, V. M., Javitt, D. C., and Foxe, J. J. (2007). Do you see what I am saying? Exploring visual enhancement of speech comprehension in noisy environments. *Cereb. Cortex* 17, 1147–1153. doi: 10.1093/cercor/bhl024
- Russo, E., Nambodiri, V. M. K., Treves, A., and Kropff, E. (2008). Free association transitions in models of cortical latching dynamics. *New J. Phys.* 10:015008. doi: 10.1088/1367-2630/10/1/015008
- Russo, E., and Treves, A. (2011). An uncouth approach to language recursivity. *Biolinguistics* 5, 133–150. Available online at: <http://www.biolinguistics.eu/index.php/biolinguistics/article/view/186>
- Saari, D. G. (1995). *Basic Geometry of Voting*. Berlin: Springer. doi: 10.1007/978-3-642-57748-2
- Sahin, N. T., Pinker, S., Cash, S. S., Schomer, D., and Halgren, E. (2009). Sequential processing of lexical, grammatical, and phonological information within Broca's area. *Science* 326, 445–449. doi: 10.1126/science.1174481
- Sakai, K., Kitaguchi, K., and Hikosaka, O. (2003). Chunking during human visuo-motor sequence learning. *Exp. Brain Res.* 152, 229–242. doi: 10.1007/s00221-003-1548-8
- Schneider, D. W. (2007). Task-set inhibition in chunked task sequences. *Psychon. Bull. Rev.* 14, 970–976. doi: 10.3758/BF03194130
- Sompolinsky, H., and Kanter, I. I. (1986). Temporal association in asymmetric neural networks. *Phys. Rev. Lett.* 57, 2861–2864. doi: 10.1103/PhysRevLett.57.2861
- Stone, E., and Armbruster, D. (1999). Noise and O(1) amplitude effects on heteroclinic cycles. *Chaos* 9, 499–506. doi: 10.1063/1.166423
- Tettamanti, M., and Weniger, D. (2006). Broca's area: a supramodal hierarchical processor? *Cortex* 42, 491–494. doi: 10.1016/S0010-9452(08)70384-8
- Treves, A. (2005). Frontal latching networks: a possible neural basis for infinite recursion. *Cogn. Neuropsychol.* 22, 276–291. doi: 10.1080/0264329042000329
- Tsuda, I. (2009). Hypotheses on the functional roles of chaotic transitory dynamics. *Chaos* 19, 015113. doi: 10.1063/1.3076393
- Varona, P., Rabinovich, M. I., Selverston, A. I., and Arshavsky, Y. I. (2002). Winnerless competition between sensory neurons generates chaos: a possible mechanism for molluscan hunting behavior. *Chaos* 12, 672–677. doi: 10.1063/1.1498155
- Venaille, A., Varona, P., and Rabinovich, M. I. (2005). Synchronization and coordination of sequences in two neural ensembles. *Phys. Rev. E Stat. Nonlin. Soft. Matter Phys.* 71:61909. doi: 10.1103/PhysRevE.71.061909

**Conflict of Interest Statement:** The authors declare that the research was conducted in the absence of any commercial or financial relationships that could be construed as a potential conflict of interest.

Received: 18 October 2013; accepted: 10 February 2014; published online: 14 March 2014.

Citation: Rabinovich MI, Varona P, Tristan I and Afraimovich VS (2014) Chunking dynamics: heteroclinics in mind. *Front. Comput. Neurosci.* 8:22. doi: 10.3389/fncom.2014.00022

This article was submitted to the journal *Frontiers in Computational Neuroscience*. Copyright © 2014 Rabinovich, Varona, Tristan and Afraimovich. This is an open-access article distributed under the terms of the Creative Commons Attribution License (CC BY). The use, distribution or reproduction in other forums is permitted, provided the original author(s) or licensor are credited and that the original publication in this journal is cited, in accordance with accepted academic practice. No use, distribution or reproduction is permitted which does not comply with these terms.

# Hierarchical Heteroclinics In Dynamical Model Of Cognitive Processes: Chunking

V. Afraimovich

Institute de Investigacion Comunicacion Optica

UASLP, A. Obregon, 7800

SLP, San Luis Potosi, Mexico

T.Young

Mathematics Department

Ohio University

321 Morton Hall

Athens OH 45701 USA

M. Rabinovich

BioCircuits Institute

University of California, San Diego

9500 Gilman Dr., #0328

LaJolla, CA 92093, USA

May 15, 2014

## Abstract

Results of brain imaging and nonlinear dynamics provide a new vision on brain networks that are hierarchical, and help to find their relation to different mental tasks. It is possible to build models for the description and prediction of different cognitive activities. The number of variables in the adequate dynamical model usually is small enough. The dynamical images of different mental processes depend on their temporal organization and, as a rule, cannot be just simple attractors - cognition is characterized by transient dynamics. The image for robust transients is a stable heteroclinic channel consisting of chain of saddles connected by unstable separatrices. We focus here on hierarchical chunking dynamics that can represent many cognitive activities. Chunking is the dynamical phenomenon that means the dividing a long information chain into

shorter items. Chunking is important in many processes of perception, learning, memory and cognition. Here we prove that in the phase space of the describing chunking model there exists a new mathematical object - heteroclinic sequence of heteroclinic cycles - by using the technique of slow-fast approximations. This new object serves as a skeleton of motions reflecting sequential features of hierarchical chunking dynamics and is an adequate image of the chunking processing.

*Keywords:* Heteroclinic network, slow-fast system, attracting manifold.

## 1 Introduction

### 1.1 Background

Chunking is the dynamical process of combining elementary pieces of information to create something more complex and meaningful. Concept of chunking has been put forward in the middle of last century by George Miller in an article [Miller, 1956]. He studied the capabilities of human short term or working memory to reproduce reliably the sequence of digits after a few minutes when person got it once. For the sequence of the sequence of simple items without chunking - his answer was: seven, plus or minus two. Dynamical origin of the small enough number of information items stored in a working memory has been investigated in [Bick & Rabinovich 2009]. The authors showed that the capacity of the memory is about 5-7 items. The chunking mechanism is able to elevate the working memory capacity essentially. To use and develop the Miller's concept about the remembering of the sequence of chunks we have to keep in mind that chunks itself can be of any nature i.e. linguistic, engineering tools and so on, and of different complexity.

Chunking is a critical aspect of learning, memory and of consciousness and is one of the main features of human life experience [Bor et al., 2012, Ribas-Fernandes et al., 2011]. By the creation of huge numbers of possible and having sense combinations of patterns, as well as combinations of combinations of patterns superchunks - and so on, mind is able to generate an amazingly rich, hierarchical presentation of the intrinsic and outside world.

Chunking is crucially important for all cognitive processes [Botvinick, 2008]. It would be impossible, for example, to read a novel without separation of the text on to sentences, paragraphs, and chapters. In the learning process chunking allows logical grouping of data for easier understanding [Sahin et al., 2009, Kiebel et al., 2009]. Non-chunked data is harder to remember and many studies support the use of chunking as a memory tool helping to perform the decision-making process [Gobet et al., 2001, Gobet et al., 2013].

It is a lot of interest in scientific community linguists, cognitive scientists, computer scientists, even musicians and chess players - to the understanding of the chunking mechanisms [Otoo et al., 2007, Dowling, 1973, Ystad et al., 2008, De Groot, 1978]. It is a visible progress in this area in the last decade, for example, it is understood now that chunking works by pre-compiling of bits of perceptual data. These chunks can then be recollected and combined into a complete picture that the mind can use to represent the situation available for rapid recall. In [Orr, 2003] the author suggests that the more information each chunk contains the better helps perceive the keys to the problem at hand. The brain can format these chunks much better if the data are logically grouped.

However, there were no attempts to build a nonlinear dynamical model of the chunking process, except our recent paper [Rabinovich et al., 2014]. Below we discuss the principles of the organization of this hierarchical model from the dynamical point of view and represent the rigorous results that confirmed that chunking behavior in the framework of suggested ODE model corresponds to a hierarchical heteroclinic network in the phase space.

## 1.2 Model

The model suggested in [Rabinovich et al., 2014] has the form:

$$\dot{x}_i^k = x_i^k(\sigma_i^k y^k - \sum_{j=i}^{N_k} \rho_{ij}^k x_j^k), \quad (1)$$

$$\tau \dot{y}^k = y^k(1 - \beta \sum_{i=1}^{N_k} x_i^k - z^k), \quad (2)$$

$$\theta \dot{z}^k = \sum_{m=1}^M \xi^{km} y^m - z^k, \quad (3)$$



$k = 1, \dots, M$ , where  $\rho_{ij}^k, \sigma_i^k, \beta$  are positive numbers, and

$$\tau = \theta \ll 1.$$

Here variable  $x^k$  represents the degree of activity of the  $i$ -th basic information item from the  $k$ -th chunk family first level of hierarchy, envelope variable  $y^k$  characterizes the activity of  $k$ -th chunks second level of hierarchy, and  $z^k$  is the strength of the competitive interaction between chunks that is characterized by the first order kinetic and is important for chunks inhibition (see for rev. [Koch et al., 2006, Schneider, 2007]).

Let us discuss the functionality of this model. If envelope variables are positive constants chunking process is absent basic informational items in standard conditions [see Afraimovich et al., 2004] demonstrate the sequential switching dynamics that is represented in the phase space of the first equation by stable heteroclinic channel. On the other hand, when the dynamical activity on the first level of hierarchy is over, the second equation is independent of  $X$ , the chunks activity also became sequential. Playing with the characteristic time scales of the variables  $x$ ,  $y$  and  $z$  one can control the number of the basic items inside the chunks, time intervals between them, and the stability of the chunking process. It is important that for organization of sequences on the different levels of hierarchy, different neural networks in the brain are responsible (see [Rabinovich et al., 2014] and Conclusion). This fact illustrates a lot of flexibility in the organization of complex behavior and thinking.

In (Rabinovich et al., 2014) we hypothesize that the mathematical image of such hierarchical sequential process is the heteroclinic of heteroclinics. The computer experiment supports this hypothesis (see Figure 1). Below we prove it rigorously.

In this article we prove rigorously that dynamics for each chunk is reflected by the existence of an asymptotically (inside the chunk subspace) heteroclinic cycle, and the inter chunk interaction corresponds to the existence of a heteroclinic network consisting of heteroclinic cycles and heteroclinic trajectories joining them.

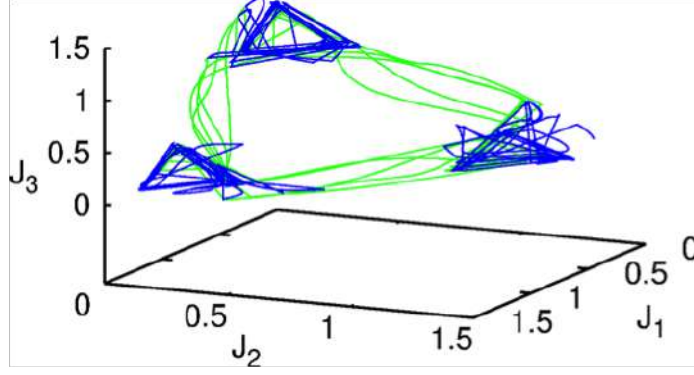


Figure 1: Image of the chunking dynamical process generated by equations (1)-(3). Represented the three-dimensional projection of the 9-D attractor that has been observed with parameters:  $J_1 = y_1 + 0.04(x_{11} + x_{12} + x_{13})$ ,  $J_2 = y_2 + 0.04(x_{21} + x_{22} + x_{23})$ ,  $J_3 = y_3 + 0.04(x_{31} + x_{32} + x_{33})$ . Blue represents the elementary informational item activity individual chunk. Green represents the chunking sequence (adapted from [Rabinovich et al., 2014]).

### 1.3 Notation and Mathematical Framework

For the sake of simplicity we assume that  $\rho_{ii}^k = 1$  for all  $i$  and  $k$ . This set of equations is in the form commonly known as a “slow time” system. By taking both  $\theta$  and  $\tau$  to zero, we obtain the corresponding “slow limit” system.

$$\dot{x}_i^k = x_i^k (\sigma_i^k y^k - \sum_{j=i}^{N_k} \rho_{ij}^k x_j^k), \quad (4)$$

$$0 = y^k (1 - \beta \sum_{i=1}^{N_k} x_i^k - z^k), \quad (5)$$

$$0 = \sum_{m=1}^M \xi^{km} y^m - z^k, \quad (6)$$

$k = 1, \dots, m$ . The “slow manifolds” for the system consist of the set described by the two algebraic equations in the slow limit. We will ignore the components of this set corresponding

to  $y^k = 0$  and rather focus on the non-zero slow manifold, in other words,

$$\mathcal{M}_0 = \left\{ (x, y, z) : 1 - \beta \sum_{i=1}^{N_k} x_i^k - z^k = 0, \sum_{m=1}^M \xi^{km} y^m - z^k = 0 \right\}.$$

The so-called “fast system” is obtained from (1)-(3) by the change of time  $s = \tau t$ :

$$\begin{aligned} \frac{dx_i^k}{ds} &= \tau x_i^k (\sigma_i^k y^k - \sum_{j=i}^{N_k} \rho_{ij}^k x_j^k), \\ \frac{dy^k}{ds} &= ((1 - \beta \sum_{i=1}^{N_k} x_i^k) - z^k), \\ \frac{dz^k}{ds} &= \frac{\tau}{\theta} \sum_{m=1}^M (\xi^{km} y^m - z^k). \end{aligned} \tag{7}$$

We then suppose that  $\tau$  and  $\theta$  go to zero to obtain the “Fast Limit” system, given by:

$$\begin{aligned} \frac{dx_i^k}{ds} &= 0, \\ \frac{dy^k}{ds} &= ((1 - \beta \sum_{i=1}^{N_k} x_i^k) - z^k), \\ \frac{dz^k}{ds} &= C_\infty \sum_{m=1}^M (\xi^{km} y^m - z^k). \end{aligned} \tag{8}$$

Here we suppose that

$$C_\infty = \lim_{\tau \rightarrow 0} \frac{\tau}{\theta}. \tag{9}$$

If  $\tau = \theta$ , then  $C_\infty = 1$ .

## 2 The limit slow manifold

Then the limit slow manifold  $\mathcal{M}_0$  (see for example [Hek, 2010, Jones, 1995]) is given by the two equations (5) and (6).

Solving for  $z^k$  in (5) and substituting into (6) we obtain:

$$y^k \left( 1 - \beta \sum_{i=1}^{N_k} x_i^k - \sum_{m=1}^M \xi^{km} y^m \right) = 0. \tag{10}$$

We are interested in the solutions for which  $y^k \neq 0$ , so instead of (10) we have the system:

$$\sum_{m=1}^M \xi^{km} y^m = 1 - \beta \sum_{i=1}^{N_k} x_i^k, \quad (11)$$

$k = 1, \dots, M$ . Denote by  $\xi$  the  $M \times M$  matrix with coefficients  $(\xi^{km})$ .

**Assumption 1:** *We will assume that  $\xi$  is invertible.*

If we denote by  $\chi$  the vector whose  $k$  component is

$$\chi^k = \sum_{i=1}^{N_k} x_i^k,$$

and by  $\mathbf{1}$  the vector of  $k$  ones, then (11) can be rewritten as

$$y = \xi^{-1}(\mathbf{1} - \beta\chi). \quad (12)$$

Let  $\zeta^{km}$  denote the cofactor of the entry  $\xi^{km}$  of  $\xi$ . Then  $y^k$  can be rewritten as

$$y^k = \frac{1}{\det \xi} \left( \sum_{m=1}^M \zeta^{mk} - \beta \sum_{m=1}^M \zeta^{mk} \sum_{i=1}^{N_m} x_i^m \right) \quad (13)$$

Let  $y_0^k = \frac{1}{\det \xi} \sum_{m=1}^M \zeta^{mk}$  then

$$y^k = y_0^k - \frac{\beta}{\det \xi} \sum_{m=1}^M \zeta^{mk} \sum_{i=1}^{N_m} x_i^m, \quad (14)$$

$k = 1, \dots, M$ .

Substituting (14) into (1) we obtain that the dynamics on the limit slow manifold is governed by the equation

$$\dot{x}_i^k = x_i^k \left( \sigma_i^k y_0^k - \sum_{j=1}^{N_k} \rho_{ij}^k x_j^k - \frac{\beta \sigma_i^k}{\det \xi} \sum_{m=1}^M \zeta^{mk} \sum_{j=1}^{N_m} x_j^m \right), \quad (15)$$

for  $i = 1, \dots, N_k, k = 1, \dots, M$ .

**Assumption 2:**

*We assume that*

$$y_0^k \equiv \frac{1}{\det \xi} \sum_{m=1}^M \zeta^{mk} > 0, \quad \text{for } k = 1, \dots, M.$$

### 3 In-chunk dynamics

Fix  $k_0$ . If  $x_i^k = 0$ , for  $k \neq k_0$ , then the equation (15) becomes

$$\dot{x}_i^{k_0} = x_i^{k_0} \left( \sigma_i^{k_0} y_0^{k_0} - \sum_{j=1}^{N_{k_0}} (\rho_{ij}^{k_0} + \sigma_i^{k_0} \frac{\beta \zeta^{k_0 k_0}}{\det \xi}) x_j^{k_0} \right), \quad (16)$$

$i = 1, \dots, N_{k_0}$ . The non-zero fixed point, call it  $P_i^{k_0}$ , on the  $x_i^{k_0}$ -axis has the coordinates  $x_j^{k_0} = 0$ , for  $j \neq i$ , and  $x_i^{k_0} = \sigma_i^{k_0} y_0^{k_0} (1 + \beta \sigma_i^{k_0} \frac{\zeta^{k_0 k_0}}{\det \xi})^{-1}$ . The coordinates of the equilibrium points should be positive, so we impose the following.

#### Assumption 3

We assume that  $1 + \beta \sigma_i^{k_0} \frac{\zeta^{k_0 k_0}}{\det \xi} > 0$ .

Let us impose conditions under which the system (16) has a stable heteroclinic cycle consisting of the points  $P_{i_1}^{k_0}, P_{i_2}^{k_0}, \dots, P_{i_t}^{k_0}$  and heteroclinic trajectories joining them.

The restriction of the system (16) on the  $(x_{i_s}^{k_0}, x_i^{k_0})$  invariant plane has the form

$$\begin{aligned} \dot{x}_{i_s}^{k_0} &= x_{i_s}^{k_0} (\sigma_{i_s}^{k_0} y_0^{k_0} - (1 + \beta \sigma_{i_s}^{k_0} \frac{\zeta^{k_0 k_0}}{\det \xi}) x_{i_s}^{k_0} - (\rho_{i_s i}^{k_0} + \beta \sigma_{i_s}^{k_0} \frac{\zeta^{k_0 k_0}}{\det \xi}) x_i^{k_0}) \\ \dot{x}_i^{k_0} &= x_i^{k_0} (\sigma_i^{k_0} y_0^{k_0} - (\rho_{i i_s}^{k_0} + \beta \sigma_i^{k_0} \frac{\zeta^{k_0 k_0}}{\det \xi}) x_{i_s}^{k_0} - (1 + \beta \sigma_i^{k_0} \frac{\zeta^{k_0 k_0}}{\det \xi}) x_i^{k_0}) \end{aligned} \quad (17)$$

It is natural to assume that the coupling in (16) is of inhibitory type, so we add to Assumption 3 the following claims:

$$\begin{aligned} \rho_{i_s i}^{k_0} + \beta \sigma_{i_s}^{k_0} \frac{\zeta^{k_0 k_0}}{\det \xi} &> 0, \\ \rho_{i i_s}^{k_0} + \beta \sigma_i^{k_0} \frac{\zeta^{k_0 k_0}}{\det \xi} &> 0. \end{aligned} \quad (18)$$

which will be referred to below as Assumption 3. Of course it is now easy to see that they hold if  $\zeta^{k_0 k_0} > 0$ .

At the equilibrium point  $x_i^{k_0} = 0$ ,  $x_{i_s}^{k_0} = \sigma_{i_s}^{k_0} y_0^{k_0} \left(1 + \beta \sigma_{i_s}^{k_0} \frac{\zeta^{k_0 k_0}}{\det \zeta}\right)^{-1}$  the eigenvalues are:

$$-\sigma_{i_s}^{k_0} y_0^{k_0} \quad \text{and} \quad \sigma_i^{k_0} y_0^{k_0} - \sigma_{i_s}^{k_0} y_0^{k_0} \left( \rho_{i i_s}^{k_0} + \beta \sigma_i^{k_0} \frac{\zeta^{k_0 k_0}}{\det \xi} \right) \left( 1 + \beta \sigma_{i_s}^{k_0} \frac{\zeta^{k_0 k_0}}{\det \xi} \right)^{-1}.$$

We will assume that this point is a saddle with the one-dimensional manifold inside the  $k_0$ -chunk.

**Assumption 4**

$$\sigma_i^{k_0} - \sigma_{i_s}^{k_0} \left( \rho_{i i_s}^{k_0} + \beta \sigma_i^{k_0} \frac{\zeta^{k_0 k_0}}{\det \xi} \right) \left( 1 + \beta \sigma_{i_s}^{k_0} \frac{\zeta^{k_0 k_0}}{\det \xi} \right)^{-1} < 0,$$

if  $i \neq i_{s+1}$ , and

$$\sigma_{i_{s+1}}^{k_0} - \sigma_{i_s}^{k_0} \left( \rho_{i_{s+1} i_s}^{k_0} + \beta \sigma_{i_{s+1}}^{k_0} \frac{\zeta^{k_0 k_0}}{\det \xi} \right) \left( 1 + \beta \sigma_{i_s}^{k_0} \frac{\zeta^{k_0 k_0}}{\det \xi} \right)^{-1} > 0,$$

for  $s = 1, \dots, l$ , with  $i_{l+1} \equiv i_1$ . If one expands these terms, the inequalities can be simplified to:

$$\rho_{i i_s}^{k_0} > \frac{\sigma_i^{k_0}}{\sigma_{i_s}^{k_0}}, \quad i \neq i_s, \quad \text{and} \quad \rho_{i_{s+1} i_s}^{k_0} < \frac{\sigma_{i_{s+1}}^{k_0}}{\sigma_{i_s}^{k_0}}. \quad (19)$$

The restriction of the system (16) on the  $(x_{i_s}^{k_0}, x_{i_{s+1}}^{k_0})$  plane has the form (17) where  $i = i_{s+1}$ .

The point:

$$x_{i_s}^{k_0} = 0 \quad x_{i_{s+1}}^{k_0} = \sigma_{i_{s+1}}^{k_0} y_0^{k_0} \cdot \left( 1 + \beta \sigma_{i_{s+1}}^{k_0} \frac{\zeta^{k_0 k_0}}{\det \zeta} \right)^{-1}$$

on this plane has as the eigenvalues of the linearization matrix:

$$-\sigma_{i_{s+1}}^{k_0} y_0^{k_0} \quad \text{and} \quad \sigma_{i_s}^{k_0} y_0^{k_0} - \sigma_{i_{s+1}}^{k_0} y_0^{k_0} \left( \rho_{i_s i_{s+1}}^{k_0} + \beta \sigma_{i_s}^{k_0} \frac{\zeta^{k_0 k_0}}{\det \zeta} \right) \left( 1 + \beta \sigma_{i_{s+1}}^{k_0} \frac{\zeta^{k_0 k_0}}{\det \zeta} \right)^{-1},$$

and thus is a stable node with the leading direction transversal to the  $x_{i_{s+1}}$ -axis if we make the following assumption.

**Assumption 5**

$$-\sigma_{i_{s+1}}^{k_0} < \sigma_{i_s}^{k_0} - \sigma_{i_{s+1}}^{k_0} \left( \rho_{i_s i_{s+1}}^{k_0} + \beta \sigma_{i_s}^{k_0} \frac{\zeta^{k_0 k_0}}{\det \xi} \right) \left( 1 + \beta \sigma_{i_{s+1}}^{k_0} \frac{\zeta^{k_0 k_0}}{\det \zeta} \right)^{-1}.$$

The right inequality in Assumption 5 can be rewritten as:

$$\frac{\sigma_{i_{s+1}}^{k_0}}{\sigma_{i_s}^{k_0}} > \frac{1}{\rho_{i_s i_{s+1}}^{k_0}}, \quad (20)$$

and the left inequality as:

$$\rho_{i_s i_{s+1}}^{k_0} < \frac{\sigma_{i_s}^{k_0}}{\sigma_{i_{s+1}}^{k_0}} + 1 + \beta \sigma_{i_{s+1}}^{k_0} \frac{\zeta^{k_0 k_0}}{\det \xi}, \quad (21)$$

so if

$$\frac{\sigma_{i_s}^{k_0}}{\sigma_{i_{s+1}}^{k_0}} < \rho_{i_s i_{s+1}}^{k_0} < \frac{\sigma_{i_s}^{k_0}}{\sigma_{i_{s+1}}^{k_0}} + 1, \quad (22)$$

then Assumption 5 is satisfied for all positive values of  $\beta$ .

We impose now the conditions under which this direction remains to be leading for the equilibrium  $P_{i_s}^{k_0}$  of the system (16). For that, we should find the eigenvalues of the linearization matrix at the point  $P_{i_{s+1}}^{k_0}$  for the system

$$\begin{aligned} \dot{x}_i^{k_0} &= x_i^{k_0} \left( \sigma_i^{k_0} y_0^{k_0} - (1 + \beta \sigma_i^{k_0} \frac{\zeta^{k_0 k_0}}{\det \xi}) x_i^{k_0} - (\rho_{i i_{s+1}}^{k_0} + \beta \sigma_i^{k_0} \frac{\zeta^{k_0 k_0}}{\det \xi}) x_{i_{s+1}}^{k_0} \right), \\ \dot{x}_{i_{s+1}}^{k_0} &= x_{i_{s+1}}^{k_0} \left( \sigma_{i_{s+1}}^{k_0} y_0^{k_0} - (1 + \beta \sigma_{i_{s+1}}^{k_0} \frac{\zeta^{k_0 k_0}}{\det \xi}) x_{i_{s+1}}^{k_0} - (\rho_{i_{s+1} i}^{k_0} + \beta \sigma_{i_{s+1}}^{k_0} \frac{\zeta^{k_0 k_0}}{\det \xi}) x_i^{k_0} \right), \end{aligned} \quad (23)$$

for  $i \neq i_{s+2}, i_s$ .

At the point  $P_{i_{s+1}}^{k_0}$ , the coordinates are  $x_i^{k_0} = 0$ ,  $x_{i_{s+1}}^{k_0} = \sigma_{i_{s+1}}^{k_0} y_0^{k_0} (1 + \beta \sigma_{i_{s+1}}^{k_0} \frac{\zeta^{k_0 k_0}}{\det \xi})^{-1}$ , and the eigenvalues are:

$$-\sigma_{i_{s+1}}^{k_0} y_0^{k_0} \quad \text{and} \quad \sigma_i^{k_0} y_0^{k_0} - y_0^{k_0} \sigma_{i_{s+1}}^{k_0} \left( \rho_{i i_{s+1}}^{k_0} + \beta \sigma_i^{k_0} \frac{\zeta^{k_0 k_0}}{\det \xi} \right) \left( 1 + \beta \sigma_{i_{s+1}}^{k_0} \frac{\zeta^{k_0 k_0}}{\det \xi} \right)^{-1}$$

### Assumption 6

$$\begin{aligned} \sigma_i^{k_0} - \sigma_{i_{s+1}}^{k_0} \left( \rho_{i i_{s+1}}^{k_0} + \beta \sigma_i^{k_0} \frac{\zeta^{k_0 k_0}}{\det \xi} \right) \left( 1 + \beta \sigma_{i_{s+1}}^{k_0} \frac{\zeta^{k_0 k_0}}{\det \xi} \right)^{-1} \\ < \sigma_{i_s}^{k_0} - \sigma_{i_{s+1}}^{k_0} \left( \rho_{i_s i_{s+1}}^{k_0} + \beta \sigma_{i_s}^{k_0} \frac{\zeta^{k_0 k_0}}{\det \xi} \right) \left( 1 + \beta \sigma_{i_{s+1}}^{k_0} \frac{\zeta^{k_0 k_0}}{\det \xi} \right)^{-1} \end{aligned} \quad (24)$$

for  $i \neq i_{s+2}, i_s$ .

Under this assumption the leading direction belongs to the  $(x_{i_s}^{k_0}, x_{i_{s+1}}^{k_0})$ -plane and corresponds to the eigenvalue in the inequality in Assumption 6. The inequality (24) can be rewritten in a much simpler form:

$$\sigma_i^{k_0} + \sigma_{i_{s+1}}^{k_0} \rho_{i_s i_{s+1}}^{k_0} < \sigma_{i_s}^{k_0} + \sigma_{i_{s+1}}^{k_0} \rho_{i i_{s+1}}^{k_0}. \quad (25)$$

**Remark.** It is useful to list our assumptions in the case  $\beta = 0$ . The assumptions 1 and 2 are independent of  $\beta$ , the assumption 3 is automatically satisfied. The assumption 4 becomes:

$$\sigma_i^{k_0} - \rho_{i i_s}^{k_0} \sigma_{i_s}^{k_0} < 0 \text{ if } i \neq i_{s+1} \quad \text{and} \quad \sigma_{i_{s+1}}^{k_0} - \rho_{i_{s+1} i_s}^{k_0} \sigma_{i_s}^{k_0} > 0. \quad (26)$$

The assumption 5 becomes

$$-\sigma_{i_{s+1}}^{k_0} < \sigma_{i_s}^{k_0} - \rho_{i_s i_{s+1}}^{k_0} \sigma_{i_{s+1}}^{k_0}, \quad (27)$$

and the assumption 6 becomes

$$\sigma_i^{k_0} - \rho_{i i_{s+1}}^{k_0} \sigma_{i_{s+1}}^{k_0} < \sigma_{i_s}^{k_0} - \rho_{i_s i_{s+1}}^{k_0} \sigma_{i_{s+1}}^{k_0}, \quad (28)$$

These are exactly the equalities in [Afraimovich et al, 2004] where they have been shown to guarantee the existence of heteroclinic sequences.

The following theorem is the direct corollary of the considerations above.

**Theorem 3.1** (1) *Under the assumptions 2-5 the system (16) has a heteroclinic cycle  $\Gamma_{k_0}$  consisting of the saddles  $P_1^{k_0}, \dots, P_{i_t}^{k_0}$  and the joining heteroclinic trajectories.*

(2) *If, in addition, the assumptions 5 and 6 are satisfied then the heteroclinic trajectory joining  $P_{i_s}^{k_0}$  to  $P_{i_{s+1}}^{k_0}$  approaches  $P_{i_{s+1}}^{k_0}$  along the leading direction on the  $(x_{i_s}^{k_0}, x_{i_{s+1}}^{k_0})$ -plane, transversal to the  $x_{i_{s+1}}^{k_0}$ -axis.*

We impose stability conditions for the heteroclinic cycle  $\Gamma$ . First, let us recall (see [Shilnikov et al, 1998, Rabinovich et al, 2006]) that if  $P$  is a saddle point with eigenvalues  $\lambda_1, \lambda_2, \dots, \lambda_p, \text{Re } \lambda_s < 0, s = 1, \dots, p$  and  $\gamma_1, \gamma_2, \dots, \gamma_q, \text{Re } \gamma_t > 0, t = 1, \dots, q$ , then the number

$$\nu = \frac{-\min_s \text{Re } \lambda_s}{\max_t \text{Re } \gamma_t}$$

is called the saddle value of  $P$  (see also [Afraimovich et al, 2004], [Afraimovich & Hsu 2003]). If  $\nu > 1$  then the saddle is dissipative. In our case:

$$\nu_{i_s}^{k_0} = \frac{\sigma_{i_{s+1}}^{k_0} \left( \rho_{i_s i_{s+1}}^{k_0} + \beta \sigma_{i_{s+1}}^{k_0} \frac{\zeta^{k_0 k_0}}{\det \xi} \right) \left( 1 + \beta \sigma_{i_{s+1}}^{k_0} \frac{\zeta^{k_0 k_0}}{\det \xi} \right)^{-1} - \sigma_{i_s}^{k_0}}{\sigma_{i_{s+1}}^{k_0} - \sigma_{i_s}^{k_0} \left( \rho_{i_{s+1} i_s}^{k_0} + \beta \sigma_{i_{s+1}}^{k_0} \frac{\zeta^{k_0 k_0}}{\det \xi} \right) \left( 1 + \beta \sigma_{i_s}^{k_0} \frac{\zeta^{k_0 k_0}}{\det \xi} \right)^{-1}} \quad (29)$$



is the saddle value of the saddle  $P_{i_s}^{k_0}$  (of the system (16)).

**Theorem 3.2** *Under the assumptions 1-6, if the inequality*

$$\prod_{s=1}^{\ell} \nu_{i_s}^{k_0} > 1$$

*is satisfied then the heteroclinic cycle  $\Gamma_{k_0}$  is asymptotically stable in the sense that for any initial point with non-negative coordinates in an open set in a neighborhood of  $P_{i_1}$ , the  $\omega$ -limit set of the trajectory going through this point is  $\Gamma_{k_0}$ .*

The proof of the theorem can be done in the same way as in [Rabinovich et al, 08; Afraimovich et al, 2004; Rabinovich et al, 06].

Of course, if  $\nu_{i_s}^{k_0} > 1$  for each  $s = 1, \dots, \ell$ , then the condition of the Theorem is automatically satisfied.

Let us mention again that the heteroclinic cycle  $\Gamma_{k_0}$  is asymptotically stable only for the "in-chunk" subsystem (16).

## 4 Inter-chunk dynamics

We impose now the conditions under which there exists a heteroclinic network consisting of sequentially coupled heteroclinic cycles, say,  $\Gamma_{k_1}, \dots, \Gamma_{k_p}$ .

For the sake of simplicity let us assume that  $k_j = j, j = 1, \dots, p$ , so that  $k_0$  in the previous considerations will take values  $1, \dots, p$ . We consider the restriction of the system (15) onto the invariant  $(x_{i_s}^m, x_{i_s}^{m+1})$ -plane,  $m = 1, \dots, p - 1, s = 1, k$ ,

$$\begin{aligned} \dot{x}_{i_s}^m &= x_{i_s}^m \left( \sigma_{i_s}^m y_0^m - \left(1 + \frac{\beta \sigma_{i_s}^m \zeta^{mm}}{\det \xi}\right) x_{i_s}^m - \frac{\beta \sigma_{i_s}^m \zeta^{m+1,m}}{\det \xi} x_{i_s}^{m+1} \right) \\ \dot{x}_{i_s}^{m+1} &= x_{i_s}^{m+1} \left( \sigma_{i_s}^{m+1} y_0^{m+1} - \left(1 + \frac{\beta \sigma_{i_s}^{m+1} \zeta^{m+1,m+1}}{\det \xi}\right) x_{i_s}^{m+1} - \frac{\beta \sigma_{i_s}^{m+1} \zeta^{m,m+1}}{\det \xi} x_{i_s}^m \right) \end{aligned} \quad (30)$$

We assume that the coupling terms in (30) are of the inhibitory type, i.e.

$$\zeta^{m+1,m} > 0, \quad \zeta^{m,m+1} > 0. \quad (31)$$

The eigenvalues at the point  $(\sigma_{i_s}^m y_0^m (1 + \frac{\beta \sigma_{i_s}^m \zeta^{mm}}{\det \xi})^{-1}, 0)$  (which is the projection of  $P_{i_s}^m$  on the  $(x_{i_s}^m, x_{i_s}^{m+1})$ -plane) are:

$$-\sigma_{i_s}^m y_0^m \quad \text{and} \quad \sigma_{i_s}^{m+1} y_0^{m+1} - \sigma_{i_s}^{m+1} y_0^m \frac{\beta \zeta^{mm+1}}{\det \xi} \left(1 + \frac{\beta}{\det \xi} \zeta^{mm}\right)^{-1}.$$

**Assumption 7**

$$y_0^{m+1} - \sigma_{i_s}^m y_0^m \frac{\beta \zeta^{m,m+1}}{\det \xi} \left(1 + \frac{\beta \sigma_{i_s}^m \zeta^{mm}}{\det \xi}\right)^{-1} > 0$$

Under this assumption we have that  $\dim W_{P_{i_s}^u} \geq 2$ .

The point  $P_{i_s}^{m+1}$  with coordinates

$$\left(0, \sigma_{i_s}^{m+1} y_0^{m+1} \left(1 + \beta \sigma_{i_s}^{m+1} \frac{\zeta^{m+1,m+1}}{\det \xi}\right)^{-1}\right)$$

on the  $(x_{i_s}^m, x_{i_s}^{m+1})$ -plane is a node if both eigenvalues of the linearization there are negative,

so

$$\sigma_{i_s}^{m+1} y_0^{m+1} - \sigma_{i_s}^m y_0^m \beta \frac{\zeta^{m,m+1}}{\det \xi} \left(1 + \frac{\beta \sigma_{i_s}^m \zeta^{mm}}{\det \xi}\right)^{-1} < 0.$$

This inequality will be referred to below as Assumption 7.

The two inequalities in this assumption can be written as:

$$y_0^{m+1} > \frac{\beta \sigma_{i_s}^m}{\det \xi} (y_0^m \zeta^{m,m+1} - y_0^{m+1} \zeta^{mm}), \quad (32)$$

$$y_0^m < \frac{\beta \sigma_{i_s}^{m+1}}{\det \xi} (y_0^{m+1} \zeta^{m+1,m} - y_0^m \zeta^{m+1,m+1}). \quad (33)$$

Since  $y_0^m > 0$ , we have to impose the following condition:

$$y_0^{m+1} \zeta^{m+1,m} - y_0^m \zeta^{m+1,m+1} > 0. \quad (34)$$

There are two logical possibilities, depending on the sign of:

$$y_0^m \zeta^{m,m+1} - y_0^{m+1} \zeta^{mm}. \quad (35)$$

We will refer to (i) as the case when this quantity is positive and (ii) when it is negative.

In case (i), equation (32) holds for every  $\beta > 0$  and (33) can be rewritten as:

$$\frac{y_0^m \det \xi}{\sigma_{i_s}^{m+1} (y_0^{m+1} \zeta^{m+1,m} - y_0^m \zeta^{m+1,m+1})} < \beta. \quad (36)$$

In case (ii), when (35) is negative, the inequalities (32) and (33) can be rewritten as:

$$\frac{y_0^m \det \xi}{\sigma_{i_s}^{m+1} (y_0^{m+1} \zeta^{m+1,m} - y_0^m \zeta^{m+1,m+1})} < \beta < \frac{y_0^{m+1} \det \xi}{\sigma_{i_s}^m (y_0^m \zeta^{m,m+1} - y_0^{m+1} \zeta^{m,m})} \quad (37)$$

There are solutions (values of  $\beta$ ) of (37) if

$$\frac{\sigma_{i_s}^{m+1}}{\sigma_{i_s}^m} < \frac{y_0^m (y_0^m \zeta^{m,m+1} - y_0^{m+1} \zeta^{m,m})}{y_0^{m+1} (y_0^{m+1} \zeta^{m+1,m} - y_0^m \zeta^{m+1,m+1})}. \quad (38)$$

We assume that if the case (i) occurs then (36) holds and if the case (ii) takes place then the inequality (38) is satisfied and then a value of  $\beta$  is chosen according to (37).

We impose now the conditions under which  $\dim W_{P_{i_s}^u}^u = 2$ . For that, we consider the restriction of the system (15) into the  $(x_{i_s}^m, x_i^k)$ -plane, where  $k \neq m, k \neq m+1$ . We obtain

$$\begin{aligned} \dot{x}_{i_s}^m &= x_{i_s}^m \left( \sigma_{i_s}^m y_0^m - (1 + \beta \sigma_{i_s}^m \frac{\zeta^{mm}}{\det \xi}) x_{i_s}^m - \beta \sigma_{i_s}^m \frac{\zeta^{km}}{\det \xi} x_i^k \right) \\ \dot{x}_i^k &= x_i^k \left( \sigma_i^k y_0^k - (1 + \beta \sigma_i^k \frac{\zeta^{kk}}{\det \xi}) x_i^k - \beta \sigma_i^k \frac{\zeta^{mk}}{\det \xi} x_{i_s}^m \right). \end{aligned} \quad (39)$$

The eigenvalues at the point  $(\sigma_{i_s}^m y_0^m (1 + \frac{\beta}{\det \xi} \zeta^{mm})^{-1}, 0)$  are

$$-\sigma_{i_s}^m y_0^m \quad \text{and} \quad \sigma_i^k y_0^k - \sigma_{i_s}^m y_0^m \frac{\beta \zeta^{mk}}{\det \xi} \left( 1 + \beta \sigma_{i_s}^m \frac{\zeta^{mm}}{\det \xi} \right)^{-1}.$$

### Assumption 8

$$\sigma_i^k y_0^k - \frac{\beta}{\det \xi} \zeta^{mk} \sigma_{i_s}^m y_0^m \left( 1 + \beta \sigma_{i_s}^m \frac{\zeta^{mm}}{\det \xi} \right)^{-1} < 0,$$

$k \neq m, k \neq m+1$ , for  $i = 1, \dots, N_k$  and  $i_s = 1, \dots, N_m$ .

Under Assumptions 7 and 8 each saddle  $P_{i_s}^m$  has a two-dimensional unstable manifold in the phase space of the system (15).

If Assumption 7 is satisfied, then there are two special heteroclinic trajectories inside the unstable manifold of  $P_{i_s}^m$ . One of them, say,  $\Gamma_{i_s i_{s+1}}^m$ , connects the saddles  $P_{i_s}^m$ , and  $P_{i_{s+1}}^m$  belonging to the same heteroclinic cycle related to the  $m$ -th chunk. Another one, say  $\Gamma_{i_s}^{m_i, m+1}$ , connects the consecutive  $i_s$ -th saddles  $P_{i_s}^m$  and  $P_{i_s}^{m+1}$  of different chunks. All together they form a heteroclinic network,  $\Gamma$ , given by:

$$\Gamma = \bigcup_{k=1}^p \bigcup_{s=1}^l (P_{i_s}^k \cup \Gamma_{i_s i_{s+1}}^k \cup \Gamma_{i_s}^{k, k+1})$$

where  $\Gamma_{i_s}^{p, p+1} = \emptyset, s = 1, \dots, l$ .

We have now proved the following.

**Theorem 4.1** *Under the assumptions of Theorem 2 and assumption 7, there exists a heteroclinic network  $\Gamma$  on the limit slow manifold consisting of heteroclinic cycles  $\Gamma_i$  and the joining heteroclinic trajectories  $\Gamma_i^{k, k+1}$ , for  $i \in \{1, 2, \dots, p\}$ ,  $k \in \{1, 2, \dots, p-1\}$ .*

**Remark.** Assumptions 7 and 8 are similar to these in [Afraimovich et al, 2008] where we studied heteroclinic networks with 2-dimensional unstable manifolds.

To guarantee that a trajectory in a neighborhood of  $\Gamma$  spends a considerable amount of time around the heteroclinic cycle  $\Gamma^{k_0}$  before coming to a vicinity of the next cycle  $\Gamma^{k_0+1}$  we impose the following.

**Assumption 9**

$$\begin{aligned} & \sigma_{i_s}^{m+1} y_0^{m+1} - \sigma_{i_s}^m y_0^m \beta \sigma_{i_s}^{m+1} \frac{\zeta^{m, m+1}}{\det \xi} \left( 1 + \beta \sigma_{i_s}^m \frac{\zeta^{mm}}{\det \xi} \right)^{-1} \\ & > y_0^m \left[ \sigma_{i_{s+1}}^m - \sigma_{i_s}^m \left( \rho_{i_{s+1}, i_s}^m + \beta \sigma_{i_{s+1}}^m \frac{\zeta^{mm}}{\det \xi} \right) \left( 1 + \beta \sigma_{i_s}^m \frac{\zeta^{mm}}{\det \xi} \right)^{-1} \right], \end{aligned}$$

$m = 1, \dots, p-1, s = 1, \dots, l, (p+1 \equiv 1)$ , i.e. the eigenvalue corresponding to  $\Gamma_{i_s i_{s+1}}^m$  is greater than the one corresponding to  $\Gamma_{i_s}^{m, m+1}$ .

**Remark** The system (15) is, in fact, similar to the system in [Rabinovich et al, 2010], the binding model. In particular, the in-chunk dynamics in (16) corresponds to the dynam-

ics in the modality subspace in [Rabinovich et al, 2010] and the inter-chunk interaction corresponds to the interaction between different modalities.

## 5 Estimates around $\Gamma$ .

The goal of this subsection is to find conditions under which the expression  $\omega_k \equiv 1 - \beta \sum_{i=1}^{N_k} x_i^k$ ,  $k = 1, \dots, M$ , will be positive in a neighborhood of the heteroclinic network  $\Gamma$ . As we shall see in the next section, this fact plays a crucial role in the proof of the persistence of the manifold for non-zero values of the small parameter  $\tau$ . The network  $\Gamma$  consists of heteroclinic cycles  $\Gamma_m$  and heteroclinic trajectories  $\Gamma_m^{k,k+1}$ .

### 5.1 In-chunk estimates

Consider first the heteroclinic trajectory in the  $(x_{i_s}^m, x_{i_{s+1}}^m)$ -plane (in chunk case). For the sake of convenience denote  $x := x_{i_s}^m$  and  $y := x_{i_{s+1}}^m$ . Then the system (17) will be rewritten as

$$\begin{aligned} \dot{x} &= x \left( \sigma_i^{k_0} y_0^{k_0} - \left(1 + \beta \sigma_i^{k_0} \frac{\zeta^{k_0 k_0}}{\det \xi}\right) x - \left(\rho_{i_{s+i}}^{k_0} + \beta \sigma_i^{k_0} \frac{\zeta^{k_0 k_0}}{\det \xi}\right) y \right), \\ \dot{y} &= y \left( \sigma_{i_{s+1}}^{k_0} y_0^{k_0} - \left(1 + \beta \sigma_{i_{s+1}}^{k_0} \frac{\zeta^{k_0 k_0}}{\det \xi}\right) y - \left(\rho_{i_{s+i}}^{k_0} + \beta \sigma_{i_{s+1}}^{k_0} \frac{\zeta^{k_0 k_0}}{\det \xi}\right) x \right), \end{aligned} \quad (40)$$

The equilibrium points we are interested in are the saddle point:

$$P_{i_s}^m = (x_\beta, 0), \quad x_\beta = \sigma_{i_s}^m y_0^m \left(1 + \beta \sigma_{i_s}^m \frac{\zeta^{mm}}{\det \xi}\right)^{-1},$$

and the stable node:

$$P_{i_{s+1}}^m = (0, y_\beta), \quad y_\beta = \sigma_{i_{s+1}}^m y_0^m \left(1 + \beta \sigma_{i_{s+1}}^m \frac{\zeta^{mm}}{\det \xi}\right)^{-1}.$$

We show now that the region  $\mathcal{D} = \{(x, y) : 0 < x \leq x_\beta, 0 < y \leq y_\beta\}$ , is positively invariant.

Indeed, for  $x = x_\beta$  and  $0 < y \leq y_\beta$  we have:

$$\dot{x} = -x_\beta \left( \rho_{i_s, i_{s+1}}^m + \beta \sigma_{i_s}^m \frac{\zeta^{mm}}{\det \xi} \right) y < 0$$

because of Assumption 3, and for  $y = y_\beta$ ,  $0 < x \leq x_\beta$

$$\dot{y} = -y_\beta \left( \rho_{i_s+1, i_s}^m + \beta \sigma_{i_s+1}^m \frac{\zeta^{mm}}{\det \xi} \right) x < 0.$$

also because of Assumption 3. It is simple to check that the eigenvector corresponding to the positive eigenvalue at the point  $P_{i_s}^m$  is directed inside  $\mathcal{D}$ , so the heteroclinic trajectory joining  $P_{i_s}^m$  to  $P_{i_s+1}^m$  must lie in  $\mathcal{D}$ .

For points on the  $(x, y)$ -plane the expression  $\omega_m = 1 - \beta(x + y)$  is positive if

$$(x + y) < \frac{1}{\beta}.$$

We find now conditions under which this holds for each point in  $\mathcal{D}$ . It will be so if

$$\sigma_{i_s}^m y_0^m \left( 1 + \beta \sigma_{i_s}^m \frac{\zeta^{mm}}{\det \xi} \right)^{-1} + \sigma_{i_s+1}^m y_0^m \left( 1 + \beta \sigma_{i_s+1}^m \frac{\zeta^{mm}}{\det \xi} \right)^{-1} < \frac{1}{\beta} \quad (41)$$

The inequality (41) is satisfied if

$$\sigma_{i_s}^m y_0^m \left( 1 + \beta_1 \sigma_{i_s}^m \frac{\zeta^{mm}}{\det \xi} \right)^{-1} + \sigma_{i_s+1}^m y_0^m \left( 1 + \beta_1 \sigma_{i_s+1}^m \frac{\zeta^{mm}}{\det \xi} \right)^{-1} < \frac{1}{\beta} \quad (42)$$

where

$$\beta_1 = \frac{y_0^m \det \xi}{\sigma_{i_s}^{m+1} (y_0^{m+1} \zeta^{m+1, m} - y_0^m \zeta^{m+1, m+1})},$$

the expression from (36). If the case in (36) takes place then we impose the condition (42) on  $\beta$ , so that (41) will be satisfied.

In the case that (37) occurs, then we assume that

$$\sigma_{i_s}^m y_0^m \left( 1 + \beta_1 \sigma_{i_s}^m \frac{\zeta^{mm}}{\det \xi} \right)^{-1} + \sigma_{i_s+1}^m y_0^m \left( 1 + \beta_1 \sigma_{i_s+1}^m \frac{\zeta^{mm}}{\det \xi} \right)^{-1} < \frac{1}{\beta_2} \quad (43)$$

where

$$\beta_2 = \frac{y_0^{m+1} \det \xi}{\sigma_{i_s}^m (y_0^m \zeta^{m, m+1} - y_0^{m+1} \zeta^{m, m})},$$

the expression from (37). If (43) holds, then (41) is satisfied for each  $\beta$  from (37).

To show that there are values of parameters satisfying (43) we assume that

$$\frac{\sigma_{i_s}^m}{\sigma_{i_s}^{m+1}} \ll 1 \quad \text{and} \quad \frac{\sigma_{i_s+1}^m}{\sigma_{i_s}^{m+1}} \ll 1,$$

the inequality (43) is approximated by the inequality

$$\sigma_{i_s}^m y_0^m + \sigma_{i_{s+1}}^m y_0^m < \sigma_{i_s}^m \frac{y_0^m \zeta^{m,m+1} - y_0^{m-1} \zeta^{mm}}{y_0^{m+1} \det \xi},$$

or

$$1 + \frac{\sigma_{i_{s+1}}^m}{\sigma_{i_s}^m} < \frac{1}{\det \xi} \left( \frac{\zeta^{m,m+1}}{y_0^{m+1}} - \frac{\zeta^{mm}}{y_0^m} \right). \quad (44)$$

Since the parameters from the left and from the right are independent, one can find their values satisfying this inequality, provided that:

$$1 < \frac{1}{\det \xi} \left( \frac{\zeta^{m,m+1}}{y_0^{m+1}} - \frac{\zeta^{mm}}{y_0^m} \right). \quad (45)$$

## 5.2 Inter-chunk estimates

We consider the system (30) possessing the heteroclinic trajectory  $\Gamma_{i_s}^{m,m+1}$ . Again let  $x := x_{i_s}^m$ ,  $y := x_{i_s}^{m+1}$ , then the system (30) becomes:

$$\begin{aligned} \dot{x} &= x \left( \sigma_{i_s}^m y_0^m - \left(1 + \frac{\beta \sigma_{i_s}^m \zeta^{mm}}{\det \xi}\right) x - \frac{\beta \sigma_{i_s}^m \zeta^{m+1,m}}{\det \xi} y \right) \\ \dot{y} &= y \left( \sigma_{i_s}^{m+1} y_0^{m+1} - \left(1 + \frac{\beta \sigma_{i_s}^{m+1} \zeta^{m+1,m+1}}{\det \xi}\right) y - \frac{\beta \sigma_{i_s}^{m+1} \zeta^{m,m+1}}{\det \xi} x \right), \end{aligned} \quad (46)$$

with the saddle point:

$$P_{i_s}^m = (x_\beta, 0), \quad x_\beta = \sigma_{i_s}^m y_0^m \left(1 + \frac{\beta \sigma_{i_s}^m \zeta^{mm}}{\det \xi}\right)^{-1},$$

and node:

$$P_{i_s}^{m+1} = (0, y_\beta), \quad y_\beta = \sigma_{i_s}^{m+1} y_0^{m+1} \left(1 + \frac{\beta \sigma_{i_s}^{m+1} \zeta^{m+1,m+1}}{\det \xi}\right)^{-1}.$$

Let us show that the region  $\mathcal{E} = \{(x, y) : 0 < x \leq x_\beta, 0 < y \leq y_\beta\}$  is positively invariant.

Indeed, for  $x = x_\beta$  and  $0 < y \leq y_\beta$  we have

$$\dot{x} = -x_\beta \frac{\beta \sigma_{i_s}^m \zeta^{m+1,m}}{\det \xi} y < 0,$$

and for  $y = y_\beta$ ,  $0 < x \leq x_\beta$ , we have:

$$\dot{y} = -y \frac{\beta \sigma_{i_s}^{m+1} \zeta^{m,m+1}}{\det \xi} x < 0,$$

since we have assumed in (31) that  $\zeta^{m+1,m} > 0$  and  $\zeta^{m,m+1} > 0$ .

For the points on the  $(x, y)$ -plane, the expression  $\omega_m = 1 - \beta x$  and  $\omega_{m+1} = 1 - \beta y$ , so  $\omega_m > 0$  if  $x < 1/\beta$ ,  $\omega_{m+1} > 0$  if  $y < 1/\beta$ , and these inequalities will be satisfied if

$$x_\beta < \frac{1}{\beta} \quad \text{and} \quad y_\beta < \frac{1}{\beta},$$

since for each point on  $\Gamma_{i_s}^{m,m+1}$  we have  $0 < x \leq x_\beta$  and  $0 < y \leq y_\beta$ . But,  $x_\beta < 1/\beta$  because of (41) and  $y_\beta < 1/\beta$ , again because of (41) where  $m$  is replaced by  $m + 1$ .

Thus we have proved the following.

**Lemma 5.1** *There exists a  $\delta$ -neighborhood of the heteroclinic network  $\Gamma$  in the phase space of the system (15) such that for each point in this neighborhood the inequality*

$$\omega_k = 1 - \beta \sum_{i=1}^{N_k} x_i^k > 0, \quad k = 1, \dots, M,$$

*holds provided that in the case (i) the inequalities (42) and (36) are satisfied and in the case (ii) the inequalities (43) and (37) are satisfied.*

## 6 Persistence of the Slow Manifold

We now use standard results due to Fenichel to show that a part of the slow manifold persists for  $\tau > 0$ .

**Proposition 6.1** *The slow manifold  $\mathcal{M}_0$  restricted to a  $\delta$  neighborhood of  $\Gamma$  is normally hyperbolic and attracting in the fast system,*

It follows (see (11) (12) that the slow limit manifold  $\mathcal{M}_0$  is the graph of the function  $y^k = \varphi_k(x)$ ,  $z^k = \psi_k(x)$ , where  $x = \{x_i^k\}$  is the vector of all  $x$ -coordinates,

$$\varphi_k(x) = \frac{1}{\det \xi} \left( \sum_{m=1}^M \zeta^{mk} - \beta \sum_{m=1}^M \zeta^{mk} \sum_{i=1}^{N_m} x_i^m \right)$$



and

$$\psi_k(x) = \sum_{m=1}^M \xi^{km} \varphi_m(x).$$

Denote by  $\mathcal{M}_0^\delta$ , the subset of  $\mathcal{M}_0$  determined by the claim that  $x$  belongs to the  $\delta$ -neighborhood of the heteroclinic network  $\Gamma$

**Proposition 6.2** *If the conditions of Theorem 4.1 and Lemma 5.1 are satisfied, then there exists  $\delta_0$  such that for every  $0 < \delta \leq \delta_0$ , the manifold  $\mathcal{M}_0^\delta$  is normally hyperbolic in the fast system.*

**Proof:** The differential of the vector field of the fast system with respect to all the variables  $y$  and  $z$  is given by the matrix in block form:

$$DF(x, y, z) = \begin{pmatrix} \mathbf{A} & -\mathbf{Y} \\ \boldsymbol{\xi} & -\mathbf{I} \end{pmatrix}. \quad (47)$$

Here  $\mathbf{I}$  is the identity matrix and  $\boldsymbol{\xi} = [\xi_{ij}]$ . The matrix  $-\mathbf{Y}$  is simply the diagonal matrix:

$$-\mathbf{Y} = \begin{pmatrix} -y^1 & 0 & \cdots & 0 \\ 0 & -y^2 & & 0 \\ \vdots & \vdots & \ddots & \vdots \\ 0 & 0 & \cdots & -y^M \end{pmatrix}.$$

$$\mathbf{A} = \begin{pmatrix} (1 - \beta \sum_{i=1}^{N_1} x_i^1) - z^1 & 0 & \cdots & 0 \\ 0 & (1 - \beta \sum_{i=1}^{N_2} x_i^2) - z^2 & & 0 \\ \vdots & \vdots & \ddots & \vdots \\ 0 & 0 & \cdots & (1 - \beta \sum_{i=1}^{N_2} x_i^M) - z^M \end{pmatrix}.$$

However, we notice that on  $\mathcal{M}_0$  the matrix  $\mathbf{A}$  is zero. Thus:

$$DF|_{\mathcal{M}_0} = \begin{pmatrix} \mathbf{0} & -\mathbf{Y} \\ \boldsymbol{\xi} & -\mathbf{I} \end{pmatrix}. \quad (48)$$

Suppose that  $v = (v_1, v_2)$  and  $\lambda$  are an eigenvector/eigenvalue pair for  $DF(\mathcal{M}_0)$ , i.e.

$$\begin{pmatrix} \mathbf{0} & -\mathbf{Y} \\ \boldsymbol{\xi} & -\mathbf{I} \end{pmatrix} \begin{pmatrix} v_1 \\ v_2 \end{pmatrix} = \begin{pmatrix} \lambda v_1 \\ \lambda v_2 \end{pmatrix},$$

or,

$$-\mathbf{Y}v_2 = \lambda v_1, \quad \text{and} \quad \boldsymbol{\xi}v_1 - v_2 = \lambda v_2 \quad (49)$$

Substituting  $v_1 = -\lambda^{-1}\mathbf{Y}v_2$  into the second equation of (49) leads to:

$$-\boldsymbol{\xi}\mathbf{Y}v_2 = \lambda(1 + \lambda)v_2.$$

Therefore,

$$\omega = -(\lambda + \lambda^2)$$

is an eigenvalue of the product matrix  $\boldsymbol{\xi}\mathbf{Y}$ . By the quadratic formula:

$$\lambda = -\frac{1}{2} \pm \frac{1}{2}\sqrt{1 - 4\omega}.$$

If  $\omega$  is positive,  $\lambda$  must have negative real part.

Now, by (12) the diagonal matrix  $\mathbf{Y}$  can be written as:

$$\mathbf{Y} = \boldsymbol{\xi}^{-1}(\mathbf{I} - \beta\boldsymbol{\chi})$$

where  $\boldsymbol{\chi}$  is the diagonal matrix with entries  $\chi^k = \sum_{i=1}^{N_k} x_i^k$ . Thus:

$$\boldsymbol{\xi}\mathbf{Y} = \mathbf{I} - \beta\boldsymbol{\chi}$$

and so the eigenvalues of this diagonal matrix are:

$$\omega_k = 1 - \beta \sum_{i=1}^{N_k} x_i^k.$$

These values are all positive in a neighborhood of the heteroclinic network by Lemma 5.1.

This implies that all the eigenvalues  $\lambda$  of  $DF|_{\mathcal{M}_0}$  have negative real part.

Thus  $\mathcal{M}_0^\delta$  is normally hyperbolic attracting in the fast system.

We can apply the standard technique of Fenichel [Fenichel, 1971] (see, for instance [Hek, 2010; Jones, 1995]) for persistence of  $\mathcal{M}_0^\delta$  for  $\tau > 0$ . Indeed,  $y \neq 0$ , because of (12)

and Lemma 5.1. Therefore, in the region of phase space under consideration, the limit slow manifold has only one connected component - the graph of the function  $y = \phi(x)$ . Furthermore, this manifold is hyperbolic attracting as we have shown.

The desired invariant manifold for  $\tau > 0$  should be the graph of the function  $y^k = \phi_k(x) + \tau \tilde{\phi}_k(x, \tau)$ ,  $z^k = \psi_k(x) + \tau \tilde{\psi}_k(x, \tau)$ , where  $\phi_k$  and  $\psi_k$  are defined above in this section and  $\tilde{\phi}_k, \tilde{\psi}_k$  are smooth functions in the  $\delta$ -neighborhood of  $\Gamma$ . Denote this invariant manifold by  $\mathcal{M}_\tau^\delta$ .

## 7 Heteroclinic sequences for $\tau \neq 0$

Our proof of the existence of a heteroclinic sequence  $\Gamma$  for  $\tau = 0$  relied heavily on the invariance of coordinate axes and two-dimensional coordinate planes. The equation (1) on the manifold  $M_\tau^\delta$  can be rewritten as

$$\dot{x}_i^k = x_i^k \left( \sigma_i^k y_0^k - \sum_{j=1}^{N_k} \rho_{ij}^k x_j^k - \frac{\beta \sigma_i^k}{\det \xi} \sum_{m=1}^M \zeta^{mk} \sum_{j=1}^{N_m} x_j^m + \tau \sigma_i^k \tilde{\phi}_k(x, \tau) \right), \quad (50)$$

so all axes and two-dimensional planes are still invariant. Moreover, all points  $P_{i_s}^k$  on the slow manifold were hyperbolic, so they persist and are hyperbolic for small values of  $\tau$ . Let them be denoted by  $P_{i_s}^k(\tau)$ . All the systems on 2-dimensional planes in equations (17), (23), (30), (39), (40) were structurally stable in their positively invariant regions, so for all small values of  $\tau$  the heteroclinic trajectories, call them  $\Gamma_{i_s i_{s+1}}^k(\tau)$  and  $\Gamma_{i_s}^{k, k+1}(\tau)$  persist and form a heteroclinic network  $\Gamma(\tau)$ . Furthermore, the heteroclinic cycles  $\Gamma_i(\tau)$  are still asymptotically stable and the conditions of Theorem 3.2 are formulated in the form of inequalities that hold for  $\tau \ll 1$ .

Thus we have proved the following main result.

**Theorem 7.1** *Under the conditions of Theorem 4.1 and Lemma 5.1 the system (1)-(3) for  $\theta = \tau \ll 1$  has a heteroclinic network  $\Gamma(\tau)$  consisting of heteroclinic cycles  $\Gamma_i(\tau)$  that are asymptotically stable within the chunk subsystems and heteroclinic trajectories  $\Gamma_{i_s}^{i, i+1}$  joining them. Further,  $\Gamma$  is the topological limit of  $\Gamma(\tau)$  as  $\tau \searrow 0$ .*

## 8 Consistency of assumptions

Let us now list the conditions we have imposed above in terms of the matrix  $\zeta = (\zeta^{mn})_{m,n=1}^M$ .

Assumption 2:

$$\sum_{m=1}^M \zeta^{mk} > 0, \quad k = 1, \dots, M. \quad (51)$$

Assumption 3 :

$$\zeta^{mm} > 0, \quad m = 1, \dots, M. \quad (52)$$

“Inhibitory” assumption (31):

$$\zeta^{m+1,m} > 0, \quad \zeta^{m,m+1} > 0, \quad m = 1, \dots, M. \quad (53)$$

“Positive value” condition (34):

$$y_0^{m+1} \zeta^{m+1,m} - y_0^m \zeta^{m+1,m+1} > 0. \quad (54)$$

Condition for hyperbolicity (45):

$$1 < \frac{1}{\det \xi} \left( \frac{\zeta^{m,m+1}}{y_0^{m+1}} - \frac{\zeta^{mm}}{y_0^m} \right). \quad (55)$$

We show now that there are values of the entries of the matrix  $\zeta$  such that all these assumptions are satisfied. We start with (54), assuming that (51)-(53) are satisfied. The inequality (54) can be rewritten as:

$$0 < \zeta^{m+1,m} \sum_{j=1}^M \zeta^{j,m+1} - \zeta^{m+1,m+1} \sum_{j=1}^M \zeta^{jm} = (\zeta^{m+1,m} - \zeta^{mm}) \sum_{j=1, j \neq m+1}^M \zeta^{jm},$$

for  $m = 1, \dots, M - 1$ . Thus if

$$\zeta^{m+1,m} > \zeta^{mm}, \quad \sum_{j=1, j \neq m+1}^M \zeta^{jm} > 0 \quad m = 1, \dots, M - 1 \quad (56)$$

then (54) will be satisfied. Of course, such entries exist.

The inequality (55) can be rewritten as:

$$1 < \frac{\zeta^{m,m+1}}{\sum_{j=1}^M \zeta^{j,m+1}} - \frac{\zeta^{mm}}{\sum_{j=1}^M \zeta^{jm}} \quad (57)$$

For example, suppose that

$$\sum_{j=1}^M \zeta^{jm} = 2, \quad \zeta^{m+1,m} = 1, \quad \zeta^{m,m+1} = 4, \quad \zeta^{mm} = \frac{1}{4}, \quad (58)$$

then  $\zeta^{m+1,m} > \zeta^{mm}$ ,  $\sum_{j=1, j \neq m+1}^M \zeta^{jm} = 2 - 1 > 0$  and the inequalities in (51)-(53), (56) are satisfied. In addition, (57) is also satisfied if the linear system (58) has solutions. This system can be rewritten as:

$$\begin{aligned} \frac{1}{4} + 1 + \zeta^{31} + \dots + \zeta^{M1} &= 2 \\ 4 + \frac{1}{4} + 1 + \zeta^{42} + \dots + \zeta^{M2} &= 2 \\ \zeta^{13} + 4 + \frac{1}{4} + 1 + \zeta^{42} + \dots + \zeta^{M2} &= 2 \\ &\dots = \dots \\ \zeta^{1M} + \zeta^{2M} + \dots + \zeta^{M-2,M} + 4 + \frac{1}{4} &= 2 \end{aligned} \quad (59)$$

This system has  $M$  equations and  $M^2 - 4M + 5$  unknowns. Since the equations are uncoupled, there exist open sets of solutions for  $M \geq 4$ . One can check that (59) in the case  $M = 3$  has a unique solution. Thus we have proved the next lemma.

**Lemma 8.1** *For  $M \geq 3$ , there are matrices  $\zeta$  satisfying all the desired conditions.*

It follows immediately that there are values of  $\rho_{ij}^k$ ,  $\sigma_i^k$  and  $\beta$  that satisfy all the conditions sufficient for the existence of the heteroclinic network  $\Gamma(\tau)$  for  $0 \leq \tau \ll 1$ .

Now, since  $\frac{1}{\det \xi} \zeta' = \xi^{-1}$ , then  $\xi = \left( \frac{1}{\det \xi} \zeta' \right)^{-1}$  and the inequalities that have been imposed on the entries of the matrix  $\zeta$  can be transformed into some inequalities for the the entries of  $\xi$ . It is a rather cumbersome business, however, and we leave it to the readers dealing with specific systems of the type (1)-(2).

## 9 Conclusion and Future directions

It became clear, since Millerss work, that chunking is one of the key mechanisms of human cognition and behavior. Nevertheless no mathematical background was found for the

description and prediction of the chunking dynamics till today. Based on the results of (Rabinovich et al., 2014), in this paper we proved that in the phase space of the describing chunking model there exists a new mathematical object heteroclinic of heteroclinic sequence (HoHS). Evidently, the HoHS is the adequate image of the chunking processing, and it is playing the similar role in the hierarchical mental activities as the stable heteroclinic channel (SHC) for the non-hierarchical robust transient cognitive dynamics (Afraimovich et al., 2004, Rabinovich et al., 2012).

There are many interesting future directions in this field. We discuss here just two branches of them: a). The study of brain-mind relationship (Meehan and Bressler, 2012) i.e. building of the bridge between brain hierarchical networks activities and the chunking behavior-cognition that is result of such activities, and b). A generalization of the model (1)-(3) for a description of more complex human behavioral and cognition-like perceptual binding, or multicomponent linguistic chunks. Special interest should to be focused on bifurcation analyses of HoHS to apply it to diagnostics and prediction of psychiatric disorders that are related to the chunking dynamics (Maas et al., 2008).

Human complex skill usually consists of a fixed sequence of movements. This is because the stereotyped temporal pattern or the rhythms emerge as human learns to perform a motor sequence, which became serial chunk during the learning process. What is important that the motor and cognitive networks responsible for the organization on the different levels of chunk hierarchy are different. Motor rhythm governed by motor networks in the cerebral cortex controls automatic movements within chunks, and cognitive networks control non-automatic movements between chunks (Sakai et al., 2004). Such structure is the result of evolution (Bor and Seth, 2012) and training that guaranties the flexibility of the chunking organization (Wymbs et al., 2014).

## **Acknowledgments**

Valentin S. Afraimovich was supported by the UASLP sabbatical program and a Glidden Visiting Professorship at Ohio University during the period when this manuscript was

written. Mikhail I. Rabinovich acknowledges support from ONR grant N00014310205.

## References

- [1] Afraimovich V.S. & Hsu S.-B. [2003] *Lectures on Chaotic Dynamical Systems*, vol 28, American Mathematical Society, International Press.
- [2] Afraimovich, V.S., Rabinovich M.I. & Varona P.I. [2004], “Heteroclinic contours in neural ensembles and the winnerless competition principle,” *Int. J. Bifurcation and chaos* **14**(4), 1195-1208.
- [3] Afraimovich V.S., Tristan I., Huerta R. & Rabinovich M.I. [2008], “Winnerless competition principle and prediction of the transient dynamics in a Lotka-Volterra model,” *Chaos* **18**, 43103.
- [4] Afraimovich V.S., Zhigulin, V.P. & Rabinovich M.I. [2004] “On the origin of reproducible sequential activity in neural circuits,” *Chaos* **14**, 1123.
- [5] Bick, C. & Rabinovich, M.I. [2009] “Dynamical origin of the effective storage capacity in the brains working memory,” *Phys. Rev. Lett.* **103**:218101. doi: 10.1103/PhysRevLett.103.218101
- [6] Bor, D. & Seth, A.K. [2012] *Front. Psychol.* **3**, 114. doi 10.3389/fpsyg.2012.00063. doi: 10.1111/j.1460-9568.2004.03438.x.
- [7] Botvinick, M.M. [2008] “Hierarchical models of behavior and prefrontal function,” *Trends Cogns. Sci.* **12**, 201208. doi:10.1016/j.tics.2008.02.009.
- [8] Dowling, W.J. [1973] *Perception & Psychophysics* **14**(1), 37-40
- [9] De Groot, A.D. [1978] *Thought and choice in chess*, The Hague: Mouton Publishers.
- [10] N. Fenichel, N. [1971] “Persistence and smoothness of invariant manifolds for flows,” *Indiana Univ. Math. Journal* **21**, 193226.
- [11] Gobet, F., Lane, P.C.R., Croker, S., Cheng, P.C.-H., Jones, G. & Oliver, I. [2001] *Trends Cogn. Sci.* **5** 236243. doi: 10.1016/S1364-6613(00)01662-4.

- [12] Guida, A., Gobet, F. & Nikolas, S. [2013] *Front. Hum. Neurosci.* **7**, 590. doi:10.3389/fnhum.2013.00590.
- [13] Hek, G. [2010] “Geometric singular perturbation theory in biological practice,” *J. Math. Biol.* **60**, 347-386.
- [14] Jones, C.K.R.T. [1995] “Geometric singular perturbation theory,” *Dynamical Systems, Lecture Notes in Mathematics* **1609** 44-118, Springer, Berlin.
- [15] Kiebel, S.J., von Kriegstein, K., Daunizeau, J. & Friston, K.J. [2009] *PLoS Comput. Biol.* **5**:e1000464. doi:10.1371/journal.pcbi.1000464.
- [16] Koch, I., Philipp, A.M. & Gade, M. [2006] *Psychol. Sci.* **17**, 346350. doi: 10.1111/j.1467- 9280.2006.01709.x.
- [17] Maas, E., Robin, D.A. Hula, S.N.A., Freedman, S.E., Wulf, G., Ballard, K.J. & R.Schmidt, R.A. [2008] *American Journal of Speech-Language Pathology* **17**, 277-98. doi: 10.1044/1058-0360(2008/025)
- [18] Meehan, T.P. & Bressler, S.L. [2012] *Neurosci. Biobehav. Rev.* **36**, 22322247. doi: 10.1016/j.neubiorev.2012.08.002.
- [19] Miller, G.A. [1956] *Psychol. Rev.* **63**, 8197. doi: 10.1037/h0043158.
- [20] Orr, M. [2003] *Interactions between chunking and perceptual learning in expertise*, (Doctoral dissertation, University of Illinois at Chicago, 2003). <http://sumo.ly/B2C>
- [21] Otoo, E., Rotem, D. & Seshadri, S. [2007] *Proceedings ACM tenth Intern. Workshop on data warehousing and OLAP*, ACM, New York, NY, 25-32.
- [22] Rabinovich, M.I., Afraimovich, V.S., Bick, C. & Varona, P. [2012] *Phys. Life Rev.* **9**, 5173. doi: 10.1016/j.pprev.2011.11.002.
- [23] Rabinovich, M.I., Afraimovich, V.S. & Varona P. [2010] “Heteroclinic binding,” *Dyn. Syst.* **25**, 433-442.
- [24] Rabinovich M.I., Huerta R. Varona P. & Afraimovich V.S. [2006] “Generation and reshaping of sequences in neural systems,” *Biological Cybernetics* **95**(6), 519-536.



- [25] Rabinovich, M.I., Huerta R., Varona P. & Afraimovich V.S. [2008] “Transient cognitive dynamics, metastability and decision making,” *PLoS Computational Biology* **4**(5): e100007. doi: 10.1371/journal.pcbi.1000072.
- [26] Rabinovich, M.I., Varona, P., Tristan, I. & Afraimovich, V.S. [2014] “Chunking Dynamics: Heteroclinics in Mind,” *Front. Comput. Neurosci.* **8**, doi: 10.3389/fncom.2014.00022.
- [27] Ribas-Fernandes, J.J.F., Solway, A., Diuk, C., McGuire, J.T., Barto, A.G., Niv, Y. et al. [2011] *Neuron* **71**, 37079. doi: 10.1016/j.neuron.2011.05.042.
- [28] Sahin, N.T., Pinker, S., Cash, S.S., Schomer, D., & Halgren, E., [2009] *Science* **326**, 445449. doi: 10.1126/science.1174481
- [29] Sakai, K., Hikosaka, O. & Nakamura, K. [2004] *Trends. Cognit. Scien.* **8**, 547-553. doi: 10.1016/j.tics.2004.10.005
- [30] Schneider, D.W. [2007] *Psychon. Bull. Rev.* **14**, 970976. doi: 10.3758/BF03194130.
- [31] LP Shilnikov, L.P., AL Shilnikov, A.L., Turaev, D. & Chua, L.O. [1998] *Methods of Qualitative Theory in Nonlinear Dynamics*, vol. 1, World Scientific.
- [32] Wymbs, N.F., Bassett, D.S., Mucha, P.J., Porter, M.A., & Grafton, S.T. [2012] *Neuron* **74**, 93646. DOI: 10.1016/j.neuron.2012.03.038
- [33] Ystad, S., Kronland-Martinet, R. & Jensen, K. (Eds.) [2008] *Computer Music Modeling and Retrieval. Genesis of Meaning in Sound and Music* 5th International Symposium, CMMR 2008 Copenhagen, Denmark, May 19-23, 67-80, 81-92.



# Symbolic Dynamics in Multidimensional Annulus and Chimera States

V. S. Afraimovich

*Instituto de Investigación en Comunicación Óptica, UASLP,  
A. Obregón 64, 78000 San Luis Potosí, SLP, México  
valentin@cactus.iico.uaslp.mx*

L. P. Shilnikov

*Research Institute for Applied Mathematics and Cybernetics,  
10 Uljanov Str., Nizhny Novgorod 603005, Russia*

Received February 2, 2014

We derive sufficient conditions for the existence of an invariant set in an absorbing region homeomorphic to the product of a multidimensional torus and a ball. This set consists of low dimensional tori labeled by symbolic sequences. It may appear as a result of the breakdown of an attracting multidimensional torus. Trajectories on the set manifest chaotic behavior for some angular coordinates and may behave regularly for others, i.e. the dynamics on the set is of the chimera state type.

*Keywords:* Chimera state; topological Markov chain; graph transformation technique; torus breakdown.

## 1. Introduction

This article has an unusual history. The main part was written about 40 years ago. Then we started working on the Lorenz attractor and other problems and forgot about this manuscript. It was discovered recently by Andrey Shilnikov in a bunch of old papers of Leonid Pavlovich. Andrey suggested to Afraimovich to look through the manuscript and to finish writing. We believe that the article still would be interesting for specialists on the field of nonlinear dynamics.

Attracting invariant tori exist in the phase space of weakly coupled dissipative oscillatory systems and serve as mathematical images of the established quasi-periodic or periodic with complex discrete Fourier spectrum motions, the regimes. The corresponding Poincaré map possesses an absorbing region  $\mathbb{B}$  homeomorphic to the direct product of the  $p$ -dimensional torus and the  $m$ -dimensional ball with the maximal attractor in  $\mathbb{B}$

being homeomorphic to the  $p$ -dimensional torus that is the intersection of the original invariant torus for the flow with the Poincaré section. But this is true only under some conditions (see the books [Shilnikov *et al.*, 1998; Afraimovich & Hsu, 2003] where these conditions are called “the annulus principle”) which are satisfied if the rates of coupling are small enough, the case of the weak coupling. When these rates grow then, while  $\mathbb{B}$  remains to be absorbing, the maximal attractor could become the strange one, and one can observe a chaotic regime, so called the “torus-chaos”. This phenomenon that is called the torus breakdown was discovered and studied in [Afraimovich & Shilnikov, 1974; Curry & Yorke, 1978; Afraimovich & Shilnikov, 1977, 1991] for the case  $p = 1$  (see also [Bryant & Jeffries, 1987] and [Arnold *et al.*, 1991]), and was observed in many natural and man-made systems (some references can be found in [Afraimovich, 2007]). For dynamical systems generated by noninvertible maps, the torus

breakdown may also occur but its mechanism can be different (see, for instance, [Maistrenko *et al.*, 2003]).

In multidimensional situations,  $p > 1$ , there is no such clear picture of the torus breakdown as for  $p = 1$  although some interesting results for specific systems have been obtained, see, for instance, [Aranson & Rulkov, 1989, 1988a, 1988b; Anishchenko & Nikolaev, 2008]. Nevertheless, one can guess that, as for  $p = 1$ , the breakdown of the torus is accompanied by the appearance of a strange attractor containing a Smale horseshoe for tori of a smaller dimension. In other words, a symbolic dynamics where each symbolic sequence labels a torus of a smaller dimension, has to work. In the paper, we present sufficient conditions for the occurrence of such symbolic dynamics.

The form of these conditions indicates the fact that a part of angular coordinates behaves chaotically while another part may manifest a regular behavior. For such kind of behavior that was discovered, first, in [Kuramoto & Battogtokh, 2002] the term “chimera state” was introduced in [Abrams & Strogatz, 2004]. Many essential features of chimera states have been discovered and studied (see, for instance, [Omelchenko *et al.*, 2010; Wolfrum *et al.*, 2011] and references therein) but all of them are related to models where only the phase (angular) coordinates are taken into account while the influence of the amplitude coordinates is neglected. In this work, we consider a situation where both the phase and the amplitude coordinates play an important role.

## 2. Set-Up and the Main Theorem

We consider a diffeomorphism  $T : \mathbb{B} \rightarrow \mathbb{B}$  where  $\mathbb{B} = \mathbb{D}^m \times \mathbb{T}^n \times \mathbb{T}^l$ ,  $\mathbb{D}^m$  is an  $m$ -dimensional ball and  $\mathbb{T}^n$  ( $\mathbb{T}^l$ ) is the  $n$ -dimensional ( $l$ -dimensional) torus, that can be presented as follows:

$$\begin{aligned} T(x, \theta, \phi) &= (\bar{x}, \bar{\theta}, \bar{\phi}) : \bar{x} = f(x, \theta, \phi), \\ \bar{\theta} &= g(x, \theta, \phi), \quad \text{mod } 1, \\ \bar{\phi} &= h(x, \theta, \phi), \quad \text{mod } 1, \end{aligned} \quad (1)$$

where  $x \in \mathbb{D}^m$ ,  $\|x\| \leq k$ ,  $\theta \in \mathbb{R}^n$  and  $\phi \in \mathbb{R}^l$  are the angle coordinates, and  $f, g, h$  are  $C^1$  smooth functions. The functions  $g$  and  $h$  can be written in the form:  $g \equiv A\theta + g_1(x, \theta, \phi)$ ,  $h \equiv \phi + h_1(x, \theta, \phi)$  where  $A$  has integer entries,  $\det A \neq 0$  and  $g_1, h_1$ , as well as  $f$ , are 1-periodic in  $(\theta, \phi)$  functions. The

differential

$$\partial T = \begin{pmatrix} f_x & f_\theta & f_\phi \\ g_{1x} & A + g_{1\theta} & g_{1\phi} \\ h_{1x} & h_{1\theta} & I + R_{1\phi} \end{pmatrix}.$$

We assume that the following condition is satisfied.

**Assumption 1.** There is a finite collection of disjoint sets

$$\begin{aligned} \mathbb{J}_i &= \{(x, \theta, \phi) : \|x\| \leq k, \\ &0 < \theta_{ij}^0 \leq \theta_j \leq \theta_{ij}^1 < 1, j = 1, \dots, n, \\ &0 \leq \phi_k \leq 1, k = 1, \dots, l\}, \quad i = 1, \dots, N, \end{aligned}$$

homeomorphic to the product of  $(m + n)$ -dimensional ball  $\mathbb{B}^{m+n}$  and the  $l$ -dimensional torus  $\mathbb{T}^l$  such that for each point  $\mathbf{P} = (x, \theta, \phi)$  inside the union  $\mathbb{J}_1 \cup \mathbb{J}_2 \cup \dots \cup \mathbb{J}_N =: \mathbb{J} \subset \mathbb{B}$  the following inequalities hold

$$\|f_x(x, \theta, \phi)\| \leq q < 1, \quad \|g_\theta^{-1}\| \leq p < 1. \quad (2)$$

It means that map  $T$  is a contraction in the  $x$ -directions and an expansion in the  $\theta$ -directions.

We consider now a family of differentiable maps  $T_{(x,\phi)} : \mathbb{T}^n \rightarrow \mathbb{T}^n$  determined by the formula

$$\bar{\theta} = g(x, \theta, \phi), \quad \text{mod } 1, \quad (3)$$

where  $x$  and  $\phi$  are parameters,  $\|x\| \leq k$ ,  $\phi \in \mathbb{R}^l$ . Denote by  $Q_t$  the ball  $\theta_{tj}^0 \leq \theta_j \leq \theta_{tj}^1$ ,  $j = 1, \dots, n$ , in  $\mathbb{R}^n$ ,  $t = 1, \dots, N$ . We say that  $Q_t$  covers  $Q_s$  with multiplicity  $m_{t,s} \in \mathbb{Z}$  if each point  $\theta \in Q_s$  has exactly  $m_{t,s}$  preimages in  $Q_t$  under the map  $T_{(x,\phi)}$  for every  $x$ ,  $\|x\| \leq k$ ,  $\phi \in \mathbb{R}^l$ .

Evidently the map  $\hat{T}_{(x,\phi)} : \theta \rightarrow \bar{\theta} = g(x, \theta, \phi)$  is a lift map for the map  $T_{(x,\phi)}$  that is the diffeomorphism on the image for each  $Q_t$ . If  $Q_t$  covers  $Q_s$  with the multiplicity  $m_{t,s}$  then for every  $(x, \phi)$ ,  $\|x\| \leq k$ ,  $\phi \in \mathbb{R}^l$ , there are  $m_{t,s}$  different integer vectors  $k_1, \dots, k_{m_{t,s}} \in \mathbb{R}^n$  such that for each  $\alpha = 1, \dots, m_{t,s}$  the set  $\{\hat{T}_{(x,\phi)}(Q_t) - k_\alpha\} \supset Q_s$ , i.e.  $\hat{T}_{(x,\phi)}^{-1}(Q_s + k_\alpha) \subset Q_t$  and  $\hat{T}_{(x,\phi)}^{-1}(Q_s + k_{\alpha_1}) \cap \hat{T}_{(x,\phi)}^{-1}(Q_s + k_{\alpha_2}) = \emptyset$ , if  $\alpha_1 \neq \alpha_2$ .

In fact, the vectors  $k_\alpha$  do not depend on  $(x, \phi)$  since: (i)  $\hat{T}_{(x,\phi)}$  is the lift map for  $T_{(x,\phi)}$  on the whole torus  $\mathbb{T}^n$ ; (ii)  $\hat{T}_{(x,\phi)}$  depends continuously on  $(x, \phi)$ , and (iii) the sets  $\{Q_s + k_\alpha\}$  do not intersect each other (for different  $\alpha$ ) in  $\mathbb{R}^n$ .

We introduce now the matrix  $B = (m_{t,s})_{t,s=1}^N$  and the corresponding graph having  $N$  vertices

$v_1, v_2, \dots, v_N$  such that the number of edges starting at the vertex  $v_t$  and ending at the vertex  $v_s$  equals  $m_{t,s}$ .

Denote by  $e_1, \dots, e_L$  the edges of the graph  $G$  and introduce the matrix  $A = (a_{ij})$ ,  $1 \leq i, j \leq L$ , where  $a_{ij} = 1$  if there is a vertex  $v_t$  which is the starting point of the edge  $e_j$  and the end point of the edge  $e_i$ , and equals 0 otherwise. We treat  $A$  as the transition matrix of the topological Markov chain  $tMc(\sigma_1 \Omega_A)$ , the edge subshift of finite type, where  $\Omega_A$  is the set of  $A$ -admissible sequences  $\mathbf{i} = (\dots i_{-1} i_0 \dots i_p \dots)$ ,  $i_p \in \{1, 2, \dots, L\}$ ,  $a_{i_k i_{k+1}} = 1$ ,  $k \in \mathbb{Z}$ , endowed with the distance  $d(\mathbf{i}, \mathbf{j}) = \sum_{k=-\infty}^{\infty} \frac{|i_k - j_k|}{q_0^{|k|}}$ ,  $q_0 > 1$ , and  $\sigma$  is the shift map  $(\sigma \mathbf{i})_k = i_{k+1}$ ,  $k \in \mathbb{Z}$ . The topological entropy  $h_{\text{top}}(\sigma) = \max \ln |\lambda_k|$ ,  $\lambda_k \in \text{spec} A$ , so if  $h_{\text{top}}(\sigma) > 0$ , the  $tMc(\sigma, \Omega_A)$  contains infinitely many periodic points and manifests a chaotic behavior on  $\Omega_A$  (or on a part of  $\Omega_A$ ).

Denote by  $\|\cdot\|_0 = \sup_{(x,\theta,\phi) \in \mathbb{J}} \|\cdot\|$  where  $\|\cdot\|$  is the usual norm of the vector or the matrix.

Let  $C_1 := \max\{\|g_x\|_0, \|h_x\|_0\}$ ,  $C_2 := \max\{\|h_{1\theta}\|_0, \|h_{1\phi}\|_0\}$ ,  $C_3 := \max\{\|f_\theta\|_0, \|f_\phi\|_0\}$ ,  $C_4 := \|g_\phi\|_0$ .

Denote by  $\Sigma$  the set of all points of all trajectories belonging to  $\mathbb{J}$ .

**Theorem 1.** *Under the Assumption 1 and provided that the following conditions are satisfied:*

$$\begin{aligned} q < \frac{1}{4}, \quad p < \frac{1}{4}, \quad C_2 < \frac{1}{4}, \quad C_4 \cdot C_2 < \frac{1}{4}, \\ qC_4 < \frac{1}{8}, \quad \sqrt{C_1 C_3} \cdot C_4 < \frac{1}{16}, \\ \sqrt{C_1 C_3} < \frac{1}{8}, \quad C_4 \leq C_2 \end{aligned} \quad (4)$$

there exists a continuous map  $\beta : \Sigma \rightarrow \Omega_A$  such that:

(1) the diagram

$$\begin{array}{ccc} \Sigma & \xrightarrow{T} & \Sigma \\ \beta \downarrow & & \beta \downarrow \\ \Omega_A & \xrightarrow{\sigma} & \Omega_A \end{array}$$

is commutative, i.e.  $\beta$  is a semi-conjugacy,

(2) for each  $\mathbf{i} \in \Omega_A$ , the set  $\beta^{-1}(\mathbf{i})$  is the graph of a 1-periodic continuous vector function  $x = x_{\mathbf{i}}(\phi)$ ,  $\theta = \theta_{\mathbf{i}}(\phi)$ ,  $\phi \in \mathbb{R}^l$ , an  $l$ -dimensional torus, say  $\mathbb{T}_{\mathbf{i}}^l$  such that  $\mathbb{T}_{\mathbf{i}}^l \cap \mathbb{T}_{\mathbf{j}}^l = \emptyset$  if  $\mathbf{i} \neq \mathbf{j}$ ;

(3) there is  $L_0 > 0$  such that the functions  $(x_{\mathbf{i}}, \theta_{\mathbf{i}})$  are Lipschitz-continuous with the constant  $L_0$ .

*Remark 2.1.* The first study of such kind of invariant sets has been performed in [Afraimovich & Shilnikov, 1982] (see [Ilyashenko & Li, 1999] for a detailed proof), where we dealt with a codimension-1 bifurcation on the boundary of the set of Morse–Smale systems. Here, we consider a general situation.

*Remark 2.2.* Conditions of Theorem 1 guarantee a chaotic behavior on the set  $\Sigma$  with respect to the  $\theta$ -coordinates. Behavior with respect to the  $\phi$ -coordinates could be, in principle, both regular (including the case  $g$  is independent of  $\phi$ ,  $h_1 = \text{const}$ , the rigid rotation in the  $\phi$ -coordinates) and even chaotic if  $l > 1$ . But this possible chaos does not imply the breakdown of  $l$ -dimensional tori (for fixed values of  $x$  and  $\theta$  the map  $h$  is a diffeomorphism), so the situation still can be treated as a chimera state.

*Remark 2.3.* The maximal attractor of the diffeomorphism  $T$  is, of course, more complex than the set  $\Sigma$  that is just a support of a simple chaotic behavior similar to chaotic subsets inside torus–chaos attractors.

### 3. Proof of the Results

We use the graph transformation technique. We present the proof in the form of several lemmas. Given  $t \in \{1, 2, \dots, N\}$  and  $L > 0$  let  $H_t^+(L)$  be the set of graphs of all continuous functions  $x = \xi(\theta, \phi)$ , 1-periodic in  $\phi \in \mathbb{R}^l$ ,  $\theta \in Q_t$ , endowed with the usual  $C^0$ -norm  $\|\cdot\|^0 = \sup_{\phi \in \mathbb{R}^l, \theta \in Q_t} |\cdot|$  and such that they are Lipschitz-continuous with the constant  $L$ :

$$|\xi(\theta_1, \phi_1) - \xi(\theta_2, \phi_2)| \leq L(|\theta_1 - \theta_2| + |\phi_1 - \phi_2|).$$

**Lemma 1.** *Let  $m_{t,s} > 0$ . Under Assumption 1 and provided that the conditions  $C_4 < C_2$  and*

$$\begin{aligned} 1 - pq - pqC_4 - q - pC_4C_2 - C_2 \\ > 2\sqrt{C_1 C_3}(p + pC_4 + 1) \end{aligned} \quad (5)$$

are satisfied there exists  $L > 0$  such that the map  $T$  induces the map

$$\mathcal{T}_{t,s}^\alpha : H_t^+(L) \rightarrow H_s^+(L), \quad \alpha = 1, \dots, m_{t,s}.$$

*Proof*

(1) Fix an arbitrary surface  $x \in \xi(\theta, \phi)$  belonging to  $H_t^+(L)$  and show that the intersection of its image under the map  $T$  with  $\mathbb{J}_s$  has  $m_{t,s}$  connected components. For that, it is sufficient to show that for each  $\alpha \in \{1, 2, \dots, m_{t,s}\}$  the map

$$\begin{cases} \bar{\theta} = g(\xi(\theta, \phi), \theta, \phi), \\ \bar{\phi} = h(\xi(\theta, \phi), \theta, \phi), \end{cases} \quad (6)$$

which we denote by  $\hat{T}_\xi$  is a homeomorphism with the domain being a subset of  $Q_t \times \mathbb{R}^l$  and with the image being  $\bigcup_{\alpha=1}^{m_{t,s}} (Q_s + k_\alpha) \times \mathbb{R}^l$ .

Because of that, and since  $(Q_s + k_{\alpha_1}) \cap (Q_s + k_{\alpha_2}) = \emptyset$ ,  $\alpha_1 \neq \alpha_2$ , it would follow that  $\hat{T}_\xi^{-1}(Q_s + k_{\alpha_1}) \cap \hat{T}_\xi^{-1}(Q_s + k_{\alpha_2}) = \emptyset$ , so connected components of the surface  $x = \xi(\theta, \phi)$  determined by inclusions  $(\theta, \phi) \in \hat{T}_\xi^{-1}(Q_s + k_\alpha) \times \mathbb{R}^l$  do not intersect each other for different values of  $\alpha$ . Therefore, their images under the map  $T$  also do not intersect each other. It would follow from this that the equation

$$\bar{x} = f(\xi(\theta, \phi), \theta, \phi), \quad (7)$$

where  $(\theta, \phi) \in \hat{T}_\xi^{-1}(Q_s + k_\alpha) \times \mathbb{R}^l$  determines  $\bar{x}$  for each  $\alpha$  as a function of  $\bar{\theta}$ ,  $\bar{\phi}$ ,  $\alpha = 1, \dots, m_{t,s}$ . It also implies that the intersection  $T\mathbb{J}_t \cap \mathbb{J}_s$  has  $m_{t,s}$  connected components.

We start now the actual proof. Given  $\bar{\theta}$ ,  $\bar{\phi}$  solve (6) by the successive approximations method:

$$\begin{cases} \bar{\theta} = g(\xi(\theta_{r-1}, \phi_{r-1}), \theta_r, \phi_{r-1}), \\ \bar{\phi} = \phi_r + h_1(\xi(\theta_{r-1}, \phi_{r-1}), \theta_r, \phi_{r-1}). \end{cases} \quad (8)$$

Because of (2) and the implicit function theorem, given  $\theta_{r-1} \in Q_s$ ,  $\phi_{r-1} \in \mathbb{R}^l$ , the first of these equations determines a unique value  $\theta_r \in Q_t$  for each  $\bar{\theta}$  such that  $\bar{\theta} - k_\alpha \in Q_s$ . Substituting it to the second equation we obtain

$$\phi_r = \bar{\phi} - h_1(\xi(\theta_{r-1}, \phi_{r-1}), \theta_r, \phi_{r-1})$$

and the equations for the next step of the procedure

$$\begin{cases} \bar{\theta} = g(\xi(\theta_r, \phi_r), \theta_{r+1}, \phi_r), \\ \bar{\phi} = \phi_{r+1} + h_1(\xi(\theta_r, \phi_r), \theta_{r+1}, \phi_r). \end{cases} \quad (9)$$

It follows from (8) and (9) that

$$\begin{aligned} |\theta_{r+1} - \theta_r| &\leq \|g_0^{-1}\|_0 \cdot \|g_x\|_0 \cdot L \cdot |\theta_r - \theta_{r-1}| \\ &\quad + \|g_\theta^{-1}\|_0 \cdot (\|g_x\|_0 \cdot L + \|g_\phi\|_0) \\ &\quad \cdot |\phi_s - \phi_{s-1}|, \end{aligned}$$

thus,

$$\begin{aligned} |\theta_{r+1} - \theta_r| &\leq pC_1L|\theta_r - \theta_{r-1}| \\ &\quad + p(C_1L + C_4)|\phi_r - \phi_{r-1}| \end{aligned} \quad (10)$$

and

$$\begin{aligned} |\phi_{r+1} - \phi_r| &\leq \|h_{1\theta}\|_0 \cdot |\theta_{r+1} - \theta_r| + \|h_{1x}\|_0L|\theta_r - \theta_{r-1}| + (\|h_{1x}\|_0 \cdot L + \|h_{1\phi}\|_0) \cdot |\phi_r - \phi_{r-1}| \\ &\leq C_2|\theta_{r+1} - \theta_r| + C_1L|\theta_r - \theta_{r-1}| + (C_1L + C_2)|\phi_r - \phi_{r-1}| \end{aligned} \quad (11)$$

and taking (10) into account

$$|\phi_{r+1} - \phi_r| \leq (C_2pC_1L + C_1L)|\theta_r - \theta_{r-1}| + (C_2pC_1L + C_2pC_4 + C_1L + C_2)|\phi_r - \phi_{r-1}|. \quad (12)$$

We rewrite (10), (12) in a matrix form

$$\begin{pmatrix} |\theta_{r+1} - \theta_r| \\ |\phi_{r+1} - \phi_r| \end{pmatrix} \leq \begin{pmatrix} pC_1L & p(C_1L + C_4) \\ C_2pC_1L + C_1L & C_2pC_1L + C_2pC_4 + C_1L + C_2 \end{pmatrix} \begin{pmatrix} |\theta_r - \theta_{r-1}| \\ |\phi_r - \phi_{r-1}| \end{pmatrix}.$$

The trace of the matrix, say,  $\gamma = pC_1L + C_2pC_1L + C_2pC_4 + C_1L + C_2$ , and the determinant, say,  $\Delta = pC_1L(C_2 - C_4)$ .

The last of the conditions (5) implies that  $\lambda_1 \cdot \lambda_2 \geq 0$  where  $\lambda_{1,2}$  are eigenvalues of this matrix. Now,  $\gamma^2 - 4\Delta > 0$ , so both  $\lambda_1$  and  $\lambda_2$  are real non-negative numbers. If the conditions  $\gamma < 2$  and  $\gamma < 1 + \Delta$  are satisfied then  $\lambda_1 < 1$  and  $\lambda_2 < 1$ .

The first of these conditions can be rewritten as

$$L < \frac{2 - C_2pC_4 - C_2}{C_1(p + pC_2 + 1)} \quad (13)$$

and the second, as

$$L < \frac{1 - C_2 - C_2pC_4}{C_1(p + pC_4 + 1)}. \quad (14)$$

Remark that, because of (4), the expressions in (13), (14) are positive. We assume that  $L$  is chosen in such a way that (13) and (14) are satisfied. Hence, the successive approximations (8) converge to a solution of (6). One can check also that for any integer vector  $k$  the point  $(\bar{\theta}, \bar{\phi} + k)$  is the image of a point  $(\theta, \phi + k)$  under the map (6), so the inverse map  $(\bar{\theta}, \bar{\phi}) \rightarrow (\theta, \phi)$  can be written as follows

$$\begin{cases} \theta = \tilde{g}(\bar{\theta}, \bar{\phi}), \\ \phi = \bar{\phi} + \tilde{h}(\bar{\theta}, \bar{\phi}), \end{cases} \quad (15)$$

where  $\tilde{g}, \tilde{h}$  are 1-periodic in  $\bar{\phi}$  functions. Therefore, the function  $\bar{x} = f(\xi(\theta, \phi), \theta, \phi)$  where  $\theta$  and  $\phi$  are expressed as in (15) is also 1-periodic in  $\bar{\phi}$ .

(2) Show that the function  $\bar{x} = f(\xi(\theta, \phi), \theta, \phi)$  where  $\theta, \phi$  are as in (15) is Lipschitz-continuous. Let

$$\begin{cases} \bar{x}_1 = f(\xi(\theta_1, \phi_1), \theta_1, \phi_1), \\ \bar{\theta}_1 = g(\xi(\theta_1, \phi_1), \theta_1, \phi_1), \\ \bar{\phi}_1 = h(\xi(\theta_1, \phi_1), \theta_1, \phi_1), \\ \bar{x}_2 = f(\xi(\theta_2, \phi_2), \theta_2, \phi_2), \\ \bar{\theta}_2 = g(\xi(\theta_2, \phi_2), \theta_2, \phi_2), \\ \bar{\phi}_2 = h(\xi(\theta_2, \phi_2), \theta_2, \phi_2), \end{cases}$$

then

$$\begin{aligned} |\theta_1 - \theta_2| &\leq \|g_\theta^{-1}\|_0 \cdot |\bar{\theta}_1 - \bar{\theta}_2| + \|g_\theta^{-1}\|_0 \\ &\quad \cdot \|g_x\|_0 \cdot L|\theta_1 - \theta_2| + \|g_\theta^{-1}\|_0 \\ &\quad \cdot (\|g_x\|_0 \cdot L + \|g_\phi\|_0)|\phi_1 - \phi_2|, \end{aligned}$$

so

$$\begin{aligned} |\theta_1 - \theta_2| &\leq p|\bar{\theta}_1 - \bar{\theta}_2| + pC_1L|\theta_1 - \theta_2| \\ &\quad + p(C_1L + C_4)|\phi_1 - \phi_2|. \end{aligned}$$

Because of (5),  $1 - pC_1L > 0$ , therefore

$$\begin{aligned} |\theta_1 - \theta_2| &\leq \frac{p}{1 - pC_1L}|\bar{\theta}_1 - \bar{\theta}_2| \\ &\quad + \frac{p(C_1L + C_4)}{1 - pC_1L}|\phi_1 - \phi_2|. \end{aligned} \quad (16)$$

Furthermore,

$$\begin{aligned} |\phi_1 - \phi_2| &\leq |\bar{\phi}_1 - \bar{\phi}_2| + (\|h_{1x}\|_0 \cdot L + \|h_{1\theta}\|_0) \\ &\quad \times |\theta_1 - \theta_2| + (\|h_{1x}\|_0 \cdot L + \|h_{1\phi}\|_0) \\ &\quad \times |\phi_1 - \phi_2| \end{aligned}$$

$$\begin{aligned} &\leq (C_1L + C_2)|\theta_1 - \theta_2| + (C_1L + C_2) \\ &\quad \times |\phi_1 - \phi_2| + |\bar{\phi}_1 - \bar{\phi}_2|. \end{aligned}$$

Substituting (16) into this inequality, we obtain

$$\begin{aligned} |\phi_1 - \phi_2| &\leq |\bar{\phi}_1 - \bar{\phi}_2| + \frac{C_1L + C_2}{1 - pC_1L} \cdot |\bar{\theta}_1 - \bar{\theta}_2| \\ &\quad + \frac{(C_1L + C_2)p(C_1L + C_4)}{1 - pC_1L} \\ &\quad + (C_1L + C_2)|\phi_1 - \phi_2| \\ &= |\bar{\phi}_1 - \bar{\phi}_2| + \frac{C_1L + C_2}{1 - pC_1L}|\bar{\theta}_1 - \bar{\theta}_2| \\ &\quad + \frac{(C_1L + C_2)(pC_4 + 1)}{1 - pC_1L}|\phi_1 - \phi_2|. \end{aligned}$$

The inequality (14) implies that

$$\frac{(C_1L + C_2)(pC_4 + 1)}{1 - pC_1L} < 1.$$

So,

$$\begin{aligned} |\phi_1 - \phi_2| &< (1 - pC_1L - (pC_4 + 1)(C_1L + C_2))^{-1} \\ &\quad \cdot \{(C_1L + C_2)p|\bar{\theta}_1 - \bar{\theta}_2| \\ &\quad + (1 - pC_1L)|\bar{\phi}_1 - \bar{\phi}_2|\}. \end{aligned} \quad (17)$$

Substituting (17) into (16) we obtain

$$\begin{aligned} |\theta_1 - \theta_2| &\leq (1 - pC_1L - (pC_4 + 1)(C_1L + C_2))^{-1} \\ &\quad \cdot \{p(1 - C_1L - C_2) \cdot |\bar{\theta}_1 - \bar{\theta}_2| \\ &\quad + p(C_1L + C_4)|\bar{\phi}_1 - \bar{\phi}_2|\}. \end{aligned} \quad (18)$$

Thus, under the conditions (13), (14) the map (15) is Lipschitz-continuous. Furthermore,

$$\begin{aligned} |\bar{x}_1 - \bar{x}_2| &\leq (\|f_x\|_0L + \|f_\theta\|_0) \cdot |\theta_1 - \theta_2| \\ &\quad + (\|f_x\|_0L + \|f_\phi\|_0)|\bar{\phi}_1 - \bar{\phi}_2| \\ &\leq (qL + C_3)(|\theta_1 - \theta_2| + |\phi_1 - \phi_2|) \end{aligned}$$

and according to (17), (18)

$$\begin{aligned} |\bar{x}_1 - \bar{x}_2| &\leq \frac{qL + C_3}{1 - pC_1L - (pC_4 + 1)(C_1L + C_2)} \\ &\quad \cdot \{p|\bar{\theta}_1 - \bar{\theta}_2| + (pC_4 + 1)|\bar{\phi}_1 - \bar{\phi}_2|\}. \end{aligned}$$

To obtain the inequality  $|\bar{x}_1 - \bar{x}_2| \leq L(|\bar{\theta}_1 - \bar{\theta}_2| + |\bar{\phi}_1 - \bar{\phi}_2|)$ , it is sufficient to satisfy the inequality

$$\frac{(qL + C_3)(p + pC_4 + 1)}{1 - pC_1L - (pC_4 + 1)(C_1L + C_2)} \leq L \quad (19)$$

or

$$L^2(pC_1 + pC_4C_1 + C_1) - L(1 - pq - pqC_4 - pC_1C_2 - C_2) + C_3(p + pC_4 + 1) \leq 0. \quad (20)$$

This inequality has positive solutions if

$$1 - pq - pqC_4 - q - pC_4C_2 - C_2 > 2\sqrt{C_1C_3}(p + pC_4 + 1).$$

But it is inequality (5) that is assumed to be satisfied.

(3) We have to show now that there are such values of  $L$  that satisfy (20) and (13), (14). They exist if the arithmetic average of the roots  $\frac{L_1+L_2}{2}$  of the polynomial in (20) is equal to

$$\frac{1 - pq - pqC_4 - q - pC_4C_2 - C_2}{2(pC_1 + pC_4C_1 + C_1)} < \frac{2 - C_2pC_4 - C_2}{C_1(p + pC_2 + 1)} \quad (21)$$

and

$$\frac{1 - pq - pqC_4 - q - pC_4C_2 - C_2}{2C_1(p + pC_4 + 1)} < \frac{1 - C_2 - C_2pC_4}{C_1(p + pC_4 + 1)}. \quad (22)$$

The first inequality holds since, under the condition of the lemma, the numerator of the left fraction is smaller than the one of the right one, and the denominator of the left fraction is greater than that of the right one. The second one holds since (5) implies that  $pC_4C_2 + C_2 < 1$ . Thus, for values of  $L$  satisfying (20) and less than  $\frac{L_1+L_2}{2}$  the inequalities (13), (14) are satisfied. Let us fix such a value of  $L$ .

Given  $\xi \in H_t^+(L)$ , denote by  $T_{t,s}^\alpha \xi$  the connected component of the set  $T(\xi) \cap \mathbb{J}_s$  corresponding to  $k_\alpha$ .

We proved above that  $T_{t,s}^\alpha \xi \in H_s^+(L)$ , so a map  $T_{t,s}^\alpha : H_t^+(L) \rightarrow H_s^+(L)$  is well defined. ■

**Lemma 2.** *Under the conditions of Lemma 1 there are such values of  $L$  satisfying (13), (14), (20) that the operator  $T_{t,s}^\alpha$  is a contraction.*

*Proof.* Let  $x = \xi_1(\theta, \phi)$ ,  $x = \xi_2(\theta, \phi)$  belong to  $H_t^+(L)$ . Their  $T_{t,s}^\alpha$ -images satisfy the equations

$$\begin{cases} \bar{x}_1 = f(\xi_1(\theta_1, \phi_1), \theta_1, \phi_1), \\ \bar{\theta} = g(\xi_1(\theta_1, \phi_1), \theta_1, \phi_1), \\ \bar{\phi} = h(\xi_1(\theta_1, \phi_1), \theta_1, \phi_1), \end{cases} \quad (23)$$

$$\begin{cases} \bar{x}_2 = f(\xi_2(\theta_2, \phi_2), \theta_2, \phi_2), \\ \bar{\theta} = g(\xi_2(\theta_2, \phi_2), \theta_2, \phi_2), \\ \bar{\phi} = h(\xi_2(\theta_2, \phi_2), \theta_2, \phi_2), \end{cases}$$

so that the points  $(\xi_1(\theta_1, \phi_1), \theta_1, \phi_1)$  and  $(\xi_2(\theta_2, \phi_2), \theta_2, \phi_2)$  are mapped into the points  $(\bar{x}_1, \bar{\theta}, \bar{\phi})$ ,  $(\bar{x}_2, \bar{\theta}, \bar{\phi})$  and  $\bar{\theta} - k_\alpha \in Q_s$ . The possibility to use the form (23) follows from (1) of the proof of Lemma 1. Equations (23) imply that

$$\begin{aligned} |\theta_1 - \theta_2| &\leq \|g_\theta^{-1}\|_0 \cdot \|g_x\|_0 \cdot |\xi_1(\theta_1, \phi_1) - \xi_2(\theta_2, \phi_2)| \\ &\quad + \|g_\theta^{-1}\|_0 \cdot \|g_\phi\|_0 \cdot |\phi_1 - \phi_2| \\ &\leq \|g_\theta^{-1}\|_0 \cdot \|g_x\|_0 \|\xi_1 - \xi_2\|^0 \\ &\quad + \|g_\theta^{-1}\|_0 \cdot \|g_x\|_0 L |\theta_1 - \theta_2| \\ &\quad + \|g_\theta^{-1}\|_0 (\|g_x\|_0 L + \|g_\theta\|_0) |\phi_1 - \phi_2| \end{aligned}$$

or

$$\begin{aligned} |\theta_1 - \theta_2| &\leq \frac{pC_1}{1 - pC_1L} \|\xi_1 - \xi_2\|^0 \\ &\quad + \frac{p(C_1L + C_4)}{1 - pC_1L} |\phi_1 - \phi_2|. \end{aligned} \quad (24)$$

Furthermore,

$$\begin{aligned} |\phi_1 - \phi_2| &\leq \|h_{1x}\|_0 |\xi_1(\theta_1, \phi_1) - \xi_2(\theta_2, \phi_2)| \\ &\quad + \|h_{1\theta}\|_0 |\theta_1 - \theta_2| + \|h_{1\phi}\|_0 |\phi_1 - \phi_2| \\ &\leq C_1 \|\xi_1 - \xi_2\|^0 + (C_1L + C_2) |\theta_1 - \theta_2| \\ &\quad + (C_1L + C_2) |\phi_1 - \phi_2|. \end{aligned} \quad (25)$$

Substituting (24) into (25) we obtain

$$\begin{aligned} |\phi_1 - \phi_2| &\leq \left\{ C_1 + \frac{pC_1(C_1L + C_2)}{1 - pC_1L} \right\} \|\xi_1 - \xi_2\|^0 \\ &\quad + \left\{ (C_1L + C_2) + \frac{(C_1L + C_2)p(C_1L + C_4)}{1 - pC_1L} \right\} \\ &\quad \times |\phi_1 - \phi_2|, \end{aligned}$$

i.e.

$$\begin{aligned} |\phi_1 - \phi_2| &\leq \frac{C_1(1 + pC_2)}{1 - pC_1L - (C_1L + C_2)(1 + pC_4)} \\ &\quad \cdot \|\xi_1 - \xi_2\|^0. \end{aligned} \quad (26)$$

The inequality (26) together with (24) imply that

$$|\theta_1 - \theta_2| \leq \frac{pC_1(1 - C_2 + C_4)}{1 - pC_1L - (C_1L + C_2)(1 + pC_4)} \times \|\xi_1 - \xi_2\|^0. \quad (27)$$

Since

$$\begin{aligned} |\bar{x}_1 - \bar{x}_2| &\leq \|f_x\|_0 \|\xi_1 - \xi_2\|^0 \\ &\quad + (\|f_x\|_0 L + \|f_\theta\|_0) |\theta_1 - \theta_2| \\ &\quad + (\|f_x\|_0 L + \|f_\phi\|_0) |\phi_1 - \phi_2| \end{aligned}$$

and (26), (27),

$$\begin{aligned} |\bar{x}_1 - \bar{x}_2| &\leq \left\{ q + \frac{(qL + C_3)(pC_1 + pC_1C_4 + C_1)}{1 - pC_1L - (C_1L + C_2)(1 + pC_4)} \right\} \\ &\quad \times \|\xi_1 - \xi_2\|^0 \end{aligned} \quad (28)$$

or, because of (19),

$$|\bar{x}_1 - \bar{x}_2| \leq (q + C_1L) \|\xi_1 - \xi_2\|^0, \quad (29)$$

thus,

$$\|\mathcal{T}_{t,s}^\alpha \xi_1 - \mathcal{T}_{t,s}^\alpha \xi_2\|^0 \leq (q + C_1L) \|\xi_1 - \xi_2\|^0.$$

The operator  $\mathcal{T}_{t,s}^\alpha$  will be a contraction if

$$L < \frac{1-q}{C_1}. \quad (30)$$

But, since  $\frac{L_1+L_2}{2}$  [see (21)] is less than  $\frac{1-q}{C_1}$  then for all values of  $L$  satisfying (13), (14) and (20) the operator  $\mathcal{T}_{t,s}^\alpha$  is a contraction. ■

**Definition 3.1.** A sequence of surfaces  $\boldsymbol{\xi} := (\dots \xi_{-1}, \xi_0, \dots, \xi_k, \dots)$  is called the invariant unstable leaf if for each  $k \in \mathbb{Z}$  there exist  $t, s, \alpha \in \mathbb{Z}$  such that  $\xi_k \in H_t^+(L)$ ,  $\xi_{k+1} \in H_s^+(L)$ , and  $\mathcal{T}_{t,s}^\alpha \xi_k = \xi_{k+1}$ .

Denote by  $X$  the set of all invariant unstable leaves endowed with a distance, say  $\text{dist}(\boldsymbol{\xi}^1, \boldsymbol{\xi}^2)$ , producing the product topology.

**Lemma 3.** *There exists a continuous map  $\gamma : \Omega_A \rightarrow X$  that is one-to-one and such as for any  $\mathbf{i} \in \Omega_A$  one has  $\gamma(\sigma \mathbf{i}) = \tilde{\boldsymbol{\xi}}$  where  $(\tilde{\boldsymbol{\xi}})_k = \xi_{k+1}$  if  $(\gamma(\mathbf{i})) = \xi_k$ .*

*Proof.* Given  $\mathbf{i} \in \Omega_A$ , an infinite itinerary on the graph  $G$  is determined, i.e. an infinite sequence

of spaces  $\{H_k^+(L)\}$  and maps  $\mathcal{T}_{s,t}^\alpha$  is defined such that

$$\dots \rightarrow H_t^+(L) \xrightarrow{\mathcal{T}_{t,s}^\alpha} H_s^+ \rightarrow \dots$$

where each space is complete and each map is a contraction. We apply now a lemma from [Shilnikov, 1967] about the existence of a fixed point in the direct product of space, that is a desired invariant unstable leaf, say  $\boldsymbol{\xi}^i$ . So, a map  $\gamma : \Omega_A \rightarrow X$  is well defined. Evidently,  $\gamma$  is one-to-one, and its continuity follows from the lemma [Shilnikov, 1967]. Moreover, by construction,  $(\boldsymbol{\xi}^{\sigma(\mathbf{i})})_k = (\boldsymbol{\xi}^i)_{k+1}$ . ■

In the rest of this section we show that each unstable invariant leaf contains a sequence of tori, “an orbit” of tori under the original map  $T$  that will allow us to determine the desired map  $\beta$ . In fact, one can repeat the procedure similar to Lemmas 1–3 and obtain stable invariant leaves, and the intersection of unstable and stable leaves would present the tori. But the formulas are too cumbersome, and it is simpler to work with unstable leaves.

Given  $\mathbf{i} = (\dots i_{-1} i_0 \dots i_k \dots) \in \Omega_A$  and the corresponding sequence  $(\dots \xi_{-1} \xi_0 \dots \xi_k \dots)$  of surfaces define for each  $\xi_k$  the space  $H_{\xi_k}^-(\tilde{L})$  of  $l$ -dimensional tori that are the graphs of the vector functions  $\theta = \eta(\phi)$ ,  $x = \xi_k(\eta(\phi), \phi)$ ,  $\phi \in \mathbb{R}^l$ , where  $\eta$  is 1-periodic and  $\eta(\phi) \in Q_t$ ,  $\phi \in \mathbb{R}^l$ , if  $\xi_k \in H_t^+(L)$ . Furthermore,  $\eta$  is Lipschitz-continuous

$$|\eta(\phi_1) - \eta(\phi_2)| \leq \tilde{L} |\phi_1 - \phi_2|. \quad (31)$$

**Lemma 4.** *Under the conditions*

$$C_2 C_4 < \frac{1}{3}, \quad p < \frac{1}{4} \quad (32)$$

*there is a constant  $\tilde{L} > 0$  such that the map  $T^{-1}$  generates the maps  $\mathcal{T}_{\xi_k \xi_{k+1}}^- : H_{\xi_{k+1}}^-(\tilde{L}) \rightarrow H_{\xi_k}^-(\tilde{L})$  that are contractions.*

*Proof.* First, we check that  $T^{-1}$  maps the torus  $\bar{\theta} = \eta(\bar{\phi})$ ,  $x = \xi_{k+1}(\eta(\bar{\theta}), \bar{\phi})$  belonging to  $H_{\xi_{k+1}}^-(\tilde{L})$  into a torus in  $H_{\xi_k}^-(\tilde{L})$ . For that, we show that the equation

$$g(\xi_k(\theta, \phi), \theta, \phi) - k_\alpha = \eta(h(\xi(\theta, \phi), \theta, \phi)) \quad (33)$$

has a unique solution  $\theta = \eta_1(\phi)$ . We fix  $\theta_0 \in Q_t$  and use the successive approximations:  $g(\xi_k(\theta_{r-1}, \phi), \theta_r, \phi) - k_\alpha = \eta(h(\xi_k(\theta_{r-1}, \phi), \theta_{r-1}, \phi))$ ,  $r = 1, 2, \dots$



The difference  $|\theta_{r+1} - \theta_r| \rightarrow 0$  exponentially if  $p(C_1L + \tilde{L}C_1L + \tilde{L}C_2) < 1$  or

$$\tilde{L} < \frac{1 - pC_1L}{p(C_1L + C_2)}. \quad (34)$$

If this is true then the successive approximations converge to a 1-periodic function  $\theta = \eta_1(\phi)$ .

Second, to show that  $\eta_1$  is  $\tilde{L}$ -Lipschitz-continuous we use the identities

$$g(\xi_k(\theta_1, \phi_1), \theta_1, \phi_1) - k_\alpha = \eta(h(\xi_k(\theta_1, \phi_1), \theta_1, \phi_1)),$$

$$g(\xi_k(\theta_2, \phi_2), \theta_2, \phi_2) - k_\alpha = \eta(h(\xi_k(\theta_2, \phi_2), \theta_2, \phi_2))$$

and the inequality (34) to obtain

$$|\theta_1 - \theta_2| \leq \frac{p(C_1L + C_4 + \tilde{L}(C_1L + C_2 + 1))}{1 - p(C_1L + \tilde{L}C_1L + \tilde{L}C_2)} \cdot |\phi_1 - \phi_2|. \quad (35)$$

We claim that the fraction is less than or equal to  $\tilde{L}$  and obtain the quadratic inequality

$$\tilde{L}^2 p(C_1L + C_2) - \tilde{L}(1 - 2pC_1L - pC_2 - p) + p(C_1L + C_2) \leq 0. \quad (36)$$

$$L < \frac{1 + p^2C_2^2 + p^2 - 2pC_2 - 2p + 2p^2C_4 - 4p^2C_2C_4}{4pC_2(1 - p + pC_4)}$$

which is satisfied if

$$\frac{1 - C_2 - pC_2C_4}{p + 1 + pC_4} < \frac{1 + p^2C_2^2 + p^2 - 2pC_2 - 2p + 2p^2C_2 - 4p^2C_2C_4}{2p(1 - p + pC_4)}.$$

This inequality is satisfied if

$$1 + p^2C_2 + p^2 - 4p + 2p^2C_2 - 2p^2C_2C_4 > 0. \quad (38)$$

By assumption,  $C_2C_4 < 1/3$ , and  $C_2 < 1$ , so (38) will be satisfied if

$$1 - 4p + \frac{10}{3}p^2 > 0.$$

This is true if  $p < \frac{1}{10}(6 - \sqrt{6})$ . By assumption  $p < \frac{1}{4} < \frac{1}{10}(6\sqrt{6})$ , so if (5) and the assumptions of the lemma are satisfied then  $\eta_1$  is Lipschitz-continuous with a constant  $\tilde{L}$ .

Third, to show that  $\mathcal{T}_{\xi_k \xi_{k+1}}$  is a contraction, we use the identities

$$g(\xi_k(\theta_1, \phi), \theta_1, \phi) - k_\alpha = \eta_1(h(\xi_k(\theta_1, \phi), \theta_1, \phi)),$$

$$g(\xi_k(\theta_2, \phi), \theta_2, \phi) - k_\alpha = \eta_2(h(\xi_k(\theta_2, \phi), \theta_2, \phi)),$$

The positive values of  $\tilde{L}$  satisfying (36) exist if

$$L < \frac{1 - pC_2 - p}{2pC_1} \quad (37)$$

and the discriminant of the quadratic polynomial in (36) is positive. The inequality (37) holds if [see (21)]

$$\frac{1 - C_2 - pC_2C_4 - q(p + pC_4 + 1)}{2C_1(p + 1 + pC_4)} < \frac{1 - pC_2 - p}{2pC_1}$$

which is true if

$$\frac{1 - C_2 - pC_2C_4}{p + 1 + pC_4} < \frac{1 - pC_2 - p}{2pC_1}$$

or

$$p < 1 + pC_4(1 - p) - p^2C_2 - p^2.$$

This inequality holds if ( $C_2 < 1$ )

$$p < 1 - 2p^2.$$

For  $p < 1/2$  it is true (and, of course, for  $p < 1/4$ ).

The discriminant of the polynomial in (36) is positive if

to obtain that

$$|\theta_1 - \theta_2| \leq p(C_1L + \tilde{L}(C_1L + C_2))|\theta_1 - \theta_2| + p\|\eta_1 - \eta_2\|_0$$

(the inequality (34) implies that  $p(C_1L + \tilde{L}C_1L + \tilde{L}C_2) < 1$ ). The operator  $\mathcal{T}_{\xi_k \xi_{k+1}}$  is a contraction if  $\frac{p}{1 - p(C_1L + \tilde{L}C_1L + \tilde{L}C_2)} < 1$  or

$$\tilde{L} < \frac{1 - pC_1L - p}{p(C_1L + C_2)}. \quad (39)$$

If the arithmetic average of the roots of the quadratic polynomial in (36) equals  $\frac{1 - 2pC_1L - pC_2 - p}{2p(C_1L + C_2)}$  less than the right-hand part of (39), then the desirable values of  $\tilde{L}$  exist. The inequality

$$\frac{1 - 2pC_1L - pC_2 - p}{2p(C_1L + C_2)} < \frac{1 - pC_1L - p}{p(C_1L + C_2)}$$

holds if

$$1 - 3p + pC_2 \geq 0$$

that is true for  $p < 1/4$ . ■

### Ending of the proof of Theorem

- (1) It is simple to see that the conditions (4) in Theorem 1 imply the validity of the inequalities in Lemma 1 and conditions (32), thus, all Lemmas 1–4 are valid.
- (2) Given  $\mathbf{i} \in \Omega_A$ , there exists a unique invariant unstable leaf  $(\dots, \xi_{-1}(\mathbf{i}), \xi_0(\mathbf{i}), \dots, \xi_k(\mathbf{i}), \dots)$ . Lemma 4 states that a sequence of spaces and maps

$$\dots H_{\xi_k}^- \xleftarrow{\mathcal{T}_{\xi_k \xi_{k+1}}^-} H_{\xi_{k+1}}^- \leftarrow \dots$$

is well defined such that all spaces are complete and all maps are contractions. Because of the already cited lemma from [Shilnikov, 1967], there exists a unique sequence of tori  $(\dots \mathbb{T}_{\xi_{-1}(\mathbf{i})}, \mathbb{T}_{\xi_0(\mathbf{i})}, \dots, \mathbb{T}_{\xi_k(\mathbf{i})}, \dots)$  such that  $\mathbb{T}_{\xi_k(\mathbf{i})} \in H_{\xi_k}^-$  and  $\mathcal{T}_{\xi_k \xi_{k+1}}^-(\mathbb{T}_{\xi_{k+1}(\mathbf{i})}) = \mathbb{T}_{\xi_k(\mathbf{i})}$ . Let  $\mathbb{T}_{\xi_0(\mathbf{i})} =: \mathbb{T}_{\mathbf{i}}$ . Denote by  $\Sigma_1$  the set of all points of all tori, i.e.  $\Sigma_1 = \bigcup_{\mathbf{i} \in \Omega_A} \mathbb{T}_{\mathbf{i}}$ .

- (3) We show now that  $\Sigma_1$  is exactly the set  $\Sigma$  from the formulation of the theorem. For that we show, first, that  $\mathbb{T}_{\mathbf{i}} \cap \mathbb{T}_{\mathbf{j}} = \emptyset$  if  $\mathbf{i} \neq \mathbf{j}$ . Indeed, there is a  $k \in \mathbb{Z}$  such that  $(\sigma^k \mathbf{i})_0 \neq (\sigma^k \mathbf{j})_0$ . It implies that the leaves  $\xi_k(\mathbf{i})$  and  $\xi_k(\mathbf{j})$  belong to different connected components of the set  $T(\mathbb{J}_t) \cap \mathbb{J}_s$  for some  $t, s$ . Thus,  $\mathbb{T}_{\sigma^k \mathbf{i}} \cap \mathbb{T}_{\sigma^k \mathbf{j}} = \emptyset$  and  $\mathbb{T}_{\mathbf{i}} \equiv T^{-k}(\mathbb{T}_{\sigma^k \mathbf{i}}) \cap \mathbb{T}_{\mathbf{j}} \equiv T^{-k}(\mathbb{T}_{\sigma^k \mathbf{j}}) = \emptyset$ .

Let  $\beta : \Sigma_1 \rightarrow \Omega_A$  be a map defined as follows:  $\beta(\mathbf{P}) = \mathbf{i}$  if  $\mathbf{P} \in \mathbb{T}_{\mathbf{i}}$ .

Since all maps  $\mathcal{T}^+$  and  $\mathcal{T}^-$  are contractions then  $\beta$  is continuous by standard arguments. The commutativity of the diagram follows from the definition of  $\beta$ . ■

## 4. Concluding Remarks

- (i) In the paper, we have dealt only with the Lipschitz version of hyperbolicity conditions. We proved here that the tori and their unstable sets are graphs of Lipschitz-continuous functions. But it is clear that the standard technique would allow to prove smoothness, as it was done in [Afraimovich & Hsu, 2003] for hyperbolic sets and in [Shilnikov *et al.*, 1998] in the context of the annulus principle. After

that, it would be possible to check conditions of partial hyperbolicity. So, one can hypothesize that  $\Sigma$  is a partially hyperbolic set.

- (ii) One can repeat (with obvious simplifications) the proof of the theorem for the case where the “amplitude coordinates”  $\{x\}$  are absent and only the  $\{\theta\}$  and  $\{\phi\}$ -coordinates are present. The invariant set similar to  $\Sigma$  will be described in terms of a one-sided topological Mark chain. It would be very interesting to do it for the case of nonlocally coupled phase oscillators [Kuramoto & Battogtokh, 2002].
- (iii) Let us mention other systems from applications where conditions of the theorem we believe can be (at least numerically) checked.

- (a) *Aranson–Rulkov case* [Aranson & Rulkov, 1989]. They considered a situation where frequencies of phases of different oscillators are very much different. After averaging with respect to high frequency oscillators, they observed the breakdown of a two-dimensional torus and the appearance of a torus–chaos attractor. Here, the Poincaré map of the original system might satisfy the conditions of the theorem.
- (b) *Generalized Lotka–Volterra and oscillatory systems coupled together in a master–slave framework* [Afraimovich *et al.*, 2013]. A system of the type

$$\dot{x} = f(x),$$

$$\dot{y}_1 = g_1(y_1, x), \quad \dot{y}_2 = g_2(y_2, x)$$

where the system  $\dot{x} = f(x)$  possesses a limit cycle bifurcated from a stable heteroclinic cycle and coupling terms in the systems  $\dot{y}_1 = g_1(y_1, x)$  and  $\dot{y}_2 = g_2(y_2, x)$  chosen in an appropriate way may satisfy the conditions of the theorem.

## Acknowledgments

V. Afraimovich thanks very much A. Shilnikov, N. Rulkov, Yu. Maistrenko and I. Tristan for their help. He was partially supported by the Ohio University Glidden Professorship program.

## References

- Abrams, D. M. & Strogatz, S. H. [2004] “Chimera states for coupled oscillators,” *Phys. Rev. Lett.* **93**, 174102.

- Afraimovich, V. & Shilnikov, L. [1974] “On small periodic perturbations of autonomous systems,” *Dokl. Acad. Nauk SSSR*, pp. 734–742.
- Afraimovich, V. & Shilnikov, L. [1977] “The ring principle in problems of interaction between two self-oscillating systems,” *Prikladnaia Matematika i Mekhanika* **41**, 618–627.
- Afraimovich, V. & Shilnikov, L. [1982] “On a bifurcation of codimension one leading to the appearance of a countable set of tori,” *Sov. Math. Dokl.* **25**, 101–105.
- Afraimovich, V., Arnold, V., Ilyashenko, Y. & Shilnikov, L. [1991] *Theory of Bifurcations in Dynamic Systems*, Vol. 5 (Springer-Verlag, NY).
- Afraimovich, V. & Shilnikov, L. [1991] “Invariant two-dimensional tori, their breakdown and stochasticity,” *Amer. Math. Soc. Transl.* **149**, 201–212.
- Afraimovich, V. S. & Hsu, S.-B. [2003] *Lectures on Chaotic Dynamical Systems*, Vol. 28 (American Mathematical Soc.).
- Afraimovich, V. S. [2007] “Torus breakdown,” *Scholarpedia* **2**, 1933.
- Afraimovich, V., Cuevas, D. & Young, T. [2013] “Sequential dynamics of master–slave systems,” *Dyn. Syst.* **28**, 154–172.
- Anishchenko, V. S. & Nikolaev, S. [2008] “Transition to chaos from quasiperiodic motions on a four-dimensional torus perturbed by external noise,” *Int. J. Bifurcation and Chaos* **18**, 2733–2741.
- Aranson, I. & Rulkov, N. [1988a] “Chaos and bifurcations of multidimensional tori in an oscillator with a ferrite resonator,” *Zhurnal Tekhnicheskoi Fiziki* **58**, 1656–1670.
- Aranson, I. & Rulkov, N. [1988b] “Synchronization and doubling of quasiperiodic movements in a multimode systems,” *Pisma V Zhurnal Tekhnicheskoi Fiziki* **14**, 830–834.
- Aranson, I. & Rulkov, N. [1989] “Nontrivial structure of synchronization zones in multidimensional systems,” *Phys. Lett. A* **139**, 375–378.
- Bryant, P. & Jeffries, C. [1987] “The dynamics of phase locking and points of resonance in a forced magnetic oscillator,” *Physica D* **25**, 196–232.
- Curry, J. H. & Yorke, J. A. [1978] “A transition from Hopf bifurcation to chaos: Computer experiments with maps on  $R^2$ ,” *The Structure of Attractors in Dynamical Systems* (Springer), pp. 48–66.
- Ilyashenko, I. S. & Li, W. [1999] *Nonlocal Bifurcations*, Vol. 66 (American Mathematical Soc.).
- Kuramoto, Y. & Battogtokh, D. [2002] “Coexistence of coherence and incoherence in nonlocally coupled phase oscillators,” *Phys. Rev. Lett.* **5**, 380–385.
- Maistrenko, V., Maistrenko, Y. & Mosekilde, E. [2003] “Torus breakdown in noninvertible maps,” *Phys. Rev. E* **67**, 046215.
- Omelchenko, E., Wolfrum, M. & Maistrenko, Y. L. [2010] “Chimera states as chaotic spatiotemporal patterns,” *Phys. Rev. E* **81**, 065201.
- Shilnikov, L. P. [1967] “On a Poincaré–Birkhoff problem,” *Matematicheskii Sbornik* **116**, 378–397.
- Shilnikov, L. P., Shilnikov, A. L., Turaev, D. & Chua, L. O. [1998] *Methods of Qualitative Theory in Nonlinear Dynamics*, Vol. 1 (World Scientific).
- Wolfrum, M., Omelchenko, O., Yanchuk, S. & Maistrenko, Y. [2011] “Spectral properties of chimera states,” *Chaos* **21**, 013112.

## Scientific Heritage of L. P. Shilnikov

Valentin S. Afraimovich<sup>1\*</sup>, Sergey V. Gonchenko<sup>2\*\*</sup>, Lev M. Lerman<sup>2\*\*\*</sup>,  
Andrey L. Shilnikov<sup>2,3\*\*\*\*</sup>, and Dmitry V. Turaev<sup>4\*\*\*\*\*</sup>

<sup>1</sup>*Universidad Autónoma de San Luis Potosí,  
Av. Karakorum 1470, Lomas 4a. San Luis Potosí, 78210, México*

<sup>2</sup>*Lobachevsky State University of Nizhny Novgorod,  
pr. Gagarina 23, Nizhny Novgorod, 603950 Russia*

<sup>3</sup>*Neuroscience Institute and Department of Mathematics and Statistics,  
Georgia State University, Atlanta 30303, USA*

<sup>4</sup>*Imperial College, SW7 2 AZ London, UK*

Received July 1, 2014; accepted July 11, 2014

**Abstract**—This is the first part of a review of the scientific works of L.P. Shilnikov. We group his papers according to 7 major research topics: bifurcations of homoclinic loops; the loop of a saddle-focus and spiral chaos; Poincare homoclinics to periodic orbits and invariant tori, homoclinic in nonautonomous and infinite-dimensional systems; Homoclinic tangency; Saddle-node bifurcation — quasiperiodicity-to-chaos transition, blue-sky catastrophe; Lorenz attractor; Hamiltonian dynamics. The first two topics are covered in this part. The review will be continued in the further issues of the journal.

MSC2010 numbers: 37-01, 37-02, 01A65, 37C29, 37D45

DOI: 10.1134/S1560354714040017

Keywords: Homoclinic chaos, global bifurcations, spiral chaos, strange attractor, saddle-focus, homoclinic loop, saddle-node, saddle-saddle, Lorenz attractor, hyperbolic set

Our dear friend, mentor and fellow researcher, Leonid Pavlovich Shilnikov was a creator of the theory of global bifurcations of high-dimensional systems and one of the founders of the mathematical theory of dynamical chaos. He built a profound research school in the city of Nizhny Novgorod (Gorky formerly) – the Shilnikov School that continues to this day. His works greatly influenced the overall development of the mathematical theory of dynamical systems as well as nonlinear dynamics in general. Shilnikov’s findings have been included in most text- and reference books, and are used worldwide by mathematics students and nonlinear dynamists to study the qualitative theory of dynamical systems and chaos. The elegance and completeness of his results let them reach “the heart of the matter”, and provide applied researchers with an in-depth mathematical understanding of the outcomes of natural experiments. The popularity and appreciation were reflected by the “living classic” status attained by Professor Shilnikov over several decades of his life through continuous hard work on bifurcation theory of multidimensional dynamical systems, mathematical chaos theory, and theory of strange attractors.

In this article we would like to overview the scientific works of Leonid Pavlovich. As the material is very large to fit in one journal publication, we will proceed its publication in further issues of this journal. We group LP’s works into 7 major topics: Bifurcations of homoclinic loops, The loop of a saddle-focus, Poincare’s homoclinic, Homoclinic tangency, Destruction of a torus, Lorenz attractor, Hamiltonian dynamics. We start with the first two topics.

\*E-mail: valentin.afraimovich@gmail.com

\*\*E-mail: gonchenko@pochta.ru

\*\*\*E-mail: lermanl@mm.unn.ru

\*\*\*\*E-mail: ashilnikov@gsu.edu

\*\*\*\*\*E-mail: d.turaev@imperial.ac.uk



## Band gap engineering of indium zinc oxide by nitrogen incorporation



J.J. Ortega<sup>a,b,\*</sup>, M.A. Aguilar-Frutis<sup>c</sup>, G. Alarcón<sup>c</sup>, C. Falcony<sup>d</sup>,  
V.H. Méndez-García<sup>b,e</sup>, J.J. Araiza<sup>a</sup>

<sup>a</sup> Unidad Académica de Física, Universidad Autónoma de Zacatecas, Calzada Solidaridad esq. Paseo la Bufa, Fracc. Progreso, C.P. 98060 Zacatecas, Mexico

<sup>b</sup> Doctorado Institucional de Ingeniería y Ciencia de Materiales, Universidad Autónoma de San Luis Potosí, Av. Salvador Nava, Zona Universitaria, C.P. 78270 San Luis Potosí, Mexico

<sup>c</sup> Centro de Investigación en Ciencia Aplicada y Tecnología Avanzada del Instituto Politécnico Nacional, Unidad Legaría, Calz. Legaría No. 694, Col. Irrigación, C.P. 11500 México D.F., Mexico

<sup>d</sup> Departamento de Física, Centro de Investigación y Estudios Avanzados del Instituto Politécnico Nacional campus Zacatenco, Av. Instituto Politécnico Nacional 2508, Col. San Pedro Zacatenco, C.P. 07360 México D.F., Mexico

<sup>e</sup> Laboratorio Nacional-CIACyT, Universidad Autónoma de San Luis Potosí, Sierra Leona 550, Lomas 2<sup>a</sup> Secc, C.P. 78210 San Luis Potosí, Mexico

### ARTICLE INFO

#### Article history:

Received 23 December 2013

Received in revised form 8 May 2014

Accepted 12 May 2014

Available online 24 May 2014

#### Keywords:

Indium zinc oxynitride

Nitrogen incorporation

Band gap engineering

Band gap narrowing

### ABSTRACT

The effects of nitrogen incorporation in indium zinc oxide films, as grown by RF reactive magnetron sputtering, on the structural, electrical and optical properties were studied. It was determined that the variation of the N<sub>2</sub>/Ar ratio, in the reactive gas flux, was directly proportional to the nitrogen percentage measured in the sample, and the incorporated nitrogen, which substituted oxygen in the films induces changes in the band gap of the films. This phenomenon was observed by measurement of absorption and transmission spectroscopy in conjunction with spectral ellipsometry. To fit the ellipsometry spectra, the classical and Adachi dispersion models were used. The obtained optical parameters presented notable changes related to the increment of the nitrogen in the film. The band gap narrowed from 3.5 to 2.5 eV as the N<sub>2</sub>/Ar ratio was increased. The lowest resistivity obtained for these films was  $3.8 \times 10^{-4} \Omega \text{ cm}$  with a carrier concentration of  $5.1 \times 10^{20} \text{ cm}^{-3}$ .

© 2014 Elsevier B.V. All rights reserved.

### 1. Introduction

The In<sub>2</sub>O<sub>3</sub>-ZnO (IZO) system has demonstrated excellent optical and electrical properties, such as high optical quality, high mobility, surface uniformity and chemical and thermal stability in various environments. For these reasons, IZO has been widely used in applications, such as transparent contacts for solar cells, light emitting diodes and several other optoelectronic devices [1–6]. For the application of IZO in optoelectronic devices, one of the relevant properties is the optical band gap, which closely depends on the change of the growth conditions, the doping impurities and, consequently, the carrier concentration. In recent years, the best control in the thin film deposition techniques allows for the design of band structures with nearly arbitrary and continuous band-gap variations showing that band-gap engineering is a powerful technique for the design of new semiconductor materials and devices.

In this way, there are many reports related to the production of shifts in the band gap of IZO [6–9]. Several of these works modified the band gap by changing the ratio between indium and zinc metal or including new metallic species within of the IZO matrix, which often results in a more complicated, costly and less reproducible process, and the shifts of the band gap are relatively small. However, before this work, nobody has studied or reported the band gap engineering of the IZO system by substituting oxygen with nitrogen.

In the present work, a method to change the optical band gap of IZO films grown by RF reactive magnetron sputtering is reported. The synthesis and the optical, structural and electrical characterization of the IZON thin films obtained by RF reactive magnetron sputtering are presented. The nitrogen incorporation in the films is also studied as a function of the nitrogen concentration in the sputtering atmosphere. The refractive index and extinction coefficient were determined as a function of the photon energy using spectroscopic ellipsometry (SE). The optical constants derived from the experimental techniques are presented, and a significant study of the optical band gap was realized from the dependence of the absorption coefficient on the photon energy. Optical band gap shifts as large as 1 eV are observed for the IZON films.

\* Corresponding author at: Unidad Académica de Física, Universidad Autónoma de Zacatecas, Calzada Solidaridad esq. Paseo de la Bufa, Fracc. Progreso, C.P. 98060 Zacatecas, Mexico. Tel.: +52 492 924 1314; fax: +52 492 924 1314.

E-mail addresses: [jjosila@hotmail.com](mailto:jjosila@hotmail.com), [jjosila@fisica.uaz.edu.mx](mailto:jjosila@fisica.uaz.edu.mx) (J.J. Ortega).

# Effect of surface states on the electrical properties of MBE grown modulation doped AlGaAs/GaAs

Alejandro Cisneros-de-la-Rosa, Irving Eduardo Cortes-Mestizo, Esteban Cruz-Hernández, and Víctor Hugo Méndez-García<sup>a)</sup>

Laboratorio Nacional, CIACyT-UASLP, Av. Sierra Leona #550, Col. Lomas 2a. Sección C.P. 78210, San Luis Potosí, S.L.P., Mexico

Luis Zamora-Peredo

Centro de Investigación en Micro y Nanotecnología, Universidad Veracruzana, Calzada Adolfo Ruiz Cortines #455, Frac. Costa Verde, C.P. 94292 Boca del Rio, Veracruz, Mexico

José Vulfrano González-Fernández, Raúl Balderas-Navarro, and Andrei Yu. Gorbachev

Instituto de Investigación en Comunicación Óptica, Universidad Autónoma de San Luis Potosí, Av. Karakorum 1470 Lomas 4a, C.P. 78210, San Luis Potosí, S.L.P., Mexico

Máximo López-López

Physics Department, Centro de Investigación y de Estudios Avanzados del Instituto Politécnico Nacional, Av. IPN 2508, Col. San Pedro Zacatenco, D.F. C.P. 07360, Mexico

(Received 13 November 2013; accepted 16 January 2014; published 10 February 2014)

The influence of near surface structure termination and surface treatments on the surface electric fields and mobility of modulation doped AlGaAs/GaAs heterostructures (MDH) were investigated. The built-in and surface electric fields were evaluated by photoreflectance spectroscopy, and these values were utilized to simulate the conduction band bending of the MDH. When the capping layer of the MDH was changed, both the built in internal electric field and the surface electric field are decreased, while the electron mobility of the samples is increased. After passivated the surface samples with Si, the surface electric fields were also reduced. Finally, a  $(\text{NH}_4)_2\text{S}_x$ -based treatment of the surface was applied, the surface electric field is annulled, and the conduction band modeling showed an important redistribution of carriers in the films. The electron mobility of the passivated samples does not show any change, neither the internal electric fields, corroborating the close relationship that exist between these two parameters. © 2014 American Vacuum Society. [<http://dx.doi.org/10.1116/1.4863677>]

## I. INTRODUCTION

Low-dimensional semiconductor systems research has acquired a great deal of interest in the route for optimizing electronic and optoelectronic devices. These systems are usually obtained when the nanometer size is reached, and at these dimensions, there exists a strong modification of the electronic and optical properties due to the quantum confinement imposed on the carriers.<sup>1</sup> Another important role in the fabrication and development of semiconductor devices is the semiconductor–vacuum interface in which surface states are created, having a detrimental effect on the optical and electrical properties of the devices.<sup>2</sup>

The surface states are created due to interruption of the periodic pattern imposed by the crystalline material atomic lattice arrangement. Top most dangling bonds produce changes at the surface potential that, for instance, bends the energy bands.

This project studies the changes induced by the surface states when modifying the cap layer structure of modulation doped AlGaAs/GaAs heterostructures (MDH). These structures are widely used in devices like high electron mobility transistor and also are employed in metrology science as the basic structure of the electrical resistance pattern<sup>3</sup> making

meritorious any characterization studies that may lead us to understand and improve their electrical properties.

On the other hand, photoreflectance spectroscopy (PR) is a fast-reading nondestructive characterization technique that has been used to characterize the MDH.<sup>4</sup> The typical short period damped oscillatory behavior of the PR spectra termed as Franz–Keldysh oscillations (FKO) is associated to internal AlGaAs/GaAs interface electric fields, while large period oscillations in the region between 1.45 and 1.75 eV are due to surface states.<sup>5</sup> Therefore, PR and Hall measurements, combined by energy band simulations, might provide a suitable scenario for the study of MDH, as it is intended in this article.

## II. EXPERIMENT

The MDH were grown by molecular beam epitaxy (MBE) on semi-insulating GaAs (100) substrates. The basic heterostructure is shown in Fig. 1. After the GaAs native oxides desorption process, a 1  $\mu\text{m}$ -thick GaAs buffer layer was deposited, followed by 7 nm undoped  $\text{Al}_{0.3}\text{Ga}_{0.7}\text{As}$  spacer layer (spacer 1). Next, the 80 nm-thick Si doped  $\text{Al}_{0.3}\text{Ga}_{0.7}\text{As}$  barrier was deposited with a carrier concentration of  $1.4 \times 10^{18} \text{ cm}^{-3}$ . Another spacer layer (spacer 2) of 7 nm-thick undoped AlGaAs was subsequently deposited. Finally, the structure was capped with undoped GaAs of thickness denoted by  $C_{\text{th}}$ . The surface states and/or near surface band

<sup>a)</sup>Electronic mail: victor.mendez@uaslp.mx

# Structural and Optical Characterization of Indium Zinc Oxynitride Thin Films

José Juan Ortega Sigala<sup>1,2</sup>, María Leticia Pérez Arrieta<sup>1</sup>, Hugo TototzintleHuitle<sup>1</sup>, Miguel Ángel Aguilar Frutis<sup>3</sup>, [Ciro Falcony](#)<sup>4</sup>, Víctor Hugo Méndez García<sup>2</sup> and José de Jesús Araiza Ibarra<sup>1</sup>

1. Academic Unit of Physics, UAZ, Zacatecas, C.P. 98060, México

2. CIACyT, UASLP, San Luis Potosí, C.P. 78210, México

3. CICATA, IPN, México D.F., C.P. 11500, México

4. Department of Physics, CINVESTAV, IPN, México D.F., C.P. 07360, México

Received: February 13, 2014 / Accepted: March 08, 2014 / Published: March 10, 2014.

**Abstract:** Indium zinc oxynitride (IZON) thin films were deposited on Si(100) substrates by RF reactive magnetron sputtering at different substrate temperature to study their structural and optical properties. All the films were deposited in a reactive atmosphere of nitrogen and argon. As precursor material, an IZO target (In<sub>2</sub>O<sub>3</sub>-ZnO, 90-10 wt%) with a purity of 99.99% was used. The crystalline structure of the films was analyzed by X-Ray diffraction technique (XRD), the deposited IZON thin films were practically amorphous with some polycrystalline contents for the films deposited at 100 °C and 300 °C. The refractive index and the extinction coefficient had been obtained from Spectral Ellipsometry (SE) analyses using the Classical and Adachi models, both results were qualitatively and quantitatively approximate. These optical results were analyzed and used to propose roughness values of the films surface, through of an appropriate proposal of the structure of the films. The roughness values obtained from optical models were compared with the morphological results studied by Atomic Force Microscopy (AFM), and the roughness values, obtained by direct and indirect measure, were consistent between them. The incorporated nitrogen reduced the typical crystallization of IZO and favored the deposition of transparent thin films with very flat surfaces, these results shows that the IZON has an ideal amorphous material for applications as conductive oxynitride layers.

**Key words:** Indium zinc oxynitride, spectral ellipsometry, nitrogen incorporation.

## 1. Introduction

Indium zinc oxynitride (IZON) is a new class of a transparent conducting amorphous semiconductor, which would be very useful in transparent conducting applications and it is very interesting due to its effective structural and optical properties. Typically, the most used transparent conducting amorphous material in the optoelectronic field is the indium zinc oxide (IZO) [1-3]. When an electrode is prepared using this transparent conductive oxide, this material started to crystallize in several phases of In<sub>2</sub>O<sub>3</sub> [4-6], due to the

heat treatment in the manufacturing process of the semiconductor device. At the time that this process occurred, the crystallization is not uniform and thus reliability of the element is degraded. Recently, there was reported a ternary oxynitride that contain indium, zinc, and including new metallic species like gallium or hafnium within of the IZO matrix [7, 8], which is not crystallized even if it is deposited or treated near to 300 °C. However, to deposit a layer with more than two metals in a reactive atmosphere, often, it results in a more complicated, costly and less reproducible process. For these reasons, it is preferable to use a light transmitting conductive oxynitride layer, which is not crystallized when it is exposed to heat treatment [9, 10].

---

**Corresponding author:** José Juan Ortega Sigala, Ph.D. candidate, research fields: thin films, transparent conductor oxides and oxynitrides films. E-mail: [jjosila@hotmail.com](mailto:jjosila@hotmail.com).



Jorge Huerta Ruelas\*

*Hace ya varias décadas que el descubrimiento y utilización de propiedades electrónicas y ópticas de materiales semiconductores iniciaron una revolución tecnológica sin precedentes que ha transformado profundamente el desarrollo de la humanidad.*

\*CICATA-IPN Querétaro.

**E**l semiconductor más ampliamente utilizado es el silicio (Si) en el que están basados la mayoría de los componentes electrónicos que han transformado nuestra vida diaria: computadoras, pantallas LED, fotoceldas, teléfonos inteligentes, consolas de videojuegos, por mencionar algunos. Adicionalmente al silicio existen otros materiales semiconductores con aplicaciones tecnológicas importantes, que se basan en compuestos binarios, ternarios y cuaternarios de elementos vecinos al silicio en la tabla periódica (N, Al, P, S, Zn, Ga, Ge, As, Se, Cd, In, Sb, Te), figura 1.

Los materiales compuestos con dimensiones nanométricas que contienen nitrógeno (N), y elementos como el aluminio (Al), galio (Ga), indio (In), han tenido un gran desarrollo en los últimos años. Estos nuevos nanomateriales denominados nitruros (III-N) poseen propiedades que permiten fabricar dispositivos electrónicos que mejoran o complementan sustancialmente los basados en silicio. Estos nacientes nanocomponentes, ya sea transistores, detectores de radiación o fuentes de luz, están posibilitando una gran cantidad de nuevas aplicaciones en muy diversos campos como la generación de energía fotovoltaica, electrónica de nueva generación, la salud, las comunicaciones y en, prácticamente, todos los ámbitos influidos por estos.

En México existe una gran variedad de posibilidades para el uso de estos dispositivos. Resalta en importancia la generación de energía eléctrica a partir de celdas solares

						Helium *** He 4.003 2	
Boron * B 10.81 5	Carbon * C 12.01 6	Nitrogen *** N 14.01 7	Oxygen *** O 16.00 8	Fluorine *** F 19.00 9	Neon *** Ne 20.18 10		
Aluminum * Al 26.98 13	Silicon * Si 28.09 14	Phosphorus * P 30.97 15	Sulfur * S 32.07 16	Chlorine *** Cl 35.45 17	Argon *** Ar 39.95 18		
Copper * Cu 63.55 29	Zinc * Zn 65.39 30	Gallium * Ga 69.72 31	Germanium * Ge 72.63 32	Arsenic * As 74.92 33	Selenium * Se 78.96 34	Bromine ** Br 79.90 35	Krypton *** Kr 83.80 36
Silver * Ag 107.87 47	Cadmium * Cd 112.41 48	Indium * In 114.82 49	Tin * Sn 118.71 50	Antimony * Sb 121.76 51	Tellurium * Te 127.60 52	Iodine * I 126.90 53	Xenon *** Xe 131.29 54
Gold * Au 196.97 79	Mercury ** Hg 200.59 80	Thallium * Tl 204.38 81	Lead * Pb 207.2 82	Bismuth * Bi 208.98 83	Polonium * Po [209] 84	Astatine * At [210] 85	Radon *** Rn [222] 86

Figura 1. Ubicación en la Tabla Periódica de los semiconductores básicos (Si y Ge) y de los elementos de los cuales derivan los Nitruros.